The University of Nottingham
School of Physics & Astronomy



INVESTIGATION OF ADVANCED SEMICONDUCTOR MATERIALS AND DEVICES FOR SOLAR CELL APPLICATIONS

by

Saud Meshal Alotaibi

M. Sc (Physics)

Thesis submitted to the University of Nottingham

for the degree of Doctor of Philosophy

July 2023

ABSTRACT

High performance optoelectronic p-i-n devices based on dilute nitride GaAsPN and InGaP have been fabricated and investigated as promising III-V semiconductor materials of choice for space and photovoltaic applications due their large direct band gaps and superior radiation resistance. However, there are several factors that can introduce defects in semiconductors, including growth methods, growth conditions, substrate orientation and structure design. These defects may affect the semiconductor properties and cause severe degradations in the device performance. For solar cell applications both impurities and crystalline defects have a detrimental effect on device efficiency. Hence, identification of the defects created during the growth of materials and/or processing of these devices is necessary to gain an insight into the performance of the devices. This work investigated three sets of p-(i/n/p)-n based solar cell heterostructures and the effects on their electrical, optical and structural properties of (i) the growth conditions, namely P/Ga flux ratio (5 and 21), and rapid thermal annealing (RTA) of p-$GaAs_{0.1}P_{0.89}N_{0.01}$ epilayers grown by molecular beam epitaxy on n-type GaP substrates, (ii) the GaAs substrate orientation (exact (100) and 2^0 off towards (111)B p-type GaAs substrates and doping of $In_{0.52}Ga_{0.48}P$ (i-layer is either undoped and n-doped) grown by metalorganic chemical vapour deposition (MOCVD), and (iii) the GaAs misorientation angles, namely on-axis (100) semi-insulating GaAs, 2° off, 6° off, 10° off, of p-$In_{0.52}Ga_{0.48}P$ grown by MOCVD. Several techniques, including atomic force microscopy, photoluminescence spectroscopy, Raman spectroscopy, Current-Voltage, Capacitance-Voltage, conventional DLTS, Laplace DLTS and

Solar Simulator were used to study their surface morphology, optical, electrical and photovoltaic properties. The results showed that (i) the p-$GaAs_{0.1}P_{0.89}N_{0.01}$ sample grown with a flux ratio of 5 exhibits superior electrical properties and lower defect density compared to the sample grown with a flux ratio of 21, (ii) n-doped $In_{0.52}Ga_{0.48}P$ grown on exact (100) GaAs substrate exhibits better electrical properties with a lower ideality factor and reduced trap concentrations than the undoped and n-doped $In_{0.52}Ga_{0.48}P$ samples grown on exact (100) and 2^0 off towards (111)B GaAs substrates, respectively, (iii) the p-$In_{0.48}Ga_{0.52}P$ sample grown on exact (100) GaAs substrate demonstrates better electrical and photovoltaic properties compared to samples grown on misorientated wafers.

PUBLICATIONS

1. Effects of substrate material on the electrical properties of self-assembled InAs quantum dots based laser structures.

M. Al Huwayz, D. Jameel, Saud Alotaibi, S. Alhassan, A. Almalki, N. Al Saqri, A. Alhassni, A. Almunyif, O. Lemine, A. Salhi, M. Henini.

Applied Physics A: Materials Science & Processing 129 (6), 405 (2023)

2. Current-induced degradation behaviours of InGaN/GaN multiple-quantum-well UV photodetectors: Role of electrically active defects.

Pradip Dalapati, Abdulaziz Almalki, Sultan Alhassan, Saud Alotaibi, Maryam Al Huwayz, Taiki Nakabayashi, Takashi Egawa, Makoto Miyoshi, Mohamed Henini.

Sensors & Actuators: A. Physical 347, 11393 (2022).

3. Optical properties of self-assembled InAs quantum dots based P–I–N structures grown on GaAs and Si substrates by Molecular Beam Epitaxy.

M. Al Huwayz, H.V.A. Galeti, O.M. Lemine, K.H. Ibnaouf, A. Alkaoud, Y. Alaskar , A. Salhi , S. Alhassan , S. Alotaibi, A. Almalki, A. Almunyif, A. Alhassni, D.A. Jameel, Y. Galvao Gobato, M. Henini.

Journal of Luminescence 251, 119155 (2022).

4. Investigation of the effect of substrate orientation on the structural, electrical and optical properties of n-type $GaAs_{1-x}Bi_x$ layers grown by molecular beam epitaxy.

Sultan Alhassan, Daniele de Souza, Amra Alhassni, Amjad Almunyif, Saud Alotaibi, Abdulaziz Almalki, Maryam Alhuwayz, Igor P. Kazakov, Alexey V.

Klekovkin, Vladimir I. Tsekhosh, Igor A. Likhachev, Elkhan M. Pashaev, Sergio Soutof, Yara Galvão Gobato, Noor Al Saqri, Helder Vinicius Avanço Galeti, Faisal Al mashary, Hind Albalawi, Norah Alwadai, Mohamed Henini.

Journal of Alloys and Compounds 885, 161019 (2021).

5. From cow manure to bioactive carbon dots: a light-up probe for bio imaging investigations, glucose detection and potential immunotherapy agent for melanoma skin cancer.

Frederico Hillesheim Horst, Carime Vitória da Silva Rodrigues, Pedro Henrique Pimenta Rocha Carvalho, Amanda Monteiro Leite, Ricardo Bentes Azevedo, Brenno A. D. Neto, José Raimundo Corrêa, Mônica Pereira Garcia, Saud Alotaibi, Mohamed Henini, Sacha Braun Chaves and Marcelo Oliveira Rodrigues.

RSC Adv., 11 6346-6352 (2021).

6. Structural and optical properties of n-type and p- type $GaAs_{(1-x)}Bi_x$ thin films grown by molecular beam epitaxy on (311)B GaAs substrates.

Daniele De Souza, Sultan Alhassan, Saud Alotaibi, Amra Alhassni, Amjad Almunyif, Hind Albalawi, Igor P Kazakov, Alexey V Klekovkin, Sergey A ZinovEv, Igor A Likhachev, Elkhan M Pashaev, Sergio Souto, Yara Galvao Gobato, Helder Vinicius Avanco Galeti, and Mohamed Henini.

Semiconductor Science and Technology 36, 075018 (2021).

7. The effect of strain and spatial Bi distribution on the band alignment of GaAsBi single quantum well structure. M. Gunes, O. Donmez C. Gumus, A. Erol, H.

Alghamdi, S. Alhassan, A. Alhassni, S. Alotaibi, M. Schmidbauer, H.V.A. Galeti, M. Henini.

Physics B 602, 41248 (2021).

8. The influence of point defects on AlGaN-based deep ultraviolet LEDs Zhanhong Ma, Abdulaziz Almalk, iXin Yang, Xing Wu, Xin Xi, Jing Li, Shan Lin, Xiaodong Li, Saud Alotaibi, Maryam Al huwayz, Mohamed Henini, Lixia Zhao.

Journal of Alloys and Compounds 854, 156177 (2020).

9. Investigation of deep defects and their effects on the properties of NiO/β Ga_2O_3 heterojunction diodes.

Abdulaziz Almalki, Labed Madani, Nouredine Sengouga, Sultan Alhassan, Saud Alotaibi, Amra Alhassni, Amjad Almunyif, Jasbinder Chauhan, Mohamed Henini, Helder Vinicius Avanço Galeti, Yara Galvão Gobato, Marcio Peron Franco de Godoy, Marcelo B. Andrade, Sérgio Souto, Hong Zhou, Boyan Wang, Ming Xiao, Yuan Qin, Yuhao Zhang.

Materials Today Electronics 4, 100042 (2023).

10. Uncooled mid-wavelength InAsSb/AlAsSb heterojunction photodetectors.

Yeongho Kim, Saud Alotaibi, Mohamed Henini, Byong Sun Chun, Sang Jun Lee.

APL Materials (submitted).

11. Investigation of the effect of GaAs substrate orientations and doping on the

electrical and optical properties of InGaP solar cell structures.

S.Alotaibi, M. A. Correa, A. Almalki, S. Alhassan, M. Alhuways, Y. Gobato, H. Galeti, H. Sodabanlu, M. Sugiyama, M. Henini.

Semiconductor Science and Technology (submitted). (Part of this thesis).

CONFERENCE PRESENTATIONS

- "The effect of the substrate orientation on the electrical properties of InGaP solar cells".

  The 2022 IEEE 12th International Conference "Nanomaterials: Applications & Properties (IEEE NAP-2022)", Krakow, Poland, 11-16 September 2022. (Part of this thesis).

- "Investigation of the electrical properties of As-grown and rapid thermal annealed dilute (GaAsPN/GaPN) quantum wells solar cells".

  Materials Science & Nanotechnology Conference (Future Materials 2020)

  Lisbon, Portugal, 26-28 February 2020.

- "Effect of V/III flux ratio on the electrical properties of dilute nitride GaAsPN based Solar cells".

  The 11th International Conference on Quantum Dots (QD2020).

  Munich, Germany, 7 -11 December 2020. (Part of this thesis).

ACKNOWLEDGEMENTS

"All gratitude is due to Allah for enabling me to finish my thesis and for rewarding me, especially given the challenging pandemic crisis the globe has been through over the last three years".

First and foremost, I must express my sincere thanks and admiration for my supervisor, Prof**. Mohamed Henini**, who has offered me unending encouragement, intellectual counselling, and important direction throughout this study journey. During the research and writing of this thesis, his direction and advice were of the utmost value. He deserves my thanks for giving me several chances throughout my PhD, including the chance to attend conferences overseas where I successfully presented my work and established relationships with other researchers from across the globe. I want to express my deep gratitude to the Saudi Cultural Bureau in the UK and the Saudi Ministry of Higher Education for their tremendous financial assistance in awarding me with an Overseas PhD Scholarship. I also want to express my sincere thanks to **Shaqra University** in Saudi Arabia for supporting my academic endeavors financially and for funding my studies.

I would like to thank all my collaborators, namely Dr Samy Almosni, (INSA, FOTON-OHM, UMR CNRS 6082, F-35708 Rennes, France) for providing dilute nitride GaAsPN-based p-i-n devices grown by MBE (Chapter 5); Dr Hassanet Sodabanlu (The University of Tokyo, Japan) for the MOCVD growth of InGaP-based p-i-n structures grown on exact (100) and 2^0 off towards (111B) GaAs substrates (Chapter 6), and Dr Suho Park (University of Science and Technology,

South Korea) for the MOCVD growth of InGaP-based solar cells grown on misoriented (100) GaAs substrates (Chapter 7). In addition, I would like to thank Prof. **Jorlandio F. Felix** (University of Brasilia, Brazil) for the useful discussions on the Raman and AFM characterizations, and Prof. **Yara Galvão Gobato** and Prof **Helder Vinicius Avanço Galeti** (Federal University of São Carlos, São Carlos-SP, Brazil) for the useful discussions on the photoluminescence spectroscopy characterizations. I am grateful to Mr. **Jasbinde**r (University of Nottingham) for his help in processing the devices investigated in this thesis. I would also like to thank all of my colleagues at the School of Physics and Astronomy for their friendship and support during my PhD studies.

I would like to express my special and sincere gratefulness and gratitude to my father**, Meshal**, and mother, **Nowar,** for the encouragement and support, not just during my PhD study but throughout my life. I wish also to thank my brothers and sisters for their support and encouragement.

Finally, I would like to express my gratitude to my beloved wife, **Nada**,to my dear son, **Meshal** and to my dear daughter, **Deem** for their patience and understanding throughout my research. Without the love and care I was given, I would not have the ability to succeed. I cannot thank you enough for always believing in my ability to succeed and encouraging me along the road.

Table of Contents

CHAPTER 1: INTRODUCTION 1

1.1 INTRODUCTION 1

1.2 MOTIVATION 7

1.3 SCHEME OF THE THESIS 10

CHAPTER 2: FUNDAMENTAL CONCEPTS OF SEMICONDUCTORS. 15

2.1 SEMICONDUCTORS 15

2.1.1 UNDOPED AND DOPED SEMICONDUCTORS 16

2.2 CRYSTAL STRUCTURES AND PROPERTIES 17

2.2.1CRYSTAL STRUCTURE 17

2.2.2 ENERGY BANDGAPS 21

2.2.3 DIRECT AND INDIRECT ENERGY BANDGAPS 23

2.2.4 TEMPERATURE DEPENDENT ENERGY BANDGAPS 24

2.2.5 DENSITY OF STATES 24

2.3 HETEROJUNCTION STRUCTURES 26

2.3.1 LATTICE MISMATCH 27

2.3.2 ATOM SIZE AND ELECTRONEGATIVITY 29

2.3.3 BAND ALIGNMENTS 29

2.4. GENERAL PROPERTIES OF SELECTED SEMICONDUCTOR MATERIALS 31

2.4.1. GaAs 31

2.4.2. GaInP 33

2.4.3. DILUTE GaAsN 35

2.4.4 DILUTE GaAsNP 38

2.5 WORKING PRINCIPLE OF PHOTOVOLTAIC SOLAR CELL 38

CHAPTER 3: DEFECTS IN SEMICONDUCTORS AND THEIR PROPERTIES 46
3.1 CLASSIFICATION OF DEFECTS 46
3.1.1 POINT DEFECTS 46
3.1.2 COMPLEXES OF POINT DEFECTS 48
3.1.3 LINEAR DEFECTS 49
3.2 DEFECTS AND THEIR CARRIER KINETICS 49
3.2.1 SHALLOW AND DEEP LEVEL DEFECTS 49
3.2.2 SHOCLEY-READ-HALL THEORY 51
3.3 DEFECTS IN COMPOUND SEMICONDUCTORS 57
3.3.1 DEFECTS IN GaAs 57
3.3.2 DEFECTS IN DILUTES NITRIDES: GaAsN 58
3.3.3 DEFECTS IN InGaP 60
3.3.4 DEFECTS IN GaAsPN 61
CHAPTER 4: EXPERIMENTAL TECHNIQUES 69
4.1 p-n Junction 69
4.1.1 P-N JUNCTION UNDER BIAS CONDITIONS 76
4.1.2 DEPLETION LAYER CAPACITANCE 78
4.2 CURRENT- VOLTAGE CHARACTERISATION 79
4.3 DEEP LEVEL TRANSIENT SPECTROSCOPY (DLTS) 82
4.3.1 CAPACITANCE TRANSIENTS 82
4.3.2 CONVENTIONAL DLTS 86
4.4 LAPLACE DLTS SPECTROSCOPY 88
4.5 SYSTEM HARDWARE IMPLEMENTATION 90
4.5.1 DESCRIPTION OF SYSTEM HARDWARE 90
4.6 SYSTEM SOFTWARE 94
4.6.1 CONVENTIONAL DLTS MEASUREMENTS MODE 95
4.6.2 LAPLACE TRANSIENT PROCESSING MODE 95

4.6.3 DLTS AND LAPLACE DLTS MEASUREMENTS 96

4.7 Electrochemical Capacitance Voltage Profiling 96

4.8 PHOTOLUMINESCENCE (PL) SPECTROSCOPY 99

4.8.1 SPECTROMETER AND DETECTORS 100

4.9 RAMAN SPECTROSCOPY 103

4.10 SOLAR CELL CHARACTERISTICS 105

CHAPTER 5: THE EFFECTS OF V(P)/III(Ga) FLUX RATIO AND THERMAL ANNEALING ON THE ELECTRICAL PROPERTIES OF DILUTE NITRIDE GaAsPN-BASED P-I-N SOLAR CELL STRUCTURES 110

5.1. INTRODUCTION 110

5.2 SAMPLE DETAILS 111

5.3. EFFECT OF V/III FLUX RATIO ON THE ELECTRICAL PROPERTIES OF DILUTE NITRIDE GaAsPN BASED P-I-N SOLAR CELL STRUCTURES 113

5.3.1 I-V CHARACTERISTICS 113

5.3.2 C-V MEASUREMENTS 118

5.3.3 DEEP LEVEL TRANSIENT SPECTROSCOPY (DLTS) AND LAPLACE DLTS CHARACTERISITICS OF GaAsPN DIODES GROWN WITH DEFERENT V(P)/III(Ga) FLUX RATIOS 119

5.4. EFFECT OF RAPID THERMAL ANNEALING ON ELECTRICAL PROPERTIES OF GaAsPN-BASED SOLAR CELL STRUCTURES GROWN WITH DIFFERENT V(P)/III(Ga) FLUX RATIOS. 124

5.4.1 I-V CHARACTERISTICS 124

5.4.2 C-V MEASUREMENTS 129

5.4.3 DLTS AND LAPLACE DLTS MEASUREMENTS 131

5.5. Summary 136

CHAPTER 6: INVESTIGATION OF THE EFFECT OF GaAs SUBSTRATE ORIENTATIONS AND InGaP DOPING ON THE ELECTRICAL AND OPTICAL PROPERTIES OF InGaP-BASED SOLAR CELL STRUCTURES 144

6.1 INTRODUCTION 144

6.2 EXPERIMENTAL DETAILS 146

6.3 PHYSICAL MODELS 147

6.4 RESULTS AND DISCUSSION 150

6.4.1 EFFECT OF GaAs SUBSTRATE ORIENTATION ON CURRENT DENSITY 150

6.4.2 EFFECT OF GaAs SUBSTRATE ORIENTATION ON CAPACITANCE –VOLTAGE CHARACTERISTICS 154

6.4.3 DLTS AND LAPLACE DLTS ANALYSIS 156

6.4.4 SIMULATION OF THE EFFECT OF GaAs SUBSTRATE MISCUT ANGLE AND DOPING OF InGaP SOLAR CELL STRUCTURE ON THE TRANSPORT MECHANISM 160

6.4.5 PHOTOLUMINESCENCE 163

6.5 SUMMARY 171

CHAPTER 7: EFFECTS OF GaAs SUBSTRATE ORIENTATION ON THE STRUCTURAL, OPTICAL, ELECTRICAL AND PHOTOVOLTAIC PROPERTIES OF InGaP-BASED SOLAR CELLS 184

7.1 INTRODUCTION 184

7.2 SAMPLE DETAILS 185

7.3 RESULTS AND DISCUSSION 187

7.3.1 RAMAN SPECTROSCOPY 187

7.3.2. ATOMIC FORCE MICROSCOPES (AFM) 190

7.3.3 CURRENT-VOLTAGE (I-V) MEASUREMENTS 191

7.3.4 CAPACITANCE-VOLTAGE (C-V) MEASUREMENTS 196

7.3.5 DLTS AND LAPLACE DLTS MEASUREMENTS 197

7.3.6: DISCUSSION OF THE ROLE OF THE DEFECTS ON THE PERFORMANCE OF SOLAR CELLS GROWN ON VARIOUS GaAs MISORIENTED SUBSTRATES 200

7.4: SUMMARY 204

REFERENCES 205

CHAPTER 8: CONCLUSION AND FUTURE WORK 211

8.1 CONCLUSION 211

8.1.1 THE EFFECT OF V(P)/III(Ga) FLUX RATIO AND THERMAL ANNEALING ON THE ELECTRICAL PROPERTIES OF DILUTE NITRIDE GaAsPN 211

8.1.2 INVESTIGATION OF THE EFFECT OF GaAs SUBSTRATE ORIENTATIONS AND InGaP DOPING ON THE ELECTRICAL AND OPTICAL PROPERTIES OF InGaP-BASED SOLAR CELL STRUCTURES 212

8.1.3 EFFECT OF GaAs SUBSTRATE ORIENTATION ON THE ELECTRICAL AND OPTICAL PROPERTIES OF InGaP SOLAR CELLS 213

8.2 SUGGESTIONS FOR FUTURE WORK 214

CHAPTER 1: INTRODUCTION

1.1 INTRODUCTION

With the rapid development of societies and the corresponding increase in energy consumption, coupled with the challenges of industrial development and climate change, the global community is increasingly recognizing energy demand as one of the major problems that needs to be addressed. Most sources of electric energy nowadays have many disadvantages, such as security (nuclear power), finite fossil fuel reserves (oil, gas, coal), negative environmental impact (hydropower), and so on. The world community faces a significant challenge in reducing fossil fuel consumption, particularly by transitioning partially and gradually to renewable energies. This necessitates major developments in energy infrastructures to support the integration and widespread adoption of renewable energy sources. Numerous projects have been undertaken by scientists focusing on harnessing renewable energy from various sources such as water, wind, biomaterials, and solar radiation. These initiatives aim to explore and utilize the potential of these resources to generate sustainable and clean energy for diverse applications. Photovoltaics (PV) is a clean and powerful way to generate electricity and fulfil most countries' growing energy demand. PV is one of the most efficient methods of harvesting solar energy for electricity generation, converting sunlight directly into electricity using solar cells (SCs). One of the key motives for developing high efficiency solar cells is to reduce the use of non-renewable energy that has been the main cause of global warming and has raised serious environmental impacts for future commercial development of electricity mass production. Furthermore, solar energy stands out

among other renewable alternatives due to its abundance. However, significant breakthroughs in energy generation from solar power have been somewhat limited due so far to two main challenges: the high cost associated with solar technologies and the intermittent nature of solar radiation. Nonetheless, solar energy technologies are currently experiencing a remarkable rate of growth, and there is a strong possibility that within the next 40 years, solar energy will emerge as one of the primary global energy source [1]. Solar radiation includes electromagnetic radiation spanning a broad spectrum. This spectrum includes various wavelengths, ranging from ultraviolet (100 nm - 400 nm) to visible light (400 nm - 700 nm) and infrared radiation (700 nm and above). The solar spectrum consists of significant wavelengths components, which play crucial roles in various applications of solar energy on a global scale. These wavelength components have particular significance in photovoltaic (PV) systems. Figure 1.1 illustrates the spectral irradiance of solar radiation as a function of photon wavelength. The term "irradiance", which refers to the amount of solar radiation that is incident on a square meter of the Earth's atmosphere or surface, is expressed in units of Watts per square meter (W/m^2).

The solar irradiance before it enters the Earth's atmosphere has a value of approximately 1,366 W/m^2. This value is commonly referred to as Air Mass Zero (AM0) [2]. When solar radiation passes through the Earth's atmosphere, it is attenuated by various factors, including the ozone layer (O_3), water molecules, nitrogen molecules, CO_2, and dust. By the time the incoming solar radiation reaches the Earth's surface at sea level, the solar irradiance is reduced to approximately 1000 W/m^2, which is identified as air mass 1.5 (AM 1.5) (ASTM G -173 International standard ISO 9845-1, 1992) and is the defined standard for terrestrial use [3].

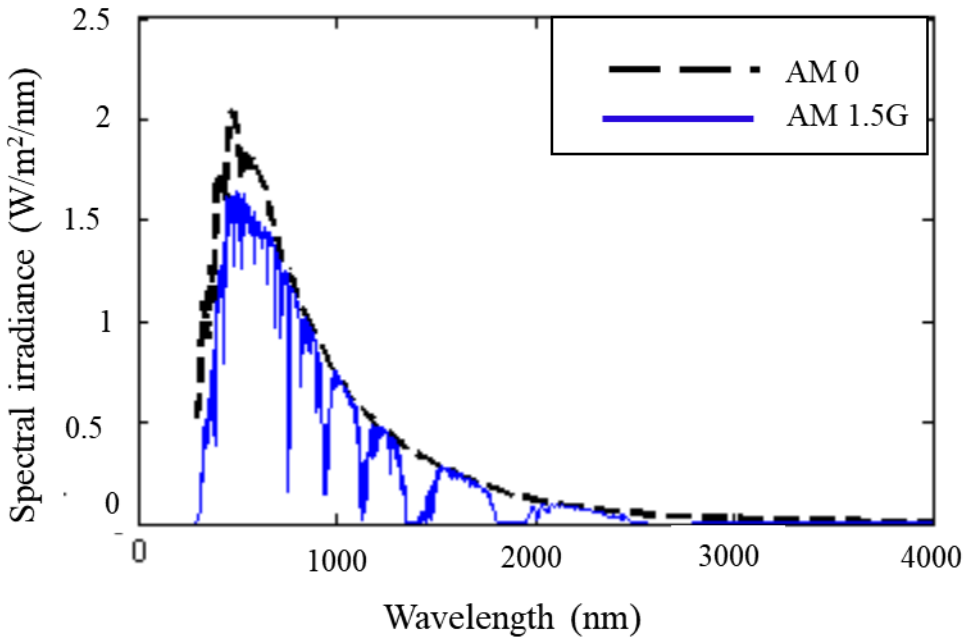


Figure 1.1: The solar spectral irradiance as a function of photon wavelength [4]. The value of irradiance is also expressed in $W/m^2/nm$, which is a measure of the flux per nm at the specified wavelength incident normally onto an element of the surface divided by the area of the surface element in m^2.

Up to date, solar cells have been classified into three different generations based on the types of materials used. These generations represent advancements and innovations in solar cell technology. The first-generation solar cells are produced on silicon wafers. The second generation utilises semiconductor thin film technology, including materials such as amorphous silicon (a-Si), copper indium gallium selenide (CIGS), polycrystalline silicon, and cadmium telluride (CdTe) as the basis for these solar cells. The third generation is based on a range of new materials, such as quantum dots, multi-junction (MJ) solar cells, nanotubes, silicon nanowires and organic materials [5, 6].

The worldwide research-based different types of PV technologies having the best power conversion efficiencies from 1975 to 2022 are shown in Figure 1.2. The highest certified efficiency of 47.6 % for four-junction III-V solar cell was developed by German photovoltaic research institute, namely Fraunhofer Institute for Solar Energy Systems (ISE) [7].

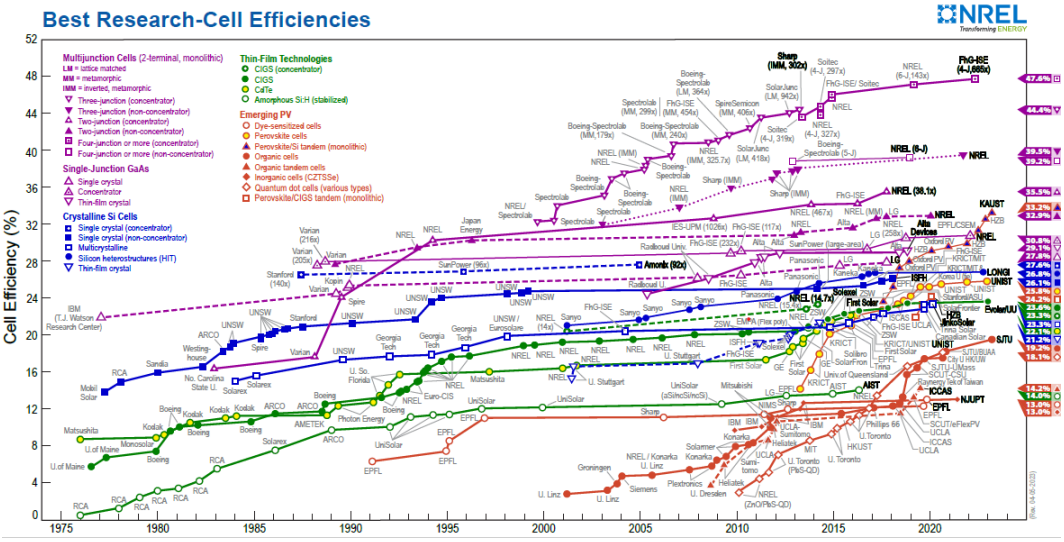


Figure 1.2: Chart showing the highest confirmed conversion efficiencies for research cells for a range of photovoltaic technologies.

(NREL: https://www.nrel.gov/pv/interactive-cell-efficiency.html)

The first generation of photovoltaics, which is based on silicon wafers, accounted for 80% of the solar cell market [8] due to their great power efficiency. The conventional and highly efficient solar cell technology based on single crystalline silicon has demonstrated notable advancements over the years. In 2004, the reported efficiency of these cells was 24.7%, which increased to 26.7% in 2022 [9]. The advantages of these types of solar cells are stability, a longer lifetime, and improved efficiency. However, one of the key concerns with this generation is the high cost

of production. Another issue with single crystal silicon solar cell panels is that as the temperature increases above 25^0 C, the efficiency of the solar cell decreases [8].

Due to the limitations of efficiency and high cost of first-generation solar cells, second-generation solar cells were developed. These solar cells are based on thin-films technology. The most successful materials for second generation are amorphous Silicon, CIGS, and CdTe [8]. CdTe and CIGS have typically power conversion efficiency of about 21-23 % under air mass 1.5 global spectrum (AM1.5G) with an incident irradiance of 1000 $W.m^{-2}$ at 25 ^{0}C [10]. In terms of cost-effectiveness, the second-generation solar PV cells have an advantage, although they exhibit lower power conversion efficiency compared to crystalline Si-based solar PV cells. However, despite their potential for mass production, the second-generation cells still face unresolved challenges and issues in achieving competitive efficiency levels at a reasonable price [11].

Among all the solar cell technologies mentioned above and beyond, III-V multijunction solar cells which are part of the third generation are the unchallenged world record holder for high efficiency photovoltaics. State-of-the-art III-V multijunction solar cells have achieved a record efficiency of 47.6% as shown in Figure 1.2. This is the highest conversion efficiency achieved till today by using multi-junction cells consisting of III/V semiconductor materials, such as GaInP/GaAs/InGaAs). However, third generation solar cells are expensive and most technologies in this generation are used in space applications.

Dilute III-V nitride semiconductor alloys have recently gained a lot of interest for applications in optoelectronics, especially for solar cells [12]. Among these alloys, GaAsPN alloys which are grown by molecular beam epitaxy (MBE) or

metalorganic vapor phase epitaxy (MOVPE) are very attractive materials for solar cells due to the high-efficiency multijunction cells and the possibility of lattice matching with GaP [13]. In general, this material whose component elements have been substituted by elements of differing size and/or electronegativity [14] is a highly mismatched alloy (HMA). The electrical and optical properties of GaAsPN with a small amount of nitrogen require detailed studies before they can be used. It is also known that increasing N composition causes crystal quality degradation which may have an impact on the efficiency of future devices. This degradation is characterised by an increase in nonradiative recombination processes via uniformly distributed defect states and the formation of a N-related defect level [14].

Gallium Indium phosphide ($Ga_xIn_{1-x}P$), which has been widely used in high efficiency solar cell devices, is a III–V compound semiconductor with a bandgap of 1.9 eV (for x= 0.52) and is lattice-matched to GaAs substrates. InGaP has superior properties [15, 16] than the well-known AlGaAs alloy, including a lower surface recombination velocity, a lower density of DX (a deep level associated with donors in III-V semiconductors) recombination centres, a lower affinity to oxygen (it is simpler to grow high crystal quality InGaP/GaAs heterolayers than AlGaAs/GaAs ones which are prone to oxidation during epitaxial growth) and a higher etching selectivity between InGaP/GaAs layers compared to AlGaAs/GaAs junctions [17].

Defects, which introduce deep levels in the semiconductor's bandgap, act as efficient recombination centres and affect device performance. As a result, significant research efforts have been made to better understand, improve and control their presence in the materials. Deep level transient spectroscopy (DLTS)

and high resolution Laplace spectroscopy (LDLTS) are powerful techniques for characterising and identifying deep levels defects [18].

1.2 MOTIVATION

p-i-n devices based on dilute nitride GaAsPN and InGaP are promising for space and photovoltaic applications due their large direct bandgaps and superior radiation resistance. However, there are several factors that can introduce defects in semiconductors, including growth methods, growth conditions, substrate orientation and structure design. These defects may affect the semiconductor properties and cause severe degradations in the device performance. For solar cell applications both impurities and crystalline defects have a detrimental effect on device efficiency. Therefore, investigating and identifying defects (both deep and shallow levels within the bandgap) created during the growth of semiconductor materials and/or processing, are critical for the future of manufacturing devices and for gaining an insight into their performance. In this regard, DLTS is a powerful technique to investigate electrically active defects in semiconductor materials and devices.

The main motivation of this thesis is to investigate the electrically active defects present in various GaAsPN and InGaP semiconductor based solar cell structures.

GaAsPN has an important impact on developing GaP-based optoelectronics and multijunction solar cells, but the complex nature of the nitrogen incorporation into GaAsP is still not fully understood. The control and understanding of the incorporation of nitrogen during GaAsPN MBE (Molecular Beam Epitaxy) growth

continues to play an important role in GaP crystal growth. Therefore, a study of the effects of the V(P)/III(Ga) flux on the electrical properties of p-i-n GaAsPN based solar cell structures grown on n-type GaP substrates by MBE is crucial in order to improve their properties for solar cell applications. Post-growth treatments, such as thermal annealing, are well known to reduce the concentration of defects, annihilate and passivate completely defects. It is therefore important to study the effect of the thermal annealing on the electrical properties of GaAsPN heterostructures grown with different flux ratios in order to understand the influence of the growth conditions.

InGaP, which has a large direct bandgap of 1.9 eV with superior radiation resistance, has been regarded as a promising material of choice for space and concentrated photovoltaic applications. However, depending on the growth conditions and substrate orientation, CuPtB-type ordering can appear in lattice matched InGaP-on-GaAs layers. Furthermore, localization and delocalization of carriers may simultaneously exist due antiphase boundaries (APBs) at the boundary of ordered domains, which have been shown to produce a pronounced impact on the electrical and optical properties of materials. This work investigates the effect of the GaAs substrate orientation ((100) and (100) 2^0 off towards (111B)) and doping on the electrically and optically active defects in p-(i/n)-n GaAs/$In_{0.48}Ga_{0.52}P$/GaAs solar cell heterostructures grown by metalorganic chemical vapour deposition (MOCVD).

The efficiencies of GaAs and GaInP III-V compound semiconductors based solar cells continue to improve as material quality and device processing are optimised. The band gap of GaInP grown lattice matched to GaAs depends on the growth conditions and substrate misorientation. These changes are the result of the

spontaneous ordering during the growth of the cation-site elements (Ga and In) in planes parallel to the (111) and reductions in the bandgap over 100 meV can appear. InGaP grown using MOCVD technique is known to have a CuPt-type ordering of alternating In-rich and Ga-rich monolayers, primarily on the $(\bar{1}11)$ and $(1\bar{1}1)$ crystallographic planes. Strain energy minimization is the main driving force for this ordering in InGaP epitaxial layers, with a large difference in bond length between the In-P and Ga-P. However, they cause significant changes in the electronic and optical properties, such as bandgap narrowing. It is well-known that the degree of CuPt-type atomic ordering is dependent on substrate's misorientation, and the change of degree of ordering of CuPt leads to corresponding changes in lattice constant. For example, the reported poor electrical quality of highly ordered GaInP solar cells, which were grown on 6^0 misoriented towards (111)B GaAs substrates, was attributed to traps introduced by the ordered/disordered domains matrix or growth native defects [19]. Therefore, studying the defects caused by substrate misorientation angles can provide useful information for fabricating high performance devices. In this work, the influence of substrate misorientation on the surface morphology, optical, electrical and photovoltaic properties of p-type InGaP-based solar cells grown by MOCVD on (100) GaAs substrates misoriented by θ_S= 0° (exact), 2°, 6°, and 10° towards (111)A are thoroughly investigated.

Several techniques, including atomic force microscopy (AFM), photoluminescence (PL) spectroscopy, Raman spectroscopy Current-Voltage (I-V), Capacitance-Voltage (C-V), conventional DLTS, Laplace DLTS (LDLTS) and Solar Simulator were used to study the surface morphology, optical, electrical and photovoltaic properties of: (i) as-grown and annealed p-i-n GaAsPN solar cells grown by MBE with different V(P)/III(Ga) flux ratios, (ii) n-doped and undoped InGaP solar cells

grown by MOCVD on p-GaAs substrates with different orientations, namely exact (100) and 2^0 off towards (111)B, (iii) p-InGaP solar cells grown by MOCVD on misoriented GaAs substrates, namely (100) exact, 2^0 off, 6^0 off and 10^0 off towards (111)A.

1.3 SCHEME OF THE THESIS

The structure of this thesis is as follows:

Chapter 1: contains an introduction of semiconductor materials and structures investigated and the motivations of the thesis.

Chapter 2: gives a description of the basic concepts of semiconductors, crystal structure and the principles of heterostructure devices. The properties of GaAs, GaAsN, GaAsPN and InGaP materials and the working principle of photovoltaic solar cell are also covered in this chapter.

Chapter 3: provides information on defects in semiconductors, theoretical background of carrier kinetics, and literature survey of defects in GaAs, InGaP, GaAsN and GaAsPN.

Chapter 4: describes the operating principles of the experimental techniques used in this thesis including current-voltage (I-V), capacitance-voltage (C-V), DLTS, Laplace DLTS, photoluminescence spectroscopy, Raman spectroscopy and Solar Simulator. Furthermore, the hardware and software required to implement these methods are also discussed. The experimental conditions and setups are also discussed.

Chapter 5: discusses the effect of electrically active defects on the electrical properties of a set of p-GaAsPN solar cell structures grown by Molecular Beam Epitaxy (MBE) using I-V, C-V, DLTS and Laplace DLTS measurements.

Chapter 6: discusses the effect of the intentional and unintentional doping, namely n-doped and undoped, on the electrical and optical properties of InGaP solar cell structures grown on exact (100) and 2^0 off towards (111)B GaAs substrates by metalorganic chemical vapour deposition (MOCVD) technique using I-V, C-V, DLTS and Laplace DLTS and PL measurements. Furthermore, I-V characteristics were analysed and modelled using Silvaco Technology Computer-Aided Design (TCAD) to understand the transport mechanisms in devices based on InGaP grown on different GaAs substrates.

Chapter 7: describes the effect of GaAs substrate orientation on the surface morphology, optical, electrical and photovoltaic properties of p-InGaP based solar cells grown by MOCVD using AFM, Raman spectroscopy, I-V, C-V, DLTS, Laplace DLTS and Solar Simulator measurements.

Chapter 8: gives a summary of the research work performed in this thesis and future work suggestions

REFERENCES

[1] N. L. Panwar, S. C. Kaushik, and S. Kothari, "Role of renewable energy sources in environmental protection: A review," *Renewable and sustainable energy reviews*, vol. 15, no. 3, pp. 1513-1524, 2011.

[2] C. A. Gueymard, "The SMARTS spectral irradiance model after 25 years: New developments and validation of reference spectra," *Solar Energy*, vol. 187, pp. 233-253, 2019.

[3] A. O. M. Maka, "Performance analysis and characterisation of a high concentrating solar photovoltaic receiver," Heriot-Watt University, 2020.

[4] H. Liang, F. Wang, L. Yang, Z. Cheng, Y. Shuai, and H. Tan, "Progress in full spectrum solar energy utilization by spectral beam splitting hybrid PV/T system," *Renewable and Sustainable Energy Reviews*, vol. 141, p. 110785, 2021.

[5] N. Kant and P. Singh, "Review of next generation photovoltaic solar cell technology and comparative materialistic development," *Materials Today: Proceedings*, vol. 56, pp. 3460-3470, 2022.

[6] J. Y. u. Muhammad, A. B. Waziri, A. M. Shitu, U. M. Ahmad, M. H. Muhammad, Y. Alhaji, A. T. Olaniyi, and A. A. Bala, "Recent progressive status of materials for solar photovoltaic cell: A comprehensive review," *Sci. J. Energy Eng*, vol. 7, no. 4, pp. 77-89, 2019.

[7] B. M. Y. Jeco-Espaldon, R. Tamaki, M. Giteau, H. Xu, N. Ahsan, R. R. King, and Y. Okada, "Electrical passivation of III-V multijunction solar cells with luminescent coupling effect," *Solar Energy Materials and Solar Cells*, vol. 249, p. 112045, 2023.

[8] K. Vijayan, S. Vijayachamundeeswari, K. Sivaperuman, N. Ahsan, T. Logu, and Y. Okada, "A review on advancements, challenges, and prospective of copper and non-copper based thin-film solar cells using facile spray pyrolysis technique," *Solar Energy,* vol. 234, pp. 81-102, 2022.

[9] M. Green, E. Dunlop, J. Hohl-Ebinger, M. Yoshita, N. Kopidakis, and X. Hao, "Solar cell efficiency tables (version 57)," *Progress in photovoltaics: research and applications,* vol. 29, no. 1, pp. 3-15, 2021.

[10] M. A. Green, E. D. Dunlop, J. Hohl-Ebinger, M. Yoshita, N. Kopidakis, and X. Hao, "Solar cell efficiency tables (Version 58)," *Progress in Photovoltaics: Research and applications,* vol. 29, no. 7, pp. 657-667, 2021.

[11] B. P. Singh, S. K. Goyal, and P. Kumar, "Solar PV cell materials and technologies: Analyzing the recent developments," *Materials Today: Proceedings,* vol. 43, pp. 2843-2849, 2021.

[12] S. Almosni, P. Rale, C. Cornet, M. Perrin, L. Lombez, A. Létoublon, K. Tavernier, C. Levallois, T. Rohel, and N. Bertru, "Correlations between electrical and optical properties in lattice-matched GaAsPN/GaP solar cells," *Solar Energy Materials and Solar Cells,* vol. 147, pp. 53-60, 2016.

[13] J. Geisz, D. Friedman, and S. Kurtz, "GaNPAs solar cells lattice-matched to GaP," in *Conference Record of the Twenty-Ninth IEEE Photovoltaic Specialists Conference, 2002.,* 2002, pp. 864-867: IEEE.

[14] M. Wełna, K. Żelazna, A. Létoublon, C. Cornet, M. Zieliński, and R. Kudrawiec, "Radiative and nonradiative recombination processes in GaNP

(As) alloys," *Materials Science and Engineering: B*, vol. 276, p. 115567, 2022.

[15] D. Ahmari, M. Fresina, Q. Hartmann, D. Barlage, M. Feng, and G. Stillman, "InGaP/GaAs heterojunction bipolar transistor grown on a semi-insulating InGaP buffer layer," *IEEE Electron Device Letters*, vol. 18, no. 11, pp. 559-561, 1997.

[16] W.-S. Lour, J.-H. Tsai, L.-W. Laih, and W.-C. Liu, "Influence of channel doping-profile on camel-gate field effect transistors," *IEEE Transactions on Electron Devices*, vol. 43, no. 6, pp. 871-876, 1996.

[17] M. Bosi and C. Pelosi, "The potential of III-V semiconductors as terrestrial photovoltaic devices," *Progress in Photovoltaics: Research and Applications*, vol. 15, no. 1, pp. 51-68, 2007.

[18] D. Lang, "Deep-level transient spectroscopy: A new method to characterize traps in semiconductors," *Journal of applied physics*, vol. 45, no. 7, pp. 3023-3032, 1974.

[19] I. Garcia, I. Rey-Stolle, C. Algora, W. Stolz, and K. Volz, "Influence of GaInP ordering on the electronic quality of concentrator solar cells," *Journal of Crystal Growth*, vol. 310, no. 23, pp. 5209-5213, 2008.

CHAPTER 2: FUNDAMENTAL CONCEPTS OF SEMICONDUCTORS

This chapter sheds light on the basic properties of semiconductors such as temperature dependent energy gaps, crystal structures, energy gaps (direct and indirect energy gaps) and density of states. The chapter also offers insight into heterostructures and the attributes of lattice mismatch, atom size and electronegativity and band alignment associated with these heterostructures. It also highlights the properties of some important III-V semiconductors, namely GaAs, InGaP, dilutes GaAsN and GaAsPN. In addition, the working principle of photovoltaic solar cell are also covered in this chapter.

2.1 SEMICONDUCTORS

Semiconductors have lately gained immense popularity and wide-ranging applications in contemporary electronics and optoelectronics. Semiconductors have been found to make up the basic and essential unit of most of the components found in electronic and optical devices [1]. Good examples of these devices are computers (memories and CPUs), optical storage media (lasers for CDs and DVDs players), optical fibre telecommunication (lasers and photo-detectors), high efficiency solar cells, screens (thin film transistors, LEDs), projection (laser diodes), LEDs [2] etc. In short, the research on semiconductor materials has become an attractive topic for fundamental research.

Semiconductors are defined as materials with lower electrical conductivity in comparison to the good conductor but higher than an insulator. The normal range of electrical resistivity of a semiconductor is between 10^{-2} and 10^{9} Ω.cm. There

are two types of semiconductors including elementary and compound semiconductors where the former contain a single element as its constituent (e.g. Si and Ge from group IV in the periodic table) while the latter contains multiple elements as its constituents (belonging for example to groups III and V, and II and VI of the periodic table). The compound semiconductors with two elements are referred to as binary compounds. For instance, GaAs and GaP are semiconductor materials containing two elements each. The semiconductor materials containing three elements are referred to as ternary compounds such as InGaP and GaAsN.

2.1.1 UNDOPED AND DOPED SEMICONDUCTORS

Semiconductor materials can be classified according to the type of doping they contain. Undoped semiconductors represent pure forms of semiconductor materials and are commonly known as intrinsic semiconductors. However, even intrinsic semiconductors that are deemed as pure forms of semiconductors are not free from impurities and may contain small amounts of impurities. These impurities could affect the electrical properties of the material. A pure semiconductor may also be defined when the number of electrons in the conduction band is equal to the number of holes in valence band. Moreover, a pure or intrinsic semiconductor becomes an insulator and does not conduct electrical charge at zero absolute temperature due to the filled valence band and empty conduction band. However, if a thermal or photo excitation is applied to the intrinsic semiconductor, the conductivity will increase.

Doping is the process whereby small amounts of impurities are added in pure semiconductor materials. When a semiconductor is doped after the addition of other atoms in the host lattice, it is referred to as extrinsic semiconductor. The

addition of the dopant material increases the number of electrons or holes leading to the conversion of a pure semiconductor into an n- or p-type semiconductor. For instance, if a semiconductor made of pure Si is doped with pentavalent impurity material (i.e. composed of the element belonging to group V of the periodic table) such as As, then the four electrons in Si react with five electrons in As leading to the formation of four bonds and one free electron resulting in an n-type conductivity. In the same manner, if the semiconductor is made of pure Si is doped with trivalent impurity material (i.e. composed of the element belonging to group III of the periodic table) such as boron (B), then the four valence electrons in Si react with three valence electrons in B leading to the formation of three covalent bonds and one free hole, and therefore leading to a p-type conductivity. Hence, formation of a p-type semiconductor involves using dopant atoms that result in the formation of holes.

2.2 CRYSTAL STRUCTURES AND PROPERTIES

Another important attribute that affects the performance of semiconductor devices is the crystal structure, which is formed by the atoms arrangement in the crystals.

2.2.1CRYSTAL STRUCTURE

The ideal crystal structure is composed of a unit cell, which includes a set of atoms arranged in an infinite periodically repetitive arrangement. There are various forms of crystal structures, but the most common ones are simple cubic (sc), body-centred cubic (bcc), and face-centred cubic (fcc) as shown in Fig. 2.1. The fundamental form of crystalline structure is simple cubic lattice with arrangement of atoms on the corners of a cubic structure (Fig. 2.1 (a)). Another crystalline structure is the body-centred cubic (bcc) lattice which is only different from the

simple cubic lattice in that the former also involves arrangement of atoms at the cube's centre besides the arrangement of atoms on cube's corners as shown in Fig. 2.1 (b). Fig. 2.1 (c) shows the face-centred cubic lattice which involves arrangement of a single atom in the centre of the facets of the cube besides the arrangement of atoms on each corner of the cube.

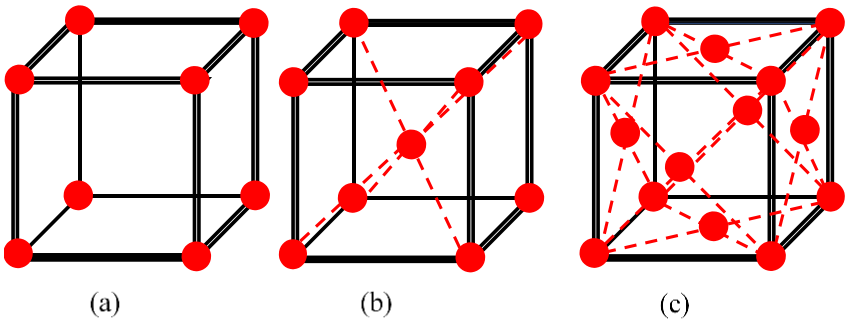


Fig. 2.1: Crystal structures: (a) simple cubic lattice (b) body-centred cubic lattice and (c) face-centred cubic lattice.

Some crystal structures are more common than others in semiconductor materials such as diamond crystal structure (Fig. 2.2 (a)) and zinc blende structure (Fig. 2.2 (b)). The atoms in each of these crystal structure types form covalent bonds with four neighbouring atoms of tetrahedron structure. Consequently, the structure obtained looks like a couple of overlapping fcc lattices.

All atoms in a diamond structure are similar. On the other hand, two different kinds of atoms are present in a zinc blende structure. Diamond structures can be seen in Si, Ge and C elemental semiconductors, whereas zinc blende structures are evident in GaAs, GaP, and InAs semiconductors composed of elements from group III and group V of the periodic table.

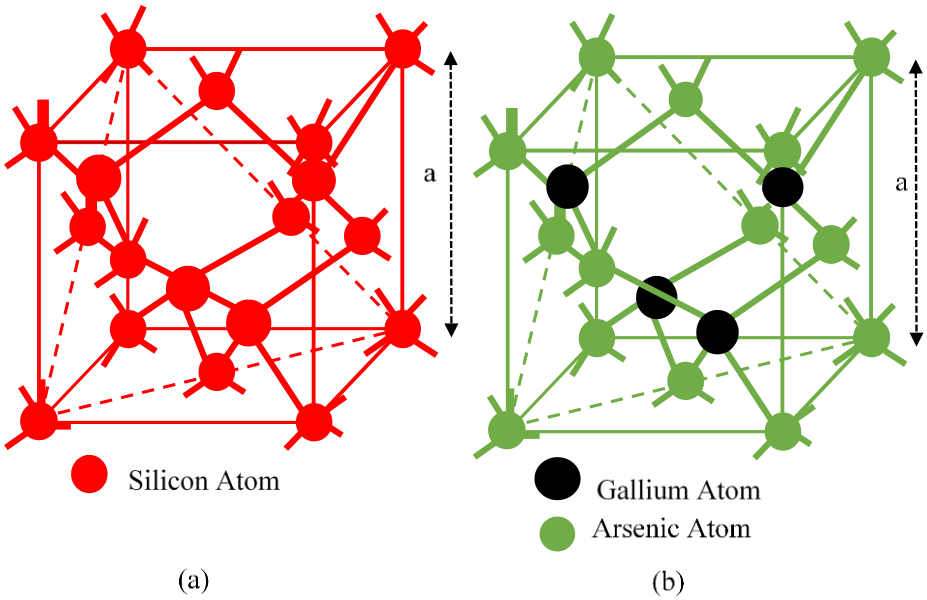


Fig. 2.2: Illustration of (a) diamond structure for Si where both types of atomic sites are occupied by Si and (b) zinc blende structure for GaAs where the sites are occupied by Ga and As atoms; a is the lattice constant [3].

It is essential to have complete information about the orientation of the semiconductor crystal and the properties of its surface which is necessary for semiconductor epitaxial growth and fabrication processes. This information about the arrangement of semiconductor crystal is obtained by using Miller indices.The Miller index involves the use of three primitive basis vectors ***a***, ***b***, and ***c.*** Each of these vectors indicates the alignment of the crystalline structure along (x, y, and z). Figure 2.3 shows an example of a lattice plane orientation described by Miller indices (322).

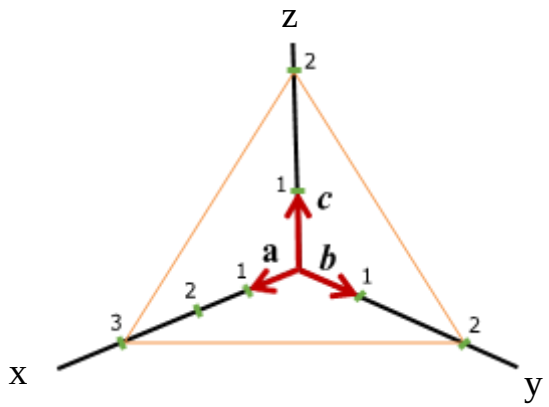


Fig. 2.3: Illustration of a plane having Miller indices (322)

A crystal structure will remain the same under any translation through a direct lattice vector (***R***), which is the sum of these primitive vectors as:

$$\boldsymbol{R} = p\boldsymbol{a} + q\boldsymbol{b} + r\boldsymbol{c} \tag{2.1}$$

In the above equation, *p*, *q* and *r* represent integers.

The reciprocal lattice basis vectors ($\boldsymbol{a}^*$, $\boldsymbol{b}^*$, and $\boldsymbol{c}^*$) and the primitive vectors (***a, b,*** and ***c***) are related as follows:

$$\boldsymbol{a}^* = \boldsymbol{2\pi}\left[\frac{(\boldsymbol{b}\times\boldsymbol{c})}{\boldsymbol{a}.(\boldsymbol{b}\times\boldsymbol{c})}\right] \tag{2.2}$$

$$\boldsymbol{b}^* = \boldsymbol{2\pi}\left[\frac{(\boldsymbol{a}\times\boldsymbol{c})}{\boldsymbol{a}.(\boldsymbol{b}\times\boldsymbol{c})}\right] \tag{2.3}$$

$$\boldsymbol{c}^* = \boldsymbol{2\pi}\left[\frac{(\boldsymbol{a}\times\boldsymbol{b})}{\boldsymbol{a}.(\boldsymbol{b}\times\boldsymbol{c})}\right] \tag{2.4}$$

In the above equations, $\boldsymbol{a}^*.\boldsymbol{a} = 2\pi$ and $\boldsymbol{a}.\boldsymbol{b}^* = 0$ and so forth.

The denominators in the above equations, which are the same because $\boldsymbol{a}.\boldsymbol{b}\times\boldsymbol{c}=\boldsymbol{b}.\boldsymbol{c}\times\boldsymbol{a}=\boldsymbol{c}.\boldsymbol{a}\times\boldsymbol{b}$, define the volume that these vectors (***a***, ***b***, ***c***) enclose.

The general reciprocal lattice vector (***G***) is defined as:

$$G = h\,\boldsymbol{a}^* + \boldsymbol{k}\,\boldsymbol{b}^* + l\,\boldsymbol{c}^* \tag{2.5}$$

where h, *k* and *l* represent integers.

Moreover, reciprocal lattice (***G***) and direct lattice (***R***) are related as follows:

$$\boldsymbol{G} \cdot \boldsymbol{R} = 2\pi \times \text{integer} \tag{2.6}$$

2.2.2 ENERGY BANDGAPS

Energy gap or bandgap is an important property in solid-state physics. It indicates the energy difference between the valence band (VB) and the conduction band (CB). It is denoted by Eg as shown in Figure. 2.4. The energy gap of the materials determines if the material is an insulator, semiconductor or metal. Materials with extremely high Eg (e.g. Eg > ~6 eV) are named insulators (Figure 2.4 a), materials with Eg between ~0.17 eV (InSb) and ~ 6 eV (AlN) are classified as semiconductors (Figure 2.4 b) and materials with Eg ~0 eV are categorised as metals (Figure 2.4 c).

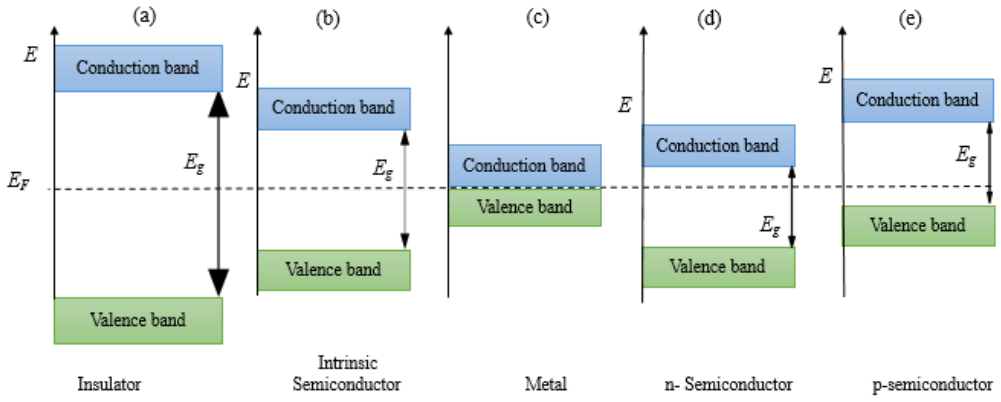


Fig. 2.4: Schematic of the energy band diagrams of (a) insulator, (b) intrinsic semiconductor, (c) metal, (d) n-type semiconductor and (e) p-type semiconductor. E_F and E_g are Fermi level and bandgap, respectively[4].

It is important to note that the Fermi level which is the highest energy level that an electron can occupy at the absolute zero temperature (0 K). In semiconductors, the

Fermi level is typically located within the bandgap, which is smaller than the bandgap of insulators. As the temperature increases, electrons in the valence band become more easily excited into the conduction band, resulting in electrical conductivity. In intrinsic semiconductors, the Fermi level is situated in the middle of the bandgap, as depicted in Figure 2.4 (b). However, doping can alter the relative position between the Fermi level and the energy bands. In n-type doping, additional electrons are introduced to the semiconductor, which shifts the Fermi level towards the conduction band as depicted in Figure 2.4 (d). Conversely, p-type doping introduces more holes into the semiconductor, thereby shifting the Fermi level towards the valence band as seen in Figure 2.4(e).

The relationship between energy and wave-vector (E-k) that is used to determine the nature of the semiconductor's band gap is shown in Fig. 2.5. The energy of the minima of the conduction band and the energy of the maxima of the valence band are expressed in the equation given below. Both these bands show parabolic shapes at k= ~0 [5].

$$E_c = E_g + \frac{h^2k^2}{8\pi^2 m_e^*}, E_v = -\frac{h^2k^2}{8\pi^2 m_h^*} \tag{2.7}$$

In the above equation, E_c and E_v represent the energy of conduction and valence bands, respectively. h is Plank's constant, k is Boltzmann constant, and m_e^* and m_h^* are the effective mass of electrons and holes, respectively. The electrons lack the energy to jump to upper conduction band when the temperature is low (~0 K). Consequently, the electrons tend to remain confined in the valence band. As a result of this, intrinsic semiconductors exhibit insulating behaviour at very low temperatures [5].

2.2.3 DIRECT AND INDIRECT ENERGY BANDGAPS

Band gaps in semiconductors can be classified into direct or indirect band gaps. The direct and indirect band gap depends on the position of the conduction band's minimum energy and the valence band's maximum energy with respect to the wave vector (k). In a direct band gap semiconductor, the maximum of the valence band and the minimum of the conduction band take place at the same value of momentum, i.e. k=0. However, for an indirect band gap semiconductor, these two bands take place at different values of momentum. GaAs and Si are examples of direct and indirect semiconductors, respectively. The E(k) relationship of GaAs and Si semiconductors is depicted in Fig. 2.5.

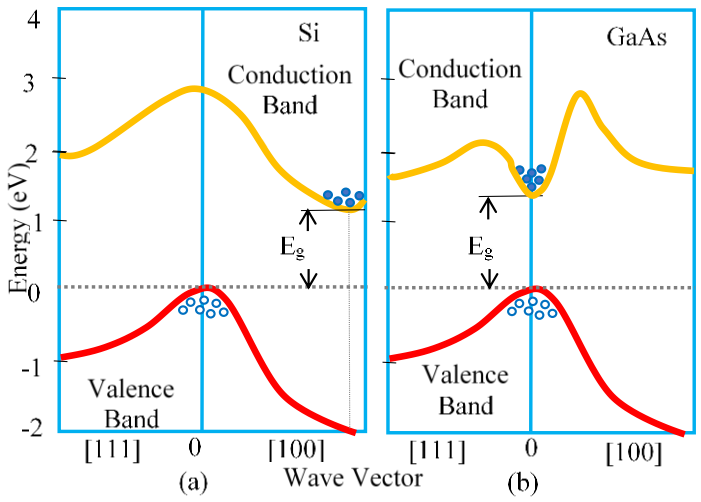


Fig. 2.5. Energy-band structures of (a) Si that has an indirect band gap and (b) GaAs that has a direct band gap [3]. The full and open circles represent electrons and holes, respectively.

2.2.4 TEMPERATURE DEPENDENT ENERGY BANDGAPS

The rise in temperature of a semiconductor leads to a reduction of the energy bandgap. The basic principle behind this is that an increase in the temperature causes a rise in the atoms' thermal vibrational energy as well as amplitude of atomic vibrations. Consequently, the interatomic spacing increases which causes a decrease of the potential seen by electrons in the material that results in a reduction of the energy gap. The relationship between temperature and energy band gap $E_g(T)$ is given by Varshni empirical equation shown below [6]:

$$E_g(T) = E_g(0) - \frac{\alpha T^2}{\beta} \tag{2.8}$$

In the above equation, the energy bandgap at 0 K is denoted by $E_g(0)$, while the empirical parameters of the material are denoted by α and β. Table 2.1 shows the empirical parameters for GaAs, GaP, GaPN and GaAsN (N=2.97%).

Table 2.1: Empirical parameters for the bandgap temperature dependency of GaP, GaAs, GaPN and GaAsN semiconductors.

Parameter	GaP [7]	GaAs [7]	GaPN (N= 1.3%) [8]	GaAsN (N=2.97%) [9]
α (meV/K)	0.5	0.5	0.36	0.61
β (K)	372	220	372	560

2.2.5 DENSITY OF STATES

The total states available at each energy level of a semiconductor represent the distribution of charge carriers in that semiconductor. Since the solid materials have closely packed atoms, the electric field of these atoms allow an interaction with

other atoms leading to splitting of energy levels to form a number of electronic states [10]. Electrons show a tendency of first occupying lower energy levels if available. As a result of this, two highest energy bands known as valence and conduction bands are created, and they are the highest two occupied energy bands at finite temperature. The density of states is denoted by N(E) and described as the number of available states for electrons in a semiconductor material at a specific energy level. Various factors affect N(E) including the confinement of the carriers and their degree of freedom. The degree of freedom of the carriers depends on the material structure. Fig. 2.6 (a) shows that for three-dimensional (3D) structures, N(E) is proportional to square root of energy. Fig. 2.6 (b) shows that in 2D (two-dimensional) materials N(E) forms a step like function with respect to energy. On the other hand, for 1D (one-dimensional) and 0D (zero-dimensional) systems N(E) is proportional to $E^{-1/2}$ and is independent of energy (delta function) as illustrated in Fig. 2.6 (c) and Fig. 2.6 (d), respectively.

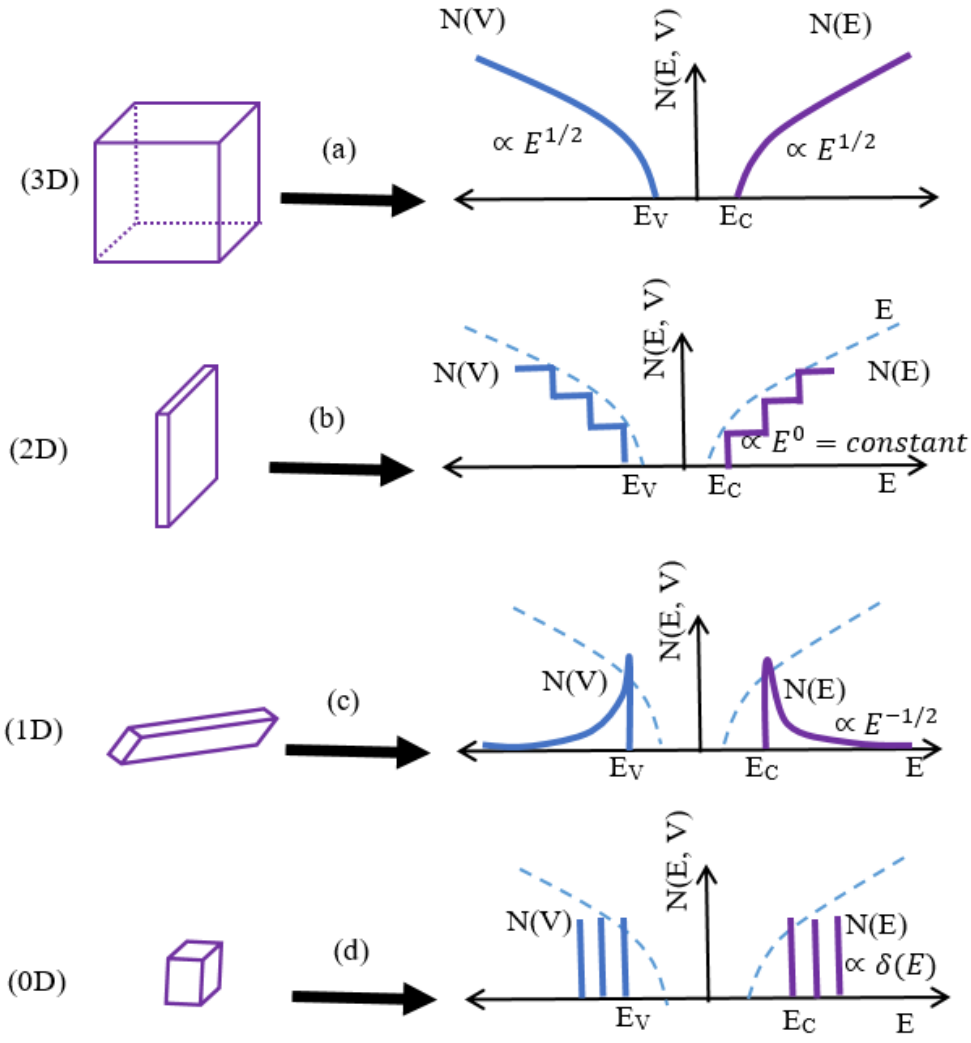


Fig 2.6: Density of states for (a) bulk semiconductor or three-dimensional system (3D), (b) two-dimensional systems (2D), (c) one-dimensional systems (1D), and (d) zero-dimensional systems (0D) [3].

2.3 HETEROJUNCTION STRUCTURES

Commonly, homojunction and heterojunction structures are two well-known types of structures. A homojunction structure involves the combination of layers of same semiconductor materials with same crystalline structure. Fig. 2.7 (a) shows that the materials involved in the formation of homojunction structures usually have

same band gaps with different doping materials. On the other hand, a heterojunction structure is formed with the combination of layers of two different semiconductor materials with different crystalline structures and different band gaps. A heterojunction structure is shown in Fig 2.7 (b).

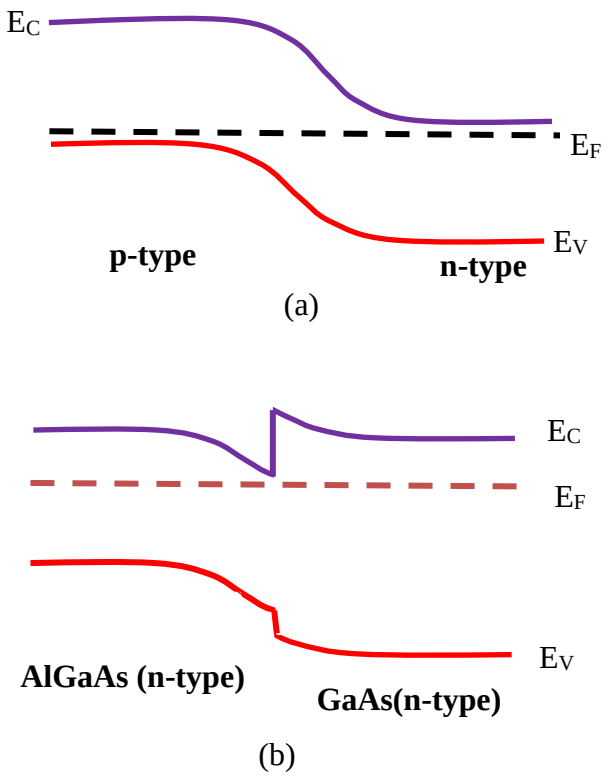


Fig. 2.7: Energy band diagram showing (a) a homojunction structure and (b) a heterojunction structure.

2.3.1 LATTICE MISMATCH

A lattice-matched structure is a structure made up of two layers of different materials with similar lattice constants (Fig. 2.8 (a)). Conversely, a lattice-mismatched structure is one that involves two layers of materials with different lattice constants. The lattice-mismatch is mathematically expressed as follows [11]:

$$\frac{\Delta a}{a} = \frac{a_{layer} - a_s}{a_s} \tag{2.9}$$

In the above equation, a_{layer} denotes the lattice constant of the epilayer while a_s denotes the lattice constant of the substrate. Lattice-mismatched structures usually have defects at the heterojunction interface during the growth process. The defects are found to increase with increasing lattice-mismatch. Usually, lattice mismatched systems are attributed with two types of strains including compressive and tensile strains. The compressive and tensile strains formed in lattice-mismatched structures are shown in Fig. 2.8 (b) and Fig. 2.8 (c), respectively. Compressive strain is created when the lattice constant of the grown semiconductor layer is larger than that of the substrate. Conversely, a tensile strain is formed when the lattice constant of the substrate is higher than the grown layer.

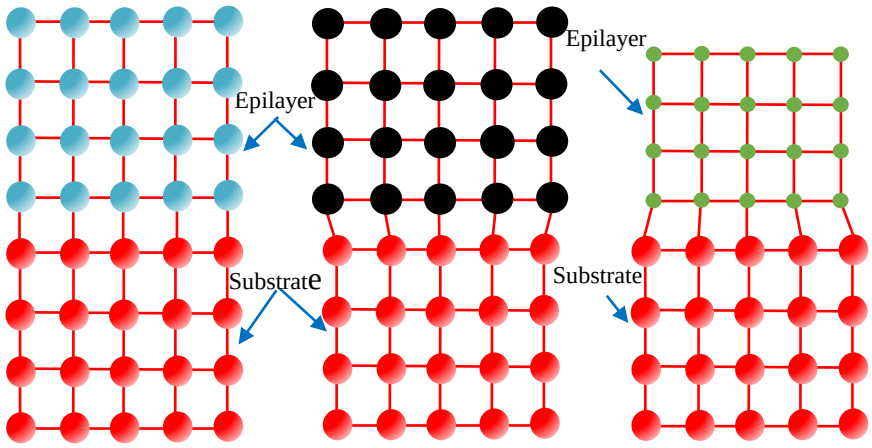


Fig. 2.8. Schematic illustration of (a) lattice matched structure, (b) compressive strain (lattice mismatched structure) and (c) tensile strain (lattice mismatched structure).

2.3.2 ATOM SIZE AND ELECTRONEGATIVITY

The formation of a heterojunction structure is dependent on various attributes of its constituent materials like size of the atoms, electronegativity (χ), energy band alignment and lattice matching or mismatching. It is important to note that the formation of a heterojunction structure with two different materials having different atom sizes may result in the creation of strain during the growth process. The electronegativity (denoted by χ) is the ability of an atom or molecule to attract an electron towards itself in order to form a chemical bond. Electronegativity χ is not expressed in any unit but in general it is known as the Pauling scale. Linus Pauling demonstrated the principle of electronegativity for the first time in 1932 [12]. The Pauling's theory can be used to evaluate the difference between the electronegativity of two different materials A and B used in the formation of heterostructures. The equation for this relationship is given as follows

$$\chi_A - \chi_B = \left[(eV)^{\frac{-1}{2}}\right] \sqrt{E_D(AB) - \frac{[E_D(AA)+E_D(BB)]}{2}} \qquad (2.10)$$

In the above equation, χ_A and χ_B represent the electronegativity of materials A and B, respectively. The dissociation energy between atoms of materials A and B is denoted by $E_D\,(AB)$, while $E_D(AA)$ and $E_D(BB)$ are the dissociation energies between the atoms AA and BB, respectively. All the dissociation energies are expressed in units of eV. The factor $\left[(eV)^{\frac{-1}{2}}\right]$ is introduced to make the value of electronegativity unitless.

2.3.3 BAND ALIGNMENTS

The band alignment of both semiconductor materials affects the structure of heterojunction. There are various types of band alignment, namely, (a) straddled

alignment or type-I alignment, (b) staggered alignment or type-II alignement, (c) broken gap alignment or type-III alignment as shown in Fig. 2.9, where material B has a smaller energy band gap than material A. In such a case, Type-I band alignment is characterised with lower energy of valence band of material B than the valence band of the higher energy gap material A and lower energy of conduction band of material B than the conduction band of the other material A. Type- I alignment is usually seen in InGaAs/InP and AlGaAs/GaAs structures. Type-II band alignment is characterised with material A having higher conduction band edge and valence band edge in comparison to band edges of material B. This kind of alignment can be seen in GaSb/GaAs heterojunctions. Finally, type- III band alignment occurs when the conduction band edge of material B is lower than the valence band edge of material A. This kind of arrangement is seen in GaSb/InAs heterostructures.

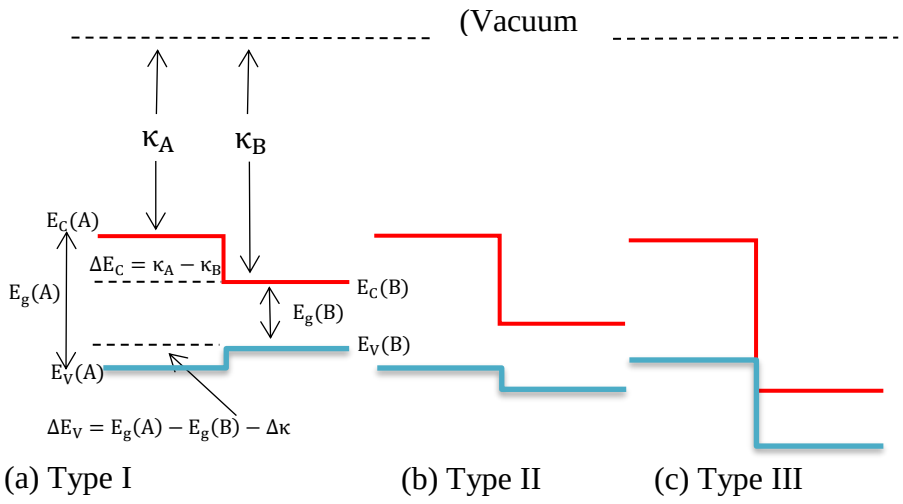


Fig. 2.9: Types of energy bands alignments in heterojunctions. E_C, E_V and Eg represent conduction band, valence band, energy gap, respectively. ΔE_C and ΔE_V represents conduction band and valence band offsets, respectively. κ_A and κ_B are electron affinities of materials A and B, respectively.

R. Anderson put forward the electron affinity rule in 1962 as the introductory theoretical model [13] for evaluation of preferred band offset to make up a perfect semiconductor heterostructure. The model suggested that the band offset of conduction band (ΔE_C) and that of valence band (ΔE_V) between two materials can be evaluated on the basis of the difference between electron affinities of both materials ($\kappa_A - \kappa_B$) as expressed below:

$$\kappa_A - \Delta E_C - \kappa_B = 0 \tag{2.11}$$

$$\Delta E_c = \kappa_B - \kappa_A \quad \text{and} \quad \Delta E_v = \Delta E_g - \Delta\kappa \tag{2.12}$$

2.4. GENERAL PROPERTIES OF SELECTED SEMICONDUCTOR MATERIALS

This section will discuss the key properties of the semiconductors considered in this study

2.4.1. GaAs

Gallium arsenide (GaAs) is widely used semiconductor material. It is a compound composed of elements from group III (Ga) and V (As) of the periodic table. The properties of GaAs were not revealed till the year 1952 despite its discovery in 1920 by Goldschmidt [14]. The energy band diagram of GaAs shown in Fig. 2.10 indicates that it has a direct band gap (minima of the conduction band and maxima of the valence band occurs at k = 0. Hence, the momentum of electrons does not change during their transition from the valence band to the conduction band. A transition from the valence band to the conduction band only requires a change in

energy. GaAs is, therefore, a potential material for optoelectronic devices due to its direct bandgap nature compared to indirect bandgap semiconductors such as Si.

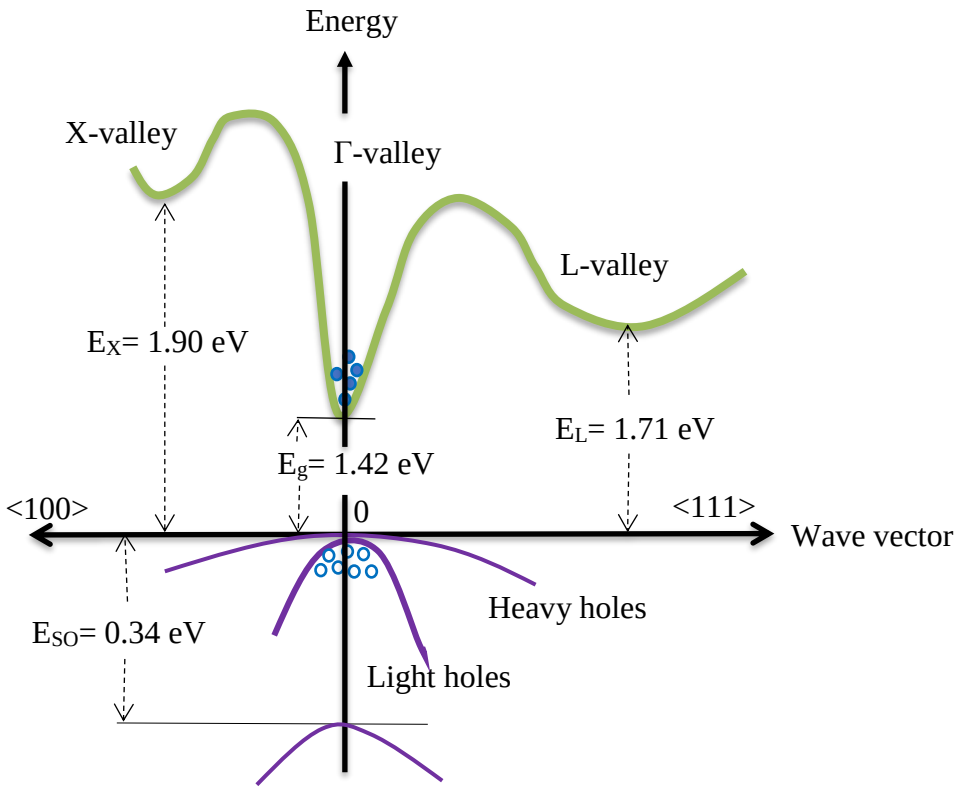


Fig. 2.10: Energy band diagram of GaAs. E_{SO}, E_{Γ}, E_L, and E_X are energies of spin-orbital splitting, Γ-valley, L-valley and of X-valley, respectively.

GaAs has a higher resistivity (~ 10^8 Ω-cm) and less parasitic capacitive effects than Si (~10^2 Ω-cm) making it the ideal choice as a semi-insulating substrate for use in high frequency integrated circuits. In addition, the energy bandgap of GaAs is larger than Si which allows devices made from GaAs to operate at higher temperatures. Table 2.2 presents the main intrinsic properties of GaAs at room temperature (300 K).

Table 2.2. Important properties of intrinsic GaAs at 300K. h_h, l_h and m_0 represent heavy hole, light hole, and rest mass of an electron, respectively [15].

Parameter	GaAs
Crystal Structure	Zincblende
Lattice constant (Å)	5.6533
Crystal density (g/cm^3)	5.360
Energy band gap (eV)	1.42
Band type	Direct
Electron effective mass	$0.063m_0$
Hole effective mass	$0.51m_0$ (h_h) $0.082m_0$ (l_h)
Dielectric constant (static)	12.85
Electron affinity (eV)	4.07

2.4.2. GaInP

Gallium Indium phosphide (GaInP), which belongs to the group III-V compound semiconductors, is a high-bandgap semiconductor ranging from 1.344 eV (InP) to 2.24 eV (GaP)]. $Ga_{1-y}In_yP$ can be lattice-matched to GaAs and Ge substrates for specific compositions of Ga (0.51) and In (0.49), and therefore it is an interesting material for top cells in multi-bandgap tandem solar cell devices [16]. $Ga_{0.51}In_{0.49}P$ alloy is a direct band gap with a bandgap energy of 1.9eV. In addition, it is used in numerous applications such as heterojunction bipolar transistors (HBTs), photovoltaic solar cells and light emitting diodes [17-19]. However, the $Ga_xIn_{1-x}P$ alloys become indirect bandgap semiconductors when the Ga content $x \geq 0.69$-0.72 corresponding to a band energy ≥2.2 eV. Therefore, for example the optical efficiency of $Ga_xIn_{1-x}P$ alloys decreases exponentially near the direct-indirect

crossover, meaning that these materials are not suitable for light-emitting applications [20].

$Ga_{1-y}In_yP$ materials with $0.18 < y < 0.30$ have a direct bandgap enabling stronger absorption and higher short-circuit current density [19]. However, the challenge in growing $Ga_{1-y}In_yP$ ($0.18 < y < 0.30$) cells is that they are lattice mismatched to low-cost conventional substrates, as illustrated in Fig.2.11.

As compared with AlGaAs alloy, InGaP has superior properties [21, 22] such as (i) lower surface recombination velocity, (ii) lower density of DX recombination centre which is a deep level associated with donors in III-V semiconductors, (iii) lower affinity to oxygen resulting in the growth of higher crystal quality of InGaP/GaAs heterolayers than AlGaAs/GaAs ones because AlGaAs layers are likely to oxidise during epitaxial growth, and (iv) higher etching selectivity between InGaP/GaAs layers compared to AlGaAs/GaAs junctions [23]. Since InGaP is lattice matched to GaAs for specific compositions of In and Ga, it is a prospective candidate for the realisation of two-junctions solar cells [23].

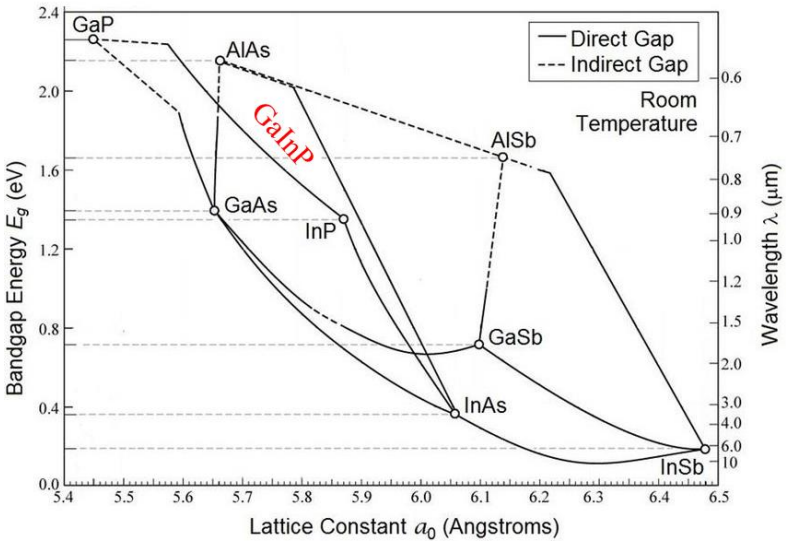


Fig. 2.11. Bandgap energy versus lattice constant of some III-V semiconductors [24].

Table 2.3. Major parameters for the ternary $Ga_{0.51}In_{0.49}P$ lattice matched to GaAs at 300K [25].

Bandgap Eg [eV]	1.9
Lattice constant a [Å]	5.65
Affinity [eV]	4.16
electron density of states NC [cm^{-3}]	$1.3x10^{20}$
hole density of states NV [cm^{-3}]	$1.28x10^{19}$

2.4.3. DILUTE GaAsN

The decade of 1990 marked the discovery of first ever epitaxial development of novel semiconductors made from elements from III-V-N groups of the periodic table [26, 27]. These materials were named as dilute nitride semiconductor materials. The materials were attributed with certain unusual physical properties and were found effective to be used in various technological applications like solar cells, optical amplifiers, and long wavelength lasers [28, 29].

Semiconductor alloys are created when the isovalent host atom is replaced by isovalent impurity atoms. Consequently, this leads to weak perturbations in the host crystal band structure. When the isovalent impurity atoms and the host atoms have different properties such as atomic radii, electronegativity, etc, the host band structure can be changed significantly.

For instance, the addition of impurity atoms like phosphorus (P) or Indium (In) to GaAs leads to replacement of As with P or replacement of Ga with indium In. Consequently, the band structure of GaAs changes slightly. However, in case of addition of nitrogen (N) atoms to GaAs, the changes in band structure were found to be significant since nitrogen atoms form bonds with GaAs to yield GaAsN

crystal. The bandgap energy reduction of GaAs is dependent on the percentage of nitrogen incorporated in the host lattice. The energy of the bandgap of GaAs is reduced by 0.1eV for every percent of N. A large crystal potential is created due to significant disparity between N atoms and host atoms in terms of their size and electronegativity [29]. Consequently, the bandgap is reduced due to the formation of localised states near the conduction band edge that are introduced by the incorporation of nitrogen atoms. The properties of GaAsN can be comprehended with the help of the band anti-crossing (BAC) model proposed by Shan *et al*. [30] and explained in the following section.

2.4.3.1. THE BAND ANTI-CROSSING (BAC) MODEL

The BAC model gives an insight into the electronic structure of N-alloys on the basis of the reaction that takes place within the host semiconductor matrix due to interaction of localised states of nitrogen with extended states of the conduction band [30, 31]. The conduction band interacts with localized states of nitrogen atoms and splits into E_- and E_+ bands. Moreover, there is a decrease in the band gap. The increase in concentration of N leads to more splitting and more reduction in the bandgap energy.

The anti-crossing behaviour depicted by the Nitrogen-related state (E_N) and conduction band edge (E_{CB}) in GaAs semiconductor is shown in Fig. 2.12. The nitrogen-related states are localised and hence, these states are attributed with constant energy throughout the reciprocal space. The dotted lines in Fig. 2.12 show the E_N energy state as well as E_{CB} energy state. The following equation represents

the energy of the localized N-states and conduction band states on the basis of BAC model after their interaction:

$$E_{\pm} = \frac{1}{2}\left(E_N + E_{CB} \pm \sqrt{(E_N - E_{CB})^2 + 4V_{CB,N}^2}\right) \quad (2.13)$$

In the above equation, $V_{CB,N}$ represents the coupling parameter which indicates the extent of interaction of localized N states with extended conduction band states. The coupling parameter can be mathematically expressed as follows:

$$V_{CB,N} = C_N . x^{\frac{1}{2}} \quad (2.14)$$

where x represents the composition of nitrogen in the alloy while C_N represents a constant with values subject to semiconductor host.

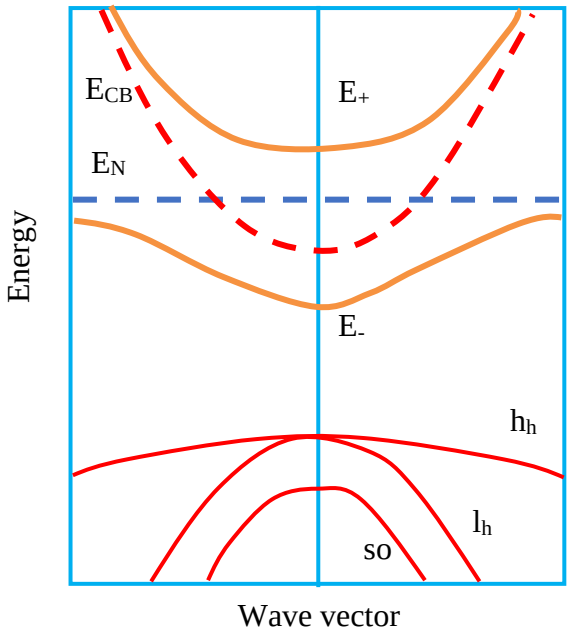


Fig. 2.12. Schematic diagram of band anti-crossing model of GaAsN.

The BAC model was not found to be an ideally effective model due to mere focus on interaction of single isovalent impurity level with conduction band edge and

overlooking the expansion of energy levels and splitting of the extrema of L-conduction band. Despite these drawbacks, the BAC model is simple and fits various alloy properties and characteristics, and therefore, it is widely applied in studies pertaining to dilute nitrides.

2.4.4 DILUTE GaAsNP

GaP is an interesting material with a wide range of applications. The addition of N and As to GaP (i.e. GaAsNP) lowers its band gap to 1.7 eV [32, 33], converts it from indirect to a direct bandgap alloy, and allows the lattice-matched epitaxial growth of GaAsNP epilayers on GaP substrates. It is important to point out that the lattice constant of GaP is close to the lattice constant of silicon, and therefore it is also possible to grow GaP and GaAsNP layers on silicon substrates. GaAsPN has recently attracted much interest from the solar cell research community. This is due to the high radiative efficiency and the possibility of lattice matching with GaP. In addition, GaAsPN quaternary alloys are very attractive and promising materials for multi-junction solar cells [33, 34], light absorbers and electroluminescent devices [35]. These materials can be grown by molecular beam epitaxy (MBE) and metalorganic vapor phase epitaxy (MOVPE) [34].

2.5 WORKING PRINCIPLE OF PHOTOVOLTAIC SOLAR CELL

In a photovoltaic cell or a solar cell, the energy of sunlight is converted directly into electricity as illustrated in Figure 2.13. The solar cell consists of two regions of doped semiconductor materials so that one has positive carriers which are holes, and the other has negative carriers, which are electrons. These two positive and negative regions are called p-type and n-type layers, respectively. The boundary

between these two layers is the pn-junction. On the front and back of the solar cells are metallic contacts. Typically, the back contact of a solar cell is a solid metallic layer. However, the front contact, to allow light in, often uses a grid of metal fingers for collecting the carriers.

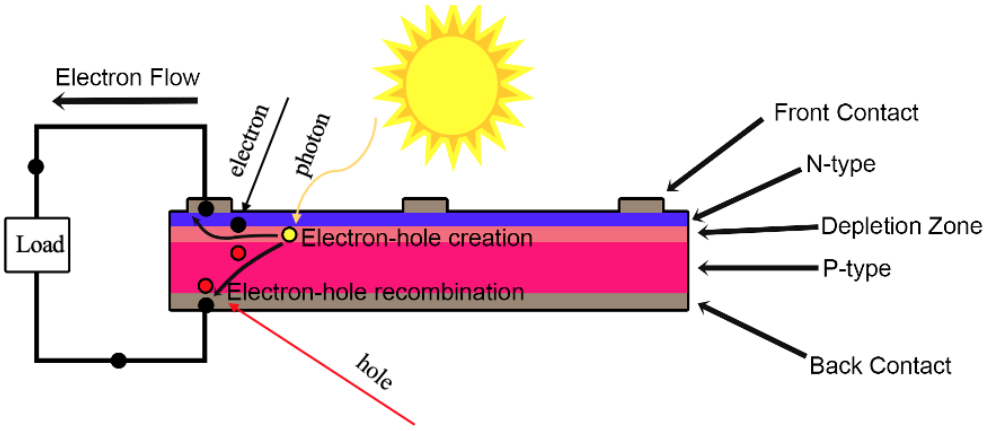


Fig. 2.13: Operation principle of a solar cell. An incoming photon is absorbed in the depletion region with the creation of an electron-hole pair. The internal potential field forces the electrons towards the front contact. Finally, the electrons return to the solar cell through the opposite electrode and recombine with the holes, completing the cycle.

The photovoltaic process is shown in Figure 2.14. When a solar cell absorbs a photon, there is a possibility that it will energise a carrier. When the energy of a photon is higher than the bandgap, an electron can be excited from the valence band to the conduction band of the semiconductor material, resulting in an electron-hole pair. The difference in energy between the valence band and the conduction band is called the bandgap. The excited carriers will now traverse the PV (photovoltaic) junction, moving towards a lower energy state. This occurs as a result of the electric field that is built up at the pn-junction. Electrons will be collected in the n-region and holes will be collected in the p-region. The separation of charges, with the collection of holes in the p-region and electrons in the n-region, results in the

creation of a voltage difference. This voltage can then drive a current to flow from one contact to the other in the solar cell. The electrons can then exit the solar cell through the n-side contact, where they can perform electrical work before returning to the p-side of the solar cell. Photons with lower energy than the bandgap are incapable of exciting a carrier across the energy gap. Consequently, these photons are unable to contribute to the generation of electric energy in the solar cell [36].

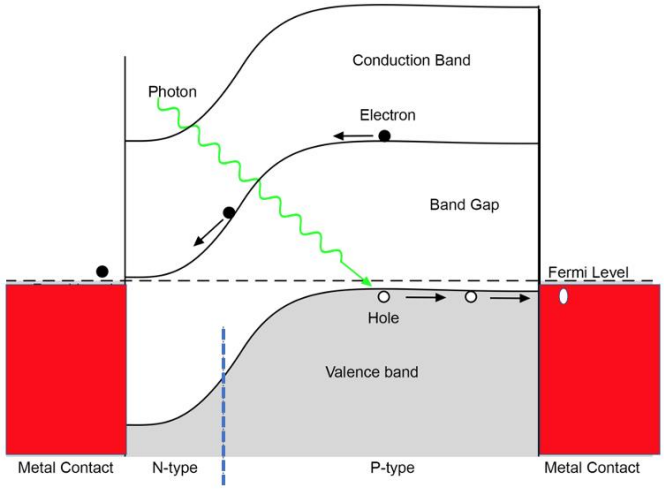


Fig 2.14: Schematic energy band diagram of a solar cell. A photon will excite an electron from the valence band into the conduction band which is normally empty. The excited electron moves towards the left (n-region) due to the potential change in the pn-junction. The electron will then travel through the metal contact and load before recombining with a hole as shown on the right side of the figure.

REFERENCES

[1] M. Grundmann, "The Physics of Phonons: An Introduction Including Devices and Nanophysics," ed: Springer, Berlin, 2006.

[2] B. Sapoval and C. Hermann, *Physics of semiconductors*. Springer Science & Business Media, 2003.

[3] S. M. Sze and K. K. Ng, *Physics of semiconductor devices*. John Wiley & Sons, 2006.

[4] X. Tang, *Investigation of Electrically Active Defects in Gan Using Deep-level Transient Spectroscopy*. The University of Manchester (United Kingdom), 2022.

[5] J.-P. Colinge and C. A. Colinge, *Physics of semiconductor devices*. Springer Science & Business Media, 2005.

[6] Y. P. Varshni, "Temperature dependence of the energy gap in semiconductors," *physica*, vol. 34, no. 1, pp. 149-154, 1967.

[7] P. Wang, S. Holmes, T. Le, R. Stradling, I. Ferguson, and A. De Oliveira, "Electrical and magneto-optical of MBE InAs on GaAs," *Semiconductor science and technology*, vol. 7, no. 6, p. 767, 1992.

[8] C.-Z. Zhao, T. Wei, N.-N. Li, S.-S. Wang, and K.-Q. Lu, "The evolution of the band gap energy of the P-rich GaNxP1− x (0< x≤ 0.05) on composition and temperature," *Physica B: Condensed Matter*, vol. 427, pp. 58-61, 2013.

[9] K. Uesugi, I. Suemune, T. Hasegawa, T. Akutagawa, and T. Nakamura, "Temperature dependence of band gap energies of GaAsN alloys," *Applied Physics Letters*, vol. 76, no. 10, pp. 1285-1287, 2000.

[10] D. Wood, "13 5 6," in *Optoelectronic Semiconductor Devices*: Prentice-Hall, 1994.

[11] D. A. Neamen, *Semiconductor physics and devices: basic principles*. New York, NY: McGraw-Hill, 2012.

[12] L. Pauling, "The nature of the chemical bond. IV. The energy of single bonds and the relative electronegativity of atoms," *Journal of the American Chemical Society,* vol. 54, no. 9, pp. 3570-3582, 1932.

[13] R. Anderson, "Germanium-gallium arsenide heterojunctions," *IBM Journal of Research and Development,* vol. 4, no. 3, pp. 283-287, 1960.

[14] J. Bernal, "The Goldschmidt memorial lecture," *Journal of the Chemical Society (Resumed),* pp. 2108-2114, 1949.

[15] S. T. Thornton and A. Rex, *Modern physics for scientists and engineers*. Cengage Learning, 2012.

[16] S. J. Wojtczuk, S. M. Vernon, and M. M. Sanfacon, "Comparison of windows for P-on-N InGaP solar cells," in *Conference Record of the Twenty Third IEEE Photovoltaic Specialists Conference-1993 (Cat. No. 93CH3283-9)*, 1993, pp. 655-658: IEEE.

[17] S. C. Patil and B. Mishra, "GaAs, InP, InGaAs, GaInP, p+-i-n+ Multiplication measurements for Modeling of Semiconductor as photo detectors," in *International Conference &Workshop on Advance Computing*, 2013, pp. 34-42: Citeseer.

[18] A. Gudovskikh, N. Kaluzhniy, V. Lantratov, S. Mintairov, M. Shvarts, and V. Andreev, "Numerical modelling of GaInP solar cells with AlInP and AlGaAs windows," *Thin Solid Films*, vol. 516, no. 20, pp. 6739-6743, 2008.

[19] Y. Sun, K. H. Montgomery, X. Wang, S. Tomasulo, M. L. Lee, and P. Bermel, "Modeling wide bandgap GaInP photovoltaic cells for conversion efficiencies up to 16.5%," in *2015 IEEE 42nd Photovoltaic Specialist Conference (PVSC)*, 2015, pp. 1-6: IEEE.

[20] C. Wang, B. Wang, R. I. Made, S.-F. Yoon, and J. Michel, "Direct bandgap photoluminescence from n-type indirect GaInP alloys," *Photonics Research*, vol. 5, no. 3, pp. 239-244, 2017.

[21] D. Ahmari, M. Fresina, Q. Hartmann, D. Barlage, M. Feng, and G. Stillman, "InGaP/GaAs heterojunction bipolar transistor grown on a semi-insulating InGaP buffer layer," *IEEE Electron Device Letters*, vol. 18, no. 11, pp. 559-561, 1997.

[22] W.-S. Lour, J.-H. Tsai, L.-W. Laih, and W.-C. Liu, "Influence of channel doping-profile on camel-gate field effect transistors," *IEEE Transactions on Electron Devices*, vol. 43, no. 6, pp. 871-876, 1996.

[23] M. Bosi and C. Pelosi, "The potential of III-V semiconductors as terrestrial photovoltaic devices," *Progress in Photovoltaics: Research and Applications*, vol. 15, no. 1, pp. 51-68, 2007.

[24] H. Lei, "GaAs-Based Distributed Feedback Lasers Based on GaAs-InGaP Regrowth Technology," University of Sheffield, 2017.

[25] P. Michalopoulos, "A novel approach for the development and optimization of state-of-the-art photovoltaic devices using Silvaco," NAVAL POSTGRADUATE SCHOOL MONTEREY CA2002.

[26] M. Weyers, M. S. M. Sato, and H. A. H. Ando, "Red shift of photoluminescence and absorption in dilute GaAsN alloy layers," *Japanese Journal of Applied Physics*, vol. 31, no. 7A, p. L853, 1992.

[27] M. Kondow, K. Uomi, T. Kitatani, S. Watahiki, and Y. Yazawa, "Extremely large N content (up to 10%) in GaNAs grown by gas-source molecular beam epitaxy," *Journal of crystal growth,* vol. 164, no. 1-4, pp. 175-179, 1996.

[28] P. J. Thijs, L. F. Tiemeijer, P. Kuindersma, J. Binsma, and T. Van Dongen, "High-performance 1.5 mu m wavelength InGaAs-InGaAsP strained quantum well lasers and amplifiers," *IEEE journal of quantum electronics,* vol. 27, no. 6, pp. 1426-1439, 1991.

[29] H. P. Hjalmarson, P. Vogl, D. J. Wolford, and J. D. Dow, "Theory of substitutional deep traps in covalent semiconductors," *Physical Review Letters,* vol. 44, no. 12, p. 810, 1980.

[30] W. Shan, W. Walukiewicz, J. Ager III, E. Haller, J. Geisz, D. Friedman, J. Olson, and S. R. Kurtz, "Band anticrossing in GaInNAs alloys," *Physical Review Letters,* vol. 82, no. 6, p. 1221, 1999.

[31] A. Lindsay and E. O'reilly, "Theory of enhanced bandgap non-parabolicity in GaNxAs1− x and related alloys," *Solid State Communications,* vol. 112, no. 8, pp. 443-447, 1999.

[32] M. Da Silva, S. Almosni, C. Cornet, A. Létoublon, C. Levallois, P. Râle, L. Lombez, J.-F. Guillemoles, and O. Durand, "GaAsPN-based PIN solar cells MBE-grown on GaP substrates: toward the III-V/Si tandem solar cell," in *Physics, Simulation, and Photonic Engineering of Photovoltaic Devices IV,* 2015, vol. 9358, p. 93580H: International Society for Optics and Photonics.

[33] J.-M. Tilli, H. Jussila, K. M. Yu, T. Huhtio, and M. Sopanen, "Composition determination of quaternary GaAsPN layers from single X-

ray diffraction measurement of quasi-forbidden (002) reflection," *Journal of Applied Physics,* vol. 115, no. 20, p. 203102, 2014.

[34] J. Geisz, J. Olson, D. Friedman, K. Jones, R. Reedy, and M. Romero, "Lattice-matched GaNPAs-on-silicon tandem solar cells," in *Conference Record of the Thirty-first IEEE Photovoltaic Specialists Conference, 2005.*, 2005, pp. 695-698: IEEE.

[35] A. Aissat, L. Chenini, S. Nacer, and J. P. Vilcot, "Modeling and simulation of GaAsPN/GaP quantum dot structure for solar cell in intermediate band solar cell applications," *International Journal of Energy Research,* 2021.

[36] J. A. Nelson, *The physics of solar cells*. World Scientific Publishing Company, 2003.

CHAPTER 3: DEFECTS IN SEMICONDUCTORS AND THEIR PROPERTIES

Different defects and their function as trapping and generation recombination centres will be discussed in this chapter. Deep level defects and theoretical background of carrier kinetics processes are also described. In addition, a brief summary of some selected defects in GaAs, InGaP and dilute III-V nitrides, namely GaAsN and GaAsPN, semiconductors are presented.

3.1 CLASSIFICATION OF DEFECTS

A periodic arrangement of unit cells beside the crystal orientation forms a perfect crystal [1, 2]. However, practically various defects are observed including point, extended and complexes defects, that make the crystal not perfect. In this section, different types of defects will be covered.

3.1.1 POINT DEFECTS

A zero dimensional defect or a point defect is created when an atom is located in an irregular place in the lattice structure or it is missing. Different forms such as vacancy, interstitial, substitutional and antisite impurities are examples for point defects. If an atom is missing at a certain crystal lattice site in a crystal structure, then it generally creates a vacancy defect as illustrated in Fig. 3.1 (a). When a regular lattice site of the host atom is replaced and occupied by a foreign atom impurity, then a substitutional impurity is formed as shown in Fig. 3.1 (b). Likewise, when a host atom occupies the site of another host atom, then a special

type of substitutional defect, namely, an antisite defect is created. Fig.3.1 (c) illustrates an antisite defect in GaAs semiconductor, where an arsenic (As) site is occupied by a gallium (Ga) atom [As antisite (Ga_{As})] and vice versa [Ga antisite (As_{Ga})]. The fourth kind of a point defect known as an interstitial impurity is demonstrated in Fig 3.1 (d). This defect is observed when an atom is inserted into an irregular site in the lattice. If this atom belongs to the host crystal, then it is called self-interstitial. However, if this atom is a foreign atom, the defect is named foreign-interstitial.

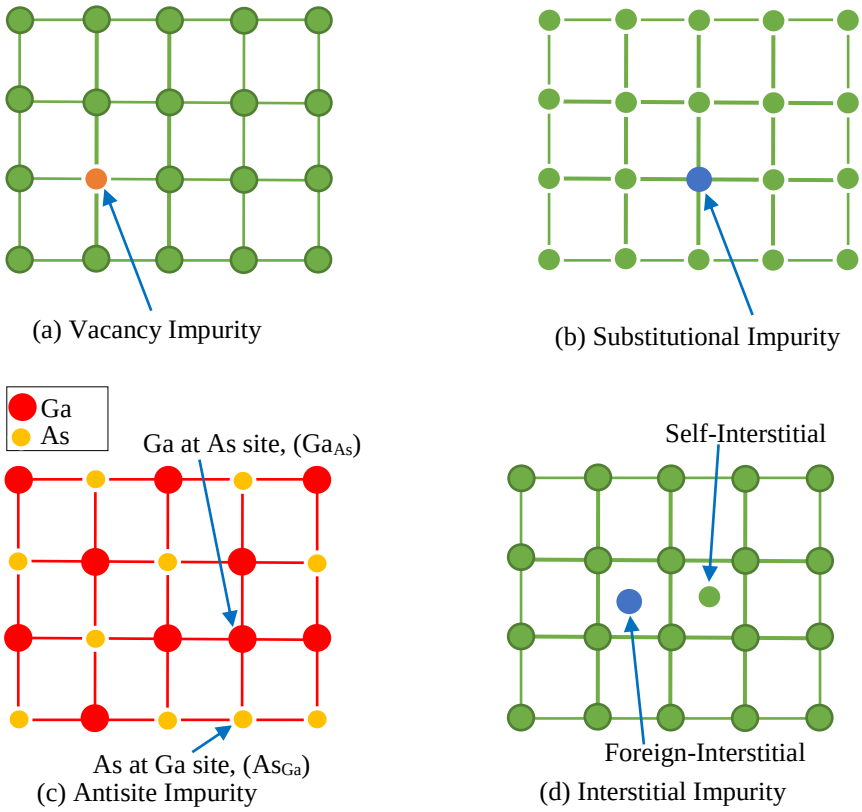


Figure 3.1: Illustration of different forms of point defects in crystalline semiconductors: (a) Vacancy impurity; (b) Substitutional impurity; (c) Antisite impurity; and (d) Interstitial impurity.

3.1.2 COMPLEXES OF POINT DEFECTS

Point defects may be bounded to each other, similar to the atoms bound in molecules. Complex point defects are formed when at least two point defects interact with each other and create what is known as a pair defect. For instance, formation of a pair by two interstitials atoms results in the creation of a complex defect and this is known as split-interstitials defect as illustrated in Fig. 3.2 (a). This formation is realised either by a pair of two impurity interstitial atoms or by a pair of two interstitial atoms of the same host material. As shown in Fig. 3.2 (b), several complexes in a crystalline material can also be formed by vacancy defects. Especially, when a pair is formed by two vacancies, the resulting complex is called a Di-vacancy. In addition, when a pair is created by a vacancy and a self-interstitial atom, then it leads to the creation of a Frenkel defect. When a pair of a vacancy interacts with a foreign-interstitial impurity, then it results in the formation of a vacancy-impurity complex. Moreover, a split vacancy is created, when a pair is formed by two vacancies and interstitial atom. A complex defect known as impurity-pair is shown in Fig. 3.2 (c). It emerges when an interstitial impurity atom interacts with a substitutional impurity atom.

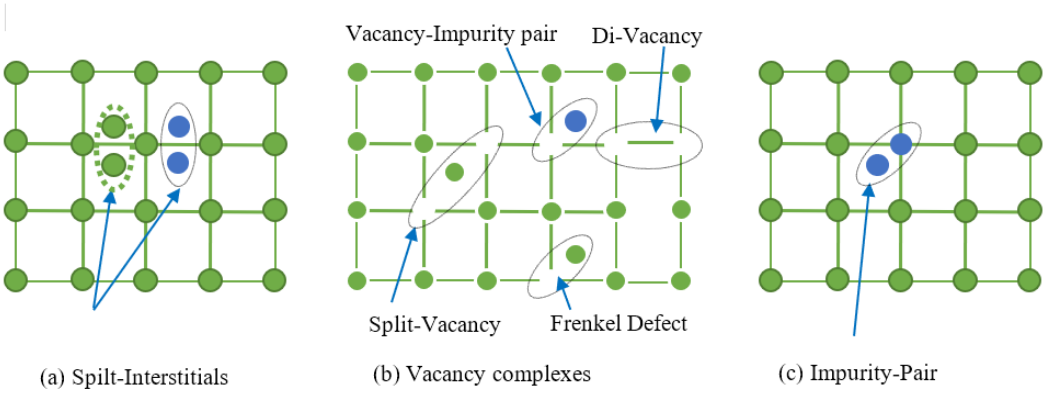
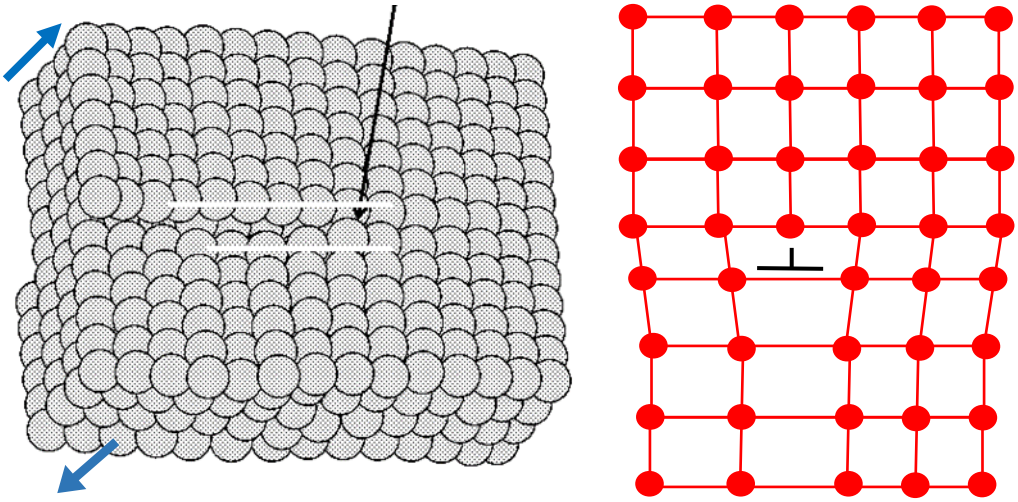


Figure 3.2: Illustration of different forms of complex defects: (a) spilt-interstitials, (b) vacancy complexes and (c) complexes of impurity-pair.

3.1.3 LINEAR DEFECTS

When a line of atoms is out of their regular position in the crystal, then linear defects (dislocations) occur, which are generally one-dimensional defects. The basic types of linear defects are known as the screw dislocations and edge dislocation. As demonstrated in Fig. 3.3 (a), an edge dislocation is created by the distortion of nearby atoms when an extra half plane of atoms is introduced into the regular crystal lattice. Furthermore, creation of a screw dislocation is observed when one part of the crystal lattice is shifted in comparison with the other crystal part (see Fig. 3.3 (b)).



(a) (b)

Figure 3.3: Illustration of different forms of linear defects: (a) edge dislocations and (b) screw dislocations.

3.2 DEFECTS AND THEIR CARRIER KINETICS

3.2.1 SHALLOW AND DEEP LEVEL DEFECTS

Within the bandgap of semiconductors, energy levels can be introduced by defects. Especially, the defects located near the valence band or conduction band as seen in

Fig. 3.4 are referred to as shallow level impurities (dopant impurities). These defects are called shallow acceptor levels if they donate a hole to the valence band (E_V) and shallow donor levels if they provide an electron to the conduction band (E_C) [3]. Moreover, these defects are intentionally introduced as dopant atoms. Shallow level impurities have low ionization energy (<100 meV) and their ionization can easily occur at room temperature, resulting in an increase of the electrical conductivity of the semiconductors.

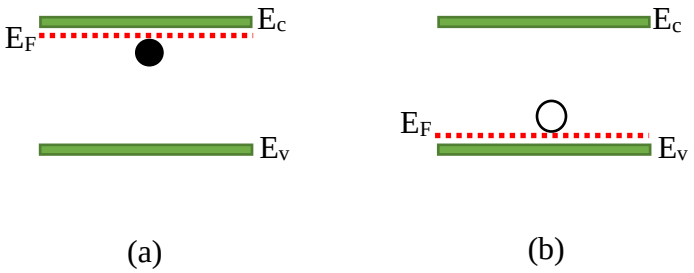


Figure 3.4: Schematic diagram of (a) shallow donor level, and (b) shallow acceptor level. E_v, E_c and E_F represent valence band energy, conduction band energy and Fermi level, respectively.

As shown in Fig. 3.5, deep level defects have energy states deep within the bandgap with activation energies greater than 100 meV. These deep level defects are also known as recombination-generation or trapping centres and they can significantly affect the optical and electrical properties of semiconductor materials. It is therefore essential to understand the conduction mechanism that involve these impurities levels, as will be explained in the next section.

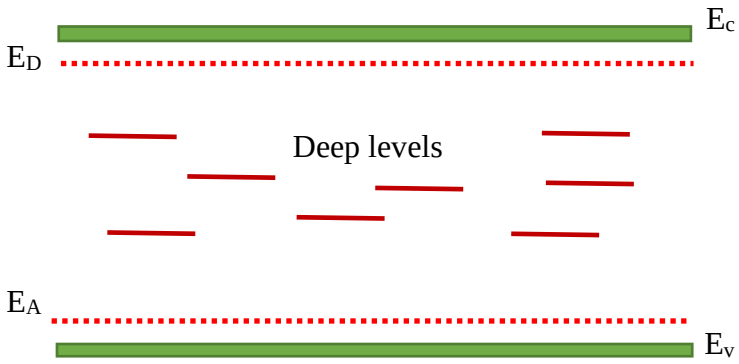


Fig. 3.5. Schematic diagram of deep level defects in semiconductors. E_D and E_A represent shallow donor level and acceptor donor level, respectively.

3.2.2 SHOCLEY-READ-HALL THEORY

Deep levels of impurities in semiconductors are often referred to as generation recombination (G–R) centers [1, 2]. The occupancy of a deep level is determined by the emission and capture rates of carriers at equilibrium. In a semiconductor, electrons and holes recombine in one of two ways. In pure semiconductors, direct recombination occurs via band-to-band processes, whereas indirect recombination occurs via deep energy levels existing within the material's bandgap

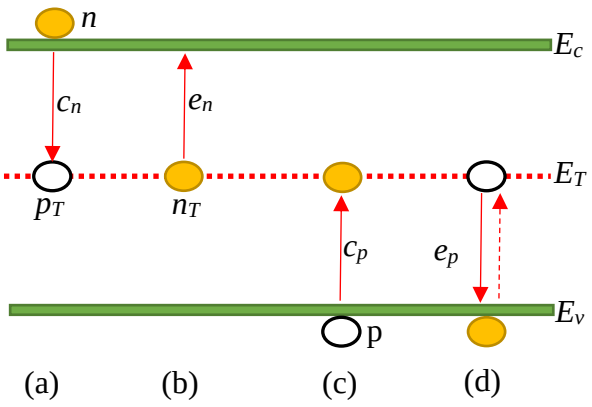


Figure 3.6: Schematic diagram of capture and emission processes: (a) capture of electron (b) emission of electron (c) capture of hole and (d) emission of hole [4].

Consider a deep-level impurity with energy E_T in the forbidden gap and concentration N_T that is distributed throughout the semiconductor. First, suppose the centre captures an electron from the conduction band (Fig. 3.6 (a)); this captured electron can be identified by its electron capture coefficient (c_n). Following this, the electron can be re-emitted to the conduction band, a process known as electron emission (e_n), (Figure 3.6 (b)), or a hole from the valence band can be captured by the centre, a process known as hole capture (c_p) (Figure 3.6 (c)). It should be noted that if either of these two processes happens, a hole will occupy the deep centre, potentially leading to the following outcomes. As shown in Fig. 3.6 (d), the centre can emit the hole back to the valence band (hole emission e_p) or can capture an electron from the conduction band as depicted in Fig.3.6 (a). It should be noted that process (d) is sometimes referred to as electron emission from the valence band to the centre, as shown by the dashed arrow in Fig. 3.6 (d). These four processes are the only ones that can occur between the conduction band, impurity energy levels, and valence band.

The process of capturing an electron (Fig. 3.6 (a)) followed by capturing a hole (Fig. 3.6 (c)) is known as recombination. A generation process occurs when an electron is emitted to the conduction band (Fig. 3.6 (b)), followed by a hole emitted to the valence band (Fig. 3.6 (d)). However, a third process known as trapping can also occur, which is neither generation nor recombination. When an electron is captured and then emitted back to the conduction band, or a hole is captured and then emitted back to the valence band, a deep level is called a trap centre. Only the conduction band or valence band participates in the trapping process with the

impurity level. In contrast, both the conduction and valence bands, as well as the impurity level, participate in the recombination or generation processes [4].

A G-R centre can be occupied by either an electron or a hole. When an electron occupies the centre, it is said to be in a n_T state, and when a hole occupies it, it is said to be in a p_T state. When the G-R centre is a donor, the n_T state is neutral and the p_T state is positively charged. In the case of an acceptor centre, n_T is a negatively charged and p_T is neutral.

The total density of G-R centers (N_T) filled by electrons (n_T) or holes (p_T), is given by [4]:

$$N_T = n_T + p_T \tag{3.1}$$

The hole density in valence band (p), electron density in the conduction band (n) and charge states of the centres n_T and p_T are time dependent when a hole or an electron is produced by a centre or recombined in a centre. Equation (3.2) gives the rate of change of n with regard to time [4]:

$$\frac{dn}{dt}|_{G-R} = (b) - (a) = e_n n_T - c_n n p_T \tag{3.2}$$

where (a) and (b) denote electron capture and emission processes, respectively. The given equation does not take into account radiative or Auger processes. Here, only the G-R mechanism is considered. This process depends only on the emission rate (e_n) and the electron density (n_T) in the G-R center. However, for the electron capture process to take place, electrons in the conduction band (n) are required. Likewise the change of holes density with respect to time is given by [4]:

$$\frac{dp}{dt}|_{G-R} = (d) - (c) = e_p p_T - c_p p n_T \tag{3.3}$$

where (c) and (d) are hole capture and hole emission processes, respectively.

It is worth noting that the electron capture coefficient c_n (or hole capture coefficient c_p) which depends on the thermal velocity of the electron (hole) $\langle v_n \rangle_{th}$ ($\langle v_p \rangle_{th}$) and the electron (hole) capture cross section of the G-R centre σ_n, can be expressed by:

$$c_n = v_{th}\sigma_n \tag{3.4}$$

During the capture or emission process, the concentration of the G-R state changes as a function of time and Equations (3.2) and (3.3) will be used to determine this rate of change. This is given by [4]:

$$\frac{dn_T}{dt}|_{G-R} = \frac{dp}{dt} - \frac{dn}{dt} = \left(c_n n + e_p\right)(N_T - n_T) - \left(c_p p + e_n\right)n_T \tag{3.5}$$

As $\frac{dn_T}{dt} = 0$ in the steady state, then Equation (3.5) can be rewritten as [4]:

$$n_T = \frac{e_p + c_n n}{e_n + c_n n + e_p + c_p p} N_T \tag{3.6}$$

At thermal equilibrium, according to the detail balance principle, the rate of creation is equal to the rate of absorption in semiconductors. As per this principle, the following equation can be used [4]:

$$e_n n_T = c_n n p_T \tag{3.7}$$

Using Equation (3.4), if the electron capture coefficient c_n is substituted into Equation (3.7), then this gives:

$$e_n n_T = \upsilon_{th} \sigma_n n p_T \tag{3.8}$$

Likewise,

$$e_p p_T = \upsilon_{th} \sigma_p p n_T \tag{3.9}$$

The total density of deep levels with respect to Fermi-Dirac distribution, f, is given by

$$N_T = n_T + p_T = N_T f + N_T(1 - f) \tag{3.10}$$

where f gives the probability of an electron occupying the energy level E_T and is expressed by:

$$f = \left[\frac{1}{1 + \exp\left(\frac{E_T - E_F}{k_B T}\right)} \right] \tag{3.11}$$

where k_B is Boltzmann constant, E_F is the energy of the Fermi level and T is temperature.

A combination of Equations (3.10), (3.11) and (3.7) yield the following expression of e_n:

$$e_n = \sigma_n \langle \upsilon_n \rangle_{th} n \exp\left(\frac{E_T - E_F}{k_B T}\right) \tag{3.12}$$

where n is the electron density in conduction band and is given by equation (3.13):

$$n = n_i \exp\left(\frac{E_F - E_i}{k_B T}\right) = N_c \exp\left(-\frac{E_c - E_F}{k_B T}\right) \tag{3.13}$$

where n_i is known as the intrinsic carrier concentration and is given as:

$$n_i = N_c \exp\left(\frac{E_i - E_c}{k_B T}\right)$$

Combining Equations (3.12) and (3.13) results in the following expression:

$$e_n = \sigma_n \langle \upsilon_n \rangle_{th} N_c \exp\left(-\frac{E_c - E_T}{k_B T}\right) \tag{3.14}$$

where N_c is the density of states in the conduction band, $N_c = 2\left(\frac{2\pi m_e^* k_B T}{h^2}\right)^{3/2}$, $\langle \upsilon_n \rangle_{th}$ is the thermal velocity of electrons, $\langle \upsilon_n \rangle_{th} = \left(\frac{3k_B T}{m_e^*}\right)^{\frac{1}{2}}$, and m_e^* is the effective mass of electrons.

Likewise, replacing $p = N_v \exp\left(-\frac{E_F - E_v}{k_B T}\right)$ in Equation (3.9) will result in the expression of e_p as given below:

$$e_p = \sigma_p \langle \upsilon_p \rangle_{th} N_v \exp\left(-\frac{E_T - E_v}{k_B T}\right) \tag{3.15}$$

where N_v is the density of states in the valence band, $N_v = 2\left(\frac{2\pi m_h^* k_B T}{h^2}\right)^{3/2}$, and m_h^* is the effective mass of holes, $\langle \upsilon_p \rangle_{th}$ is the thermal velocity of holes, $\langle \upsilon_p \rangle_{th} = \left(\frac{3k_B T}{m_h^*}\right)^{\frac{1}{2}}$

By substituting the values of $\langle \upsilon_n \rangle_{th}$ and N_c, $\langle \upsilon_p \rangle_{th}$ and N_v , in Equations (3.14) and (3.15), respectively, then one gets the following equations:

$$e_n = AT^2 \sigma_n \exp\left(-\frac{E_c - E_T}{k_B T}\right) \tag{3.16}$$

$$e_p = AT^2 \sigma_p \exp\left(-\frac{E_T - E_v}{k_B T}\right) \tag{3.17}$$

where A is a constant given by:

$$A = 2\left(\frac{2\pi m_e^* k_B}{h^2}\right)^{3/2}\left(\frac{3k_B}{m_e^*}\right)^{1/2} = 4m_e^*\frac{\sqrt{6\pi^3}(k_B)^2}{h^3}$$

The Arrhenius plot of $\left(\frac{e_{n,p}}{T^2}\right)$ versus $\left(\frac{1000}{T}\right)$ yields in a straight line graph. Hence, the activation energy of the deep level can be extracted from the slope of this plot.

3.3 DEFECTS IN COMPOUND SEMICONDUCTORS

The semiconductors industries have significantly grown due to the rapid use of semiconductor materials in most modern electronic devices. Producing perfect crystals is the key obstacle in these industries. In fact, certain defects or imperfections are associated with all crystals, since foreign atoms can be incorporated unintentionally and/or there can be missing atoms in the host lattices or crystal structures [3]. As a result, the performance of devices can be impacted since defects can affect their optical and electrical properties. Hence, identification of the defects created during the growth of materials and/or processing of these devices is necessary to gain an insight into the performance of the devices [4]. A brief literature review of defects in GaAs, GaAsN, GaAsPN and InGaP materials are given in the following section.

3.3.1 DEFECTS IN GaAs

Several applications in electronics and optoelectronics devices witness the use of gallium arsenide (GaAs) compound such as hetero-junction bipolar transistors (HBTs), high electron mobility transistors (HEMTs, laser diode and photovoltaic (PV) cell applications [5, 6]. Different native defects can be present in this III-V

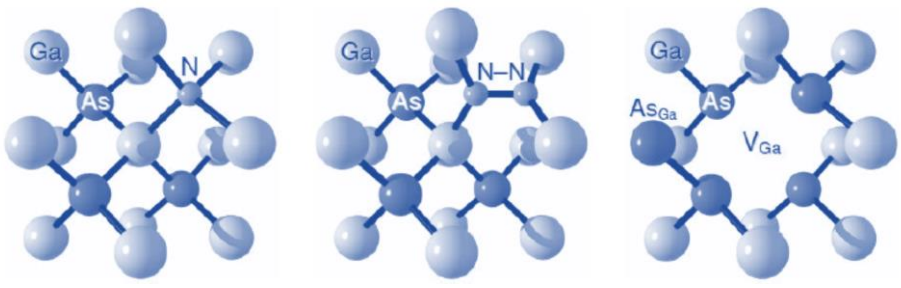
compound semiconductor. During the growth process, defects such as interstitials, vacancies and antisite are created in the crystal.

The most dominant intrinsic defect in GaAs is the EL2 trap. The activation energy of this defect ranges from 0.70 eV to 0.85 eV [7] with concentrations of ~ 10^{16} cm^{-3} and ~ 10^{14} cm^{-3} in bulk and epitaxially grown materials, respectively [8]. Its origin is assigned to the isolated Arsenic antisite defect (As_{Ga}) [9-11] or complex defect containing arsenic interstitial and As_{Ga} [11, 12]. EL3, another well-known trap in GaAs with an activation energy of ~ 0.575 eV [13], has been attributed to complexes of off-centre substitutional oxygen on arsenic sites (oc-O_{As}) [14]. Another complex defect found in GaAs is EL5 with an activation energy of ~ 0.43 eV involves As interstitials-Ga vacancies (As_iV_{Ga}) [15]. EL6 is also a common intrinsic defect in GaAs with an activation energy of ~ 0.35 eV [13]. This complex defect was associated with arsenic vacancy (V_{As}) and arsenic antisite defect (As_{Ga}) [16]. Moreover, the EL10 (~0.18eV) [13] intrinsic defect in GaAs was related to an arsenic vacancy (V_{As}) complex defect containing an impurity [17, 18].

3.3.2 DEFECTS IN DILUTES NITRIDES: GaAsN

The exclusive attributes of dilute nitrides have made this material significant and center of attention due to the strong downward bowing of its bandgap when incorporating a small quantity of nitrogen into the GaAs host lattice [19]. When incorporating small amounts of nitrogen atoms into the GaAs crystal, it results in a major perturbation in the electronic band structure. In dilute GaAsN materials, N atoms substitute As atoms which result in the formation of localised energy states near the conduction band edge. As a result, the bandgap of GaAs is reduced by ~100 meV/%N [20]. Therefore, this bandgap energy reduction of GaAs influences the

electrical and optical properties of GaAsN materials [21]. However, the occupation of N atoms in non-substitutional sites create defects in the lattice of GaAs causing a degradation of the quality of the crystal by reducing the carrier lifetime and optical efficiency of the material [22-24]. As described by various studies, different point defects such as As-antisites, N-interstitials and Ga-vacancies can be associated with this dilute nitride semiconductor. For instance, from thermodynamic calculations, the substitutional N, N–N split interstitial, Ga vacancies and As antisites have been reported by Zhang and Wei [25]. These defects have also been found in GaAsN materials grown by Molecular Beam Epitaxy (MBE) and Metal-Organic Vapour Phase Epitaxy (MOVPE) [26]. Fig. 3.7. illustrate these defects. However, according to T. Ahlgren *et al*. [27], the increase of N contents in GaAsN will likely increase the N substitutional concentration. Though, it was reported that the concentration of N interstitials remained constant (2.3×10^{19} cm^{-3}), while the N incorporation was raised from 0.7% to 3%. They presumed that the optical efficiency of dilute GaAsN nitride materials could significantly be reduced as a result of these non-radiative recombination centres.



(a) (b) (c)

Fig. 3.7. Configurations of nitrogen in GaAsN: (a) substitutional N; (b) N–N split interstitial; (c) Ga vacancy and As antisite (after Zhang and Wei [25]).

Most importantly, the DLTS technique has been adopted by various research groups to investigate the electrically active defects in GaAsN. For instance, hole traps, such as HK1 (0.16 eV), HK2 (0.39 eV), HK3 (0.35 eV), HK4 (0.45 – 0.55 eV) and HK5 (0.69 eV) have been reported by P. Krispin *et al.*[28] in MBE grown p-type GaAsN samples. It was found that the HK1 trap has the highest concentration at the interface of GaAsN/GaAs. They also correlated HK2 and HK5 traps with Ga_{As} (Ga on As site), which are similar to the traps found in GaAs grown by liquid phase epitaxy (LPE). The copper and iron impurities from the N cell were linked with HK3 and HK4 traps, respectively. Moreover, P. Kripsin *et al.* [29] reported two N-related electron traps with thermal activation energies of 0.8 eV and 1.1 eV in Si-doped GaAsN samples and these were associated with (N-N) and (As-N) split interstitials, respectively. It is worth mentioning that the GaAsN and GaInNAs structures also have common defects as in GaAs, such as EL2, EL3 and EL6 [30].

3.3.3 DEFECTS IN InGaP

Native defects play an important role in the optoelectronic and electronic properties of indium gallium phosphide (InGaP) based devices.

Epitaxial InGaP layers generally show intrinsic n-type conductivity [31-33]. Several groups have found an intrinsic deep level in undoped and Si-doped InGaP [34-36] using DLTS measurements and they suggested that it may be related to a certain kind of anion vacancy. Other studies have concluded that impurities such as phosphorous vacancies and related complexes [31] and Si [37] could affect the electrical properties of GaInP layers. D and E are an example of these deep levels and they are normally found in unintentionally doped and n-type InGaP [31]. In particular, the deep level D, with activation energy ranging from 0.31 eV to 0.34

eV was associated with silicon [38]. While E level with activation energy in the range 0.51-0.57 eV is believed to originate from phosphorous vacancies [39].

3.3.4 DEFECTS IN GaAsPN

The GaAsPN alloy material, which contains a small amount of nitrogen (several atomic percent) is a viable option for next-generation solar cell applications [40]. It is also known that increasing N content causes crystal quality to degrade, which might affect the efficiency of future devices. This degradation is characterised by an increase in nonradiative recombination processes via uniformly distributed defect states and the formation of a N-related defect level. To improve the efficiency of GaAsPN devices, the optical and electrical [41, 42] properties were studied intensively. DLTS [43, 44], photoluminescence [40], Infrared (IR) luminescence [45] and other experimental methods were used to investigate the defects. For example, from DLTS measurements Rumyantsev et al [46] found two electron traps, namely E1 (0.17 eV) and E2 (0.08 eV), in lattice- mismatched GaPN/GaP hetero-structures samples grown on GaP substrates. In addition , two N-related deep traps with thermal activation energies of 0.23 eV and 0.25 eV were reported by Alburaih *et al* [43]. Electron traps T5 and T6 located below the conduction band (Ec) at $E_C - 0.97$ eV and $E_C - 1.04$ eV have been attributed to phosphorus gallium antisites (P_{Ga}) [47]. Furthermore, another defect related to phosphorus vacancy (V_P) with activation energy of 0.26 eV has been reported in the crystal lattice [48].

REFERENCES

[1] W. Shockley and W. Read Jr, "Statistics of the recombinations of holes and electrons," *Physical review*, vol. 87, no. 5, p. 835, 1952.

[2] R. N. Hall, "Electron-hole recombination in germanium," *Physical review*, vol. 87, no. 2, p. 387, 1952.

[3] M. D. McCluskey and E. E. Haller, *Dopants and defects in semiconductors*. CRC press, 2018.

[4] D. K. Schroder, *Semiconductor material and device characterization*. John Wiley & Sons, 2015.

[5] J. Liang, Y. Nakamura, T. Zhan, Y. Ohno, Y. Shimizu, K. Katayama, T. Watanabe, H. Yoshida, Y. Nagai, and H. Wang, "Fabrication of high-quality GaAs/diamond heterointerface for thermal management applications," *Diamond and Related Materials*, vol. 111, p. 108207, 2021.

[6] N. Papež, R. Dallaev, Ş. Ţălu, and J. Kaštyl, "Overview of the Current State of Gallium Arsenide-Based Solar Cells. Materials 2021, 14, 3075," ed.

[7] J. Bourgoin and T. Neffati, "The energy level of the EL2 defect in GaAs," *Solid-State Electronics*, vol. 43, no. 1, pp. 153-158, 1999.

[8] H. Von Bardeleben, D. Stievenard, D. Deresmes, A. Huber, and J. Bourgoin, "Identification of a defect in a semiconductor: EL2 in GaAs," *Physical Review B*, vol. 34, no. 10, p. 7192, 1986.

[9] J. Lagowski, M. Kaminska, J. Parsey Jr, H. Gatos, and M. Lichtensteiger, "Passivation of the dominant deep level (EL2) in GaAs by hydrogen," *Applied Physics Letters*, vol. 41, no. 11, pp. 1078-1080, 1982.

[10] M. Baeumler, U. Kaufmann, and J. Windscheif, "Photoresponse of the AsGa antisite defect in as-grown GaAs," *Applied physics letters*, vol. 46, no. 8, pp. 781-783, 1985.

[11] A. Irvine and D. Palmer, "First observation of the EL2 lattice defect in indium gallium arsenide grown by molecular-beam epitaxy," *Physical review letters*, vol. 68, no. 14, p. 2168, 1992.

[12] M. Kaminska and E. R. Weber, "EL2 defect in GaAs," in *Semiconductors and semimetals*, vol. 38: Elsevier, 1993, pp. 59-89.

[13] G. Martin, A. Mitonneau, and A. Mircea, "Electron traps in bulk and epitaxial GaAs crystals," *Electronics Letters*, vol. 13, no. 7, pp. 191-193, 1977.

[14] U. Kaufmann, E. Klausmann, J. Schneider, and H. C. Alt, "Negative-U, off-center O As in GaAs and its relation to the EL3 level," *Physical Review B*, vol. 43, no. 14, p. 12106, 1991.

[15] R. Yakimova, T. Paskova, and C. Hardalov, "Behavior of an EL5-like defect in metalorganic vapor-phase epitaxial GaAs: Sb," *Journal of applied physics*, vol. 74, no. 10, pp. 6170-6173, 1993.

[16] K. Yokota, H. Kuchii, K. Nakamura, M. Sakaguchi, H. Takano, and Y. Ando, "EL2, EL3, and EL6 defects in GaAs highly implanted with sulfur," *Journal of Applied Physics*, vol. 88, no. 9, pp. 5017-5021, 2000.

[17] D. V. Lang, A. Y. Cho, A. Gossard, M. Ilegems, and W. Wiegmann, "Study of electron traps in n-GaAs grown by molecular beam epitaxy," *Journal of Applied Physics*, vol. 47, no. 6, pp. 2558-2564, 1976.

[18] P. Blood and J. Harris, "Deep states in GaAs grown by molecular beam epitaxy," *Journal of applied physics*, vol. 56, no. 4, pp. 993-1007, 1984.

[19] A. Erol, "Dilute III-V nitride semiconductors and material systems," *Physics and Technology*, 2008.

[20] L. Bellaiche, S.-H. Wei, and A. Zunger, "Localization and percolation in semiconductor alloys: GaAsN vs GaAsP," *Physical Review B*, vol. 54, no. 24, p. 17568, 1996.

[21] S. Ding, S. R. Barman, K. Horn, H. Yang, B. Yang, O. Brandt, and K. Ploog, "Valence band discontinuity at a cubic GaN/GaAs heterojunction measured by synchrotron-radiation photoemission spectroscopy," *Applied physics letters*, vol. 70, no. 18, pp. 2407-2409, 1997.

[22] I. Buyanova, W. Chen, B. Monemar, H. Xin, and C. Tu, "Effect of growth temperature on photoluminescence of GaNAs/GaAs quantum well structures," *Applied Physics Letters*, vol. 75, no. 24, pp. 3781-3783, 1999.

[23] S. R. Kurtz, J. Klem, A. Allerman, R. Sieg, C. Seager, and E. Jones, "Minority carrier diffusion and defects in InGaAsN grown by molecular beam epitaxy," *Applied physics letters*, vol. 80, no. 8, pp. 1379-1381, 2002.

[24] A. Fleck, B. Robinson, and D. Thompson, "Characterization of defects in doped InGaAsN grown by molecular-beam epitaxy," *Applied Physics Letters*, vol. 78, no. 12, pp. 1694-1696, 2001.

[25] S. Zhang and S.-H. Wei, "Nitrogen solubility and induced defect complexes in epitaxial GaAs: N," *Physical Review Letters*, vol. 86, no. 9, p. 1789, 2001.

[26] W. Li, M. Pessa, T. Ahlgren, and J. Decker, "Origin of improved luminescence efficiency after annealing of Ga (In) NAs materials grown

by molecular-beam epitaxy," *Applied Physics Letters*, vol. 79, no. 8, pp. 1094-1096, 2001.

[27] T. Ahlgren, E. Vainonen-Ahlgren, J. Likonen, W. Li, and M. Pessa, "Concentration of interstitial and substitutional nitrogen in GaN x As 1− x," *Applied Physics Letters*, vol. 80, no. 13, pp. 2314-2316, 2002.

[28] P. Krispin, S. Spruytte, J. Harris, and K. Ploog, "Origin and annealing of deep-level defects in p-type GaAs/Ga (As, N)/GaAs heterostructures grown by molecular beam epitaxy," *Journal of Applied Physics*, vol. 89, no. 11, pp. 6294-6301, 2001.

[29] P. Krispin, V. Gambin, J. Harris, and K. Ploog, "Nitrogen-related electron traps in Ga (As, N) layers (⩽ 3% N)," *Journal of Applied Physics*, vol. 93, no. 10, pp. 6095-6099, 2003.

[30] N. Al Saqri, J. Felix, M. Aziz, D. Jameel, C. De Araujo, H. Albalawi, F. Al Mashary, H. Alghamdi, D. Taylor, and M. Henini, "Investigation of the effects of gamma radiation on the electrical properties of dilute GaAs1− xNx layers grown by Molecular Beam Epitaxy," *Current Applied Physics*, vol. 15, no. 10, pp. 1230-1237, 2015.

[31] R. Jakomin, A. Parisini, L. Tarricone, M. Longo, B. Fraboni, and S. Vantaggio, "On the electrical properties of Si-doped InGaP layers grown by low pressure-metalorganic vapor phase epitaxy," *Thin solid films*, vol. 520, no. 21, pp. 6619-6625, 2012.

[32] S. Hatatani, K. Yuasa, and M. Konagai, "MOMBE growth of InGaP on (1 0 0) and (4 1 1) A GaAs substrates using tertiarybutylphosphine (TBP)," *Journal of crystal growth*, vol. 188, no. 1-4, pp. 17-20, 1998.

[33] J. Bettini, M. de Carvalho, M. Pudenzi, E. Laureto, and E. Meneses, "Residual carbon and carrier concentration in InGaP layers grown by chemical beam epitaxy," *Thin solid films,* vol. 429, no. 1-2, pp. 91-95, 2003.

[34] Y. Su, M. Wu, C. Chang, and K. Cheng, "Electrical and optical properties of high purity In0. 5Ga0. 5P grown on GaAs by liquid phase epitaxy," *Journal of crystal growth,* vol. 76, no. 2, pp. 299-304, 1986.

[35] K. Kitahara, M. Hoshino, K. Kodama, and M. Ozeki, "Donor-Related Deep Level in S-Doped Ga0. 52In0. 48P Grwon by Chloride VPE," *Japanese journal of applied physics,* vol. 25, no. 7A, p. L534, 1986.

[36] T. Matsumoto, T. Kato, M. Takiguchi, and T. Ishida, "Main Electron Traps in In1-xGaxP ($0.12 \leq x \leq 0.96$)," *Japanese Journal of Applied Physics,* vol. 28, no. 3R, p. 410, 1989.

[37] K. Cherkaoui, M. Murtagh, P. Kelly, G. M. Crean, S. Cassette, S. Delage, and S. Bland, "Defect study of GaInP/GaAs based heterojunction bipolar transistor emitter layer," *Journal of applied physics,* vol. 92, no. 5, pp. 2803-2806, 2002.

[38] E. Paloura, A. Ginoudi, G. Kiriakidis, and A. Christou, "Effect of doping on electron traps in metalorganic molecular-beam epitaxial Ga x In1− x P/GaAs heterostructures," *Applied physics letters,* vol. 59, no. 24, pp. 3127-3129, 1991.

[39] Z. Huang, C. Wie, J. Varriano, M. Koch, and G. Wicks, "Phosphorus-vacancy-related deep levels in GaInP layers," *Journal of applied physics,* vol. 77, no. 4, pp. 1587-1590, 1995.

[40] M. Wełna, K. Żelazna, A. Létoublon, C. Cornet, M. Zieliński, and R. Kudrawiec, "Radiative and nonradiative recombination processes in GaNP (As) alloys," *Materials Science and Engineering: B*, vol. 276, p. 115567, 2022.

[41] S. Ilahi, C. Cornet, N. Yacoubi, and O. Durand, "Improvement of carriers diffusion length and mobility in annealed GaAsPN materials for intermediate band solar cells," *Solar Energy Materials and Solar Cells*, vol. 215, p. 110622, 2020.

[42] S. Almosni, P. Rale, C. Cornet, M. Perrin, L. Lombez, A. Létoublon, K. Tavernier, C. Levallois, T. Rohel, and N. Bertru, "Correlations between electrical and optical properties in lattice-matched GaAsPN/GaP solar cells," *Solar Energy Materials and Solar Cells*, vol. 147, pp. 53-60, 2016.

[43] H. Alburaih, H. Albalawi, and M. Henini, "Effect of rapid thermal annealing on the electrical properties of dilute GaAsPN based diodes," *Semiconductor Science and Technology*, vol. 34, no. 10, p. 105009, 2019.

[44] K. Zdánský, J. Zavadil, D. Nohavica, and S. Kugler, "Degradation of commercial high-brightness GaP: N green light emitting diodes," *Journal of applied physics*, vol. 83, no. 12, pp. 7678-7684, 1998.

[45] F. Domínguez-Adame, J. Piqueras, and P. Fernandez, "Local distribution of deep centers in GaP studied by infrared cathodoluminescence," *Applied physics letters*, vol. 58, no. 3, pp. 257-259, 1991.

[46] O. Rumyantsev, P. Brunkov, E. Pirogov, and A. Y. Egorov, "Study of defects in heterostructures with GaPAsN and GaPN quantum wells in the GaP matrix," *Semiconductors*, vol. 44, no. 7, pp. 893-897, 2010.

[47] S. Das, S. K. Chaudhuri, and K. C. Mandal, "Deep level studies in high-resistive Gallium Phosphide single crystals," *ECS Journal of Solid State Science and Technology,* vol. 5, no. 4, p. P3059, 2015.

[48] A. Skazochkin, Y. K. Krutogolov, and G. Bondarenko, "Models of deep centres in gallium phosphide," *Semiconductor science and technology,* vol. 11, no. 4, p. 495, 1996.

CHAPTER 4: EXPERIMENTAL TECHNIQUES

Semiconductors materials have the ability to form many types of electrical junctions leading to a huge range of optoelectronic and electronic devices [1]. P-I-N, P-N and Schottky diodes are examples of these junctions that are preferred for deep level transient spectroscopy (DLTS) measurements. Having an insight how these junctions work is a first step to understand and interpret the physics of some semiconductor devices. The basic characteristic of a p-n junction diode will be discussed in this chapter. In addition, there are wide range of techniques for characterising and investigating semiconductor diodes. In this study, current-voltage (I-V), capacitance-voltage (C-V), DLTS and Laplace DLTS techniques are used to investigate the electrical properties of the samples. Furthermore, the main principles and information of the hardware and software implemented by these techniques are discussed in this chapter. Finally, a description will be presented of other methods used to characterise some of the samples, such as photoluminescence, Raman spectroscopy, Electrochemical Capacitance Voltage and Solar cell characteristics

4.1 p-n Junction

If n-type and p-type semiconductor materials are joined together they will form a junction between them which is called p-n junction or diode [2]. When electrons from n-type region flow to p-type side and holes from p-type to n-type region, a depletion region is created that acts as a barrier for further diffusion flow from both sides of the junction. Figure 4.1 shows the energy band diagram of a p-n junction before and after the junction formation under thermal equilibrium condition and in the absence of an applied voltage bias. X_s is the affinity of electrons in semiconductor materials. E_{Fp} and E_{Fn} represent hole and electron Fermi levels,

respectively. E_v and E_c are the valence band and conduction band energies, respectively. E_{Fi}, q, V_{bi} are the intrinsic Fermi level, the charge of electron and built-in voltage, respectively. The potential difference between the Fermi level and intrinsic Fermi level in n-region and p-region are represented as V_n and V_p, respectively. x_n and x_p are the width of the depletion layer in the n and p regions [3, 4].

The p–n junction's Fermi level (E_F) is constant across the entire region when the junction itself is at thermodynamic equilibrium, as indicated in Figure 4.1(b). Furthermore, the Figure indicates that the n and p regions are uniformly doped and there is an abrupt transition between these two regions, leading to the formation of an abrupt junction (or step junction). However, a linearly graded junction, which is also defined as a deep diffused junction, is established when the p-n junction region's doping concentration is not uniform, i.e. the change in the doping at the metallurgical junction is graded.

Figure 4.1(c) describes the three separate regions in a p-n junction, namely the quasi-neutral p and n regions (QNR) which are located far away from the metallurgical junction and the space charge (or depletion) regions (SCR) which have ionised shallow acceptors and ionised shallow donors within the p-depletion and n-depletion regions, respectively.

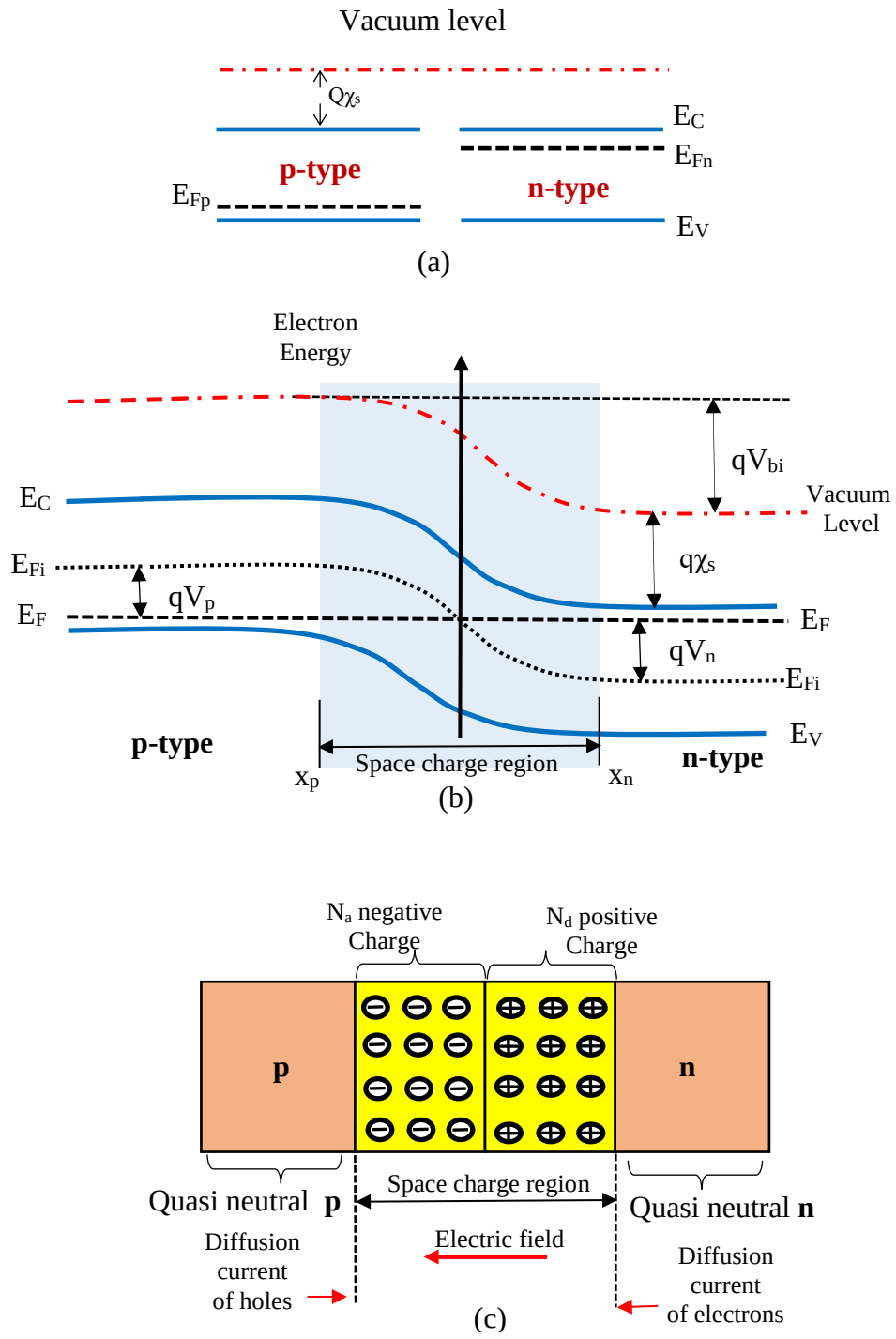


Figure 4.1: p-n junction: (a) the energy band diagram of p-type and n-type semiconductors before forming the junction, (b) the energy band diagram of p-n junction after junction formation, (c) p-n junction showing the depletion regions (or space charge regions).

In general, the concentrations of electrons and holes in the n and p regions of the p-n junction are described by:

$$n = n_i \exp\left(\frac{V_n}{V_T}\right) \tag{4.1}$$

and

$$p = n_i \exp\left(\frac{-V_p}{V_T}\right) \tag{4.2}$$

where n_i represents the intrinsic carrier density, V_T indicates the thermal voltage, which is equal to $\frac{k_B T}{q}$, where k_B is Boltzmann constant, T is the temperature and q is the electrical charge. V_n and V_p are electrostatic potentials within the n and p regions of the junction.

For abrupt and linearly graded p-n junctions, it is possible to use Poisson's equation and the continuity equation to determine the carrier distribution, built-in potential, electric field, and potential profile in the junction's SCR.

Generally, at equilibrium the relation between the charge distribution and the potential *V* (or the electric field *E*) of a junction is described by a one-dimension Poisson's equation:

$$\frac{d^2V}{dx^2} = \left(\frac{dE}{dx}\right) = \frac{\rho(x)}{\varepsilon_s} = \frac{q}{\varepsilon_s}[N_D^+(x) - n(x) - N_A^-(x) + p(x)] = 0 \tag{4.3}$$

where ρ is the charge density, ε_s is the semiconductor's permittivity, $n(x)$ and $p(x)$ are carrier densities at distance x from the junction, $N_D^+(x)$ and $N_A^-(x)$ are uncompensated donor and acceptor ions, respectively.

To solve equation (4.3), it is simplified by using the depletion approximation where it is assumed that: (i) the doping impurities are ionised (N_D^+ and N_A^-) in the SCR,

(ii) the free carriers, namely electrons and holes contributing to the local charge is negligible, and (iii) the space-charge regions are completely depleted meaning no free electrons and holes in the depletion regions on the n-type and p-type sides, respectively. Therefore, the charge densities in the n-type and p-type depletion regions are equal by considering the metallurgical junction as the origin. Therefore, it is possible to utilise suitable boundary conditions using equations (4.1), (4.2), and (4.3) to determine the built-in potential, electric field, and charge distribution in various regions of the p–n junction. It is known that the total charge density is equal to zero within the QNR region meaning that under the assumption of complete ionisation, equation (4.3) can be rewritten into equation (4.4):

$$[n - p - N_D - N_A] = 0 \tag{4.4}$$

where N_A and N_D are the densities of hole and electron densities on the p-side and n-side, respectively. In the quasi-neutral n region, if it is assumed that N_A is zero (or $N_A << N_D$), and p<<n, it is possible to obtain the electrostatic potential (V_n) at the edge of the depletion layer by introducing the above assumptions into equations (4.4) and (4.1), resulting in equations (4.5) and (4.6):

$$n = N_D \tag{4.5}$$

$$N_D = n_i exp\left(\frac{V_n}{V_T}\right) \tag{4.6}$$

Thus, by taking the natural log of both sides of Equation (4.6) and solving for the potential, yields:

$$V_n = V_T \ln\left(\frac{N_D}{n_i}\right) \tag{4.7}$$

Similarly, the electrostatic potential V_p at the edge of the depletion layer can be

written as follows:

$$V_p = -V_T \ln\left(\frac{N_A}{n_i}\right) \tag{4.8}$$

The internal built-in potential V_{bi}, which results from the diffusion of charges, can be calculated by subtracting Equation (4.8) from Equation (4.7) as given below:

$$V_{bi} = \mathrm{V}_n - \mathrm{V}_p = V_T ln\left(\frac{N_A N_D}{{n_i}^2}\right) \tag{4.9}$$

Due to the presence of positive and negative ions in the depletion regions results in the formation of an electric field in the depletion region. For simplicity, assuming n=p=0 and complete ionization of the dopant impurities inside the depletion region, Poisson equation (4.3) be used as follows:

$$\frac{d^2V}{dx^2} = \left(\frac{dE}{dx}\right) = \begin{cases} \frac{qN_A}{\varepsilon_s} & -x_p \le x \le 0 \\ -\frac{qN_D}{\varepsilon_s} & 0 \le x \le x_n \\ 0 & x \le x_n \text{ and } x \ge X_n \end{cases} \tag{4.10}$$

where x_n and x_p are the depletion layer widths in the n and p regions, respectively (see Figure 4.1(b)). By integrating Equation (4.10), the electrical field is given by:

$$E\,(x) = -\frac{qN_A(x_p+x)}{\varepsilon_s} \quad \text{for} \quad -x_p \le x \le 0 \tag{4.11}$$

$$E(x) = -\frac{qN_D(x_n-x)}{\varepsilon_s} \quad \text{for} \quad 0 \le x \le x_n \tag{4.12}$$

The electric field is related to the potential (V) since $E(x) = -\frac{dV}{dx}$. In view of this, the integration of Equations (4.11) and (4.12) gives the following:

$$V(x) = \frac{qN_A}{2\varepsilon_s}\left(x_p + x\right)^2 \quad \text{for } -x_p \le x \le 0 \tag{4.13}$$

$$V(x) = V(0) + \frac{qN_D}{\varepsilon_s}\left(x_n x - \frac{x^2}{2}\right) \quad \text{for } 0 \le x \le x_n \tag{4.14}$$

Therefore, from Equation (4.13), the potential across the p-region can be expressed by:

$$V_p = \frac{qN_A x_p^2}{2\varepsilon_s} \tag{4.15}$$

Similarly, using Equation (4.14) the potential across the n-region is given by:

$$V_n = \frac{qN_D x_n^2}{2\varepsilon_s} \tag{4.16}$$

Hence, the built-in potential can be expressed as follows:

$$V_{bi} = V_p + V_n = V(x_n) = \frac{\mathrm{E}_m}{2}\left(x_p + x_n\right) \tag{4.17}$$

where

$$|E_m| = \sqrt{\frac{2qN_A V_p}{\varepsilon_s}} = \sqrt{\frac{2qN_D V_n}{\varepsilon_s}} \tag{4.18}$$

Due to the continuity of the electrical field at the junction interface, the following should be noted:

$$N_A x_p = N_D x_n \tag{4.19}$$

It is possible to calculate the depletion widths x_p and x_n on either side of the junction by using Equations (4.17) and (4.19).

$$x_p = \left(\frac{2\varepsilon_s V_{bi}}{q}\frac{N_D}{N_A(N_A+N_D}\right)^{\frac{1}{2}} \tag{4.20}$$

Similarly, x_n can be written as:

$$x_n = \left(\frac{2\varepsilon_s V_{bi}}{q}\frac{N_A}{N_D(N_A+N_D}\right)^{\frac{1}{2}} \tag{4.21}$$

Consequently, the total space charge width, W, in the p-n junction is given by:

$$W = x_n + x_p = \left(\frac{2\varepsilon_s V_{bi}}{q}\frac{N_A+N_D}{N_A N_D}\right)^{\frac{1}{2}} \quad (4.22)$$

In Equation (4.22) the depletion width depends on the doping density of the lightly doped side, meaning that the depletion region fraction is greater on the side of the junction with lower doping. For example, if $N_A >> N_D$, $W \approx \left(\frac{2\varepsilon_s V_{bi}}{qN_D}\right)^{\frac{1}{2}}$ and the depletion layer is mainly on the junction's n-side. This is referred to as a one-sided abrupt p–n junction [2, 4].

4.1.1 P-N JUNCTION UNDER BIAS CONDITIONS

A p-n junction will no longer be in equilibrium if an external bias is applied between the p and n regions, and current will begin to flow through the junction. The flow of the current is dependent on the polarity of the applied external bias known as the forward bias and a reverse bias conditions. As seen in Figure 4.2(c), the reverse bias voltage condition involves an increase in the potential barrier (V_{bi} + V) across the junction. In addition, the depletion width is increased so that the current flow through the junction becomes very small. This leads to conclude that, in the reverse bias condition the flow of current is due to the thermal effects and minority carriers. Figure 4.2 (b) shows that the implementation of the forward bias voltage condition results in reduced potential barrier across the junction (V_{bi} – V), thereby resulting in reduction of the depletion width. This creates a situation in which the flow of current across the junction rises considerably. Moreover, Figure 4.2 (a) shows that for a zero applied bias condition, the Fermi level remains constant throughout the junction, while when a forward bias voltage is applied to the diode, E_{Fn} moves down to the half-occupancy level of equilibrium for holes within the p region, and

E_{Fp} does the reverse. In addition, Figure 4.2 (c) shows that, in the context of a reverse bias condition, the Fermi level on the n region is lower than the Fermi level on the p region.

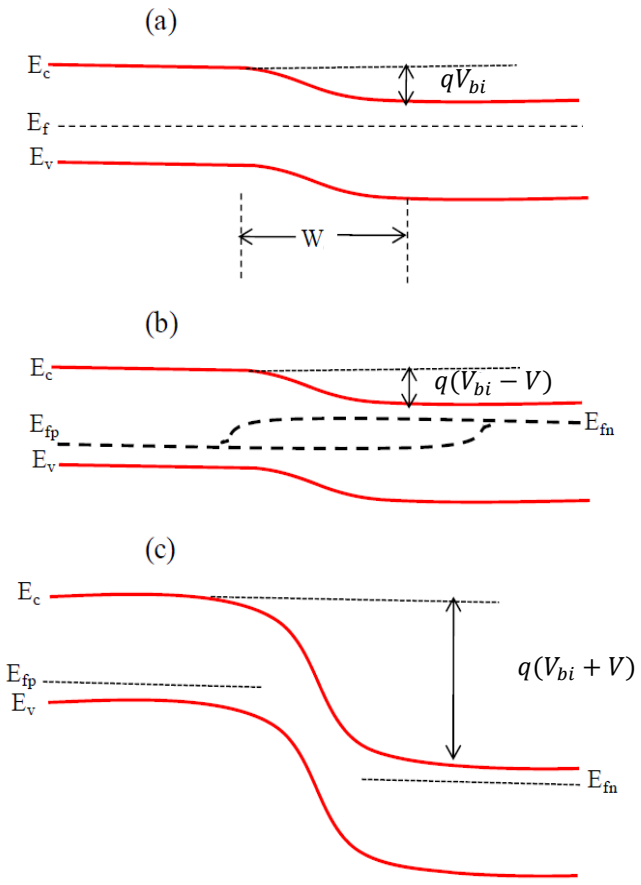


Figure 4.2: Energy band of a p-n junction under different bias conditions (a) zero bias, (b) forward bias and (c) reverse bias [5].

By neglecting the voltage drop in the p and n quasi-neutral regions and modifying Poisson's equation at zero bias, i.e. replacing V_{bi} with (V_{bi} + V), the depletion width for abrupt junction under different bias conditions can be obtained as shown by Equation 4.23 [5]:

$$W = \left(\frac{2\varepsilon_s(N_A+N_D)}{qN_AN_D}(V_{bi} \pm V) \right)^{\frac{1}{2}} \quad (4.23)$$

In equation 4.23 the plus and minus signs refer to reverse and forward bias conditions, respectively.

4.1.2 DEPLETION LAYER CAPACITANCE

One of the most important parameters that helps to understand a p-n junction is the depletion capacitance of the space charge region. The measurements of the capacitance of the device as a function of reverse bias voltage enable to estimate the built-in potential of the junction. Moreover, the capacitance-voltage (C-V) analysis is a standard method used to determine the carrier density profile of a Schottky diode or p-n junction [5]. Since a p-n junction is a double layer of electrons (donors) and holes (acceptors) charge carriers, its related capacitance can be expresses as [3]:

$$C = \frac{dQ}{dV} = \frac{d(qN_Ax_p)}{dV} = \frac{d(qN_Dx_n)}{dV} \quad (4.24)$$

where dQ is the charge in the depletion region and dV is the applied voltage. Moreover, this capacitance can be given as a function of the junction depletion width as follows:

$$C = \frac{A\varepsilon_S}{W} \quad (4.25)$$

where A is the area of the junction and ε_S is the dielectric constant of the semiconductor. When applying a reverse bias and assuming $N_A >> N_D$, using Equations (4.24) and (4.25), the capacitance can be written as:

$$C = \frac{dQ}{dV} = \frac{A}{2}\left[\frac{2\varepsilon_s q N_D}{V_{bi} \pm V_R}\right]^{\frac{1}{2}} \quad (4.26)$$

From Equation (4.26) it can be seen that the capacitance of the diode decreases as the reverse bias is increased. Also, it is possible to obtain the doping concentration (N_D) from the slope of the plot of $1/C^2$ versus V (reverse-bias voltage) as shown in Figure 4.3. The built-in potential (V_{bi}) can be obtained from the intercept at $1/C^2 = 0$

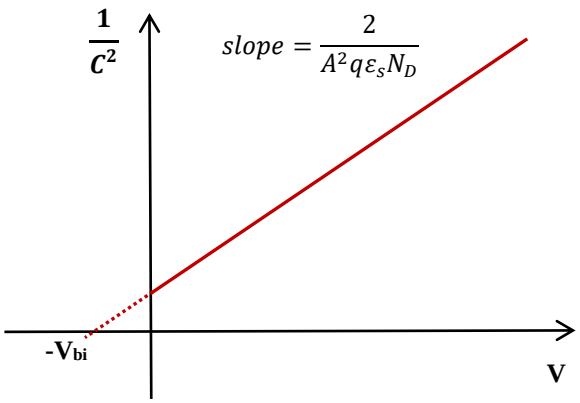


Figure 4.3: Plot of $1/C^2$ versus applied reverse bias voltage for a one step- junction diode [5].

4.2 CURRENT- VOLTAGE CHARACTERISATION

If the device is considered to be a Schottky, p-n or p-i-n diode the current-voltage (I-V) characteristics can be explained by the thermionic emission model with a series resistance (Rs) as follows [5]:

$$I = I_S[exp(\frac{q(V-IR_S}{nK_BT}) - 1] \quad (4.27)$$

where q is the electronic charge, V is the applied voltage, k_B is the Boltzmann constant, n is the ideality factor, I_S is the saturation current and T is the absolute temperature in Kelvin. The values of I_S and n are determined from the

experimental data. The saturation current I_S can be determined from Equation (4.28):

$$I_S = AA^{**}T^2 exp(\frac{-q\emptyset_B}{K_B T}) \quad (4.28)$$

where A is the area of the junction and A^{**} is the effective Richardson's constant for a given semiconductor material, and $\emptyset_B$ is the built-in potential barrier. In case of forward bias voltage for $V - IRs >> kT$ and hence Equation 4.27 can be rewritten as:

$$I = I_S exp(\frac{q(V-IR_S}{nK_B T}) \quad (4.29)$$

By taking the first derivative of I with respect to V from equation (4.29) will give:

$$\frac{dI}{dV} = I_s \left(\frac{q}{nk_B T} exp\left(\frac{q(V-IR_s)}{nk_B T}\right) - \frac{q}{nk_B T} exp\left(\frac{q(V-IR_s)}{nk_B T}\right) R_s \frac{dI}{dV}\right) \quad (4.30)$$

Note that $dI/dV = G$, and G is the conductance. Equation 4.30 can be rewritten as:

$$G = \frac{q}{nk_B T} I_s \, exp\left(\frac{q(V-IR_s)}{nk_B T}\right)(1 - G.R_s) = \frac{q}{nk_B T} I \, (1 - G.R_s) \quad (4.31)$$

$$\frac{G}{I} = \frac{q}{nk_B T} - \frac{qR_s}{nk_B T} \mathrm{G} \quad (4.32)$$

Thus, by plotting the values of G/I versus (G) a straight line is obtained, as shown in Figure 4.4. Values of n and R_S can be extracted from the y-intercept and the

slope, respectively. This method of extracting *n* and R_S experimentally is known as Werner's method [6].

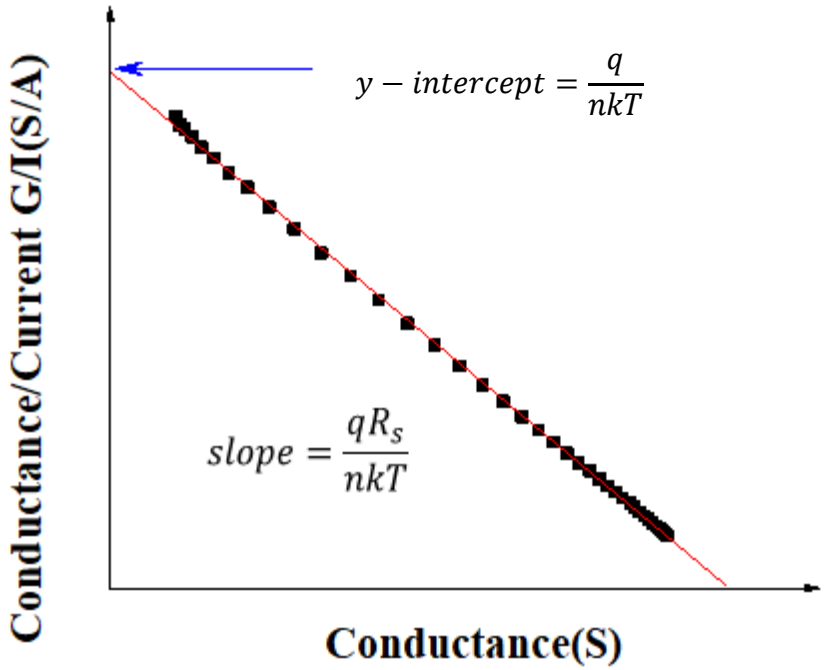


Figure 4.4: Plot of G/I versus G.

For the determination of I_S and $\emptyset_B$, the natural logarithm of Equation 4.27 is used as given below:

$$\text{In}(I)=\text{In}(I_S)+\frac{q(V-IR_S)}{nkT} \tag{4.33}$$

By plotting $\text{In}(I)$ versus $(V - IR_S)$, I_S can be found from the y-intercept of the plot and by substituting the I_S value in equation (4.28) , $\emptyset_B$ can be calculated as:

$$\emptyset_B = \frac{k_B T}{q} ln\left(\frac{AA^* T^2}{I_S}\right) \tag{4.34}$$

4.3 DEEP LEVEL TRANSIENT SPECTROSCOPY (DLTS)

Investigating deep level defects in semiconductor experimentally can be done via microscopic defect analysis methods [7]. Deep level transient spectroscopy (DLTS) is one of these techniques, which is a novel, powerful tool used to characterise the deep levels defects in semiconductors via the observation of charge carriers emission [8]. DLTS was first discovered by Lang in 1974 [9]. This technique is totally based on the change of the depletion capacitance as a function of temperature in order to determine the activation energy of traps and capture cross-section.

4.3.1 CAPACITANCE TRANSIENTS

The DLTS method measures the capacitance transients which result from the change in the depletion charge region. A Schottky diode or a p-n junction device is needed to carry out these measurements. Figure 4.5 shows the changes in the charge occupancy of a defect level at different bias conditions in a Schottky diode. Considering Figure 4.5, at a stage (a), a space charge region is established when a reverse bias V_R is applied and traps above the Fermi level are empty. At stage (b), the depletion region width decreases after a filling pulse V_P is applied which leads to the traps to capture electrons (filling traps). The rate at which the traps capture electrons is given by:

$$\frac{dn_T}{dt} = c_n(N_T - n_T) \tag{4.35}$$

where N_T , c_n and n_T represent the total number of trap states, the capture coefficient of electrons and number of trap states occupied by electrons, respectively. The electron capture coefficient can be given by the following equation:

$$c_n = \sigma_n \langle v_{th} \rangle n \tag{4.36}$$

where σ_n is the electron capture cross-section, $\langle \upsilon_{th} \rangle$ is the mean thermal velocity of the electrons, and $n = N_d - N_T \approx N_d$ is the effective doping concentration.

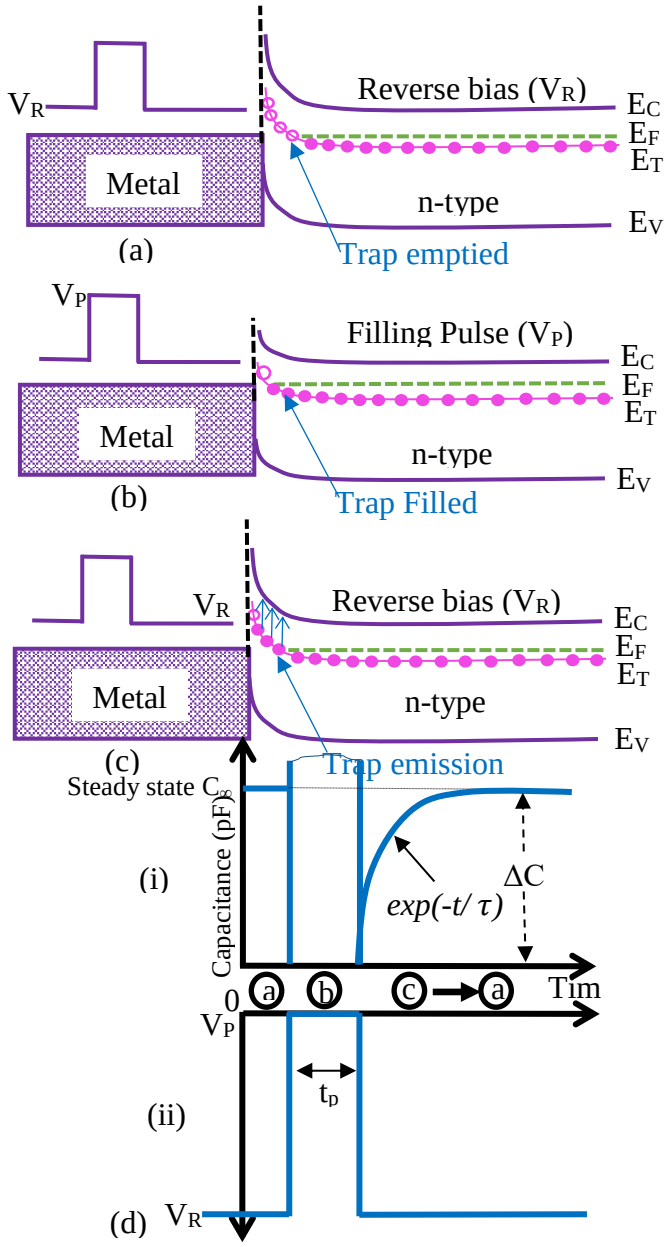


Figure 4.5: Plot of energy diagrams of a Schottky diode showing the charge occupancy changes of the defects level during (a) emptying traps at steady applied reverse bias ($V=V_R$), (b) filling traps during filling pulse $V=V_P$, (c) thermal emission of electrons due to the increase in the temperature at $V=V_R$ and (d) DLTS pulse and corresponding capacitance transient. t_p and E_T represent a pulse width and a trap energy level [10].

At stage (c), the depletion region moves back to its original width after the reverse bias is re-established, and the filled traps will start to emit the trapped carriers and the corresponding emission rate is given by:

$$\frac{dn_T}{dt} = e_p N_T - (e_n + e_p) n_T \tag{4.37}$$

where e_n and e_p are electron emission and hole emission, respectively.

Assuming that the deep level is an electron interacting centre, the solution of Equation (4.35) (capture process) and Equation (4.37) (emission process) are given by [11]:

$$n_T(t) = N_T\{1 - \exp(-c_n t)\}, \quad c_n \gg e_n, e_p, c_p \tag{4.38}$$

and

$$n_T(t) = N_T \exp\left(\frac{-t}{\tau}\right), \quad e_n \gg c_n, e_p, c_p \tag{4.39}$$

where c_p is the capture coefficient of holes and the inverse of the electron emission rate is $= \frac{1}{e_n}$.

As shown by the above equations, the reduction of the filled trap concentration has an exponential trend with a time constant τ and this process leads to a rise in the capacitance transient as illustrated schematically in Figure 4.5 (d).

The change of traps occupancy can be measured indirectly by monitoring the capacitance changes of the junction. By adding the filled traps contribution, $n_T(t)$ in the space charge region, Equation (4.26) can be modified as:

$$C = \frac{dQ}{dV_R} = \frac{A}{2}\left[\frac{2\varepsilon_s q N_D^*}{V_{bi}+V_R}\right]^{1/2} \tag{4.40}$$

where $N_D^* = N_D - n_t$.

If $n_t << N_D$, Equation (4.38) could be written as:

$$\Delta C = C_\infty \left(1 - \frac{n_T}{2N_d}\right) \tag{4.41}$$

where ΔC is the amplitude of the capacitance transient and C_∞ the steady state capacitance:

$$C_\infty = \frac{A}{\sqrt{2}} \left[\frac{2\varepsilon_s q N_D^*}{V_{bi}+V_R}\right]^{1/2}.$$

Combining Equation (4.39) and Equation (4.41) provides the time dependence of the capacitance for majority carrier traps emission and this can be determined from:

$$\Delta C = C_\infty \left[1 - \frac{N_T}{2N_D} \exp\left(-\frac{t}{\tau}\right)\right] \tag{4.42}$$

Consequently, the trap concentration and the emission rate of electrons can be obtained from the amplitude of the capacitance transient and the time constant, respectively. Figure 4.5 (d) shows the trap emission process and consequent change in the capacitance as a function of time. It is worth pointing out that the sign of the capacitance transient for minority carriers traps is opposite to the majority carrier traps.

4.3.2 CONVENTIONAL DLTS

The conventional DLTS technique [9] is dependent on the rate window concept, where the capacitance of the depletion region for a p-n junction or Schottky diode is measured between two interval times, t_1 and t_2 ($t_2 > t_1$) which are a result of capture and emission of carriers. A DLTS spectra can be obtained through the measurement of the capacitance transient as a function of temperature T, allowing the determination of the trap parameters such as activation energy, E_T, capture cross section σ, and density N_T. In particular, Equation (4.42) can be used to give the DLTS output signal as function of temperature, S(T), and can mathematically be expressed as:

$$S(T) = C(t_1) - C(t_2) = \Delta C_\circ \left[exp\left(-\frac{t_2}{\tau}\right) - exp\left(-\frac{t_1}{\tau}\right)\right] \quad (4.43)$$

where $\Delta C_\circ$ is the change in the capacitance at time t = 0, and it is expressed as:

$$\Delta C_\circ = \frac{C_\infty N_T}{2N_D} \quad (4.44)$$

where N_T is the concentration of the trap and C_∞ is the capacitance at a maximum reverse bias (when the trap is completely empty). S(T) changes as the emission rate e_n changes with temperature as shown in Figure 4.6 (a).

When $\tau \ll (t_1 - t_2)$ and $\tau \gg (t_1 - t_2)$, the DLTS signal will be small, if $\tau \approx (t_1 - t_2)$ the DLTS signal is maximum. The maximum signal of S(T) (maximum emission) corresponds to the maximum amplitude of the DLTS signal and can be obtained by using $\frac{dS(T)}{d\tau} = 0$, the rate window equation can be written as:

$$\tau = \tau_{max} = \frac{(t_1 - t_2)}{ln\left(t_1/t_2\right)} \tag{4.45}$$

The value of the rate window τ can be changed by changing the values of two-measurement times t_1 and t_2, Changing the rate window will generate different maximum peaks (DLTS peaks) at different temperatures, as shown in Figure 4.6 (b). Typical rate windows values are from 5 s^{-1} to 5000 s^{-1}. To obtain the trap activation energy, the Arrhenius plot of the emission rates (from DLTS peaks) as a function of temperature is used, as shown in Figure 4.6 (c). The activation energy is extracted from the slope of the Arrhenius plot whereas the apparent capture cross-section can be obtained from the y-intercept. Additionally, the trap concentration, N_T can be calculated using Equation (4.44), where $\Delta C_\circ$ corresponds to the conventional DLTS peak amplitude. It is worth pointing out that the DLTS signal does not depend on the value of t_1 and t_2 as Equations (4.44) and (4.45) indicate, but it depends on the ratio (t_2/t_1).

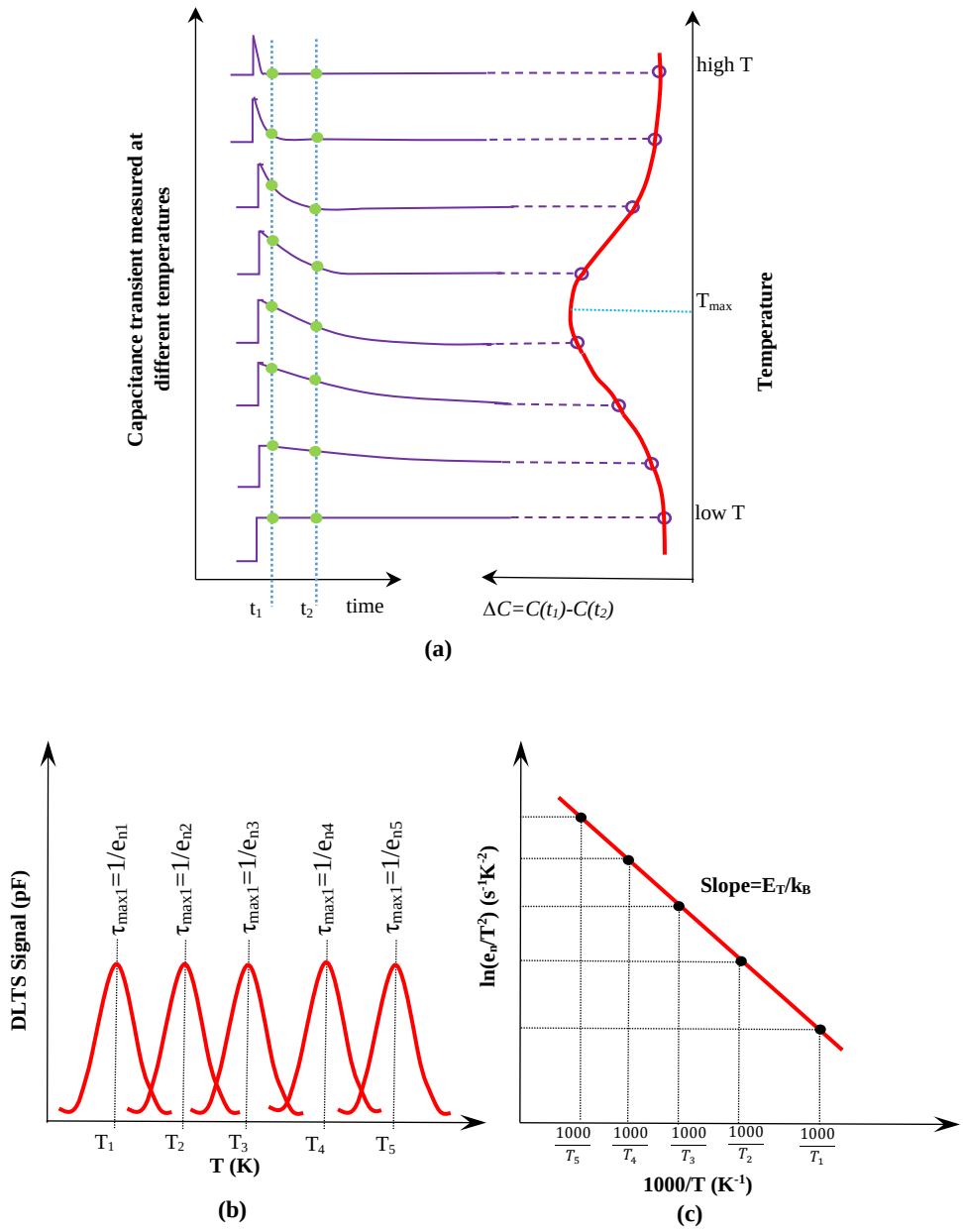


Figure 4.6: schematics diagrams illustrating (a) the generation of DLTS peaks for one rate window, (b) DLTS peaks for different rate windows and (c) Arrhenius plot obtained from different rate windows [9].

4.4 LAPLACE DLTS SPECTROSCOPY

Conventional DLTS is a powerful technique and is widely applied in order to investigate deep-level defects. However, it has some problems that affect its resolution. One of these issues of DLTS is the accuracy of temperature

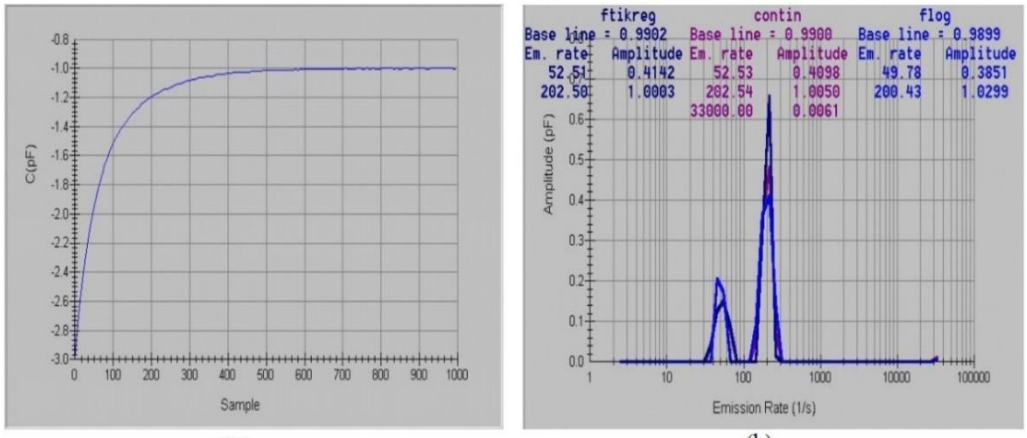
measurements associated with the thermal scanning process. Increase or decrease the temperature causes inaccurate measurement of the traps' activation energies. Another problem is the difficulty of separating the time constants of the exponential emission transient from various defect states which leads to a broadening of the DLTS spectra peaks [12]. To overcome the constraints of the conventional DLTS, Laplace DLTS (LDLTS) technique is applied. LDLTS is an isothermal technique where the device under investigation is kept at a constant temperature throughout the measurement process. The Laplace equation can be used to provide the mathematical description of the LDLTS transient.

$$f(t) = \int_0^\infty F(s)e^{-st}ds \tag{4.46}$$

where $f(t)$ and $F(s)$ are the recorded transient and the spectral function, respectively. Figure 4.7(a) shows the capacitance transient which is obtained from LDLTS measurements.

Equation 4.46 represents the transient capacitance as the Laplace transform of the actual spectral density function $F(s)$. Figure 4.7 (a) presents an example of a capacitance transient obtained using Laplace DLTS. The real spectrum of emission rates within the transient is obtained by using an appropriate mathematical algorithm, which performs an inverse Laplace transform for the recorded transient $f(t)$.

Three main algorithm routines, namely CONTIN, FLOG and FTIKREG are used to solve Equation (4.46) [13] and achieve a spectrum of delta-like peaks as shown in Figure 4.7 (b).



(a) (b)

Figure 4.7: (a) Laplace DLTS capacitance transient and (b) a spectrum of delta-like peaks [14].

4.5 SYSTEM HARDWARE IMPLEMENTATION

4.5.1 DESCRIPTION OF SYSTEM HARDWARE

This section gives details of the experimental setup used to perform the conventional DLTS and Laplace DLTS measurements. Figure 4.8 shows an experimental photograph of the DLTS system and Figure 4.9 illustrates a block diagram of DLTS and Laplace DLTS setup, which consists of (i) capacitance meter, (ii) Janis cryostat and temperature controller, (iii) Current-Voltage meter, and (iv) data acquisition and BNC connectors box for analogue Input (I)/Output (O). A computer via a GPIB interface controls all equipment.

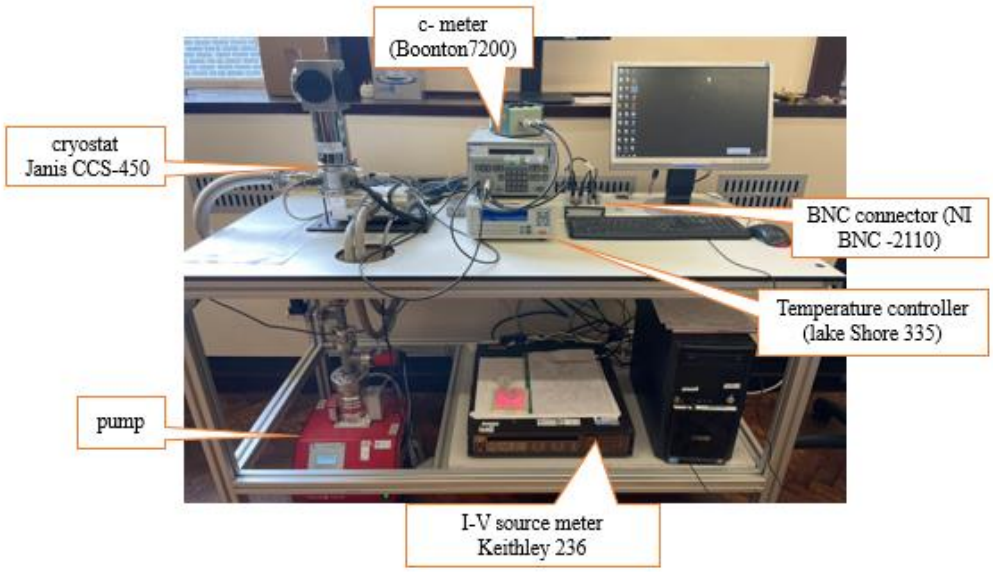


Figure 4.8: Photograph of the DLTS system used in this thesis.

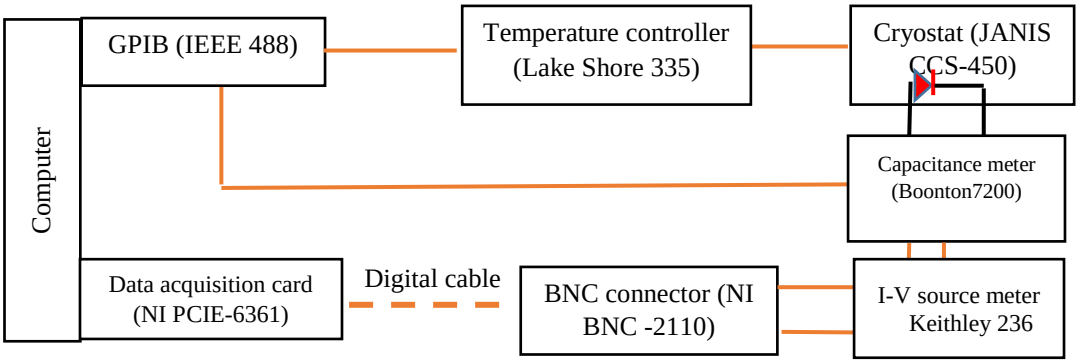


Figure. 4.9: Block diagram of DLTS and Laplace DLTS system.

4.5.1.1 CRYOSTAT AND TEMPERATURE CONTROLLER

Thermal energy is required for the process of emitting charge carriers from the traps. A cryostat (type Janis CCS-450) and a temperature controller (Model Lake

Shore 335 are used to control and monitor the sample temperature in DLTS and Laplace DLTS experiments.

The cryostat is based on a closed-loop cycle refrigeration system which operates with a compressor that ensures a continuous flow of helium gas (He) through a high efficiency flexible six feet cryogen transfer line.

The internal structure of the cryostat system as shown in Figure 4.10 consists of (i) a cold finger which accommodates the sample holder, (ii) lightweight aluminium vacuum shroud, (iii) a radiation shield, and (iv) electrical ports for sample contacts and thermal sensors.

The cryostat can operate over a temperature range from 10 K to 450 K with a stability of ±1K. Lake Shore 335 was used to control two temperature sensors, one of which was situated very close to the device under investigation in order to control its temperature more accurately.

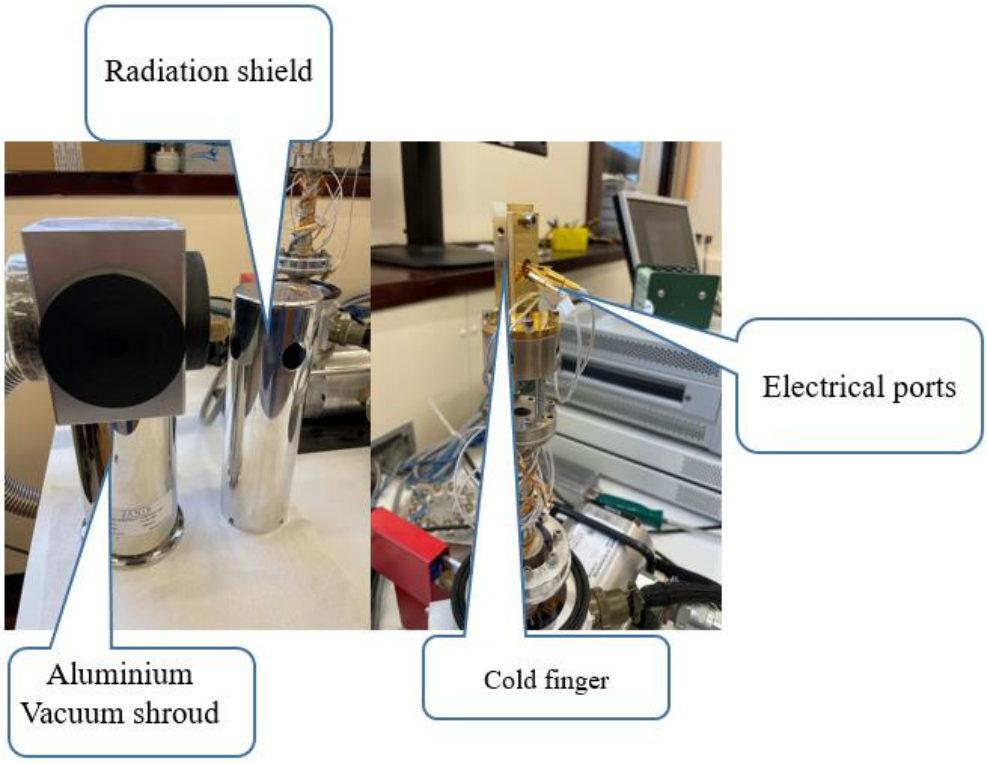


Figure 4.10: Photograph of the cryostat structure used for the DLTS experiments.

4.5.1.2 CAPACITANCE METER

A high response time capacitance metre is needed to monitor the capacitance transient in DLTS and determine the background doping concentration and trap concentration. The Boonton 7200 meter that has a response time of ~120 μs has been used and this meter has only 1 MHz sampling frequency.

4.5.1.3 CURRENT-VOLTAGE SOURCE METER

To determine the diode parameters such as ideality factor (n) and the built-in potential barrier (ϕ_b), I-V measurements were performed at different temperatures for each sample. In addition, a low reverse current, in the range of μA, is required for DLTS and Laplace DLTS measurements and hence, the current-voltage (I-V)

characteristics were obtained using a Keithley 236 current meter, which is controlled by a computer software via GPIB interface. It provides a source voltage ranging from 100 μV to 110 V with a sensitivity of ±10 μV and a source current in the range of 100 fA to 100 mA, with a sensitivity of 10 fA.

4.5.1.4 DATA ACQUISITION AND BNC-2100 CONNECTOR

A National Instruments (NI) data acquisition (DAQ) card is used for biasing and pulsing the diodes. The card can be used to apply a maximum input voltage of ± 10.0V to the samples with a pulse width of 0.5 μs. A BNC-2110 connector box is used to collect information from the diodes and send it to the computer for processing. An NI PCIe-6321 card and BNC-2110 connection box were connected via a suitable SHC68-68 EPM cable.

4.5.1.5 COMPUTER INTERFACE

General-purpose interface bus (GPIB) is used to connect all experimental equipment to a computer for remote control via software.

4.6 SYSTEM SOFTWARE

The Laplace DLTS software was developed as part of a joint project "Project Copernicus CIPA CT-94-0172 and the Polish Science Foundation, serial number: C3.2.041" between the Institute of Physics of the Polish Academy of Sciences, Warsaw, Poland (late Prof. L. Dobachevsky) and the University of Manchester (Prof. A.R. Picker). This software can run in normal DLTS and Laplace DLTS modes as described below.

4.6.1 CONVENTIONAL DLTS MEASUREMENTS MODE

In traditional DLTS mode, the sample temperature is scanned at a rate of 2K / min. In this mode, the software displays three different routines, namely Multi-rate window, Trap View, and Exponential Fitting modes, which all use the rate window concept. These modes are discussed briefly below.

In the "Multi-Rate" mode nine different rate windows are recorded, namely 5 s^{-1}, 10 s^{-1}, 20 s^{-1}, 50 s^{-1}, 100 s^{-1}, 200 s^{-1}, 500 s^{-1}, 1000 s^{-1} and 2000 s^{-1}. In the Trap View mode, a pair of rate windows out of five pairs can be selected at a time: (4, 10 s^{-1}), (20, 50 s^{-1}), (80, 200 s^{-1}), (400, 1000 s^{-1}) and (2000, 5000 s^{-1}). For Exponential Fitting modes only one rate window could be chosen for this procedure, a lock-in mode can be selected instead of the rate window mode. Lock-in mode has a better resolution as compared to rate window mode but also has a poor signal to noise ratio. When the measurement is run in "Exponential Fitting" mode, the Arrhenius plot is obtained. Thus, defects activation energies and capture cross-sections can be estimated. It should be noted that, parameters of a DLTS experiment such as reverse bias, forward bias, pulse duration, and temperature range can be remotely tuned in all these three modes.

4.6.2 LAPLACE TRANSIENT PROCESSING MODE

In Laplace DLTS mode, the sample is kept at a constant temperature during the measurements. The Laplace DLTS mode is used to improve the signal to noise (S/N) ratio. Three algorithms are applied to generate the Laplace DLTS signals (FLOG, CONTIN and FTIKREG).

4.6.3 DLTS AND LAPLACE DLTS MEASUREMENTS

The electrically active defects detected in the material systems studied in this thesis are characterised using DLTS and Laplace DLTS techniques, which are discussed in previous section. This section provides a brief description of the experimental procedures. First, the samples were formed into circular mesas ranging in diameters from 200 to 1000 μm and mounted on 10-pins TO5 headers which are installed in a sample holder within a closed loop cycle refrigerator, model CCS-450 cryostat. The samples were then cooled to a temperature of 10K and the DLTS measurements were performed by gradually increasing the temperature up to 450 K at a rate of 2 K/min. A National Instrument Box generates an electrical pulse sequence that is applied to the samples. The transient capacitance is measured using a Boonton 7200 capacitance meter. The change in capacitance transient is recorded in the form of a DLTS signal and stored in a computer at selected reverse bias (V_R) and filling pulse (V_P).

High resolution Laplace DLTS measurements were performed to resolve the broad features detected in the conventional DLTS peaks. As it is an isothermal process, the temperature of the sample is fixed during the Laplace DLTS measurements, which are carried out within the temperature range of the conventional DLTS peak.

4.7 Electrochemical Capacitance Voltage Profiling

Conventional capacitance-voltage (C-V) measurements are commonly used to determine the distribution of free charge carriers in semiconductors, which is related to the dopant concentration profile. However, the main limitation of the conventional C-V method is the electrical breakdown voltage of the semiconductor samples, which imposes limitations on the maximum measurement depth from the

junction of metal/semiconductor (Schottky diode) or p-i-n structures. To overcome the limitations of the conventional C-V technique, the electrochemical capacitance-voltage (ECV) method was developed by Ambridge et al [15] to characterize the free charge carriers profile at various depths. The technique is based on making a liquid electrolyte-semiconductor Schottky contact and measuring the capacitance at a constant reverse bias. The semiconductor is electrolytically etched between capacitance measurements, leading to depth profiling. This technique has a significant advantage over conventional CV profiling in that the maximum depth is not limited by the maximum breakdown voltage. However, ECV is a destructive technique.

The ECV process involves two primary steps, (i) the measurement of the capacitance-voltage (CV) characteristics, and (ii) controlled etching of the semiconductor material. The etching method used in ECV profiling depends on the type of doping in the semiconductor material. For n-type samples, the etching is done using a high-intensity lamp to activate the dopants and create a region of high conductivity, while for p-type samples voltage etching is typically used to remove a thin layer of the material. Repeated cycles of etching and measurement allow for obtaining a depth profile of active dopant concentration (free charge carrier concentration).

The carrier concentration at the depletion depth W_{DEPL} is extracted from the slope of the $1/C^2$ vs. V curve using the relationship [16]:

$$N_d(W_{DEPL}) = \frac{2}{q.\varepsilon_s.\varepsilon_0 \cdot A^2} \cdot \frac{1}{\frac{d(1/c^2)}{dV}} \tag{4.47}$$

$$W_{DEPL} = \frac{\varepsilon_s \cdot \varepsilon_0 .A}{C} \tag{4.48}$$

where, q is the electronic charge, ε_s is the dielectric constant of the semiconductor, ε_0 is the permittivity of free space and A is the area of the electrolyte-semiconductor junction.

ECV measurements were performed in collaboration with Dr Hassanet Sodabanlu (The University of Tokyo, Japan) utilizing the commercial Nanometrics ECV Pro profiler (see Figure 4.11). First the electrolyte EDTA (ethylenediaminetetraacetic acid).2Na mixed with ethylenediamine 1:10 dilution with deionised (DI) water was prepared. This consisted of 950 mls DI water, 50mls ethylenediamine (5% by volume) and 37.24 gms of EDTA (0.1M) (or short for edetic acid). Then a 100 ml of the above solution was diluted to 1 litre of DI water and used to profile the top n-type layer of the p-i-n structures. The samples were measured at room temperature using pulse anodizing etching mode. It is worth pointing out that the above solution combined with the pulse anodizing etching mode allowed fast etching but at low resolutions (5 nm and larger).



Figure 4.11: Photograph of the Nanometrics Electrochemical Capacitance Voltage (ECV) Pro profiler apparatus. Courtesy of Dr Hassanet Sodabanlu (The University of Tokyo, Japan).

4.8 PHOTOLUMINESCENCE (PL) SPECTROSCOPY

Photoluminescence (PL) is an optical characterization technique that analyses the optical emission from materials which are exposed to an optical excitation source. The optical emission results from radiative recombination between an electron-hole pair in a material that was previously excited by a photon absorption, which have energy higher than the bandgap of the material. PL spectroscopy is a non-destructive and effective technique used to examine the optical characteristics of semiconductor materials, nanostructures and devices.

In PL measurements, when the investigated sample is subjected to a light source such as a laser, lamp or LED with a photon energy *hv* greater than the material bandgap E_g, the electrons in the semiconductor absorbs these photons, and the excess energy is transferred to the semiconductor material, a phenomenon called photo-excitation. After photo-excitation, the electrons in the semiconductor material will release the excess energy in the form of light, which is referred to as photoluminescence. Information about the bandgap, impurity levels, and material quality can be obtained by examining the spectral content and intensity of the photoluminescence spectrum.

During photo-excitation, electrons are raised to higher energy states and later return to their original equilibrium states by releasing energy in the form of light as shown in Figure 4.12. This process is called radiative recombination, and the energy difference between the excited and equilibrium states is emitted as light. In addition to radiative recombination, a non-radiative process occurs when the difference in the energy is lost as heat. It is important to note that the PL technique does not necessitate any sample preparation or electrical contacts.

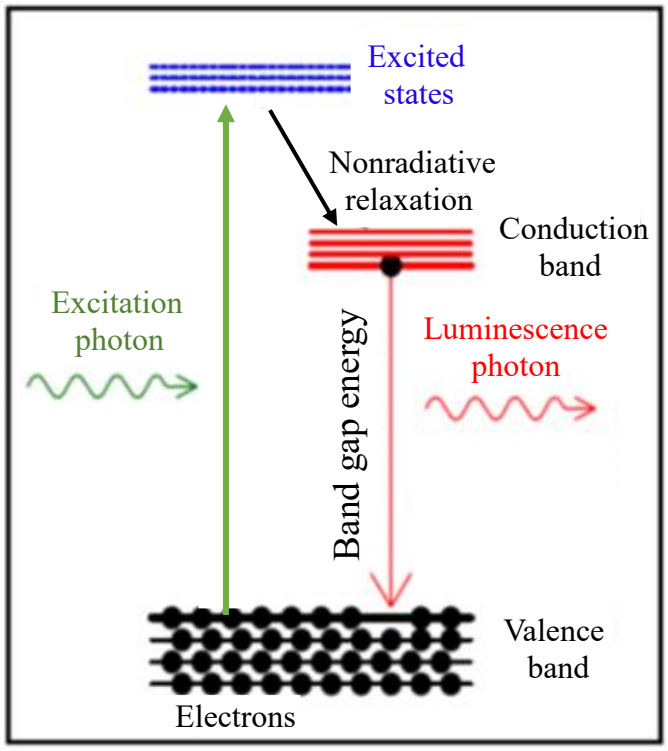


Figure 4.12: Principle of photoluminescence spectroscopy (PL) [17].

4.8.1 SPECTROMETER AND DETECTORS

A photograph and a schematic diagram of the setup of the spectrometer are shown in Figure 4.13 and Figure 4.14, respectively.

In collaboration with Prof Yara Galvão Gobato and Prof Helder Vinicius Avanço Galeti (Federal University of São Carlos, São Carlos-SP, Brazil), the PL study was performed a function of laser power and temperature using a state-of-the-art Janis closed-loop helium cryostat which has a fitted quartz window in order to provide optical access. A temperature controller, model Lake Shore 331, was employed to control the temperature of the samples from 10 K to 300 K. Initially, each sample was mounted in a dedicated holder and inserted inside the cryostat, where a high vacuum ($<10^{-5}$ mbar) was obtained using a combination of mechanical and turbo

pumps. The cryostat was cooled down to 10 K. The samples were excited with a 532 nm (2.33 eV) CW (continuous wave) DPSSL (Advanced Diode-Pumped Solid-State) laser with a spot diameter on the sample of around 400 μm. The optical excitation pathway drives the laser beam to the sample using silver mirrors, a neutral density filter to control the delivery laser power, and a 15 cm focal distance quartz lens in order to obtain a focused laser beam on the sample surface. The scattered PL signal was collected using a set of two convergent lenses, one in front of the sample (10 cm focal length) and another one (25 cm focal length) in front of the monochromator entrance (500M Spex Horiba model). In addition, a long pass optical filter (550 nm cut-off) was used to avoid detection of the mixed scattered laser with the PL signal. The monochromator has (i) entrance and exit slits which can be adjusted from 0 to 500 μm, (ii) 1200 lines/mm diffraction grating (blaze 600nm), and (iii) a GaAs photomultiplier (R928 Hamamtsu) with water-cooled thermoelectric cooler. The photomultiplier was powered with 950 V. The acquisition system has components combining a photon count device, a transducer communication system (Spectra Acquire Horiba Model) as well a computer that was controlled using SynerJY Horiba data software. The integration time of all spectra was chosen depending on the relative PL signal intensity and was between 0.1s to 1.0 s, and the scanning step for all spectra was 1nm. The PL data treatment takes into account the eventual difference in the acquisition parameter (time integration mainly) in order to become the set of data comparable in terms of relative intensity.

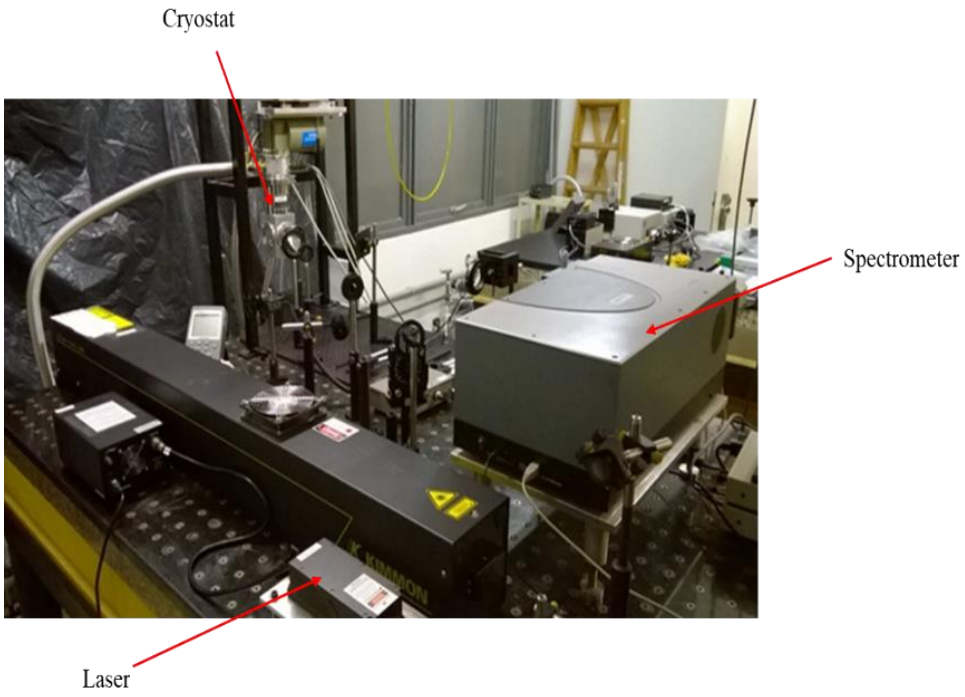


Figure 4.13: Photograph of the photoluminescence (PL) apparatus. Courtesy of Dr Helder Galeti (Federal University of São Carlos, São Carlos-SP, Brazil).

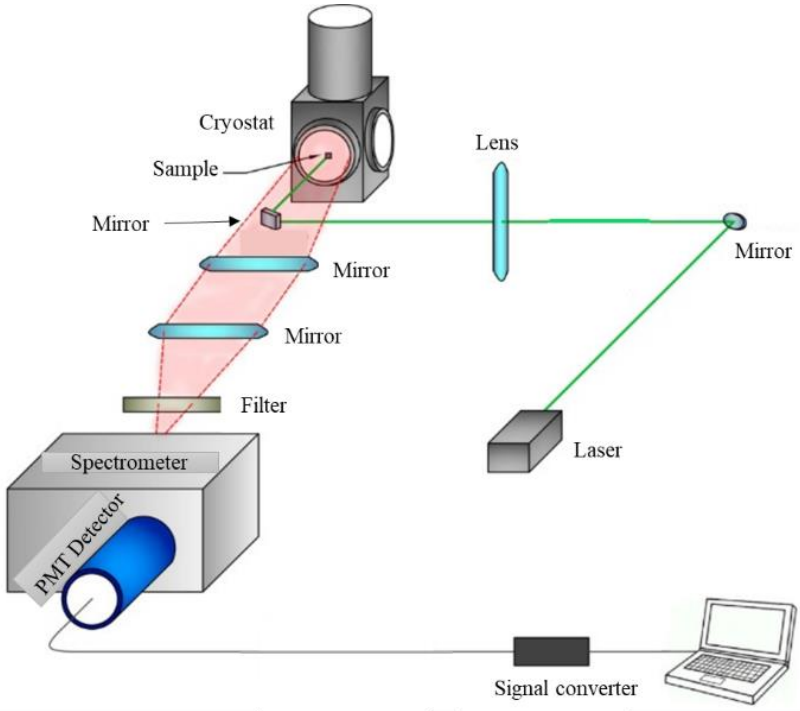


Figure 4.14: A schematic diagram of the photoluminescence (PL) apparatus.

4.9 RAMAN SPECTROSCOPY

Raman spectroscopy involves illumination of a sample with a monochromatic light and examining the scattered light from a sample. Raman spectroscopy is a non-destructive method that can reveal intricate details about a sample's chemical structure, crystallinity, and molecular interactions without requiring any sample preparation. It is based on the inelastic scattering of photons, known as Raman scattering which involves an energy exchange and a change in the direction of light. If the scattered photon has higher energy than the incident light, then the scattering light is called anti-Stokes. If the scattered light has a smaller energy than the incident light, Stokes scattering occurs. The energy difference will be caused by a change in the vibrational energy of the molecule that absorbs the light. The shift in energy gives information about the vibrational modes in the system. The schematics of the Stokes and anti-Stokes Raman scattering are shown in Figure 4.15.

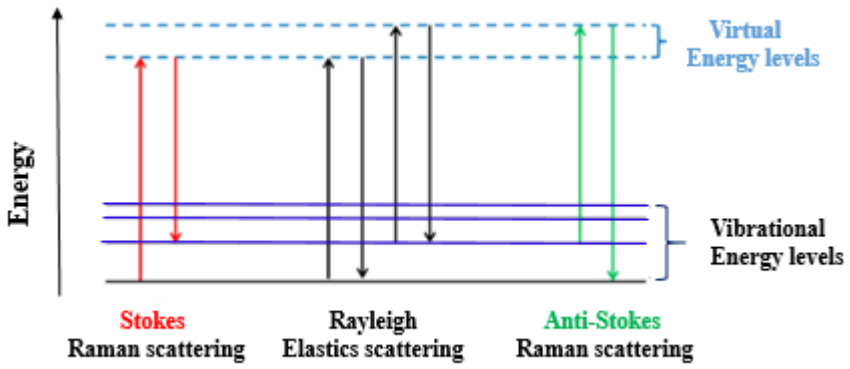


Figure 4.15: Schematic diagram of energetic transitions involved in Raman scattering. Rayleigh scattering is an elastic process where the incident photon is of the same energy as the scattered photon. Raman scattering is an inelastic process: (i) in Stokes scattering, the incident photon is of greater energy than the scattered photon, (ii) in anti-Stokes scattering, the incident photon is of lower energy than the scattered photon [18].

Optical phonons refer to the out-of-phase movement of atoms within a lattice that contains two or more atoms. Raman active optical phonons, which interact with light by means of Raman scattering, can be classified into longitudinal optical (LO) and transverse optical (TO) phonon modes, and their splitting is determined by the Lyddane-Sachs-Teller relation [18]. The frequencies of optical phonons are usually measured and expressed in units of spectroscopic wavenumbers, which are represented in cm^{-1}. The observation of LO and TO phonon modes in Raman spectroscopy is affected by the crystal plane orientation of the sample being measured.

The Raman spectroscopy used to study the properties of InGaP-based p-i-n structures (Chapter 8) was performed in collaboration with the group of Prof. Jorlandio F. Felix (University of Brasilia, Brazil) using a confocal micro-spectrometer (LabRAM HR Evolution, Horiba Scientific, France) equipped with 1800 lines/mm grating and CCD detector, with a spectral resolution of ~ 1.0 cm^{-1} and spatial resolution of ~ 1 μm. The excitation laser beam (532 nm) with 1.1 mW power was focused onto the sample using a long-working distance microscope objective MPLANFL N 50× (0.50 NA, Olympus). Figure 4.16 shows a picture of Raman spectroscopy instrument which was used in this thesis.

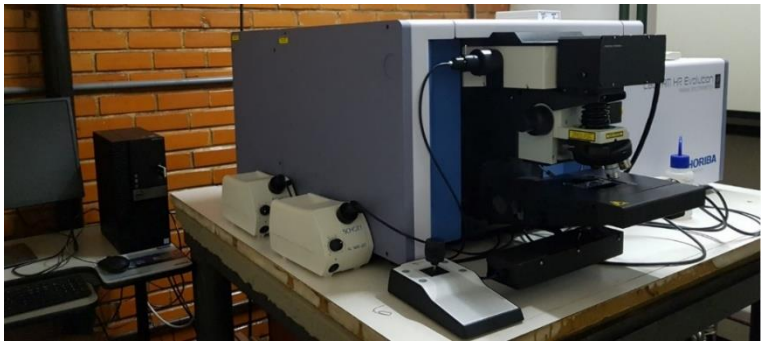


Figure 4.16: Photograph of Raman spectroscopy apparatus. Courtesy of Prof. Jorlandio F. Felix (University of Brasilia, Brazil).

4.10 SOLAR CELL CHARACTERISTICS

Photovoltaic (PV) cells are usually characterised with four performances: open circuit voltage V_{oc}, short-circuit current I_{sc}, fill factor FF and conversion efficiency η. These parameters can be characterised using Figure 4.17

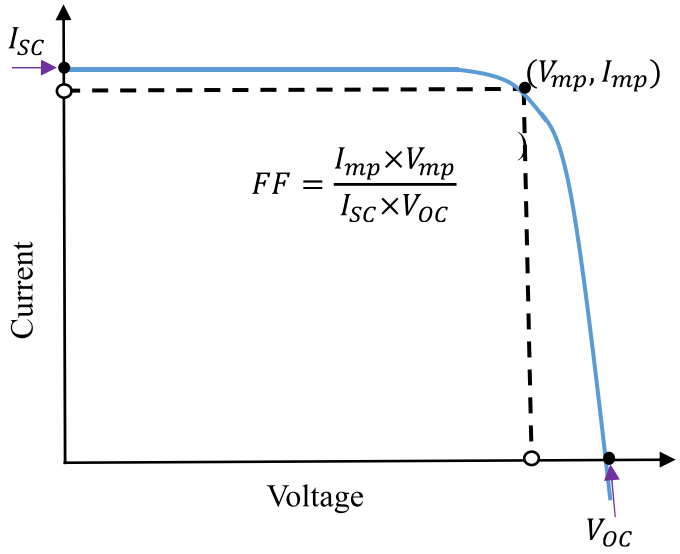


Figure 4.17: Typical plot of a solar cell's I-V characteristic and its parameters where (V_{mp}, I_{mp}) is the maximum power point.

The open circuit voltage V_{oc} is the maximum possible voltage generated across the terminals of a solar cell when they are kept open, i.e. I =0 (see Figure 4.17).

The short-circuit current I_{sc} is the current through the solar cell when the voltage across the solar cell is zero (i.e., V=0). I_{sc} is characterised in terms of (mA/cm^2).

The fill factor FF, which is a measure of quality of a solar cell, is defined as the ratio of maximum power $P_m = V_{mp}.I_{mp}$ that can be extracted from a solar cell to the

ideal power $P_0 = V_{OC}.I_{SC}$. FF is typically expressed as a percentage and is given by the following equation [19].

$$FF = \frac{V_{mp}.I_{mp}}{V_{OC}.I_{SC}} \text{ x } 100\% \tag{4.49}$$

The conversion efficiency η of a solar cell is a crucial characteristic that determines its performance. It is calculated as the ratio between the maximum power generated by the solar cell, P_m, and the incident power it receives, P_{in} [19].

$$\eta = \frac{P_m}{P_{in}} = \frac{I_{mp}V_{mp}}{P_{in}} = \frac{FF.I_{SC}.V_{OC}}{P_{in}} \text{ x } 100\% \tag{4.50}$$

In this thesis, the current density-voltage curves of solar cells were obtained in collaboration Dr Suho Park (University of Science and Technology, South Korea) using a Keithley 4200-SCS semiconductor characterisation system. The illuminated current density-voltage curves of the solar cells were measured under AM 1.5G spectrum at 1 sun intensity (100 mW/cm^2) using a solar simulator (McScience Incorporation; K201-LAB50, 150 W Xe lamp, AM 1.5G filter) (see Figure 4.18).

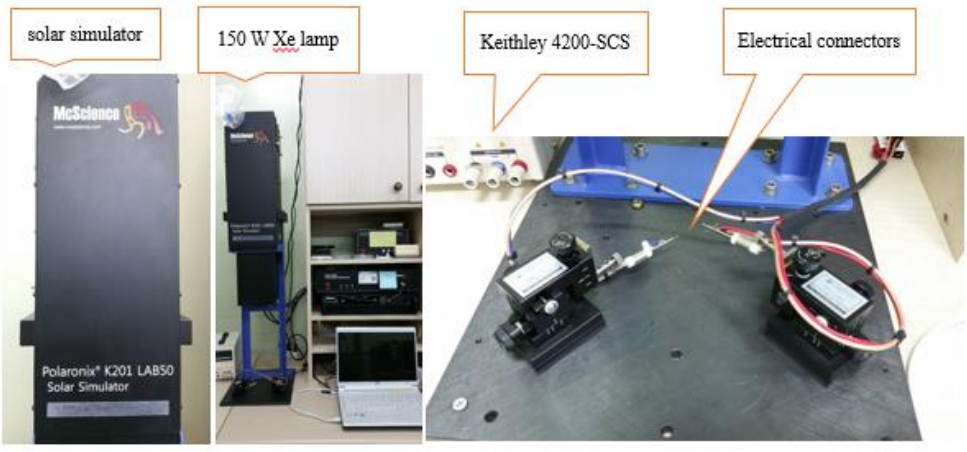


Figure 4.18: Photograph of the solar simulator system used in this thesis. Courtesy of Dr Suho Park, University of Science and Technology (UST), South Korea.

REFERENCES

[1] S. J. Sweeney and J. Mukherjee, "Optoelectronic devices and materials," in *Springer handbook of electronic and photonic materials*: Springer, 2017, pp. 1-1.

[2] J. Colinge and C. Colinge, "The PN junction diode," *Physics of Semiconductor Devices,* pp. 95-137, 2002.

[3] D. A. Neamen, *Semiconductor physics and devices: basic principles*. New York, NY: McGraw-Hill, 2012.

[4] B. G. Yacobi, *Semiconductor materials: an introduction to basic principles*. Springer Science & Business Media, 2003.

[5] S. M. Sze and K. K. Ng, *Physics of semiconductor devices*. John wiley & sons, 2006.

[6] J. H. Werner, "Schottky barrier and pn-junction I/V plots—Small signal evaluation," *Applied physics A,* vol. 47, pp. 291-300, 1988.

[7] S. Pandey, P. Middelkamp, Z. Li, and V. Eremin, "New experimental and analysis methods in I-DLTS," *Nuclear Instruments and Methods in Physics Research Section A: Accelerators, Spectrometers, Detectors and Associated Equipment,* vol. 426, no. 1, pp. 109-113, 1999.

[8] A. Peaker and M. Brozel, "Electrical techniques for the measurement of deep states," *III-Vs Review,* vol. 12, no. 1, pp. 44-51, 1999.

[9] D. Lang, "Deep-level transient spectroscopy: A new method to characterize traps in semiconductors," *Journal of applied physics,* vol. 45, no. 7, pp. 3023-3032, 1974.

[10] A. Saqri and N. alhuda Ahmed, "Investigation of deep level defects in advanced semiconductor materials and devices," University of Nottingham, 2017.

[11] D. K. Schroder, *Semiconductor material and device characterization*. John Wiley & Sons, 2015.

[12] L. Dobaczewski, I. Hawkins, and A. Peaker, "Laplace transform deep level transient spectroscopy: new insight into defect microscopy," *Materials science and technology,* vol. 11, no. 10, pp. 1071-1073, 1995.

[13] L. Dobaczewski, A. Peaker, and K. Bonde Nielsen, "Laplace-transform deep-level spectroscopy: The technique and its applications to the study of point defects in semiconductors," *Journal of applied physics,* vol. 96, no. 9, pp. 4689-4728, 2004.

[14] M. Shafi, "Electrical and optical studies of dilute nitride and bismide compound semiconductors," University of Nottingham, 2011.

[15] T. Ambridge, C. Elliott, and M. Faktor, "The electrochemical characterization of n-type gallium arsenide," *Journal of Applied Electrochemistry,* vol. 3, no. 1, pp. 1-15, 1973.

[16] V. Gopal, E.-H. Chen, E. Kvam, and J. Woodall, "Electrochemical capacitance voltage profiling of the narrow band gap semiconductor InAs," *Journal of electronic materials,* vol. 29, pp. 1333-1339, 2000.

[17] M. Vallikkodi, "Synthesis, growth and characterization of piperazinium P-aminobenzoate and piperazinium P-chlorobenzoate nonlinear optical single crystals," *Alagappa University, Karaikudi, India,* 2018.

[18] L. Srinivasan, "Properties of epitaxial lateral overgrowth of GaAsP and GaAs grown by hydride vapor phase epitaxy," ed, 2020.

[19] J. A. Nelson, *The physics of solar cells*. World Scientific Publishing Company, 2003.

CHAPTER 5: THE EFFECTS OF V(P)/III(Ga) FLUX RATIO AND THERMAL ANNEALING ON THE ELECTRICAL PROPERTIES OF DILUTE NITRIDE GaAsPN-BASED P-I-N SOLAR CELL STRUCTURES

In this Chapter, an investigation will be reported on the effects of the growth conditions, namely P/Ga flux ratio, on the electrical properties of GaAsPN-based p-i-n solar cell structures grown by molecular beam epitaxy (MBE) using current-voltage (I-V), capacitance-voltage (C-V), conventional DLTS, and Laplace DLTS characterisation techniques. In addition, a detailed study of the effect of rapid thermal annealing (RTA) was carried out .

5.1. INTRODUCTION

The unique physical properties of dilute nitride III-V-N materials set them apart from traditional alloy semiconductors. These materials have unusual physical properties that are not seen in other conventional semiconductor materials making them useful for technological applications, such as solar cells, optical amplifiers, and lasers operating at long wavelengths [1, 2]. For example, nitrogen content can be modulated to alter the band gap energy of III–V semiconductors. To grow dilute nitride III-V semiconductors, i.e. a ternary III-V-N compound such as GaPN, small quantities of nitrogen (1% to 4%) are incorporated into the host lattice of III-V alloys. Furthermore, quaternary GaAsPN alloys can be synthesised by incorporating As in GaPN [3]. These materials, which can be grown by molecular beam epitaxy (MBE) and metalorganic vapor phase epitaxy (MOVPE), are very attractive for devices that require efficient light emission and light absorption [3].

The optical properties and crystal structure of these quaternary GaAsPN semiconductor alloys are highly desirable because they can be lattice matched to common substrates such as Si and GaP [4] substrates.

On the other hand, the presence of defects, including both deep defects and shallow defects, related to nitrogen incorporation into GaAs, has been observed [5]. A thorough understanding of the origin of these defects has yet to be completely understood [6]. Moreover, the achievement of high quality GaAsPN required for device applications necessitates an understanding of the effects of growth conditions, such as growth temperature and V/III flux ratio on the electrical and optical properties of the alloys. Furthermore, post growth annealing processes have been used to decrease and/or annihilate the defects which were introduced during the growth. Therefore, the optimization of the growth conditions and thermal annealing treatment play key roles in the enhancement of the electrical and optoelectronic properties of these semiconductor alloys [7].

In this study, a detailed investigation was carried out on electrically active defects in p-i-n GaAsPN-based solar cell structures grown with different V(P)//III(Ga) flux ratios. This investigation will help to understand the effect of the growth conditions on the efficiency of the solar cell devices using current-voltage (I-V), capacitance- voltage (C-V), conventional DLTS, and Laplace DLTS characterisation techniques.

5.2 SAMPLE DETAILS

In this work, two p-i-n $GaAs_{0.1}P_{0.89}N_{0.01}$ based solar cells with the same structure were grown by MBE on 400 μm thick n+ (100) GaP substrates using different

V(P)/III(Ga) ratios. The structure of the devices, as illustrated in Figure 5.1, consists of a 500 nm thick n-type GaP buffer layer (n=1x$10^{18}$$cm^{-3}$), followed by a 300 nm p-type $GaAs_{0.1}P_{0.89}N_{0.01}$ (p=1x $10^{17}$$cm^{-3}$) i-layer and a 30 nm p-type GaP cap layer (p=1x$10^{18}$$cm^{-3}$).

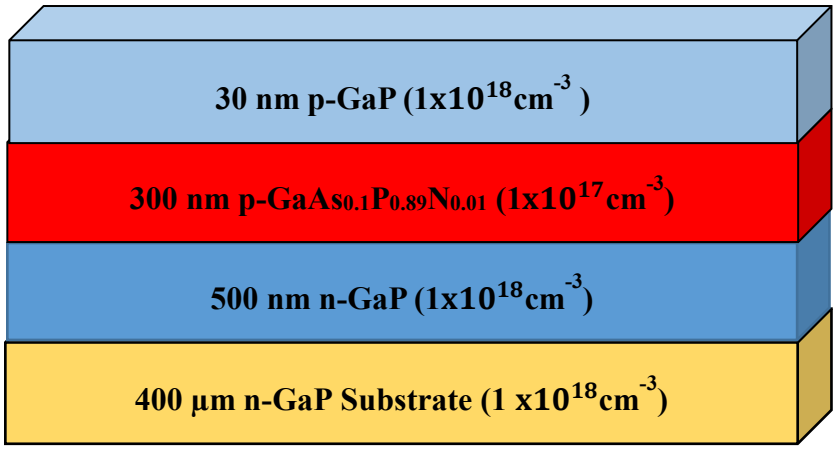


Figure 5.1: Schematic diagram of the p-i-n GaAsPN based solar cell structures.

Zn and Si were used as p-type and n-type dopants, respectively. Ga was provided through a conventional Knudsen effusion cell containing pure Ga metal solid source while the group V elements (P, As) were supplied via valved-cracker cells where solid sources of these elements are heated. Upon heating, phosphorus and arsenic are released in the form of tetramers (P_4, As_4). They are then cracked to form P_2 and As_2 molecules which have higher sticking coefficients [8, 9]. Nitrogen was incorporated into GaP using a valved radio frequency (RF) plasma source with nominal 0.5 sccm N_2 flow and a 400 W RF power. The growth rate was 0.2 monolayer/s (ML/s). The V(P)/III(Ga) beam equivalent pressure (BEP) used for the growth of two structures was 5 and 21. It is important to note that the growth rate of the III-V compounds is controlled by the group III flux. To achieve lattice matching between GaAsPN and GaP substrate, the As flux was set at 0.2 µTorr.

After growth, the samples were annealed by using a JetFirst (Jipelec) rapid thermal annealer (RTA) system at 800 ^{0}C for 5 mins under forming gas (mixture of N_2 and H_2) ambient. The ramp-up temperature rate was 100 ^{0}C/s.

Ni/Au/Ge/Au/Ni/Au and Pd/Zn /Pd metallisations were performed to the back and front of the solar cell structures, respectively, in order to form Ohmic contacts [10, 11].

5.3. EFFECT OF V/III FLUX RATIO ON THE ELECTRICAL PROPERTIES OF DILUTE NITRIDE GaAsPN BASED P-I-N SOLAR CELL STRUCTURES

The growth conditions of this important GaAsPN quaternary alloy could affect the electrical properties of p-i-n solar cell devices. Therefore, it is important to optimise the growth conditions in order to minimise the number of electrically active defects and their concentrations.

In this work, I-V, C-V, DLTS and Laplace DLTS techniques were carried out to investigate the effect of different V(P)/III(Ga) flux ratios on the electrical properties of p-i-n GaAsPN based solar cell structures.

5.3.1 I-V CHARACTERISTICS

The I-V characteristics were obtained at room temperature for both samples grown with different V/III ratios, namely 5 and 21, as shown in Figure 5.2. As can be seen from this Figure, the leakage current of the sample grown with low P/Ga flux ratio is lower than the sample grown with high P/Ga flux ratio. The low reverse current observed in the sample grown with a P/Ga ratio=5, could indicate that there is a reduction of the concentration of the defects which act as generation recombination

centres [12] and/or a lower number of defects [13]. In addition, the turn-on voltage (V_{on}) increases from 1 V to 1.2 V when the P/Ga flux ratio increases from 5 to 21, respectively. This behaviour could be attributed to defects and traps [11].

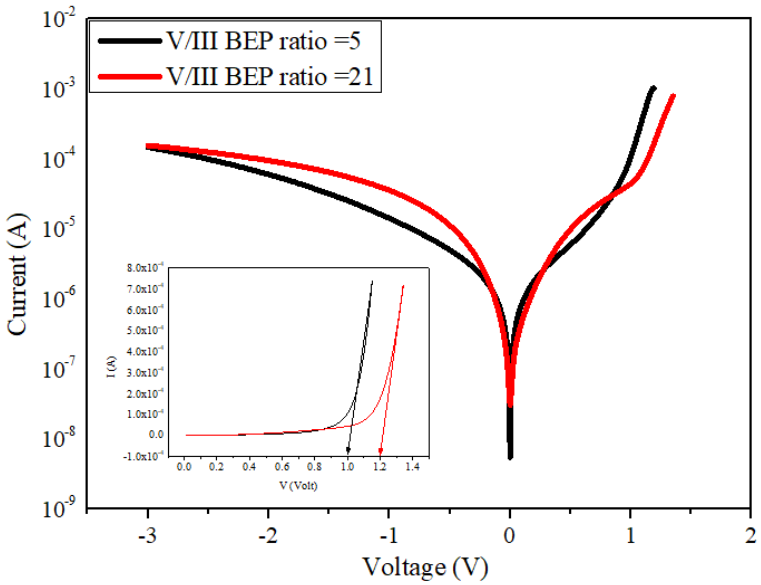


Figure 5.2: Room temperature semi-logarithmic I-V characteristics of p-i-n GaAsPN based solar cells grown with different P/Ga flux ratios. The inset shows linear I-V characteristics.

As the devices investigated are p-i-n junctions, the I-V characteristics could be explained by the thermionic emission model with a series resistance (Rs), as follows [14, 15]:

$$I = I_S[exp(\frac{q(V-IR_S}{nk_BT}) - 1] \quad (5.1)$$

where q is the electronic charge, $k_B$is the Boltzmann constant, V is the applied voltage, n is the ideality factor, I_S is the saturation current, and T is the absolute temperature in Kelvin. The values of n and I_S are determined from the experimental data. The saturation current I_S can be expressed as:

$$I_S = AA^{**}T^2exp(\frac{-q\emptyset_B}{k_BT}) \quad (5.2)$$

where A is the effective device area and A^{**}=98.2 $Acm^{-2}K^{-2}$ is the effective Richardson's constant [16].

The characteristics parameters of these devices such as (n, $\emptyset_B$ and I_S) were calculated by using the Werner's method [17], which was discussed in Chapter 4, Section 4.2. Figure 5.3 shows the plots of G/I versus G and ln (I) versus (V-IRs) for as-grown samples. Similar procedure was used to extract the diode parameters of all samples investigated in this thesis.

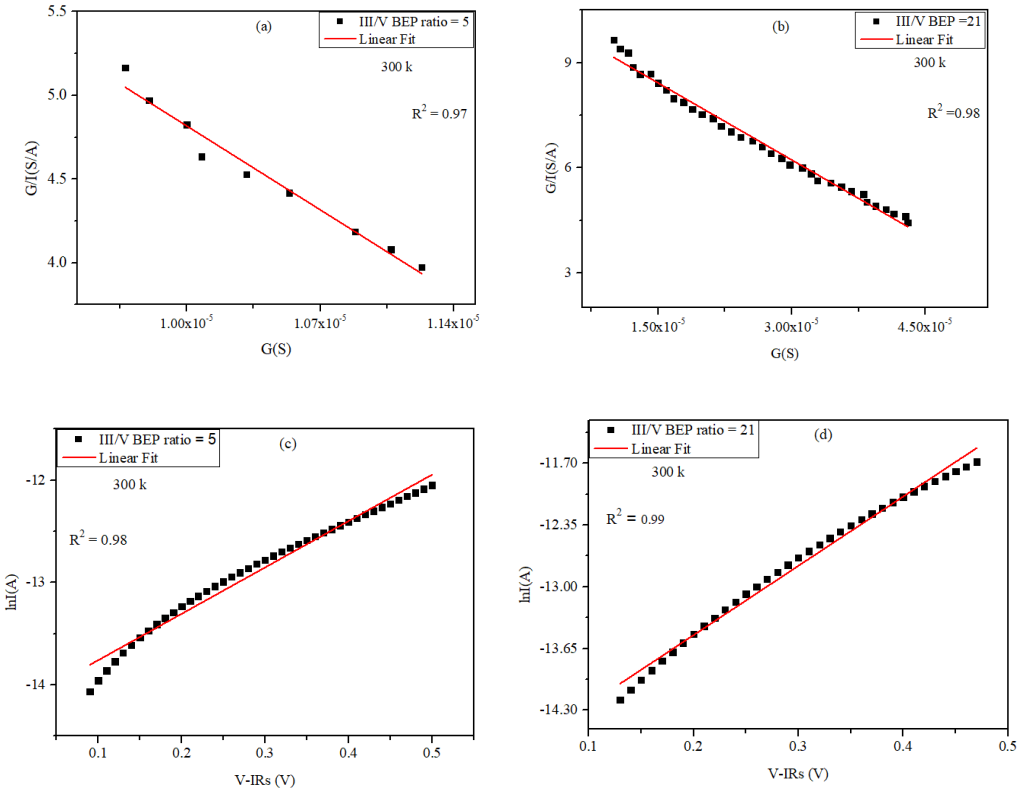


Figure 5.3: (a and b) plots of G/I versus G obtained from I-V curves at room temperature for forward bias conditions for both samples. These plots were used to determine the ideality factors. (c and d) plots of $ln\ (I)$ versus $(V - IR_s)$ for both samples are used to obtain $\emptyset_B$. R^2 values, which are given in each figure, give a measure of how close the data are to the fitted regression line. R^2 is always between 0 and 1.

The semi-logarithmic I-V characteristics of the GaAsPN based solar cell structures at room temperature are illustrated in Figure 5.2. Figure 5.4 (a and b) shows the temperature dependence of the ideality factor and built-in potential barrier calculated from the I-V curves for samples grown with different P/Ga flux ratios over the temperature range 260 K - 360 K.

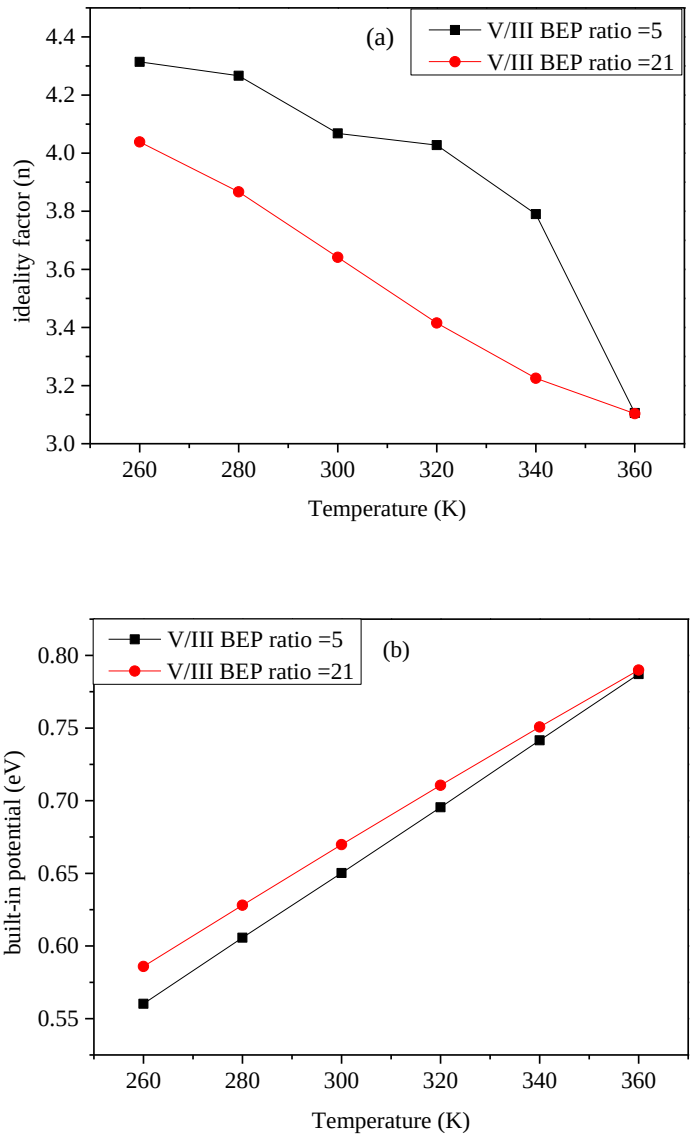


Figure 5.4: Temperature dependence of (a) Ideality factor (n); (b): the built-in potential barrier (ϕ_B) calculated from forward I-V curves of p-i-n GaAsPN based solar cells grown with different P/Ga flux ratios. The errors bars for both n ($\Delta n \sim \pm 0.03$) and ϕ_B ($\Delta\phi_B = \sim\pm 0.001$eV) were not added as the errors were too small.

From Figure 5.4(a) the ideality factor (n) of both samples increases with decreasing temperature. Similar behaviours have been reported by many researchers [18] [19]. This is due to the fact that the current transport across the p-i-n interface is a temperature activated process [20]. For all samples, the values of the ideality factor are greater than unity, and these higher values can be attributed to the generation – recombination currents, interface states, and the series resistance effect [21, 22]. However, as the P/Ga flux ratio increases from 5 to 21, the ideality factor decreases. This could be due to the creation of more electron traps at the dislocation sites [23]. It is important to point out that when the deality factor is greater than 1 the conduction process of the diode has both thermionic emission and field emission component. Both thermionic and field emissions dominate the conduction for samples grown at low and high P/Ga ratios. As can be seen in Figure 5.4(a), the ideality factor of the diodes decreases when the P/Ga ratio increases from 5 to 21 evidencing that higher V/III ratios generate more electron traps at the dislocation sites and could not contribute in the quantum tunneling and other transport processes making the thermionic emission transport process dominant.

The built-in potential barrier values were calculated from I-V measurements of both samples grown with different P/Ga flux ratios, as shown in Figure 5.4(b). The values of built-in potential barrier increase as the temperature increases. Similar phenomena have also been reported by other researchers [18, 24]. This is due to the effect of barriers inhomogeneities at the p-i-n interface [25]. The values of the built-in potential barrier of p-i-n GaAsPN based solar cell increase as the P/Ga flux ratio increases from 5 to 21, as clearly seen in Figure 5.4(b).

5.3.2 C-V MEASUREMENTS

Figure 5.5(a) shows the C-V characteristics of the GaAsPN based heterostructures grown with different P/Ga flux ratios (5 and 21). Figure 5.5(b) displays the plot of $1/C^2$ vs V for both samples at room temperature. From the slope of the best fit to the plot $1/C^2$ versus reverse bias, the free carrier concentration (N_d) was obtained for both samples at room temperature (see Chapter 4, Section 4.1.2). The linearity of these plots indicate that the doping is uniform.

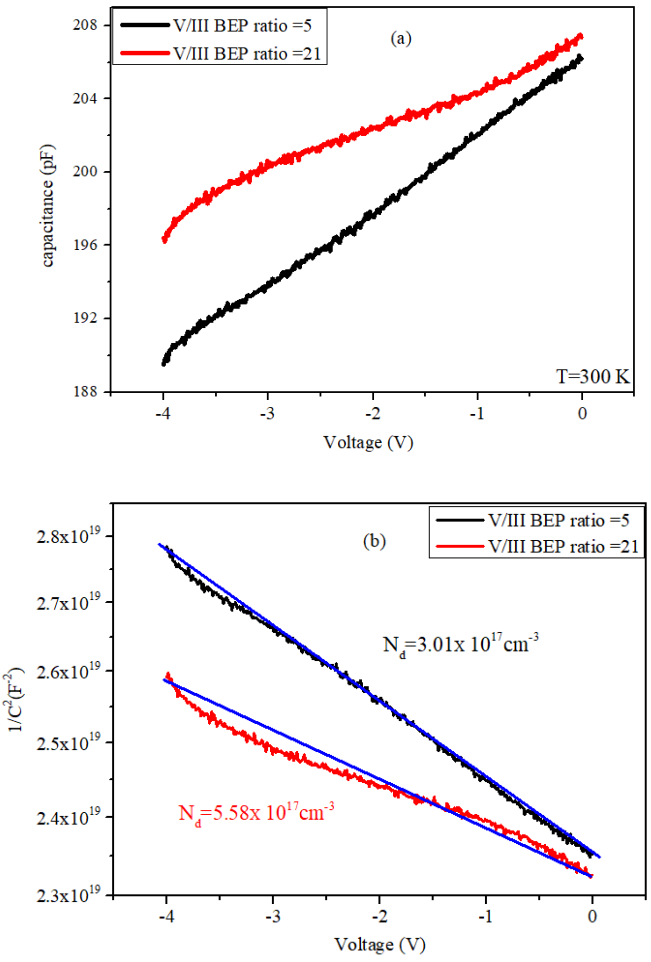


Figure 5.5 : (a) Plots of C-V characteristics; (b)**:** $1/C^2$ vs V plots for GaAsPN-based heterostructures grown with different P/Ga flux ratios. The solid blue lines represent the best fit of the $1/C^2$ vs V plots.

The net acceptor concentration was calculated to be 3.01 x 10^{17} cm^{-3} and 5.58 x $10^{17} cm^{-3}$ for samples grown with V/III flux ratios 5 and 21, respectively. The sample grown with the higher V/III flux ratio exhibits a higher value of net acceptor concentration, as compared with the sample that was grown with low V/III flux ratio. This increase in the free carrier concentration is probably related to impurity and native defects [26]. This will be confirmed in the DLTS section.

5.3.3 DEEP LEVEL TRANSIENT SPECTROSCOPY (DLTS) AND LAPLACE DLTS CHARACTERISITICS OF GaAsPN DIODES GROWN WITH DEFERENT V(P)/III(Ga) FLUX RATIOS

DLTS and Laplace DLTS measurements were carried out on p-i-n GaAsPN devices in order to study the electrically active defects, and to resolve the broad peaks in the DLTS spectra, respectively. The parameters that were used for these measurements are a reverse bias voltage $V_R = -4$ V, a filling pulse V_P= 0 V, with a duration of t_p=1 msec, and a rate window of e_n=200 s^{-1}. The scanning temperature range was from 75 K to 450 K. Figure 5.6 shows DLTS signals for both samples grown with different flux ratios.

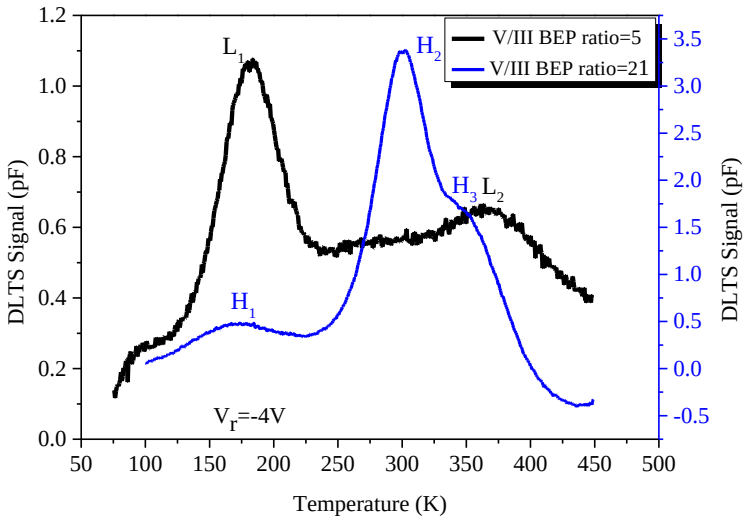


Figure 5.6: DLTS spectra of GaAsPN heterostructures grown with different flux ratios using reverse bias of -4 V, rate window of 200 H_Z, filling pulse V = 0 V. Filling pulse duration is t_p=1 msec.

From the above spectra it can be seen that the samples grown with low and high P/Ga flux ratios show two (L_1 and L_2) and three (H_1, H_2 and H_3) traps, respectively. It is important to note that all the DLTS signals are positive indicating that the defects are majority carriers traps, i.e. hole traps since the $GaAs_{0.1}P_{0.89}N_{0.01}$ layer is p-type doped. L and H refer to samples grown with low and high flux ratios, respectively. As shown in Figure 5.5, L_2 and H_2 traps, which have been observed in the temperature range ~275 K - 325 K and ~350 K - 380 K, respectively, could be of the same nature as they have similar activation energies. L_1 and H_1 detected in the temperature range 150 K - 200 K could also have the same origin, i.e. similar defects in both samples. The H_3 trap detected in the temperature range ~ 325 K - 350 K was present only in the sample grown with high P/Ga flux ratio.

The activation energies, capture cross-sections, and trap concentrations were obtained from Arrhenius plots of $\ln(e_n/T^2)$ versus 1000/T, as shown in Figure 5.7, and are given in Table1.

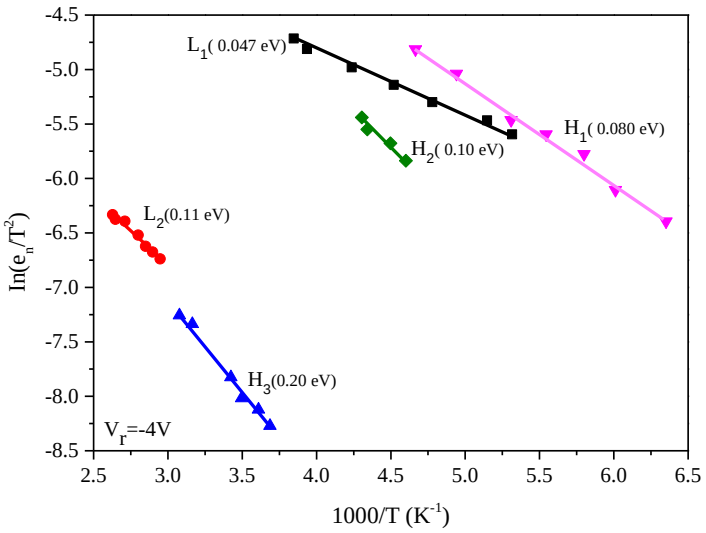


Figure 5.7: Arrhenius plots of the traps detected in both samples using the experimental parameters: V_R = - 4 V, V_P = 0 V, duration of filling pulse tp= 1ms and rate window of 200 s^{-1}.

Table 5.1: Summary of activation energies, capture cross-sections, and concentrations of the hole traps detected in both samples for V_R = - 4 V, V_P = 0 V, duration of filling pulse tp= 1ms and rate window of 200 s^{-1}.

Sample	Trap label	E_T (eV)	Trap concentration N_t (cm^{-3})	Capture cross section σ_n(cm^2)
BEP ratio P/Ga= 5	L_1	0.047±0.001	2.2×10^{14}	7.5×10^{-21}
	L_2	0.11±0.01	2.3×10^{14}	5.2×10^{-21}
BEP ratio P/Ga= 21	H_1	0.080±0.003	2.0×10^{15}	2.5×10^{-22}
	H_2	0.10±0.01	1.5×10^{15}	1.2×10^{-22}
	H_3	0.20±0.01	2.2×10^{16}	4.2×10^{-22}

Deep and shallow hole traps were observed in both samples within the temperature range of 80 K - 450 K. The L_2 and H_2 deep hole traps have activation energies of 0.11eV and 0.10 eV, respectively. Abulfotuh et al investigated nitrogen-doped p-GaAs thin films grown by MOVPE using DLTS technique [27]. It was found that the presence of N creates a high density of shallow hole traps related to the N atom and structural defects in the devices. Two major hole traps, namely HN1 (0.13 eV) and HN2 (0.16 – 0.22 eV) were observed. The activation energy of HN2 was dependent on the concentration of N. It was argued that the density and energy level of HN2 is affected by the presence of C impurities, which could form C-N complex states. It is important to note that the holes traps L_2 and H_2, detected in p-$GaAs_{0.1}P_{0.89}N_{0.01}$ samples studied in this work have similar activation energies and could be of the same origin. In addition, Suzuki et al studied the effects carbon and hydrogen atoms on the electrical properties of GaAsN films grown by Chemical Beam Epitaxy (CBE) [27, 28]. Two acceptor levels (A1=0.13 eV and A2= 0.055 eV) were reported in the GaAsN films. They assigned these traps to N–H complexes which behave as acceptors in the GaAsN films.

Both samples exhibit shallow traps, which are L_1 and H_1, with activation energies of 0.047 eV and 0.08 eV, and concentrations of ~$2.2x10^{14}$ cm^{-3} and ~$2.0x10^{15}$ cm^{-3}, respectively. The origin of these traps could be assigned to intrinsic point defects. Rumyantsev et al. studied p^+-n junctions based on GaP/GaPN and GaP/$GaP_{1-x-y}As_xN_y$ quantum well (QWs) heterostructures grown on n+ GaP (100) substrates by MOCVD using C-V and DLTS techniques [29]. Their results revealed intrinsic defects with deep levels of 0.17 eV and 0.08 eV only in the structures with GaPN QWs. They believed that the intrinsic point defects appear because of the large lattice mismatch between GaP and GaPN. It was shown that the defect

concentration in GaPAsN QWs structures is at least two orders of magnitude smaller than in the structures with GaPN QWs. This effect was explained by the fact that the substitution of V-Group atoms by As atoms compensates for elastic stresses occurring during the epitaxial growth of the N containing layers and eliminates the defect formation. It is therefore concluded that GaPAsN quaternary alloy is a more promising material for use in LEDs, solar cells, semiconductor lasers, and other devices. The 0.08 eV reported by Rumyantsev et al. could be related to L_1 and H_1 traps detected in $GaAs_{0.1}P_{0.89}N_{0.01}$ solar cell devices investigated in this work [29].

The H_3 hole trap with actvation energy of 0.20 eV is present only in the sample grown with high flux ratio. H_3 has an energy close to the *H_2* trap (0.16 eV-0.40 eV) reported by Choi at al. [30] in p^+-GaInAs/n-GaAs devices grown by MBE using DLTS technique. They observed two hole traps *H1* (0.64 eV) and *H2* (0.16 eV-0.40 eV) and they suggested that they could be related to mismatch-induced interface defects. In addition, they reported that the concentration of *H2* trap increased as the in-plane mismatch increased, i.e. as the In composition increased. mismatch.

V. Polojärvi at al. [31] studied the effects of V/III flux ratios on defects and photovoltaic performance of GaInNAs-based solar cells grown by MBE. The V/III BEP ratio was varied from 6 to 9 by changing only the As flux while all other growth parameters were kept constant. They observed a linear dependence between defect densities, photoluminescence peak intensity and the flux ratio. They reported a considerable increase in solar cell performance with a maximum external quantum efficiency of 90% when the growth conditions were kept close to the stoichiometric limit, i.e. for a BEP flux ratio of 6. In this work, the sample grown with V/III flux

ratio of 21 showed defects with concentrations about one order of magnitude higher than those of the sample grown with V/III flux ratio of 5. It is therefore expected that GaAsPN-based solar cells grown with V/III flux ration close to the stoichiometric limit (i.e. V/III flux ratio closer to 1) have higher efficiencies.

5.4. EFFECT OF RAPID THERMAL ANNEALING ON ELECTRICAL PROPERTIES OF GaAsPN-BASED SOLAR CELL STRUCTURES GROWN WITH DIFFERENT V(P)/III(Ga) FLUX RATIOS.

Post-growth treatments, such as thermal annealing, are well known to reduce the concentration of defects, annihilate and passivate completely defects. It is therefore important to study the effect of the thermal annealing on the electrical properties of GaAsPN heterostructures grown with different flux ratios in order to understand the influence of the growth conditions. Rapid thermal annealing (RTA) was performed as described in Section 2.

5.4.1 I-V CHARACTERISTICS

Figures 5.8 and 5.9 illustrate the I-V characteristics at room temperature for p-i-n GaAsPN based solar cells grown with flux ratios 5 and 21 before and after annealing, respectively. As can be seen from Figures 5.8 and 5.9, the leakage currents for both samples decreased after annealing as compared with as-grown samples. The decrease of the leakage current after annealing, could be attributed to the decrease of the number and/or concentration of defects which act as generation recombination centres [12]. Similar behavior of the lower leakage current after annealed was observed by Xie et al [32] in their study of annealed Be-doped

InGaAsN samples. They showed that the leakage current of the annealed samples was 2–3 orders of magnitude lower than that of the as-grown diodes. They attributed this decerease in the leakage current to the decrease of the defects concentrations.

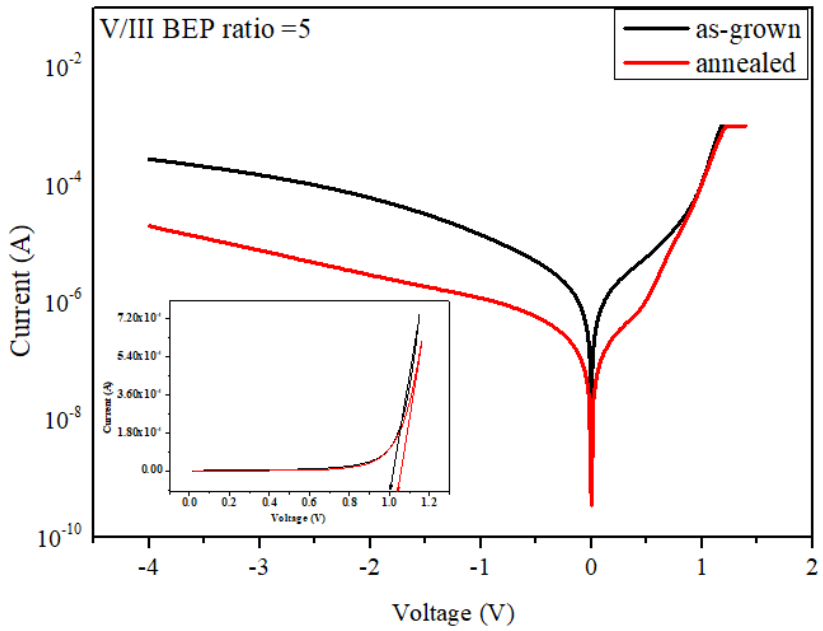


Figure 5.8: Room temperature semi-log I-V characteristics of p-i-n GaAsPN heterostructures grown with P/Ga flux ratio = 5 before and after annealing. The inset shows linear I-V characteristics from where the turn-on voltage is determined.

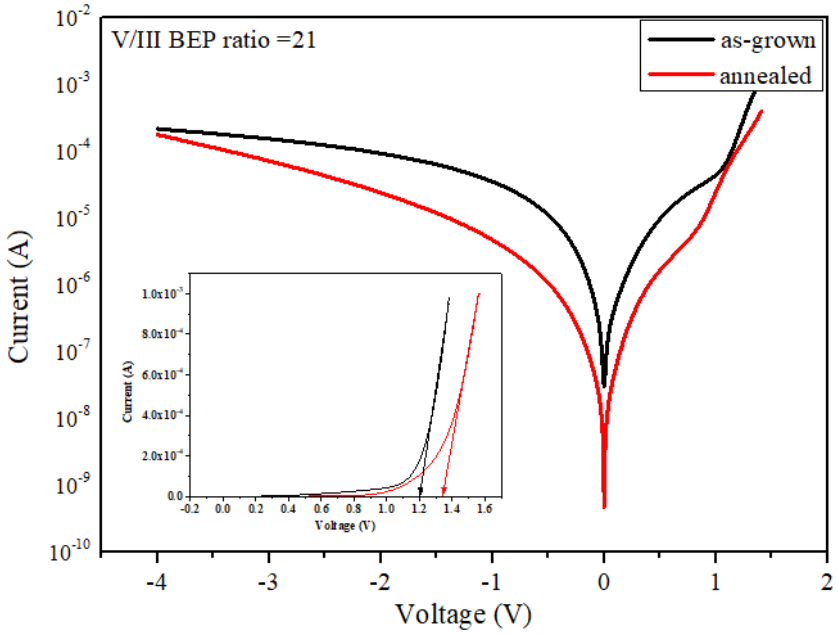


Figure 5.9: Room temperature semi-log I-V characteristics of p-i-n GaAsPN heterostructures grown with P/Ga flux ratio = 21 before and after annealing. The inset shows linear I-V characteristics from where the turn-on voltage is determined.

Therefore, the thermal annealing method is an effective way to improve the electrical properties of the devices. A reduction in the concentration of defects and /or their transformation could be attributed to this improvement. The effect of the heat treatment on the defects will be further investigated using DLTS measurements. Moreover, as can be seen from Figures 5.8 and 5.9 the turn–on voltage (V_{on}) increases when the samples are annealed. V_{on} increases from 1 V to 1.1 V and from 1.2 V to 1.3 V after annealing the samples grown with flux ratio 5 and 21, respectively. This increase in turn–on voltage after annealing could be related to the increase of the excess capacitance due to interface states [33]. The I-V characteristics as a function of temperature (260 K-360 K) were measured for all

samples in order to determine the parameters of the diodes such as ideality factor (n) and built-in potential barrier (ϕ_b).

The I-V curves could be described by the thermionic emissions (TE) model as given by equation (5.1) in previous section. Figure 5.10 shows the temperature dependence of the ideality factor calculated from the semi-logarithmic I-V curves for as-grown and annealed samples over the temperature range 260 K- 360 K. For both samples grown with different V(P)/III(Ga) flux ratios before and after annealing, it is evident that the ideality factor (n) increases with decreasing temperature. Similar behaviours have been reported by other researchers [19, 32]. This is due to the current transport across the p-i-n interface which is a thermally activated process [20, 34]. For all samples in the temperature range 260 K - 360 K, the values of ideality factor are greater than unity. This behaviour can be attributed to the generation-recombination mechanism, interface states and barrier height inhomogeneities [35].

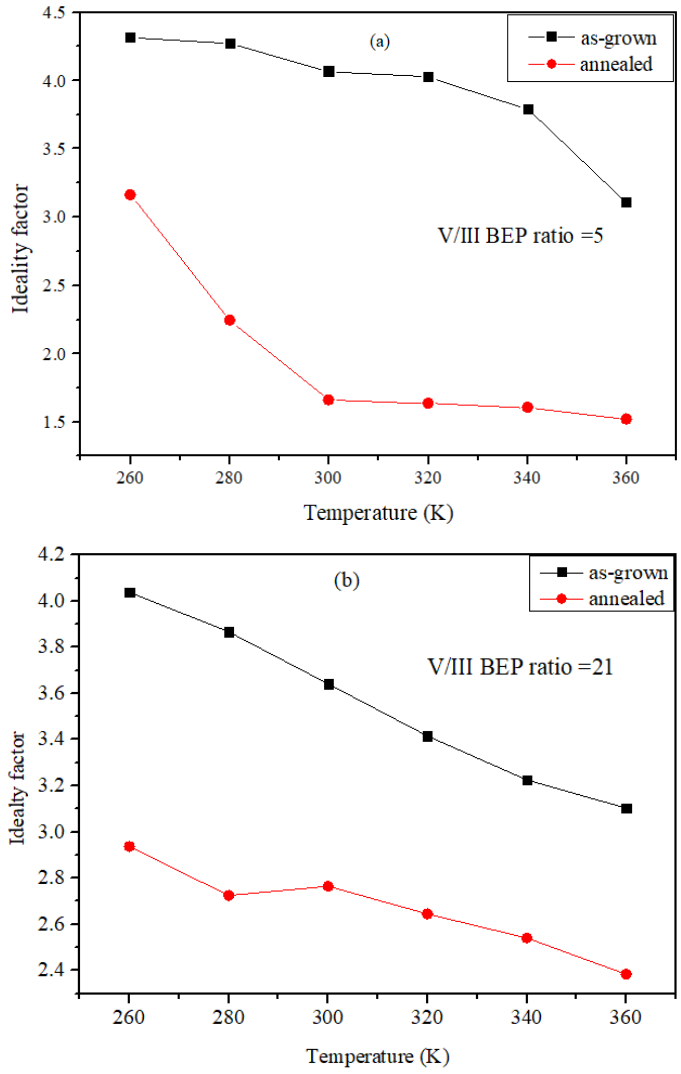


Figure 5.10: Ideality factors (n) were calculated from forward I-V curves for as-grown and annealed samples grown with P/Ga flux ratios (a) 5 and (b) 21. The errors bars were not added as the errors were too small (Δn= ~± 0.03).

From Figure 5.10 it can be seen that the annealed samples have lower ideality factor values than the as-grown samples suggesting that the annealed samples are closer to ideal solar cell diodes than the as-grown devices. The values of the built-in potential barrier ($\emptyset_b$) calculated from the I-V characteristics of as-grown and annealed p-i-n GaAsPN based solar cells are shown in Figure 5.11.

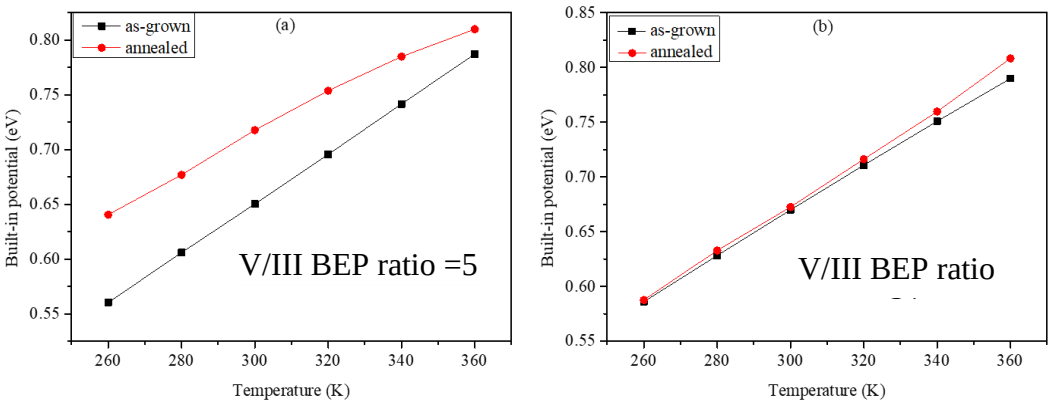


Figure 5.11: Built-in potential barriers ($\emptyset_b$) were calculated from forward I-V curves for as-grown and annealed samples grown with P/Ga flux ratios (a) 5 and (b) 21. The errors bars were not added as the errors were too small ($\Delta\emptyset_b$ =~± 0.001 eV).

The built-in potential barrier (ϕ_b) increases with increasing temperature for both samples before and after annealing. However, for the sample grown at P/Ga flux ratio = 21 the built-in potential energy barrier is not affected appreciably by the heat treatment as compared with the sample grown with V/III=5 where the built-in potential energy barrier increases after annealing. This temperature dependence of the built-in potential barrier is due to the effect of barrier in-homogeneities at the p-i-n interface [25].

5.4.2 C-V MEASUREMENTS

Figure 5.12 (a,b) shows plots of $1/C^2$ versus V characteristics of the GaAsPN heterostructure samples grown with different V/III flux ratios before and after annealing. These are used to determine the free carrier concentration of GaAsPN devices. The net acceptor concentrations were calculated to be 3.01×10^{17} cm^{-3} and 5.58×10^{17} cm^{-3} for the as-grown samples with flux ratios 5 and 21, respectively.

After annealing the free carrier concentration was found to be 3.87x10^{17} cm^{-3} for GaAsPN solar cells devices grown with low ratios 5. For samples grown with high flux ratio 21, the free carrier concentration is found to be non-uniform and there are two different free carrier concentrations of 6.56x10^{17} cm^{-3} and 9.89x10^{17} cm^{-3}. The annealed samples have higher values of free carrier concentration than the as-grown devices. This increase in the free carrier concentration could be attributed to a de-passivation of acceptors during thermal annealing [32].

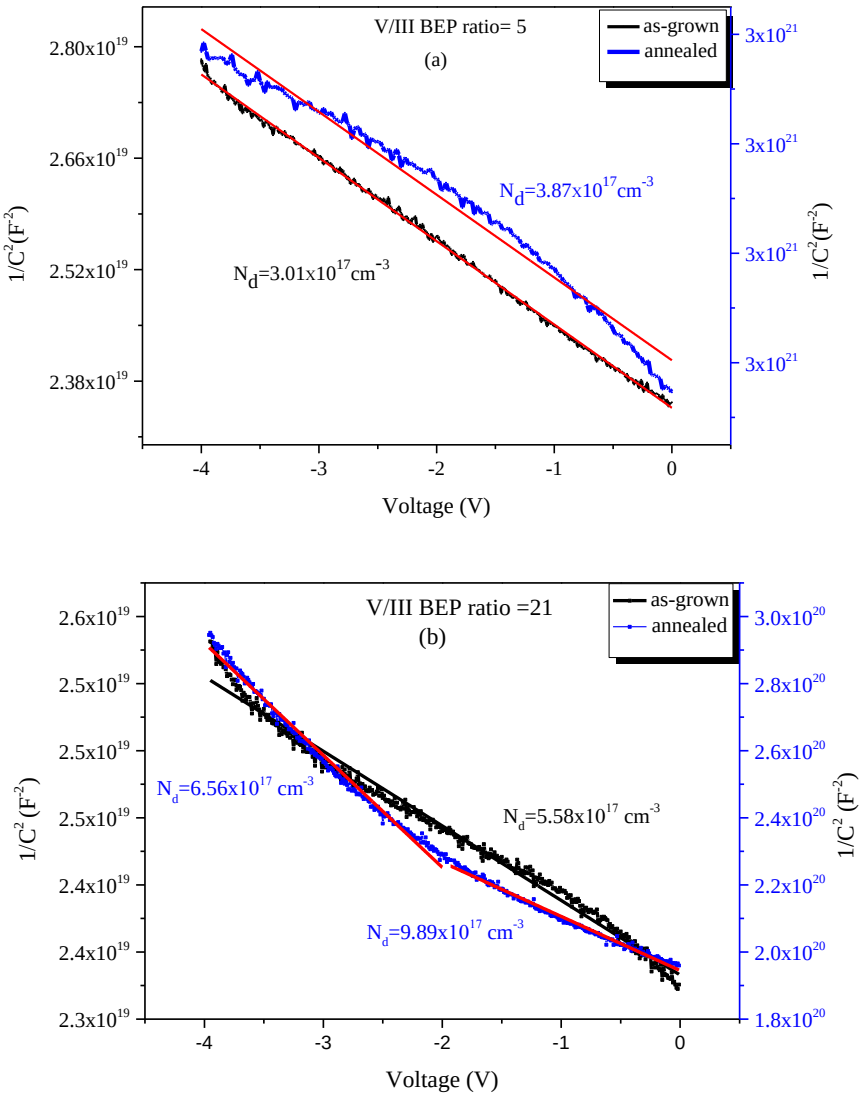


Figure 5.12: Room temperature 1/C^2 vs V plots for as-grown and annealed GaAsPN based solar cell samples grown with a flux ratio of (a) 5 and (b) 21. The solid lines represent the best fit of the 1/C^2 vs V plots.

5.4.3 DLTS AND LAPLACE DLTS MEASUREMENTS

The parameters that were used for the DLTS measurements are a reverse bias voltage $V_{R=}$ -4 V with V_P= 0 V, a filling pulse width t_p=1 msec, and a rate window of e_n=200 s^{-1}. The scanning temperature range was from 75 K to 450 K. Figure 5.13 shows DLTS signals for both as-grown and annealed samples grown with different V(P)/III(Ga) flux ratios.

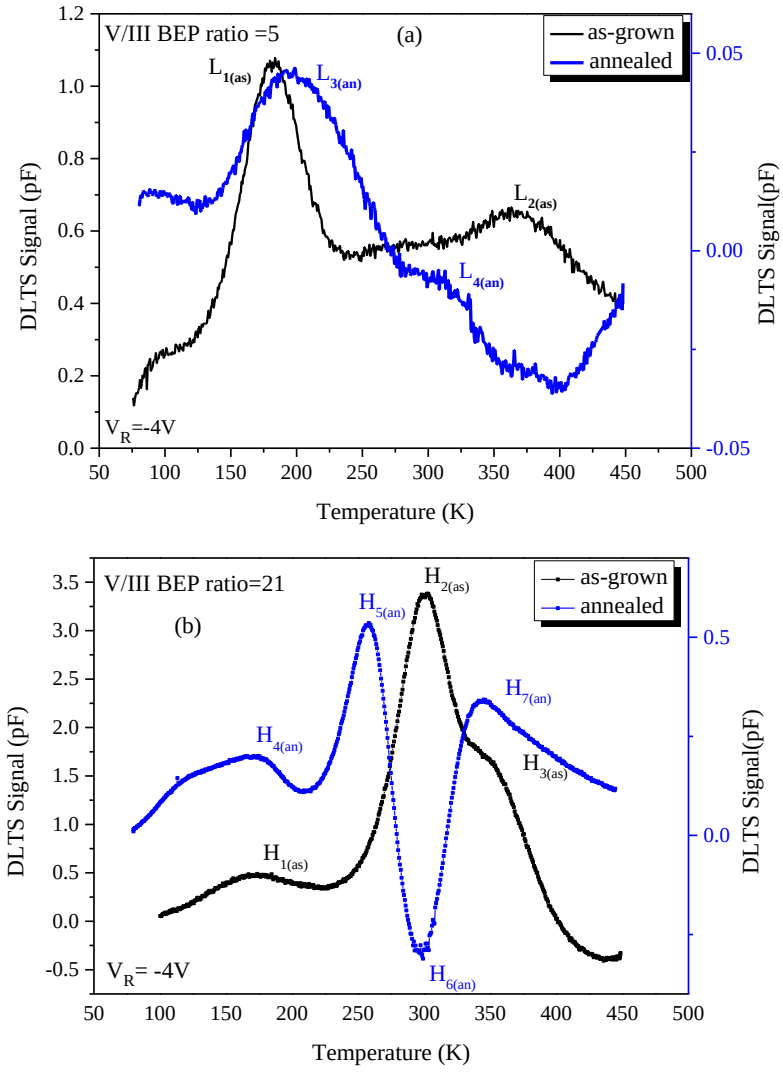


Figure 5.13: DLTS spectra of GaAsPN based solar cells using a reverse bias $V_{R=}$ -4 V, a rate window of 200 Hz, a filling pulse Vp=0 V and filling pulse duration tp=1msec before and after RTA for samples grown with V(P)/III(Ga) flux ratio (a) 5 and (b) 21, respectively.

It can be seen from Figure 5.13 (a) that the sample grown with low V/III flux ratio of 5 exhibit two hole traps before and after annealing labelled as $L_{1(as)}$ and $L_{2(as)}$, and $L_{3(an)}$ and $L_{4(an)}$, respectively. The subscripts (as) and (an) referef to as-grown and annealed samples, respectively. For the sample grown with high V(P)/III(Ga) flux ratio of 21 (Figure 5.13 (b)), the annealed and as-grown samples exhibit each three holes traps (DLTS signal is positive) labelled as $H_{4(an)}$, $H_{5(an)}$, and $H_{7(an)}$, and $H_{1(as)}$, $H_{2(as)}$ and $H_{3(as)}$, respectively. In addition, the negative DLTS signal $H_{6(an)}$ detected in the anneled sample grown at high flux ratio is due to an electron trap. It is worth mentioning that the hole traps $H_{2(as)}$ and $H_{3(as)}$ are annihilated after the RTA process. As seen in Figure 5.13 (a,b), $L_{1(as)}$, $L_{3(an)}$, $H_{1(as)}$ and $H_{4(an)}$ traps, which are detected in the temperature range 150 K - 250 K could have the same nature. Similarly, $L_{2(as)}$, $L_{4(an)}$ and $H_{2(as)}$ detected in the temperature range 300 K- 380 K could originate from the same defect. The activation energies, capture cross-sections, and trap concentrations were obtained from Arrhenius plots of $In(e_n/T^2)$ versus 1000/T, as shown in Figure 5.14 and 5.15, and are given in Table 5.2 and 5.3.

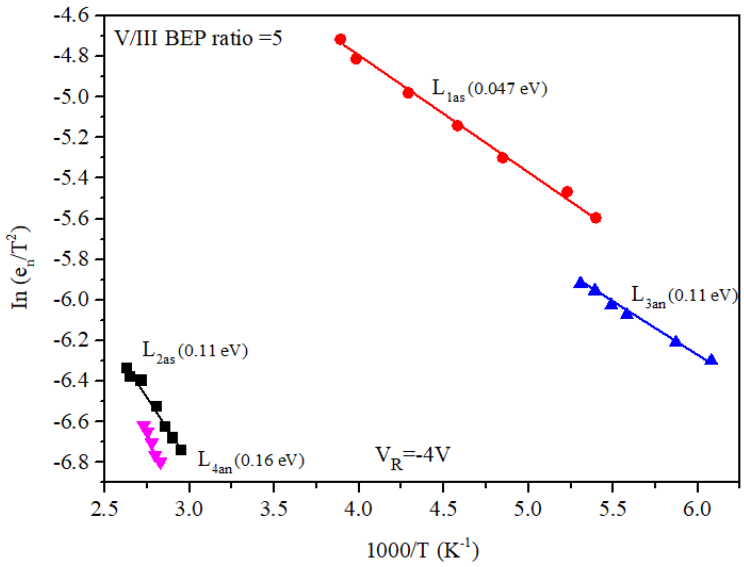


Figure 5.14. Arrhenius plots obtained from Laplace DLTS of as-grown and annealed GaAsPN based solar cells grown with V/III flux ratio= 5.

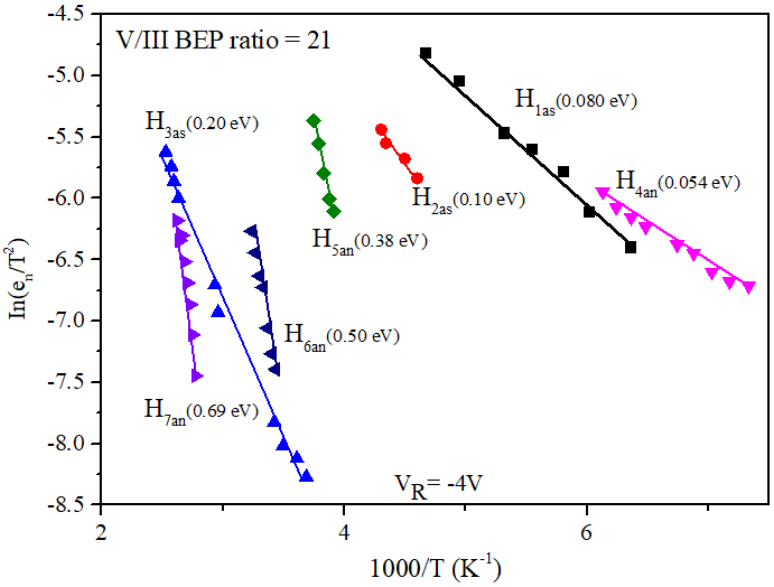


Figure 5.15. Arrhenius plots obtained from LDLTS of as-grown and annealed GaAsPN based solar cells grown with V/III flux ratio= 21.

Table 5.2. Summary of traps activation energies, capture cross-sections and concentrations of as-grown and annealed p-i-n GaAsPN based solar cells grown with V(P)/III(Ga) flux ratio= 5.

Sample	Trap label	E_T (eV)	trap concentration $N_t(cm^{-3})$	capture cross section σ_n (cm^2)
As-grown	$L_{1(as)}$	0.047±0.001	$2.85x10^{15}$	$7.5x10^{-21}$
	$L_{2(as)}$	0.11±0.01	$2.3x10^{15}$	$5.2x10^{-21}$
Annealed	$L_{3(an)}$	0.042±0.002	$2.41x10^{14}$	$1.45x10^{-23}$
	$L_{4(an)}$	0.16±0.01	$3.42x10^{14}$	$1.02x10^{-22}$

Table 5.3. Summary of traps activation energies, capture cross-sections and concentrations for as-grown and annealed PIN GaAsPN based solar cells grown with V(P)/III(Ga) flux ratio= 21. All the defects are hole traps (majority charge carrier traps) except $H_{6(an)}$which is an electron trap (minority charge carrier trap).

Sample	Trap label	E_T (eV)	trap concentration $N_t(cm^{-3})$	capture cross section σ_n (cm^2)
As-grown	$H_{1(as)}$	0.080±0.003	$2.0x10^{15}$	$2.5x10^{-22}$
	$H_{2(as)}$	0.10±0.01	$1.5x10^{15}$	$1.2x10^{-22}$
	$H_{3(as)}$	0.20±0.01	$2.2x10^{16}$	$4.2x10^{-22}$
Annealed	$H_{4(an)}$	0.054±0.002	$2.74x10^{14}$	$3.17x10^{-21}$
	$H_{5(an)}$	0.38±0.03	$1.05x10^{15}$	$3.73x10^{-17}$
	$H_{6(an)}$	0.50±0.02	$1.98x10^{15}$	$1.37x10^{-16}$
	$H_{7(an)}$	0.69±0.03	$7.53x10^{14}$	$1.26x10^{-15}$

Shallow and deep traps were observed in the annealed and the as-grown samples grown with different V(P)//III(Ga) flux ratios in the temperature range 150 K – 450 K. It is worth pointing out that for samples grown with flux ratio 21, four traps were observed after annealing while only three defects were detected in as-grown samples. However, for samples grown with flux ratio 5 the number of traps did not change after annealing. The tentative origin of the defects observed in the solar cell samples before annealing were explained in the previous section. The annealed sample grown with high flux ratio showed new deeper level hole traps namely H_5, H_7 and one electron trap H_6 with activation energies of 0.38eV, 0.69eV and 0.50eV, respectively. To identify the origin of trap H_5, it was found that its activation energy and peak temperature are identical to those of the hole defect HT2 (0.39 eV) which was observed by Xie et al [32] who investigated the effects of thermal annealing on deep-level defects in Be-doped InGaAsN structures grown by solid source molecular-beam epitaxy (SSMBE). They suggested that this trap could be associated with arsenic vacancy-type defects which were created during the annealing process. The electron trap H_6 which appeared after annealing could be of the same origin as electron trap ET3 (0.41 eV) which was attributed to nitrogen-related defects in InGaAsN materials [32]. The hole trap H_7 (0.69 eV) has an activation energy closer to the hole trap H2 (0.62 eV) that was detected by DLTS by Ashizawa et al. [36] in p-type InGaAs grown by MBE and they suggested that it could be related to Fe impurities originating from the Liquid Encapsulated Czochralsk (LEC) GaAs substrate. Schaff et al studied the effect of superlattice buffer layers on the electrical characteristics of GaAs power metal–semiconductor field-effect transistors (MESFET's) grown by MBE using DLTS and Hall measurements, It was found that the Fe concentrations and the related HL3 hole

trap concentration were reduced when a superlattice buffer layer is used [37], resulting in improved device performance. It is thought that the high concentration of Fe from the LEC GaAs substrate is responsible for this defect. It is worth mentioning that undoped LEC grown GaAs substrates have higher Fe concentrations than in Cr doped semiinsulating substrates.

5.5. Summary

I-V, C-V, DLTS, and Laplace DLTS techniques were used to investigate the influence of the V(P)/III(Ga) flux ratio and the effect of rapid thermal annealing on the electrical properties of GaAsPN based solar cells grown by molecular beam epitaxy. Shallow and deep traps were detected in both samples before and after annealed. The electrical properties of GaAsPN devices such as ideality factors changed when the V/III flux ratio changed.This can be attributed to the increase or decrease of the number of defects and concentration values. By using the thermionic model, the values of ideality factors were calculated from I-V characteristics. It was observed that the ideality factor increases with increasing temperature. Additionally, the annealed samples showed an ideality factor lower than the as-grown samples. The C-V characterisitcs showed that the doping concentration at room temperature is uniform for all samples except the samples grown with high flux ratio after annealing, and the free carrier concentrations and turn-on voltage increased after rapid thermal annealing. DLTS and LDLTS techniques were used to investigate the electrically active defects in all samples. Two traps have been detected in the sample grown with flux ratio 5 whereas three traps have been observed in the sample grown with flux ratio of 21. After annealing two hole traps H5 and H7 and one electron trap H6 were observed in the sample grown with high

P/Ga flux ratio. However, for samples grown with flux ratio of 5 the number of traps did not change after annealing. However, the concentrations of all defects decreased after postgrowth thermal annealing treatment.

REFERENCES

[1] I. Buyanova, W. Chen, and B. Monemar, "Electronic properties of ga (in) nas alloys," *Materials Research Society Internet Journal of Nitride Semiconductor Research*, vol. 6, 2001.

[2] M. Shafi, R. Mari, M. Henini, D. Taylor, and M. Hopkinson, "Electrical properties of nitrogen-related defects in n-type GaAsN grown by molecular-beam epitaxy," *physica status solidi c*, vol. 6, no. 12, pp. 2652-2654, 2009.

[3] J. Geisz, J. Olson, D. Friedman, K. Jones, R. Reedy, and M. Romero, "Lattice-matched GaNPAs-on-silicon tandem solar cells," in *Conference Record of the Thirty-first IEEE Photovoltaic Specialists Conference, 2005.*, 2005, pp. 695-698: IEEE.

[4] J. Geisz and D. Friedman, "III–N–V semiconductors for solar photovoltaic applications," *Semiconductor Science and Technology*, vol. 17, no. 8, p. 769, 2002.

[5] S. Zhang and S.-H. Wei, "Nitrogen solubility and induced defect complexes in epitaxial GaAs: N," *Physical Review Letters*, vol. 86, no. 9, p. 1789, 2001.

[6] B. Bouzazi, N. Kojima, Y. Ohshita, and M. Yamaguchi, "Effect of electron and proton irradiation on recombination centers in GaAsN grown by chemical beam epitaxy," *Current Applied Physics*, vol. 13, no. 7, pp. 1269-1274, 2013.

[7] I. Németh, B. Kunert, W. Stolz, and K. Volz, "Heteroepitaxy of GaP on Si: Correlation of morphology, anti-phase-domain structure and MOVPE

growth conditions," *Journal of Crystal Growth,* vol. 310, no. 7-9, pp. 1595-1601, 2008.

[8] T. Chin, J. Chang, J. Woodall, W. Chen, G. Haddad, C. Parks, and A. Ramdas, "Operation and device applications of a valved-phosphorus cracker in solid-source molecular-beam epitaxy," *Journal of Vacuum Science & Technology B: Microelectronics and Nanometer Structures Processing, Measurement, and Phenomena,* vol. 13, no. 2, pp. 750-753, 1995.

[9] G. Wicks, M. Koch, J. Varriano, F. Johnson, C. Wie, H. Kim, and P. Colombo, "Use of a valved, solid phosphorus source for the growth of Ga0. 5In0. 5P and Al0. 5In0. 5P by molecular beam epitaxy," *Applied physics letters,* vol. 59, no. 3, pp. 342-344, 1991.

[10] O. Durand, S. Almosni, Y. P. Wang, C. Cornet, A. Létoublon, C. Robert, C. Levallois, L. Pedesseau, A. Rolland, and J. Even, "Monolithic integration of diluted-nitride III–VN compounds on silicon substrates: toward the III–V/Si concentrated photovoltaics," *Energy Harvesting and Systems,* vol. 1, no. 3-4, pp. 147-156, 2014.

[11] L. Baojun, L. Enke, and Z. Fujia, "Pd/Zn/Pd ohmic contacts to p-type GaP," *Solid-State Electronics,* vol. 41, no. 6, pp. 917-920, 1997.

[12] Z. Rebaoui, W. B. Bouiajra, M. A. Abid, A. Saidane, D. Jammel, M. Henini, and J. Felix, "SiC polytypes and doping nature effects on electrical properties of ZnO-SiC Schottky diodes," *Microelectronic Engineering,* vol. 171, pp. 11-19, 2017.

[13] H. Sodabanlu, A. Ubukata, K. Watanabe, T. Sugaya, Y. Nakano, and M. Sugiyama, "Impacts of V/III ratio on the quality and performance of GaAs

pn solar cells by ultrafast MOVPE," in *2018 IEEE 7th World Conference on Photovoltaic Energy Conversion (WCPEC)(A Joint Conference of 45th IEEE PVSC, 28th PVSEC & 34th EU PVSEC)*, 2018, pp. 0249-0252: IEEE.

[14] H. Altuntas and S. Ozcelik, "The interface states and series resistance analyzing of Au/SiO2/n-GaAs at high temperatures," *Journal of alloys and compounds,* vol. 577, pp. 143-147, 2013.

[15] Ö. Demircioglu, Ş. Karataş, N. Yıldırım, and Ö. Bakkaloglu, "Effects of temperature on series resistance determination of electrodeposited Cr/n-Si/Au–Sb Schottky structures," *Microelectronic engineering,* vol. 88, no. 9, pp. 2997-3002, 2011.

[16] I. Orak, K. Ejderha, and A. Turut, "The electrical characterizations and illumination response of Co/N-type GaP junction device," *Current Applied Physics,* vol. 15, no. 9, pp. 1054-1061, 2015.

[17] J. H. Werner, "Schottky barrier and pn-junction I/V plots—Small signal evaluation," *Applied physics A,* vol. 47, pp. 291-300, 1988.

[18] H. Alburaih, H. Albalawi, and M. Henini, "Effect of rapid thermal annealing on the electrical properties of dilute GaAsPN based diodes," *Semiconductor Science and Technology,* vol. 34, no. 10, p. 105009, 2019.

[19] B. Akkal, Z. Benamara, H. Abid, A. Talbi, and B. Gruzza, "Electrical characterization of Au/n-GaN Schottky diodes," *Materials Chemistry and Physics,* vol. 85, no. 1, pp. 27-31, 2004.

[20] S. Chand and J. Kumar, "Electron transport and barrier inhomogeneities in palladium silicide Schottky diodes," *Applied physics A,* vol. 65, no. 4-5, pp. 497-503, 1997.

[21] S. Almosni, C. Robert, T. Nguyen Thanh, C. Cornet, A. Létoublon, T. Quinci, C. Levallois, M. Perrin, J. Kuyyalil, and L. Pedesseau, "Evaluation of InGaPN and GaAsPN materials lattice-matched to Si for multi-junction solar cells," *Journal of applied physics,* vol. 113, no. 12, p. 123509, 2013.

[22] W. Chen, I. Buyanova, C. Tu, and H. Yonezu, "Point defects in dilute nitride III-N–As and III-N–P," *Physica B: Condensed Matter,* vol. 376, pp. 545-551, 2006.

[23] S. Suresh, M. Balaji, V. Ganesh, and K. Baskar, "Investigations on the nonidealities in Pd/n-GaN Schottky diodes grown by MOCVD," *Journal of alloys and compounds,* vol. 506, no. 2, pp. 615-619, 2010.

[24] V. T. Rangel-Kuoppa, O. Reentilä, M. Sopanen, and H. Lipsanen, "Temperature Dependence Of Current-Voltage Characteristics Of Au/p-GaAsN Schottky Barrier Diodes, With Small N Content," in *AIP Conference Proceedings*, 2011, vol. 1399, no. 1, pp. 171-172: American Institute of Physics.

[25] A. Chitnis, A. Kumar, M. Shatalov, V. Adivarahan, A. Lunev, J. Yang, G. Simin, M. A. Khan, R. Gaska, and M. Shur, "High-quality p–n junctions with quaternary AlInGaN/InGaN quantum wells," *Applied Physics Letters,* vol. 77, no. 23, pp. 3800-3802, 2000.

[26] T. Yu, Y. Pan, Z. Yang, K. Xu, and G. Zhang, "Influence of V/III flux ratio on electrical properties of AlInGaN/Gan heterostructures grown by MOCVD," *Journal of crystal growth,* vol. 298, pp. 211-214, 2007.

[27] F. Abulfotuh, A. Balcioglu, D. Friedman, J. Geisz, and S. Kurtz, "Investigation of deep levels in GaInNAs," in *AIP Conference*

Proceedings, 1999, vol. 462, no. 1, pp. 492-498: American Institute of Physics.

[28] H. Suzuki, K. Nishimura, K. Saito, T. Hashiguchi, Y. Ohshita, N. Kojima, and M. Yamaguchi, "Effects of residual carbon and hydrogen atoms on electrical property of GaAsN films grown by chemical beam epitaxy," *Japanese Journal of Applied Physics*, vol. 47, no. 8S2, p. 6910, 2008.

[29] O. Rumyantsev, P. Brunkov, E. Pirogov, and A. Y. Egorov, "Study of defects in heterostructures with GaPAsN and GaPN quantum wells in the GaP matrix," *Semiconductors*, vol. 44, no. 7, pp. 893-897, 2010.

[30] Y. Choi, K. Xie, H. Kim, and C. Wie, "Interface trap and interface depletion in lattice-mismatched GaInAs/GaAs heterostructures," *Journal of electronic materials*, vol. 20, no. 8, pp. 545-551, 1991.

[31] V. Polojärvi, A. Aho, A. Tukiainen, M. Raappana, T. Aho, A. Schramm, and M. Guina, "Influence of As/group-III flux ratio on defects formation and photovoltaic performance of GaInNAs solar cells," *Solar Energy Materials and Solar Cells*, vol. 149, pp. 213-220, 2016.

[32] S. Xie, S. Yoon, and S. Wang, "Effects of thermal annealing on deep-level defects and minority-carrier electron diffusion length in Be-doped InGaAsN," *Journal of applied physics*, vol. 97, no. 7, p. 073702, 2005.

[33] M. Aziz, A. Mesli, J. Felix, D. Jameel, N. Al Saqri, D. Taylor, and M. Henini, "Effect of post-growth annealing treatment on interfacial misfit GaSb/GaAs heterostructures," *Journal of Crystal Growth*, vol. 424, pp. 5-10, 2015.

[34] S. Zhu, C. Detavernier, R. Van Meirhaeghe, F. Cardon, G.-P. Ru, X.-P. Qu, and B.-Z. Li, "Electrical characteristics of CoSi2/n-Si (1 0 0) Schottky

barrier contacts formed by solid state reaction," *Solid-State Electronics,* vol. 44, no. 10, pp. 1807-1818, 2000.

[35] J. M. Shah, Y.-L. Li, T. Gessmann, and E. F. Schubert, "Experimental analysis and theoretical model for anomalously high ideality factors (n≫ 2.0) in AlGaN/GaN pn junction diodes," *Journal of applied physics,* vol. 94, no. 4, pp. 2627-2630, 2003.

[36] Y. Ashizawa, S. Akbar, W. Schaff, L. Eastman, E. Fitzgerald, and D. Ast, "Influence of lattice misfit on heterojunction bipolar transistors with lattice-mismatched InGaAs bases," *Journal of applied physics,* vol. 64, no. 8, pp. 4065-4074, 1988.

[37] W. Schaff, L. Eastman, B. Van Rees, and B. Liles, "Superlattice buffers for GaAs power MESFET's grown by MBE," *Journal of Vacuum Science & Technology B: Microelectronics Processing and Phenomena,* vol. 2, no. 2, pp. 265-268, 1984.

CHAPTER 6: INVESTIGATION OF THE EFFECT OF GaAs SUBSTRATE ORIENTATIONS AND InGaP DOPING ON THE ELECTRICAL AND OPTICAL PROPERTIES OF InGaP-BASED SOLAR CELL STRUCTURES

In this chapter, the effects of the GaAs substrate orientation and InGaP doping on the electrical and optical properties of p-i-n InGaP-based solar cell structures have been investigated using Current density-voltage (J-V), capacitance-voltage (C-V), Deep Level Transient Spectroscopy (DLTS), Laplace DLTS, SILVACO TCAD (technology computer aided design), and Photoluminescence (PL).

6.1 INTRODUCTION

III-V semiconductor alloy systems have been extensively investigated as efficient light emitters and absorbers [1-3]. Because of its large direct bandgap of 1.9 eV and superior radiation resistance, InGaP has been regarded as a promising material choice for space and concentrated photovoltaic applications. High performance photonic, optoelectronic and high reliability electronic devices based on InGaP/GaAs have been fabricated previously [4, 5]. However, depending on the growth conditions and substrate orientation, CuPtB-type ordering can appear in lattice matched InGaP-on-GaAs layers [6, 7]. Transmission electron diffraction (TED) technique has revealed that such ordering typically occurs on (111)B and (111) planes in InGaP epilayers, which is called CuPt B-type ordering [8].

Furthermore, localization and delocalization of carriers may simultaneously exist due antiphase boundaries (APBs) at the boundary of ordered domains since they are commonly created by this dual variant ordering [9], which has been shown to produce a pronounced impact on the electrical and optical properties of materials [10, 11]. These effects have been studied extensively using optical techniques such as photoluminescence spectroscopy (PL) [12, 13]. Particularly, a previous study reported a charge accumulation at the InGaP/GaAs interface due to unknown defects, resulting in a parallel conduction channel [3]. In addition, it was suggested that an unstable surface due to the presence of defects, for example P desorption, can deteriorate the InGaP surface and leads to a degradation of its properties [3]. In general, defects can have a significant impact on devices' performance. Therefore, investigating defects (deep and shallow) is critical for the future of manufacturing devices [14]. In this regard, deep level transient spectroscopy (DLTS) is a powerful technique to investigate electrically active defects in semiconductor materials and devices [15].

In this study, DLTS technique has been used to investigate electrically active defects present within the bandgap of InGaP grown by metalorganic chemical vapour deposition (MOCVD) method. In addition, capacitance-voltage measurements were used to determine the free carrier concentration. Furthermore, current-voltage characteristics were analyzed and modelled using SILVACO TCAD (technology computer aided design) to understand the transport mechanism in devices based on InGaP (undoped and n-doped) grown on different GaAs substrates. Moreover, PL was used to investigate their optical properties. The PL spectra have shown different emission peaks associated with excitonic, free carriers transitions in fully disordered InGaP and spatially indirect transition in ordered

domains, involving electrons at donors and photoexcited holes. Furthermore, the PL spectra, which were also affected by distinct degree of atomic ordering between the samples, showed higher ordering domains for the n-doped InGaP sample grown on tilted substrate orientation than the n-doped InGaP sample grown on exact (100). In addition, a reduced ordering was observed in the n-doped InGaP sample as compared to the undoped InGaP sample grown on exact (100).

6.2 EXPERIMENTAL DETAILS

The crystal growth process was carried out in a planetary MOCVD reactor (AIXTRON, AIX2000) equipped with Laytec Epicurve DA-IR-T in-situ optical system. Trimethylgallium, trimethylindium, tertiarybutylarsine and tertiarybutylphosphine were used as sources for Ga, In, As, and P, respectively. p-type and n-type epitaxial layers were doped with Zn and Te using dimethylzinc and diethyltelurium dopants, respectively. During the growth, the reactor pressure was set at 100 mbar and the substrate temperature was 560 °C. p-type GaAs (100) substrates ($1x10^{19}$ cm^{-3} $Zn-doped$) with exact orientation and 2° off towards (111)B were used in this work as illustrated in Figure 6.1. The growth rate of GaAs and InGaP were 27 nm/min and 21 nm/min, respectively. V/III ratios during growth of both materials were 20. Ag/Au and AuGe/Au were utilized for Ohmic contacts to p-GaAs and n-GaAs, respectively. Reflection High Energy Electron Diffraction (RHEED) technique, which was used to monitor the growth process and determine In/Ga compositions, provided evidence of the crystallinity of the investigated structures.

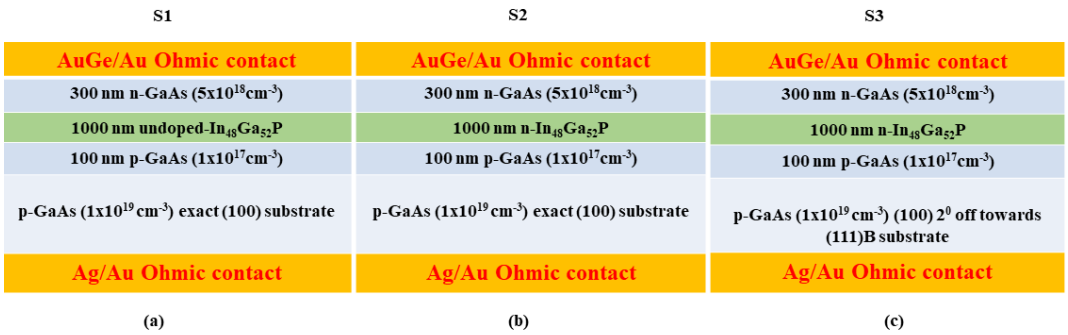


Figure 6.1: Schematic diagrams of the solar cell structures grown on GaAs substrates with different orientations (a) n-i-p device grown on exact (100) (S1 sample: i-region undoped $In_{0.48}Ga_{0.52}P$); (b) p-n-n device grown on exact (100) (S2 sample: i-region n-doped $In_{0.48}Ga_{0.52}P$); (c) p-n-n device grown on 2^0 off towards (111)B (S3 sample: i-region n-doped $In_{0.48}Ga_{0.52}P$).

The PL spectra of the samples were investigated as a function of laser power and temperature using a Janis closed-loop helium cryostat. The samples were excited with a 532 nm (2.33 eV) CW (continuous wave) DPSSL (Advanced Diode-Pumped Solid-State) laser with a laser spot diameter on the sample of around 400 μm. The PL signal was collected using a 500M Spex monochromator coupled with a GaAs photomultiplier with water-cooled thermoelectric cooler.

6.3 PHYSICAL MODELS

SILVACO TCAD [16] was used to model the heterojunctions shown in Figure 6.1. TCAD solves the basic drift-diffusion semiconductor equations, Poisson and continuity equations and include thermionic and tunnelling above and through the heterojunction, respectively [17-19].

Poisson equation is given by [17-19] :

$$div(\varepsilon\nabla\psi) = -q\left(p - n + N_D - N_A \pm N_t^{\pm}\right) \tag{6.1}$$

where ψ is the electrostatic potential, ε is the permittivity, p and n are free holes and electrons concentrations, respectively, $N_D(N_A)$ is the donor (acceptor) doping density and $N_t^{\pm}$ is the ionized traps density.

The continuity equations for electrons and holes defined in steady states are given by [17-19]:

$$0 = \frac{1}{q} div\overrightarrow{J_n} + G_n - R_n \tag{6.2}$$

$$0 = -\frac{1}{q} div\overrightarrow{J_p} + G_p - R_p \tag{6.3}$$

where G_n and G_p are the generation rates for electrons and holes, R_n and R_p are the recombination rates for electrons and holes. $\vec{J}_n$ and $\vec{J}_p$ are the electron and hole current densities which are given in terms of quasi-Fermi level (ϕ_n and ϕ_p) and mobility ($\mu_n$and μ_p) as [16–18]:

$$\vec{J}_n = -q\mu_n n\nabla\phi_n \tag{6.4}$$

$$\vec{J}_p = -q\mu_p p\nabla\phi_p \tag{6.5}$$

Traps are represented by their ionized density $N_t^{\pm}$. The sign $\pm$ depends on whether the trap is a majority or a minority charge carrier so that $N_t^{+} = fN_t$ and $N_t^{-} = (1-f)N_t$, f is the occupancy function given by $f = \frac{\sigma_n n + \sigma_p p}{\sigma_n(n+n_t)+\sigma_p(p+p_t)}$, $\sigma_{n(p)}$ is the

trap capture cross-section for electrons (holes). Furthermore, the recombination rate is related to traps through the well-known Shockley-Read-Hall (SRH) formula:

$$R_{n,p} = \frac{pn - n_i^2}{\tau_{0n}(p + p_t) + \tau_{0p}(n + n_t)} \tag{6.6}$$

with

$$n_t = n_i exp\left(-\frac{(E_i - E_t)}{kT}\right) \tag{6.7}$$

and

$$p_t = n_i exp\left(-\frac{(E_t - E_i)}{kT}\right) \tag{6.8}$$

where τ_{0n} and τ_{0p} are the minority carrier lifetimes which are also related to traps through:

$$\tau_{0n(p)} = \frac{1}{v_{thn(p)}\sigma_{n(p)}N_t} \tag{6.9}$$

where $v_{thn(p)}$ is the thermal velocity of electrons (holes).

In addition, the tunnelling via dislocation current can be modelled with a hopping model, which is given by:

$$J = N_{TD}.q.n_D.\mu.E \tag{6.10}$$

where N_{TD} is the dislocation density, q is the elementary charge, n_D is the linear carrier concentration along the dislocation, μ is the electron mobility, and E is the electric field.

6.4 RESULTS AND DISCUSSION

Current density-voltage (J-V), capacitance-voltage (C-V), DLTS and Laplace DLTS techniques were performed in order to investigate the electrically active defects and extract some important parameters of the InGaP-based solar cell structures investigated in this work.

6.4.1 EFFECT OF GaAs SUBSTRATE ORIENTATION ON CURRENT DENSITY

Figure 6.2 (a) shows room temperature semi-logarithmic and linear J-V plots of S1, S2 and S3 samples. From the room temperature J-V characteristics it is clear that there is a reduction in the leakage current density in the undoped devices as compared to the doped devices. However, the doped sample (S3) grown on (100) 2° off towards (111B) has the highest dark current density at all reverse bias voltages amongst all devices. The decrease or increase in the leakage current could be (i) attributed to a decrease or increase of the number of defects and their concentrations, which will be investigated further using DLTS experiments and/or (ii) related to the domination of new transport mechanisms such as tunneling via dislocations as will be discussed in the modeling section. Moreover, from the linear J-V characteristics shown in Figures 6.2 (b and c), the device grown on (100) 2° off towards (111)B substrate has a turn-on voltage (V_{on}) of 1.15 V, which is higher than the V_{on} of S1 (0.61 V) and S2 (0.68 V) devices.This behaviour can be explained by the creation of new defects states which increase the carrier trapping effect or could be related to charge carrier trapping by dislocations [20]. However, the undoped samples grown on exact (100) (S1) have the lowest V_{on} of ~0.61 V.

Furthermore, a high forward current was obtained for S3 sample in comparison with the other samples as shown in Figure 6.2 (a). The high increase in forward current may indicate the activation of new transport mechanism as will be discusscussed in the simulation part.

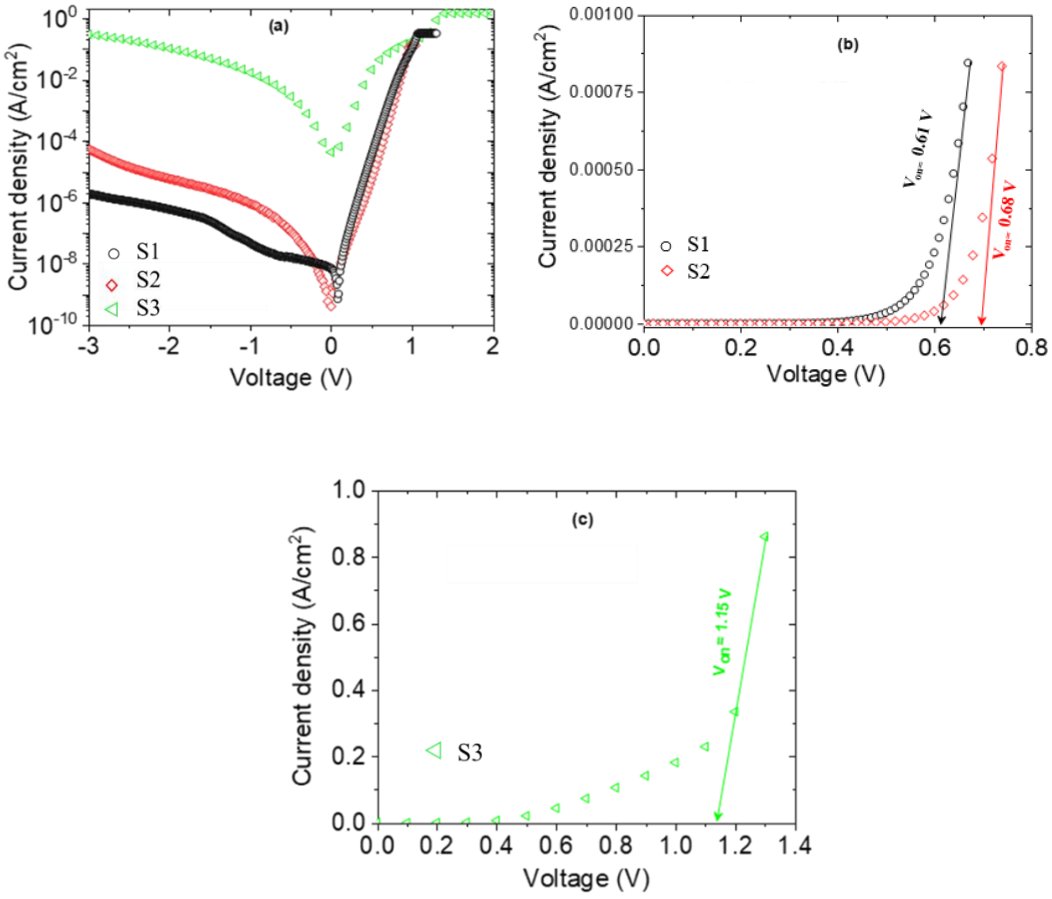


Figure 6.2: Room temperature (a) Semi-log plots of dark J-V characteristics for all samples and, (b) and (c) linear plots of J-V characteristics of samples S1 and S2, and S3 sample, respectively.

J-V measurements as function of temperature have been carried out for all samples in the range of 200-400 K (with 20 K intervals) to extract the diode parameters. By using a general diode model, the current–voltage relationship is as follows [21]:

$$J = J_0[exp\left(\frac{q(V-JRs)}{nKT}\right) - 1] \quad (6.11)$$

$$J_s = AA^*T^2\, exp\left(\frac{-q\phi_b}{KT}\right) \quad (6.12)$$

where q is the elementary charge, n is the ideality factor, k is Boltzmann's constant, T is the temperature, ϕ_b is the built-in potential barrier, R_s is the series resistance. $A^*$is the effective Richardson's constant ($A^* = 14.1$ Acm^{-2}K^{-2} for InGaP) [22]. Furthermore, the effective areas of the diodes A are: A = 1.96 x 10^{-3} cm^2 for undoped InGaP grown on exact (100) (S1), A = 7.85 x 10^{-3} cm^2 for n-doped samples grown on exact (100) (S2) and (100) 2^0 off towards (111B) (S3). The room temperature ideality factor (n) and the built-in potential ($\emptyset_b$) for all samples, which were determined by using the method developed by Werner [23] as described in Chapter 5, section (5.3.1), are summarised in Table 6.1.

Table 6.1: Ideality factor (n) and built-in potential (ϕ_b) at room temperature for all samples

Sample	ideality factor (n)	built-in potential (ϕ_b (eV))
Undoped InGaP grown on exact (100) (S1)	2.16 ± 0.01	0.840 ± 0.001
n-doped InGaP grown on exact (100) (S2)	1.55 ± 0.04	0.910 ± 0.006
n-doped InGaP grown on (100) 2-degrees off towards (111)B (S3)	2.05 ± 0.04	0.660 ± 0.001

As Table 6.1 shows, n-doped InGaP sample grown on exact (100) GaAs (S2) substrate has the lowest ideality factor (n=1.55) as compared to S1 (*n*=2.16; undoped InGaP grown on exact (100)) and S3 (*n*=2.05; n-doped InGaP grown on (100) 2^0 off towards (111)B samples. The temperature evolution of n is shown in Figure 6.3. The ideality factors are high at low temperature and decrease as the temperature increases. The increase in ideality factor with the decrease in temperature is related to the domination of tunneling transport mechanism [24]. The same behaviors were also observed by Han *et al.* [25] in single-junction GaAs solar cell by means of J-V measurements in the 100–400 K temperature range. They reported ideality factors of 4.38 and 1.7 at 100 K and 300 K, respectively. Fiat *et al.* [26] investigated CdTe-based solar cells and observed that the ideality factor *n* decreases from 5.43 at 80 K to 1.4 at 300 K. Özavci *et al*. investigated Au/GaAs Schottky diodes and they obtained ideality factors of 5.43 at 80 K and 1.4 at room-temperature [27]. Furthermore, the lowest $ø_b$ was obtained for S3 sample as presented in Table 6.1. An ideality factor higher than 2 with a low $ø_b$ compared to the other samples indicates the domination of tunneling transport mechanism as will be discussed later.

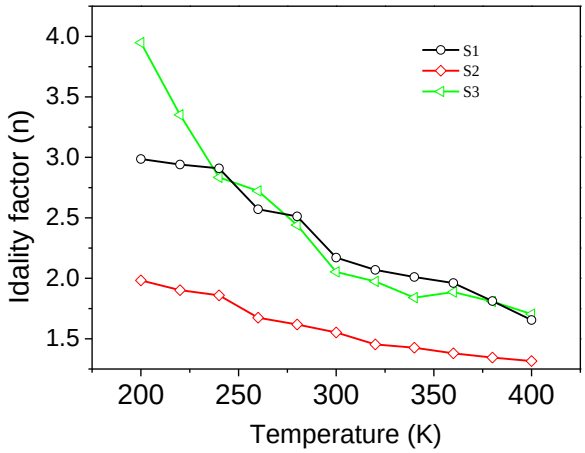


Figure 6.3: Temperature-dependent ideality factor of all samples. The solid lines are guide to the eyes.

6.4.2 EFFECT OF GaAs SUBSTRATE ORIENTATION ON CAPACITANCE –VOLTAGE CHARACTERISTICS

C-V measurements at room temperature have been carried out for all solar cells samples in order to calculate the free carrier concentrations. As figuer 6.4 hows, undoped-InGaP grown on (100) exact GaAs substrate (S1) has the highest capacitance while sample grown on (100) 2^0 off towards (111)B (S3) has the lowest capacitance. The free carrier concentrations, N_d, for all samples were calculated using the slope of the best fit of the plot $1/C^2$ versus reverse bias (V), as shown in Figure 6.5. The doping concentration is found to be uniform for all doped samples as evidenced by the linear behaviour of the plot of $1/C^2$ versus V, except for the n-doped InGaP grown on exact (100) substrate sample (S2) which has a non-uniform free carrier concentration. The free carrier concentration is ~9.23×10^{17} cm^{-3} and ~3.15×10^{18} cm^{-3} for S1 and S3 samples, respectivly. For S2 sample, the free carrier concentration is non-uniform and there are three different free carrier concentrations. From 0 to -1V $Nd \approx 1.30 \times 10^{17}$ cm^{-3}, from -1 to -2V $Nd \approx 2.45 \times 10^{17}$ cm^{-3} and from -2 to at -4V $Nd \approx 4.30 \times 10^{17} cm^{-3}$. This non-uniform electron profile is also evidenced from electrochemical capacitance-voltage measurements as shown in Figure 6.10 and will be also discussed in the modelling section.

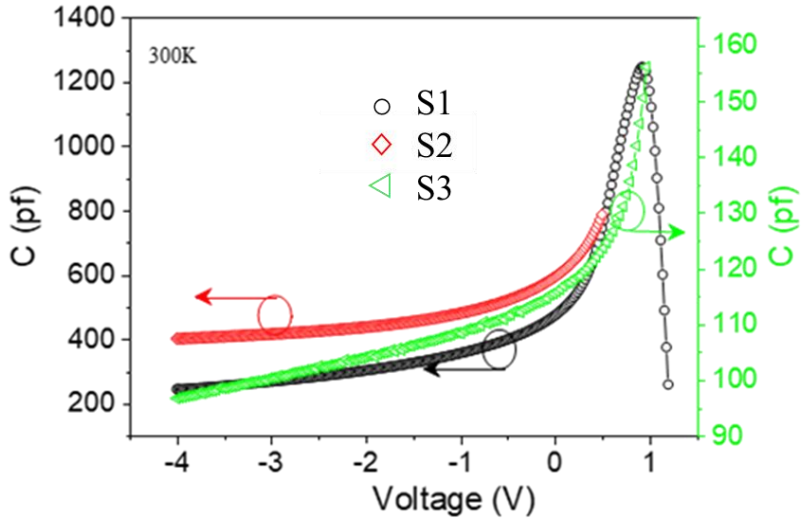


Figure. 6.4: C-V characteristics at room temperature for all samples

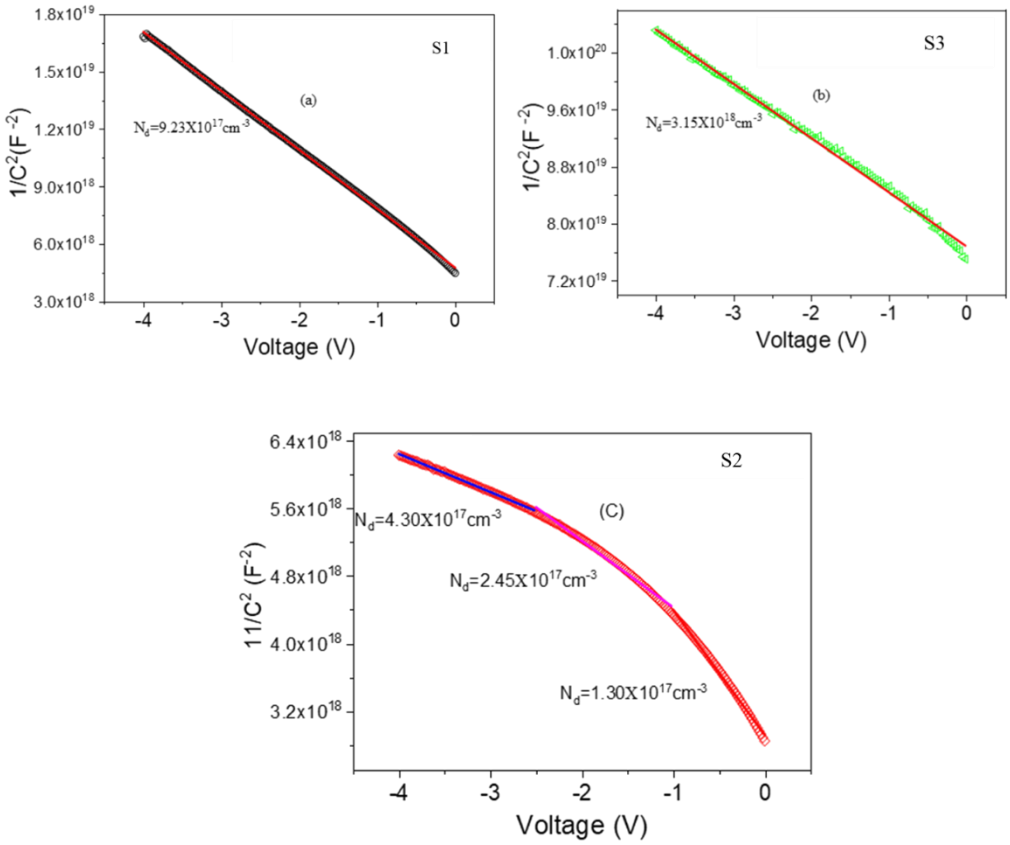


Figure 6.5: $1/C^2$ versus reverse applied bias plots at room temperature for (a) undoped InGaP grown on exact (100) (S1), (b) sample grown on (100) 2^0 off towards (111B) (S3) and (c) n-doped InGaP grown on exact (100) (S2).

The low capacitance of S3 sample is related to the trapping effect. For this sample two trap levels were observed while only one trap is detected in the other two samples S1 and S2, as will be discussed in the defect analysis section below.

6.4.3 DLTS AND LAPLACE DLTS ANALYSIS

DLTS measurements have been performed for all samples, as shown in Figure 6.6, over the scanned temperature range of 10-450 K with a reverse bias V_R= -4V, filling pulse height V_P = 0V, filling pulse time t_P = 1 msec and rate windows of 200 s^{-1}. Very broad peaks have been detected in all samples as shown in Figure 6.6. Laplace DLTS [28], which is a powerful technique for resolving the broader peaks, has been used. Laplace DLTS measurements have revealed two traps in sample S3 (C_E and C_H) whereas one trap has been observed in samples S1 (A_E) and S2 (E_E). The subscripts E and H refer to electron and hole traps, respectively. It worth pointing out that in DLTS spectra a positive and a negative peak are associated with electron and hole traps, respectively. Figure 6.7 illustrates the Arrhenius plots for the traps in each sample, which have been calculated from Laplace DLTS measurements. The parameters of all traps in each sample are summarised in Table 6.2.

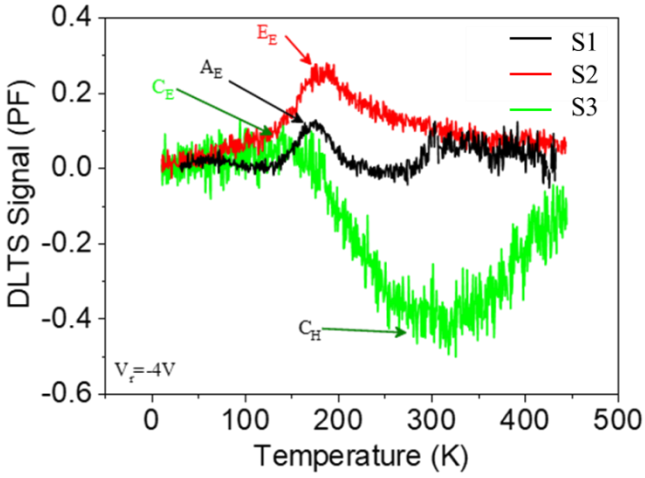


Figure 6.6: DLTS spectra for undoped InGaP grown on exact (100) (S1), n-doped InGaP grown on exact (100) (S2) and n-doped InGaP grown on (100) 2^0 off towards (111B) (S3).

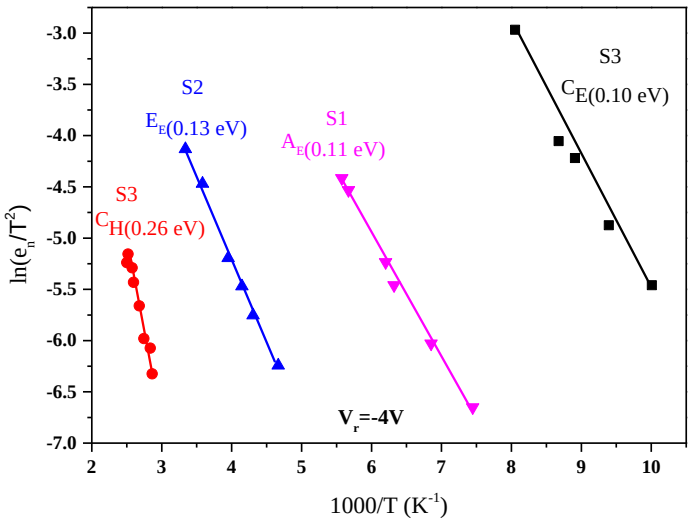


Figure 6.7: Arrhenius plots of the traps depicted in Figure 6.6, where the DLTS spectra were recorded for all samples with the following parameters: V_R =- 4 V, V_P = 0 V, and filling pulse t_p= 1ms.

Table 6.2: Apparent activation energy, E_T, capture cross section, σ_n, and trap concentration of the defects, N_t, observed in all samples. The DLTS experimental conditions were: V_R=-4 V, V_P=0 V, and t_p= 1 msec.

Sample	Trap	Activation Energy E_T (eV)	Capture Cross-Section (σ_∞) (cm^2)	Trap Concentration N_t (cm^{-3})
undoped InGaP grown on exact (100) (S1)	A_E	0.11± 0.01	7.18 x10^{-20}	3.25x10^{15}
n-doped InGaP grown on exact (100) (S2)	E_E	0.13±0.01	2.64 x10^{-20}	2.80x10^{14}
n-doped InGaP grown on (100) 2^0 off towards (111B) (S3)	C_E	0.10±0.01	8.311x10^{-18}	4.80x10^{15}
	C_H	0.26±0.02	9.45x10^{-20}	7.82x10^{15}

As shown in Figure 6.6, traps A_E, E_E and C_E which are detected in the temperature range 150 K - 220 K, could have the same nature but the concentration N_t is different in the different samples. N_t is highest in S3 sample (7.82×10^{15} cm^{-3}) compared to S1 (3.25×10^{15} cm^{-3}) and S2 (2.80×10^{14} cm^{-3}) samples.

The A_E, E_E and C_E deep traps have activation energies of 0.11eV 0.13 eV and 0.10 eV, respectively. These values are close to the trap with activation energy of 0.14 eV that was reported by Kwon *et.al*. [29] in $In_{49}Ga_{51}P$ and attributed to the well-known DX center which is related to deep levels associated with donors in III-V semiconductors. Moreover, Dharmaras *et al.* [30] observed an electron trap labelled E1 with an activation energy of 0.20 eV and concentration of 2.3×10^{15} cm^{-3} in p-type $In_{0.5}Ga_{0.5}P$ solar cells grown by MOCVD. E1 was associated with DX centre. Furthermore, Sung *et al.* [31] found a similar DX center in n-type InGaP layers grown by MOCVD with an activation energy of 0.13 eV in the temperature range 150 K to 200K.

The hole trap C_H with energy of 0.26 eV is observed in the sample grown on (100) 2^0 off towards (111B) (S3). To our knowledge this trap has not been reported before. However, this defect could be similar to the one observed by Huang and Wie at the Al/GaInP interface [32] and which was tentatively attributed to oxygen contamination, or a vacancy-related defect such as V_{In} or V_{Ga} vacancies.

DLTS measurements employing different reverse biases are usually performed to control the depletion region width (moving it away or close to the interface) where the process of trapping and de-trapping of carriers happen.

DLTS measurements have been carried out for all samples at reverse biases V_R = -1 V, as shown in Figure 6.8. The filling pulse height V_P = 0V and the filling pulse time t_P = 1 msec, were kept the same for all measurements. As the reverse bias V_R

is changed from -4V to -1V, only one trap has been detected in samples S1 and S2, however, no DLTS signal was detected in sample S3 (sample grown on (100) 2^0 off towards (111B)). Table 6.3 shows the trap parameters for V_R= -1 V. Arrhenius plots for V_R= -1V are presented in Figure 6.9. The traps found at V_R= -1 V have similar activation energies as those detected at V_R= -4 V whose origin could be related to DX centers as explained before.

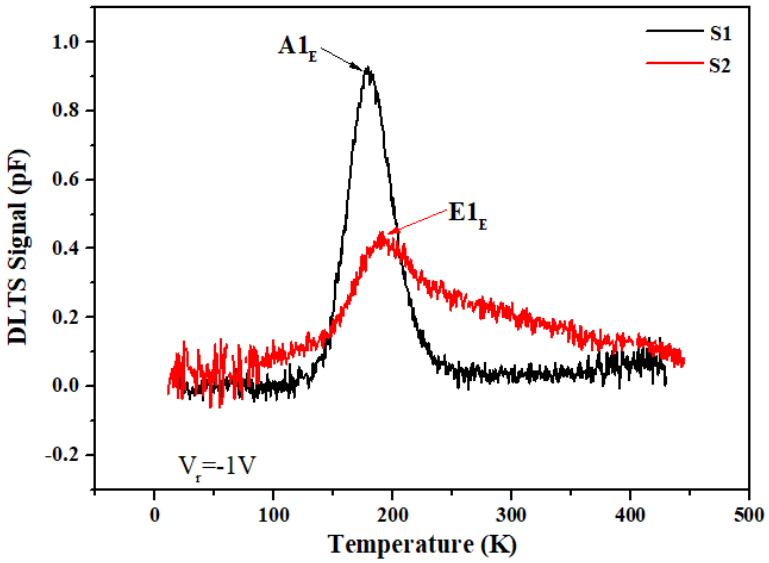


Figure 6.8: DLTS spectra for samples S1 and S2 at V_R = -1 V. No DLTS signal was detected in sample S3

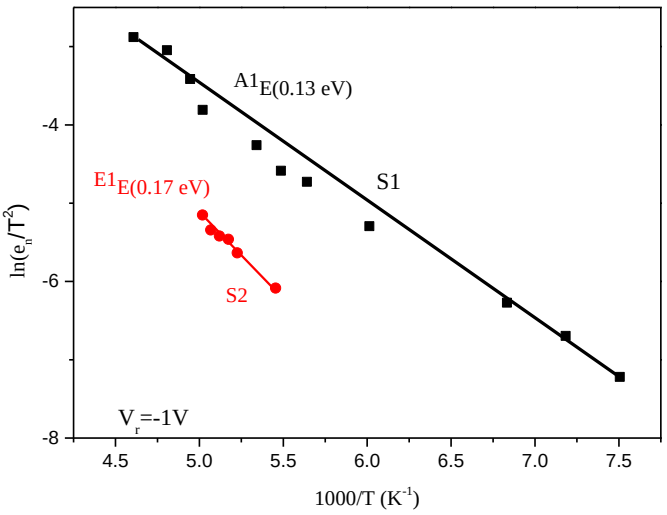


Figure 6.9: Arrhenius plots for samples S1 and S2 obtained from Laplace DLTS at V_R= -1 V.

Table 6.3: Traps pameters for undoped (S1) and n-doped (S2) InGaP samples grown on (100) exact GaAs substrates at V_R= -1 V,V_P= 0 V and t_P= 1 msec.

Sample	Trap	Activation Energy E_T (eV)	Capture Cross-Section (cm^2)	Trap Concentration N_t (cm^{-3})
S1	$A1_E$	0.13 ± 0.02	$3.03x10^{-19}$	$3.37x10^{15}$
S2	$E1_E$	0.17 ± 0.01	$1.26x10^{-18}$	$2.17x10^{14}$

6.4.4 SIMULATION OF THE EFFECT OF GaAs SUBSTRATE MISCUT ANGLE AND DOPING OF InGaP SOLAR CELL STRUCTURE ON THE TRANSPORT MECHANISM

In collaboration with Dr Labed Madani (Sejong University, Seoul, Republic of Korea), SILVACO TCAD simulator, which is used to understand the conduction mechanisms in InGaP-based solar cell structures, requires knowledge of the electron concentration profiles. It is important to note that the main limitation of the conventional C-V method discussed in the previous sections is the electrical breakdown voltage of the samples, which imposes limitations on the maximum measurement depth from the junction of the p-i-n structures. To overcome the limitations of the conventional C-V technique, the electrochemical capacitance-voltage (ECV) measurements were performed in collaboration with Dr Hassanet Sodabanlu (The University of Tokyo, Japan) to characterize the diffusion profile at various depths. This method was explained in Chapter 4, Section 4.7. The electron concentration profiles, which were obtained from ECV measurements, are presented in Figure 6.10 for each sample and are used in the simulation.

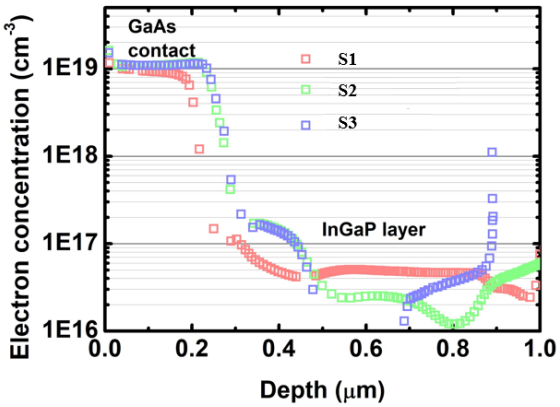


Figure 6.10: Electron concentrations profiles obtained for each sample from electrochemical capacitance-voltage measurements.

Furthermore, with the consideration of traps characteristics mentioned above and the assumption that all mentioned trap levels are in the InGaP layer, the first comparison between simulations and measurements at forward bias are presented in Figure 6.11.

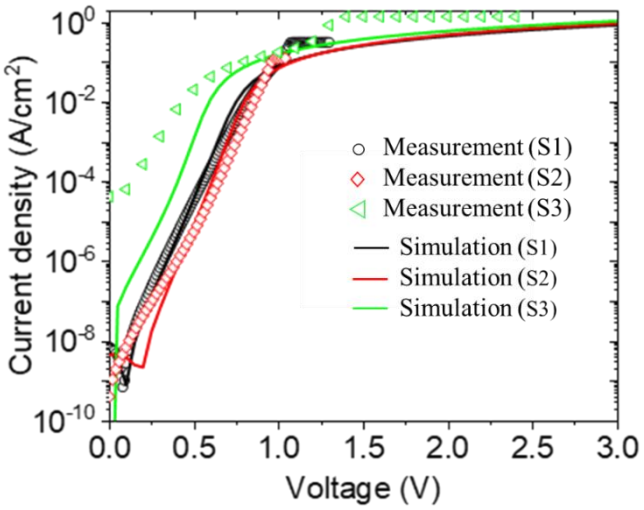


Figure 6.11: Comparison between simulations and measurements of forward J-V characteristics of all samples.

There is a good agreement between simulations and measurements for S1 and S2 samples. On the other hand, a huge disagreement was obtained for S3 sample. This deviation may be related to several reasons such as domination of new transport mechanism.

Li *et al*. [33] studied the effect of substrate miscut angle on dislocation density in (Al)GaInP buffer layers grown by MOCVD and reported that the larger the miscut results in larger dislocation densities. Furthermore, Oshima *et al*. [8] investigated the effect of substrate miscut on the performance of lattice-matched $In_{0.52}Ga_{0.48}P$ solar cells grown on (100) GaAs substrates by solid-source molecular beam epitaxy. They found that the substrate miscut angle affects the InGaP atomic ordering and impacts the InGaP solar cell performance. According to these observations, one expects the domination of tunneling via dislocation transport mechanism especially at low voltages. As shown in Figure 6.12, the effect of dislocation density was studied. With increasing dislocation density, the tunneling via dislocation current increases. A good comparison between simulation and measurement for S3 sample was obtained for a dislocation density of about ~1×10^3 cm^{-2}.

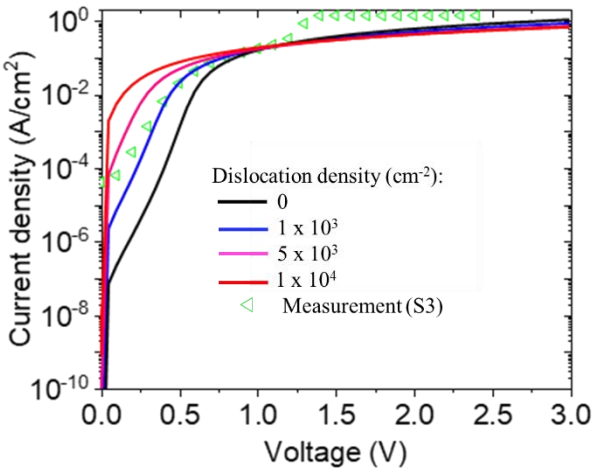


Figure 6.12: The effect of dislocation density on forward current and comparison with measurement for S3 sample.

6.4.5 PHOTOLUMINESCENCE

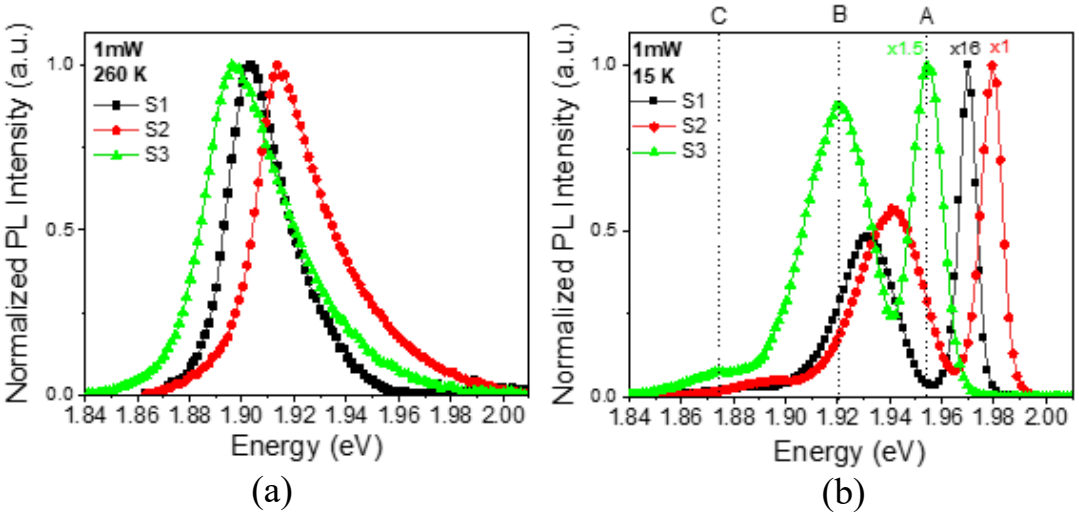


Figure 6.13: Normalized PL spectra for samples S1, S2 and S3 at (a) 260K and (b) 15K, using 1mW laser power excitation.

Typical PL spectra at 260K and 15K are shown in Figure 6.13. At high temperature of 260 K all samples show a broad band peak. On the other hand, all samples exhibit three bands at 15K denoted as A, B and C for sample S3 spectra (Fig. 6.13(b)). These spectra are normalized to the peak A, which has the narrowest full width at half maximum (FWHM) and the highest energy peaks with values of 1.954 eV, 1.970 eV and 1.979 eV for samples S3, S1 and S2, respectively. The lower energy peak B is located about 30-40 meV below peak A, while the wide peak C is located at 80 meV below peak A, for all samples. The nature of each emission peak will be discussed below by analysing PL as function of temperature and laser power.

The InGaP layers grown on GaAs substrates by MOCVD typically suffer from the CuPt-type ordering, which means a CuPt superlattice structure of alternating In-rich ($In_{0.5+\eta/2}Ga_{0.5-\eta/2}P$) and Ga-rich ($In_{0.5-\eta/2}Ga_{0.5+\eta/2}P$) layers formed along the [$\bar{1}$ 11]

and [$1\bar{1}$ 1] directions [34-36]. The formation of this superlattice is commonly referred to as ordering which is strongly influenced by the growth temperature, V/III ratio, doping, and surfactant effects [37-41]. When compared to InGaP a completely disordered alloy (η=0), the partially ordered materials exhibit the degraded luminescent properties such as a weaker emission intensity, broader emission linewidth, and slower recombination rate, in addition to the bandgap reduction [42-45]. The expected bandgap of completely disordered $In_{0.48}Ga_{0.52}P$ alloy is expected to be 2.01 eV at 5K [46, 47], while the ordering reduces the crystal symmetry of GaInP and change its electronic band structure, where the conduction band minimum is lowered and the valence band splits, resulting in a bandgap reduction for more ordered alloys [48-50]. The ordering parameter of InGaP is usually not homogeneous. Instead, domains with different degrees of ordering are formed within a disordered InGaP layer [51], which leads to a spatially fluctuating bandgap and consequently to a localisation of excited carriers in ordered domains with lower bandgap energy. The size of these ordered domains has a strong influence on the PL properties [48], since the recombination of electron–hole pairs occur in both, carriers quantum-mechanically confined in the superlattice-like ordered domains and remaining disordered regions. The observation of these two PL peaks (A and B) separated by 20 meV to 40 meV is a common feature in partially ordered InGaP layers at low temperature, where peak A and B are typically attributed to transitions in the disordered regions and ordered domains, respectively [46, 48-50, 52-54]. The highest-energy peak A is commonly ascribed to free-exciton transition and its energy is close to the low temperature bandgap of 1.96 eV to 1.98 eV of disordered InGaP layers [55, 56], corresponding to a degree of ordering between η=0.1 [57] and η=0.3 [36]. In a partially ordered GaInP alloy,

local atomic ordering domains of InP/GaP monolayer superlattices are embedded inside a disordered lattice matrix where Ga and In atoms are randomly distributed. They may have different periods (sizes), and lead to localized states with deeper potential energy minima so that carriers prefer to occupy at low temperatures and exhibiting a dominant luminescence mechanism from the radiative recombination of carriers within the local atomic ordering domains [58]. It should be noted that such localized states still have lower potential energy minima compared with the bandgap of the disordered region. The low-energy peak B typically originates from spatially indirect radiative recombination of carriers localized at the quantum confined states by local atomic ordering [52, 59]. The PL peak C could be due to an LO-phonon replica, for which a 46.8 meV energy separation from the ordered peak B is predicted [60, 61].

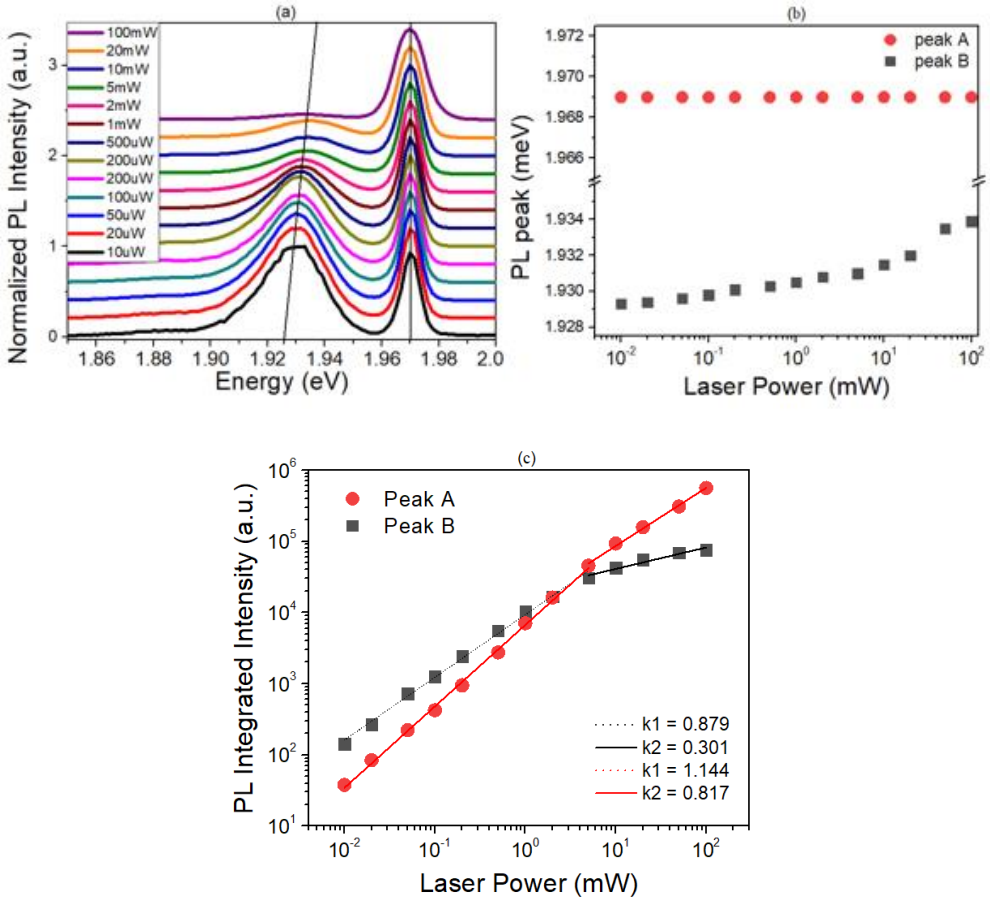


Figure 6.14: (a) PL spectra for different laser power, (b) PL peak position and (c) PL Integrated intensity for peaks A and B as function of laser power, for S1 sample at 15K.

The laser power excitation-dependence of PL was investigated for all samples at 15K in order to understand the nature of the emission peaks A and B. Figure 6.14 shows the typical laser power dependence of the PL spectra (a) only for S1 sample and the correspondent PL peak position (b) dependence at 15K. As the laser power increases, the energy of peak B also shows a remarkable blue-shift, whereas the energy of peak A shows negligible energy shift with increasing laser power. The blue shift of peak B with increasing excitation power is attributed to the band filling effect of the localized states by photogenerated carriers in disordered regions. This

effect was observed for all samples and has been identified previously as the PL from spatially indirect transitions [52, 59], while peak A which shows that electrons and holes recombinations are not spatially separated [60], assert the recombination origin from ordered and disordered of each peak, respectively.

The PL integrated intensity for peaks A and B, at 15K, was plotted as a function of excitation laser power as shown in Figure 6.14 (c), where a crossover point is observed around 5 mW and lies in between two different excitation regimes, similar to that observed in the GaInP epilayers by DeLong *et al*. [43]. In each excitation regime alone, the photoluminescence intensities increase according to a simple power law $I_{PL} = \beta P_{EXC}^{k}$ [62]. I_{PL} is the integrated PL intensity and β and k are fitting parameters. Two k values (k_1 and k_2) for each peak (A and B) were obtained and plotted as fitting curve using solid and dotted lines. Under low power excitation (k_1 regime, where the PL temperature dependence was performed), peak A shows a value of $k_1 > 1$ indicating that both free excitons and free carriers contribute to the recombination process and in which parallel radiationless processes participate [60, 62]. Peak B shows a value of $k_1 \sim 0.88$ indicating spatially separated recombination between electrons at donors in the ordered regions and photoexcited holes (D-h) [60, 62, 63]. However, as P_{EXC} increases to a high-power regime (k_2 regime), defect levels can saturate, leading to a crossover point as observed in Figure 6.14(c). The peak A obtained value of k_2 is <1 and is dominated by free-to-bound and donor-acceptor pair recombinations, while peak B shows k_2 is < 0,5 indicating possible donor to bound recombination [60, 62, 63] .

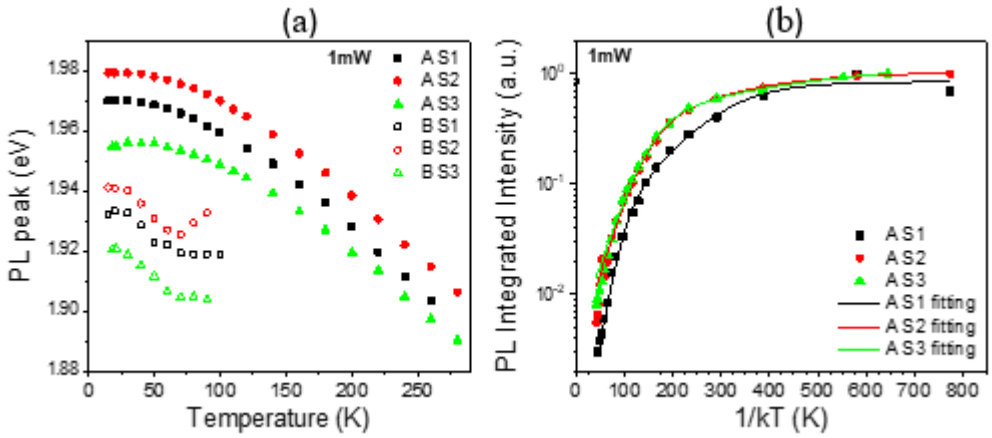


Figure 6.15: Temperature dependence of (a) PL peak position A (filled) and B (open), (b) Arrhenius fitting for peak A.

Figure 6.15(a) shows a typical temperature dependence (T = 15 - 280 K) of PL peaks (A and B only) from samples S1, S2 and S3. It was observed that peak A exhibits a monotonic redshift with increasing temperature due to the bandgap reduction by the thermal expansion of lattices, as expected by typical Varshni relation. The peak B has a different behaviour. Particularly, this band is only observed in a limited range of temperature. It has significant PL intensity at low temperatures, but its intensity decreases when the temperature is increased up to 90 K. For T>90 K, only peak A is observed as shown in Figure 6.13(b). In addition, the peak B also shows an S-shaped behaviour, i.e. it is red shifted first and then blue shifted [53, 58]. The anomalous temperature dependence of the ordered peak B is attributed to the radiative recombination of the carriers in strongly localized states with lower energies, i.e. quantum confined states created by local atomic ordering embedded within disordered matrix with larger potential energy [64].

Table 6.4: Samples doping, ordering degree, fitting parameters and activation energies E_1 and E_2 obtained from Figure 6.15(b)

Sample	nominal doping (cm^{-3})	Peak A (eV)	Peak A relative PL intensity	η	I_0	A_1	E_1 (meV)	A_2	E_2 (meV)
S1	undoped	1.970	1/16	0.27	0.84	42.00	12.9	3995.00	59.66
S2	$1x10^{17}$	1.979	1	0.25	1,03	5.00	6.98	319.00	32.86
S3	$1x10^{17}$	1.954	1/1.5	0.33	1.24	3.58	4.22	292.00	30.34

The temperature dependence of PL intensity was also analyzed (Figure 6.15 (b)) using a modified Arrhenius equation (6.13), considering two non-radiative recombination processes, labelled as 1 and 2 in the equation below [42, 53]:

$$\frac{I_{PL}(T)}{I_0} = \frac{1}{1+A_1 e^{\frac{-E_1}{k_B T}} + A_2 e^{\frac{-E_2}{k_B T}}} \tag{6.13}$$

where I_{PL} is the integrated PL intensity, A_1 and A_2 are constants related to the density of non-radiative recombination centers, E_1 and E_2 are activation energies, k_B is the Boltzmann constant, T the temperature and I_0 the approximate PL intensity when $T \rightarrow 0$. Table 6.4 shows the obtained results of Arrhenius fitting and the activation energy values for all three samples. The obtained values for lower activation energies E_1 range from 4 to 13 meV and are characteristic of trapped carriers thermalizing from localized regions of order induced band-edge fluctuations followed by nonradiative recombination. The increase in temperature enables the carriers to gain sufficient kinetic energy to diffuse to the vicinity of a nonradiative recombination center [42] in disordered GaInP layers [46]. Moreover, the E_2 higher activation energies range from 30 to 60 meV and are suggested to be

indicative of a deep level trap, arising from possible deep acceptor, neutral impurity or even a vacancy related defect [42].

The difference in the PL bandgap between the samples at 15K shown in Figure 6.15(a) could be explained in terms of ordering degree, since the alloy fluctuation composition of In and Ga is the same for all samples [48, 49, 65, 66]. The doped S2 sample, grown on exact (100) GaAs substrate, shows the highest energy of PL peak A, as compared with the undoped S1 sample (intermediate) and the tilted doped S3 sample (lowest). Additionally, it is possible to use low-temperature PL measurements to estimate quantitatively the long-range degree of atomic ordering (η), which is characterized by (i) the atomic fraction of Ga and In atoms on one (111)B lattice plane within the ordered domain; (ii) the size; and (iii) the density of ordered domain, according to the η formula [67]:

$$\eta = \sqrt{\frac{2.005 - E_g(\eta)}{0.471}} \tag{6.14}$$

where $E_g(\eta)$ represents the bandgap of ordered GaInP characterized by η and can be found from the PL peak energy (peak A) at low temperature regime, and 2.005 eV represents the bandgap value of the nominally fully disordered GaInP epilayer at the same temperature [49, 68]. The estimated ordering degree resulting values for each sample is shown in Table 6.4 The ordering degree reduces from sample S1 (undoped) to the less ordered sample S2 (n-doped), and this finding could evidence a change of the atomic ordering due to doping. The presence of n-type doping impurities influences the surface stability during the growth and significantly reduces the dimension of the domains [69, 70] becoming, therefore, less ordered. In particular, a density of doping impurities of ~10^{18} cm^{-3} could completely destroy

the ordering, whereas the latter is only reduced in case of low doping [71]. On the other hand, tilted sample S3 (n-doped) shows a higher ordering degree than sample S1 (undoped), which cannot be explained just by doping differences in the samples. In this case, the doped sample grown on misoriented substrate (S3), the degree of ordering would be higher than S1 and S2 samples because a remarkable dependence on substrate misorientation is attributed to different degrees of atomic ordering of group III sublattice which are caused by the different atomic surface reconstruction rate during the growth [72]. In particular, the degree of order increases from zero until a maximum misorientation angle and is reached at values of 4° to 5°, after that the ordering degree starts to drop. At small misorientation angles, one expects an increase in ordering with increasing misorientation angles simply due to the slower steps velocity allowing more atomic interchange at the steps to produce the ordered structure [72].

6.5 SUMMARY

In summary, the effects of GaAs substrate orientation and doping of InGaP on the electrical and optical properties of InGaP-based solar cells grown by MOCVD technique were studied and analyzed using J-V, C-V and DLTS measurement techniques, SILVACO TCAD modeling and PL spectroscopy. From the J-V characteristics, the reverse current density and turn-on voltage (V_{on}) were higher for sample grown on (100) 2^0 off towards (111B) (S3). In addition, the C-V measurements indicated that the free carrier concentration is non-uniform in the n-InGaP grown on exact (100) (S2). Furthermore, the DLTS technique has been used to investigate the electrically active defects in all samples. One common electron trap (0.10 – 0.13 eV) has been detected in all samples except for the sample grown on (100) 2^0 off towards (111B) where an additional hole trap (0.26 eV) was

observed at a reverse bias of -4 V. However, the DLTS measurements carried out at a reverse bias of -1V (i.e. region probed by DLTS is close to the interface) indicated that no traps were found in sample grown on (100) 2^0 off towards (111B) (S3), but for samples S1 and S2 the traps were similar to those observed at -4 V. SILVACO TCAD was used for modelling the effect of GaAs substrate orientations and doping of InGaP layer on the forward current. Good agreements between simulations and measurements were obtained for S1 and S2 samples by considering the characteristics of the traps detected in the samples by DLTS and the electron profiles obtained from electrochemical capacitance-voltage measurements. However, for S3 sample, a disagreement between simulation and measurement was obtained which could be related to the dominance of tunnelling via dislocation transport mechanism and a good agreement was obtained for a dislocation density of 1×10^3 cm^{-2}. PL spectra as function of temperature and laser power intensity have evidenced two different emission bands depending on the experimental conditions. At high temperatures and laser intensity, it was observed that the highest energy emission peak A dominates the PL spectrum. This band was associated with excitonic and free carriers transitions in fully disordered InGaP. An additional and lowest energy emission peak B was also observed at lower temperatures which was attributed to spatially indirect transition in ordered domains, involving electrons at donors and photoexcited holes. Furthermore, the PL spectra were also affected by different degree of ordering of the samples, showing a highest ordered degree for samples grown on 2^0 off towards (111B) GaAs substrate and lowest ordering for doped samples grown on exact (100) GaAs wafers. The n-doped samples grown on exact (100) showed a reduced ordering as compared to undoped samples grown on exact (100).

REFERENCES

[1] M. Ackland, P. Dunstan, M. Brown, K. Teng, S. Wilks, and R. Cobley, "Characterisation of the influence of multi-quantum barrier reflectors within GaInP/AlGaInP quantum well lasers using near-field imaging techniques," *Applied surface science,* vol. 255, no. 3, pp. 649-652, 2008.

[2] S. Park, T. T. Nguyen, L. Q. Nguyen, Y. Kim, and S. J. Lee, "Material and device characterization of InGaP solar cells grown on GaAs misoriented substrates by metal-organic chemical vapor deposition," *Solar Energy,* vol. 220, pp. 406-411, 2021.

[3] R. Jakomin, A. Parisini, L. Tarricone, M. Longo, B. Fraboni, and S. Vantaggio, "On the electrical properties of Si-doped InGaP layers grown by low pressure-metalorganic vapor phase epitaxy," *Thin solid films,* vol. 520, no. 21, pp. 6619-6625, 2012.

[4] J.-H. Tsai, "Comparative Studies on InGaP/GaAs Heterostructure-Emitter Bipolar Transistors with Tunneling-and Superlattice-Confinement Structures," *Journal of The Electrochemical Society,* vol. 158, no. 5, p. H583, 2011.

[5] Z. Zhang, T. Yoshie, X. Zhu, J. Xu, and A. Scherer, "Visible two-dimensional photonic crystal slab laser," *Applied physics letters,* vol. 89, no. 7, p. 071102, 2006.

[6] A. Gomyo, T. Suzuki, and S. Iijima, "Observation of strong ordering in Ga x In 1− x P alloy semiconductors," *Physical review letters,* vol. 60, no. 25, p. 2645, 1988.

[7] M. Zorn, P. Kurpas, A. Shkrebtii, B. Junno, A. Bhattacharya, K. Knorr, M. Weyers, L. Samuelson, J. Zettler, and W. Richter, "Correlation of InGaP (001) surface structure during growth and bulk ordering," *Physical Review B,* vol. 60, no. 11, p. 8185, 1999.

[8] R. Oshima, Y. Nagato, Y. Okano, and T. Sugaya, "Effects of substrate miscut on the properties of InGaP solar cells grown on GaAs (001) by solid-source molecular beam epitaxy," *Japanese Journal of Applied Physics,* vol. 56, no. 8S2, p. 08MC08, 2017.

[9] S. Mahajan, "Two-dimensional phase separation and surface-reconstruction driven atomic ordering in mixed III–V layers," *Materials Science and Engineering: B,* vol. 30, no. 2-3, pp. 187-196, 1995.

[10] S. H. Wei, D. B. Laks, and A. Zunger, "Erratum:‘‘Dependence of the optical properties of semiconductor alloys on the degree of long-range order’’[Appl. Phys. Lett. 62, 1937 (1993)]," *Applied Physics Letters,* vol. 63, no. 9, pp. 1292-1292, 1993.

[11] J. Novák, S. Hasenöhrl, R. Kúdela, M. Kučera, D. Wüllner, and H.-H. Wehmann, "Resistivity anisotropy in ordered In x Ga 1− x P grown at 640° C," *Applied physics letters,* vol. 73, no. 3, pp. 369-371, 1998.

[12] P. Ernst, C. Geng, F. Scholz, H. Schweizer, Y. Zhang, and A. Mascarenhas, "Band-gap reduction and valence-band splitting of ordered GaInP2," *Applied physics letters,* vol. 67, no. 16, pp. 2347-2349, 1995.

[13] M. Longo, A. Parisini, L. Tarricone, L. Toni, and R. Kudela, "Photoluminescence investigation of superlattice ordering in

organometallic vapour phase epitaxy grown InGaP layers," *Materials Science and Engineering: B*, vol. 86, no. 2, pp. 157-164, 2001.

[14] A. Knauer, P. Krispin, V. Balakrishnan, and M. Weyers, "Defect study of MOVPE-grown InGaP layers on GaAs," *Journal of crystal growth*, vol. 272, no. 1-4, pp. 627-632, 2004.

[15] D. Lang, "Deep-level transient spectroscopy: A new method to characterize traps in semiconductors," *Journal of applied physics*, vol. 45, no. 7, pp. 3023-3032, 1974.

[16] M. J. Islam, R. Sami, M. S. Islam, and M. I. Bahar, "Silvaco TCAD," *Journal of Electronic Design Engineering*, vol. 3, no. 3.

[17] M. Labed, N. Sengouga, M. Labed, A. Meftah, S. Kyoung, H. Kim, and Y. S. Rim, "Modeling a Ni/β-Ga2O3 Schottky barrier diode deposited by confined magnetic-field-based sputtering," *Journal of Physics D: Applied Physics*, vol. 54, no. 11, p. 115102, 2021.

[18] M. Labed, N. Sengouga, M. Labed, A. Meftah, S. Kyoung, H. Kim, and Y. S. Rim, "Modeling and analyzing temperature-dependent parameters of Ni/β-Ga2O3 Schottky barrier diode deposited by confined magnetic field-based sputtering," *Semiconductor Science and Technology*, vol. 36, no. 3, p. 035020, 2021.

[19] M. Labed, N. Sengouga, A. Meftah, A. Meftah, and Y. S. Rim, "Study on the improvement of the open-circuit voltage of NiOx/Si heterojunction solar cell," *Optical Materials*, vol. 120, p. 111453, 2021.

[20] M. Schreck, P. Ščajev, M. Träger, M. Mayr, T. Grünwald, M. Fischer, and S. Gsell, "Charge carrier trapping by dislocations in single crystal diamond," *Journal of Applied Physics,* vol. 127, no. 12, p. 125102, 2020.

[21] W. Dawidowski, B. Ściana, K. Bielak, M. Mikolášek, J. Drobný, J. Serafińczuk, I. Lombardero, D. Radziewicz, W. Kijaszek, and A. Kósa, "Analysis of Current Transport Mechanism in AP-MOVPE Grown GaAsN pin Solar Cell," *Energies,* vol. 14, no. 15, p. 4651, 2021.

[22] D. Zhang, X. Wang, and S. Yoon, "Schottky contacts on wide bandgap InGaP grown with phosphorous cracker cells and their thermal reliability," *Materials Science and Engineering: B,* vol. 74, no. 1-3, pp. 143-146, 2000.

[23] J. H. Werner, "Schottky barrier and pn-junction I/V plots—Small signal evaluation," *Applied physics A,* vol. 47, pp. 291-300, 1988.

[24] M. Labed, J. H. Park, A. Meftah, N. Sengouga, J. Y. Hong, Y.-K. Jung, and Y. S. Rim, "Low temperature modeling of Ni/β-Ga2O3 Schottky barrier diode interface," *ACS Applied Electronic Materials,* vol. 3, no. 8, pp. 3667-3673, 2021.

[25] I. S. Han, J. S. Kim, S. K. Noh, and S. J. Lee, "Structural Optimization and Temperature-Dependent Electrical Characterization of GaAs Single-Junction Solar Cells," *Journal of the Korean Physical Society,* vol. 76, pp. 1096-1102, 2020.

[26] S. Fiat, Z. Merdan, and T. Memmedli, "Current-conduction mechanisms in Au/n-CdTe Schottky solar cells in the wide temperature range," *Physica B: Condensed Matter,* vol. 407, no. 13, pp. 2560-2565, 2012.

[27] E. Özavcı, S. Demirezen, U. Aydemir, and Ş. Altındal, "A detailed study on current–voltage characteristics of Au/n-GaAs in wide temperature range," *Sensors and Actuators A: Physical,* vol. 194, pp. 259-268, 2013.

[28] L. Dobaczewski, A. Peaker, and K. Bonde Nielsen, "Laplace-transform deep-level spectroscopy: The technique and its applications to the study of point defects in semiconductors," *Journal of applied physics,* vol. 96, no. 9, pp. 4689-4728, 2004.

[29] S. Kwon, H. K. Kwon, B. D. Choe, and H. Lim, "Chemical trends of S-, Se-, and Te-related DX centers in InGaP," *Applied physics letters,* vol. 67, no. 17, pp. 2533-2535, 1995.

[30] N. Dharmarasu, M. Yamaguchi, A. Khan, T. Takamoto, T. Ohshima, H. Itoh, M. Imaizumi, and S. Matsuda, "Deep-level transient spectroscopy analysis of proton-irradiated n+/p InGaP solar cells," *Physica B: Condensed Matter,* vol. 308, pp. 1181-1184, 2001.

[31] W.-J. Sung, T.-Y. Liu, S.-L. Yang, K.-F. Huang, T.-Y. Tseng, F.-I. Chou, Y.-Y. Wei, and Y.-R. Wu, "Gamma-ray induced deep electron traps in GaInP," *Japanese Journal of Applied Physics,* vol. 40, no. 9R, p. 5306, 2001.

[32] Z. Huang and C. Wie, "Contact-Related Deep States in AI-GaInP/GaAs Interface," *MRS Online Proceedings Library (OPL),* vol. 325, 1993.

[33] K. Li, Y. Sun, J. Dong, Y. Zhao, S. Yu, C. Zhao, X. Zeng, and H. Yang, "Effects of substrate miscut on dislocation glide in metamorphic (Al) GaInP buffers," *Journal of crystal growth,* vol. 380, pp. 261-267, 2013.

[34] B. Philips, A. Norman, T. Seong, S. Mahajan, G. Booker, M. Skowronski, J. Harbison, and V. Keramidas, "Mechanism for CuPt-type ordering in mixed III–V epitaxial layers," *Journal of crystal growth,* vol. 140, no. 3-4, pp. 249-263, 1994.

[35] G. B. Stringfellow and G. Chen, "Atomic ordering in III/V semiconductor alloys," *Journal of Vacuum Science & Technology B: Microelectronics and Nanometer Structures Processing, Measurement, and Phenomena,* vol. 9, no. 4, pp. 2182-2188, 1991.

[36] Y. Zhang, A. Mascarenhas, and L.-W. Wang, "Dependence of the band structure on the order parameter for partially ordered Ga x In 1− x P alloys," *Physical Review B,* vol. 63, no. 20, p. 201312, 2001.

[37] A. Gomyo, T. Suzuki, K. Kobayashi, S. Kawata, I. Hino, and T. Yuasa, "Evidence for the existence of an ordered state in Ga0. 5In0. 5P grown by metalorganic vapor phase epitaxy and its relation to band-gap energy," *Applied Physics Letters,* vol. 50, no. 11, pp. 673-675, 1987.

[38] H. Murata, I. Ho, Y. Hosokawa, and G. Stringfellow, "Surface photoabsorption study of the effect of substrate misorientation on ordering in GaInP," *Applied physics letters,* vol. 68, no. 16, pp. 2237-2239, 1996.

[39] R. Schneider Jr, E. Jones, J. Lott, and R. Bryan, "Photoluminescence linewidths in metalorganic vapor phase epitaxially grown ordered and disordered InAlGaP alloys," *Journal of applied physics,* vol. 72, no. 11, pp. 5397-5400, 1992.

[40] J.-F. Lin, M.-J. Jou, C.-Y. Chen, and B.-J. Lee, "Effect of substrate misorientation on the optical properties and hole concentration of Ga0.

5In0. 5P and (Al0. 5Ga0. 5) 0.5 In0. 5P grown by low pressure metalorganic vapor phase epitaxy," *Journal of crystal growth,* vol. 124, no. 1-4, pp. 415-419, 1992.

[41] S. Jun, C. Fetzer, R. Lee, J. Shurtleff, and G. Stringfellow, "Bi surfactant effects on ordering in GaInP grown by organometallic vapor-phase epitaxy," *Applied Physics Letters,* vol. 76, no. 19, pp. 2716-2718, 2000.

[42] J. Lambkin, L. Considine, and S. Walsh, "GM O'connor, CJ McDonagh and TJ Glynn," *Appl. Phys. Lett,* vol. 65, p. 73, 1994.

[43] M. DeLong, P. Taylor, and J. Olson, "Excitation intensity dependence of photoluminescence in Ga0. 52In0. 48P," *Applied physics letters,* vol. 57, no. 6, pp. 620-622, 1990.

[44] R.-H. Horng and M. Lee, "Ordering effect on the performance of Ga0. 5In0. 5P visible light-emitting diodes grown by metalorganic chemical vapor deposition," *Journal of applied physics,* vol. 71, no. 3, pp. 1513-1516, 1992.

[45] J. Song, S. Seo, Y. Choi, H. Song, Y. Chang, M. Oh, D. Oh, T. Yao, J. Chang, and C. Han, "High external emission efficiency in intentionally ordered GaInP/GaAs structures," *Applied Physics Letters,* vol. 94, no. 5, p. 051902, 2009.

[46] M. DeLong, D. Mowbray, R. Hogg, M. Skolnick, J. Williams, K. Meehan, S. R. Kurtz, J. Olson, R. Schneider, and M. Wu, "Band gap of ‘‘completely disordered’’Ga0. 52In0. 48P," *Applied physics letters,* vol. 66, no. 23, pp. 3185-3187, 1995.

[47] S. Froyen, A. Zunger, and A. Mascarenhas, "Polarization fields and band offsets in GaInP/GaAs and ordered/disordered GaInP superlattices," *Applied physics letters*, vol. 68, no. 20, pp. 2852-2854, 1996.

[48] P. Ernst, C. Geng, G. Hahn, F. Scholz, H. Schweizer, F. Phillipp, and A. Mascarenhas, "Influence of domain size on optical properties of ordered GaInP2," *Journal of applied physics*, vol. 79, no. 5, pp. 2633-2639, 1996.

[49] P. Ernst, C. Geng, F. Scholz, and H. Schweizer, "Ordering in GaInP2 studied by optical spectroscopy," *Physica status solidi (b)*, vol. 193, no. 1, pp. 213-229, 1996.

[50] J. Fouquet, V. Robbins, S. Rosner, and O. Blum, "Unusual properties of photoluminescence from partially ordered Ga0. 5In0. 5P," *Applied physics letters*, vol. 57, no. 15, pp. 1566-1568, 1990.

[51] J. Zeman, S. Jullian, G. Martinez, P. Yu, and K. Uchida, "Nanometer size determination of type-II domains in CuPt-ordered GaInP2 with high-pressure magneto-luminescence," *Europhysics Letters*, vol. 47, no. 2, p. 260, 1999.

[52] M. DeLong, W. Ohlsen, I. Viohl, P. Taylor, and J. Olson, "Evidence for spatially indirect recombination in Ga0. 52In0. 48P," *Journal of applied physics*, vol. 70, no. 5, pp. 2780-2787, 1991.

[53] T. Kita, M. Sakurai, K. Yamashita, T. Nishino, C. Geng, F. Scholz, and H. Schweizer, "Cooling Process of Hot Excitons in Ordered Ga0. 5In0. 5P," *Japanese Journal of Applied Physics*, vol. 39, no. S1, p. 328, 2000.

[54] S. Smith, A. Mascarenhas, S. Ahrenkiel, M. Hanna, and J. Olson, "Spatially resolved below-gap emission in partially ordered Ga x In 1− x P alloys," *Physical Review B,* vol. 68, no. 3, p. 035310, 2003.

[55] W. T. Masselink, M. Zachau, T. Hickmott, and K. Hendrickson, "Electronic and optical characterization of InGaP grown by gas-source molecular-beam epitaxy," *Journal of Vacuum Science & Technology B: Microelectronics and Nanometer Structures Processing, Measurement, and Phenomena,* vol. 10, no. 2, pp. 966-968, 1992.

[56] C. Nozaki, Y. Ohba, H. Sugawara, S. Yasuami, and T. Nakanisi, "Growth temperature dependent atomic arrangements and their role on band-gap of InGaAlP alloys grown by MOCVD," *Journal of Crystal Growth,* vol. 93, no. 1-4, pp. 406-411, 1988.

[57] T. Kanata, M. Nishimoto, H. Nakayama, and T. Nishino, "Valence-band splitting in ordered Ga 0.5 In 0.5 P studied by temperature-dependent photoluminescence polarization," *Physical Review B,* vol. 45, no. 12, p. 6637, 1992.

[58] Z. Su, J. Ning, Z. Deng, X. Wang, S. Xu, R. Wang, S. Lu, J. Dong, and H. Yang, "Transition of radiative recombination channels from delocalized states to localized states in a GaInP alloy with partial atomic ordering: a direct optical signature of Mott transition?," *Nanoscale,* vol. 8, no. 13, pp. 7113-7118, 2016.

[59] A. Sasaki, K. Tsuchida, Y. Narukawa, Y. Kawakami, S. Fujita, Y. Hsu, and G. Stringfellow, "Ordering dependence of carrier lifetimes and

ordered states of Ga 0.52 In 0.48 P/GaAs with degree of order⩽ 0.55," *Journal of Applied Physics,* vol. 89, no. 1, pp. 343-347, 2001.

[60] F. Driessen, G. Bauhuis, S. Olsthoorn, and L. Giling, "Effects of confined donor states on the optical and transport properties of ordered GaInP 2 alloys," *Physical Review B,* vol. 48, no. 11, p. 7889, 1993.

[61] D. As, S. Korf, Z. Wang, J. Windscheif, K. Bachem, and W. Jantz, "Low-temperature photoluminescence topography of MOCVD-grown InGaP, AlGaAs and AlGaAs/GaAs single quantum wells," *Semiconductor Science and Technology,* vol. 7, no. 1A, p. A27, 1992.

[62] T. Schmidt, K. Lischka, and W. Zulehner, "Excitation-power dependence of the near-band-edge photoluminescence of semiconductors," *Physical Review B,* vol. 45, no. 16, p. 8989, 1992.

[63] C. Spindler, T. Galvani, L. Wirtz, G. Rey, and S. Siebentritt, "Excitation-intensity dependence of shallow and deep-level photoluminescence transitions in semiconductors," *Journal of Applied Physics,* vol. 126, no. 17, p. 175703, 2019.

[64] J. Ning, S. Xu, Z. Deng, and Z. Su, "Polarized and non-polarized photoluminescence of GaInP 2 alloy with partial CuPt-type atomic ordering: ordered domains vs. disordered regions," *Journal of Materials Chemistry C,* vol. 2, no. 30, pp. 6119-6124, 2014.

[65] G. Moriarty, M. Kildemo, J. Beechinor, M. Murtagh, P. Kelly, G. Crean, and S. Bland, "Optical and structural properties of InGaP heterostructures," *Thin Solid Films,* vol. 364, no. 1-2, pp. 244-248, 2000.

[66] S. Kurtz, J. Olson, and A. Kibbler, "Effect of growth rate on the band gap of Ga sub 0. 5 In sub 0. 5 P," *Applied Physics Letters;(USA),* vol. 57, no. 18, 1990.

[67] J. Song, J. Kim, and Y. Lee, "Growth of highly disordered InGaP on (100) GaAs by molecular beam epitaxy with a GaP decomposition source," *Applied Physics A,* vol. 72, pp. 625-627, 2001.

[68] T. S. Moss and C. Hilsum, "Handbook on semiconductors," 1993.

[69] L. Francesio, P. Franzosi, M. Caldironi, L. Vitali, M. Dellagiovanna, A. Di Paola, F. Vidimari, and S. Pellegrino, "Investigation of the cationic ordering in InGaP/GaAs epilayers grown by low-pressure, metal organic vapour phase epitaxy," *Materials Science and Engineering: B,* vol. 28, no. 1-3, pp. 219-223, 1994.

[70] L. Francesio, L. Alagna, B. Capelle, C. Ferrari, P. Franzosi, and M. Sauvage, "X-ray diffraction study on the correlation between ordered domains size and ordering degree in InGaP/GaAs alloy layers," *Il Nuovo Cimento D,* vol. 19, pp. 537-543, 1997.

[71] S. R. Kurtz, J. Olson, D. Friedman, A. Kibbler, and S. Asher, "Ordering and disordering of doped Ga 0.5 In 0.5 P," *Journal of electronic materials,* vol. 23, pp. 431-435, 1994.

[72] L. Su, I. Ho, and G. Stringfellow, "Effects of substrate misorientation and growth rate on ordering in GaInP," *Journal of applied physics,* vol. 75, no. 10, pp. 5135-5141, 1994.

CHAPTER 7: EFFECTS OF GaAs SUBSTRATE ORIENTATION ON THE STRUCTURAL, OPTICAL, ELECTRICAL AND PHOTOVOLTAIC PROPERTIES OF InGaP-BASED SOLAR CELLS

7.1 INTRODUCTION

III-V semiconductors have been investigated as active materials for high-speed electronic, optoelectronic and solar energy devices. The inherent advantages of direct band gap and high electron mobility have led to the widespread use of III-V semiconductors such as GaInP [1]. The efficiencies of GaAs and GaInP III-V compound semiconductors based solar cells continue to improve as material quality and device processing are optimised. The band gap of GaInP grown lattice matched to GaAs is depending on the growth conditions and substrate misorientation. These changes are the result of the spontaneous ordering during the growth of the cation-site elements (Ga and In) in planes parallel to the (111) and reductions in the band gap over 100 meV can appear [2]. InGaP lattice matched to GaAs has a direct bandgap of 1.9 eV, which is a very interesting property [3]. InGaP grown using metal-organic chemical vapor deposition (MOCVD) technique is known to have a CuPt-type ordering of alternating In-rich and Ga-rich monolayers, primarily on the $(\bar{1}11)$ and $(1\bar{1}1)$ crystallographic planes, as evidenced by the $\left\{\frac{1}{2}\frac{1}{2}\frac{1}{2}\right\}$ superlattice reflections that can be observed using electron diffraction. Strain energy minimization is the main driving force for this ordering in InGaP epitaxial layers, with a large difference in bond length between the In-P and Ga-P. However, they cause significant changes in the electronic and optical properties, such as bandgap narrowing, valence band splitting, and polarization anisotropy. Previous reports

suggested that the degree of CuPt-type atomic ordering is dependent on substrate's misorientation [4]. In addition, the change of degree of ordering of CuPt leads to corresponding changes in lattice constant and photoluminescence (PL) peak energy [5]. Another report showed that the strain mismatches of the epitaxial layers in the GaInP structure decreased with increasing substrate misorientation [6]. The observed poor electrical quality of highly ordered GaInP solar cells, which were grown on 6^0 misoriented towards (111)B GaAs substrates, was attributed to traps introduced by the ordered/disordered domains matrix or growth native defects [2]. Furthermore, studying the defects caused by misorientation angles can provide useful information for fabricating high performance devices. In this work, the influence of substrate misorientation on the surface morphology, optical, electrical and photovoltaic properties of p-type InGaP-based solar cells grown by MOCVD on (001) GaAs substrates misoriented by θ_S= 0° (exact), 2°, 6°, and 10° towards (111)A are thoroughly investigated using different techniques, namely, Atomic Force Microscopy (AFM), Raman spectroscopy, Current-Voltage (I-V) , Capacitance-Voltage (C-V), Deep Level Transient Spectroscopy (DLTS), Laplace DLTS and Solar Simulator.

7.2 SAMPLE DETAILS

In collaboration with Dr Suho Park (University of Science and Technology, South Korea) a series of InGaP-based solar cells were grown in an MOCVD reactor (Veeco D180) on (100) GaAs substrates misoriented by θ_S = 0° (exact), 2°, 6°, and 10° towards (111)A. Trimethylgallium (TMGa) and trimethylindium (TMIn) were used as group-III precursors and pure phosphine (PH_3) was used as group-V precursors. Diethylzinc (DEZn) and disilane (Si_2H_6) were employed for p-type and n-type doping, respectively.

Figure 7.1 shows a schematic diagram of InGaP single-junction solar cells grown on the GaAs substrate with different substrate misorientations. The undoped InGaP and GaAs buffers were first grown with high resistance to block current flow into the substrate, followed by a 500 nm thick p^+-GaAs contact layer. A highly doped 50 nm thick p^+-InGaP back surface field (BSF) layer was grown to reduce the rear surface recombination velocity and to repel the minority carrier away from the backside. Thereafter, a p-type InGaP base layer with a 550 nm thickness was followed by a 50 nm thick n^+-type InGaP emitter layer. A thin emitter layer was adopted to provide minimal parasitic absorption in the blue energy region, and the base layer thickness was designed to be much bigger than the depletion layer length. A sufficiently thin n^+-InAlP wide bandgap material was used for the transparent window layer to avoid front surface recombination. Finally, a 100 nm thick n^+-GaAs contact layer was deposited. All layers were grown under the optimal growth conditions with a growth temperature of 650℃ and a growth rate of ~3.0 Å/s.

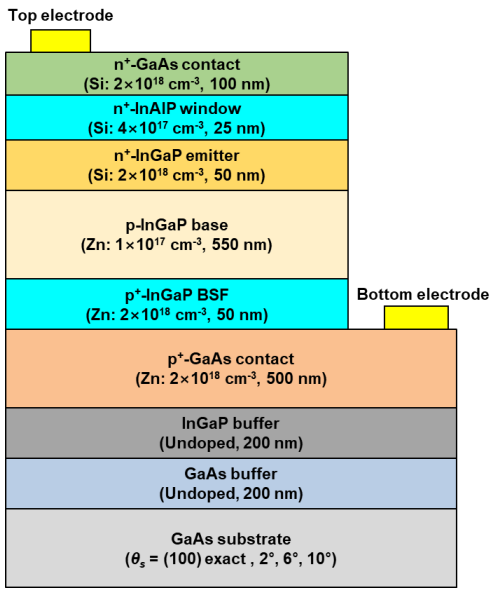


Figure 7.1: Schematic structure of InGaP single-junction solar cells grown on GaAs substrates with different orientations.

7.3 RESULTS AND DISCUSSION

7.3.1 RAMAN SPECTROSCOPY

Raman spectroscopy, which is a very powerful tool for material characterization that permits the investigation of the properties of a wide range of nanomaterials, was performed in collaboration with the group of Prof. Jorlandio F. Felix (University of Brasilia, Brazil). The experimental details are presented in Chapter 4, Section 4.9. In this work, the GaAs substrate misorientation can cause disorder and/or residual strains that can significantly influence the phonon frequencies and lifetimes, leading to broadening of the Raman peaks and the breakdown of the Raman selections rules [7]. Indeed, the frequency shifts of longitudinal optical (LO) phonon mode is strongly related to the compressive and tensile strains, resulting in positive and negative frequency shifts, respectively [8, 9].

Figure 7.2(a) shows a typical Raman spectrum (green) of the samples with $\theta_s = 0°$ at room temperature. This Raman spectrum, which has been deconvoluted into Lorentzian functions shows peaks located at ~267, ~290, ~333, ~360 and 381 cm^{-1} that are associated with the transverse optical (TO) and longitudinal optical (LO) phonon modes TO-GaAs (Γ), LO-GaAs (Γ), TO-InP (Γ), LO-InP (Γ) and TO-GaP (Γ), respectively [10-13]. In addition, all samples show an asymmetric broader structure at ∼269 cm^{-1} originating from the longitudinal optical plasmon coupled (LOPC) modes superimposed on the sharp TO-GaAs phonon peak at ∼267 cm^{-1}, which can be also associated to the doping effect [11]. The dotted line represents the fit obtained from the deconvolution. Only LO scattering is nominally allowed in the zincblende structure for backscattering from the [001] plane [12]. Although TO modes are prohibited for this geometry based on Raman selection rules, they

can be observed due to the large numerical aperture of the setup used in this work [10, 12].

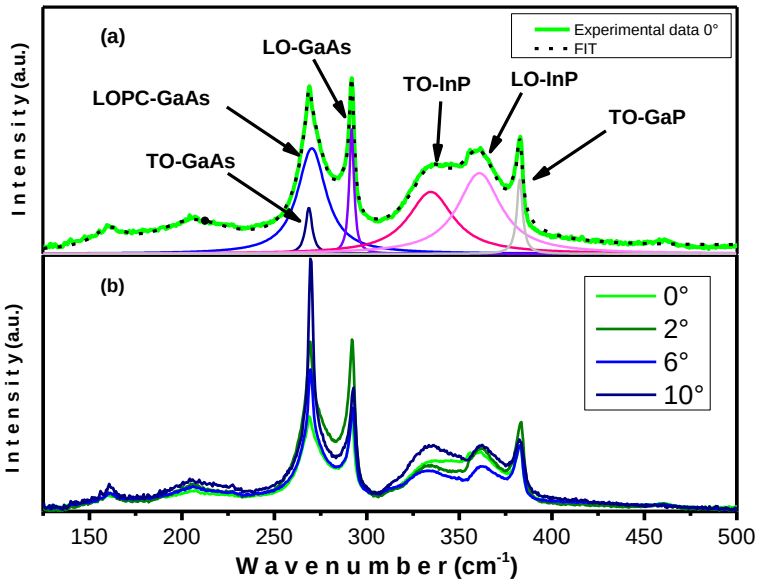


Figure 7.2: (a) Raman spectrum of the samples with θ_s = 0° (green). The internal curves represent the deconvolution into six Lorentzian peaks. (b) Raman spectra from InGaP based solar cells grown on GaAs substrates with misorientation angles of θ_s = 0°, 2°, 6° and 10°.

The Raman spectra shown in Figure 7.2(b) were obtained from the InGaP single-junction solar cell structures grown on the GaAs substrates with misorientation angles θ_s = 0°, 2°, 6° and 10° at room temperature. It was found that some of the peak positions shifted, and their relatives' intensities changed as a function of GaAs substrates misorientation angles. These changes are clearly evidenced in Figure 7.2(a), where the intensity of the characteristics GaAs phonon modes increases as a function of increase of misorientation angles.

Figure 7.3(a) shows Raman spectra from InGaP based solar cells grown on GaAs substrates with misorientation angles of θ_s = 0°, 2°, 6° and 10° around the characteristic region of the GaAs phonon modes. The vertical dashed line is used as a guide to the eyes to indicate the shift of the GaAs TO and LO phonon modes as the GaAs substrate misorientation θ_s increases. Interestingly, there is a blueshift of the GaAs LO phonon mode which is linearly proportional with the increase of the substrate misorientation, as can be seen in Figure 7.3(b).

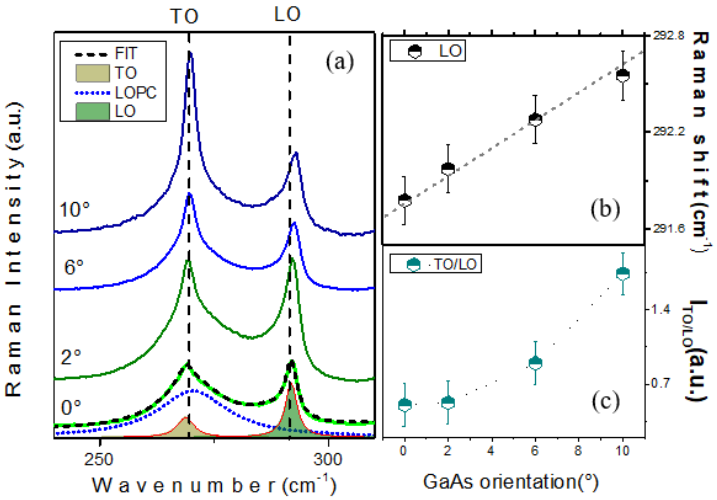


Figure 7.3: (a) Raman spectra from InGaP based solar cells grown on GaAs substrates with misorientation angles of θ_s = 0°, 2°, 6° and 10° around the characteristic region of the GaAs phonon modes. (b) GaAs LO phonon mode shifts as a function of the misorientation. The dotted lines serve as a guide to the eyes. (c) ratio between the peak intensities of the GaAs TO and LO phonon modes.

As shown in previous studies, the lattice constant of the InGaP layer decreases with increasing misorientation [14]. This phenomenon introduces a small compressive strain that makes the GaAs-like LO phonons shift towards higher frequencies. Figure 7.3(c) shows the ratio between TO and LO peak intensities ($I_{TO/LO}$) as a function of substrate misorientation. Since the presence of the TO phonon is indicative of structural disorder [15], the result of $I_{TO/LO}$ can be used accordingly to

assess the disorder of the samples [16]. It can be concluded that the disorder is quite irrelevant when comparing samples grown on GaAs substrates with θ_s = 0° and 2°, however, it becomes relevant when the misorientation angle θ_s is greater than 2°. In terms of defects, as will be shown later, this result is very important to understand the role of misorientation on electrically active defects.

7.3.2. ATOMIC FORCE MICROSCOPES (AFM)

AFM analysis was subsequently conducted to investugate the effect of the substrate misorientation on the surface morphologies of the samples. Figure 7.4 shows the AFM images of all samples studied in this work. By performing a qualitative analysis in all samples, it is clear from Figure 7.4 that there is a change in surface morphology with the substrate misorientation θ_s. Figure 7.4(a) reveals that for θ_s = 0° sample, grains with pyramidal shape with Root Mean Square (RMS) surface roughness of 30.34 nm. Figure 7.4(b) shows that for θ_s = 2°, the sample exhibited a step-flow characteristic with RMS surface roughness of 14.03 nm. While for θ_s = 6°, the sample showed a narrowing and elongation of the terraces (when compared with θ_s = 2° sample) with RMS surface roughness of 18.12 nm. Finally, for θ_s = 10°, the sample showed the lowest RMS roughness (9.77 nm) when compared to the other samples, and the step-flow characteristic observed in the last two samples (θs = 2° and 6°) practically disappeared. These results indicate that the θ_s = 2° sample showed a step-flow characteristic with the greatest prominence on its surface morphology.

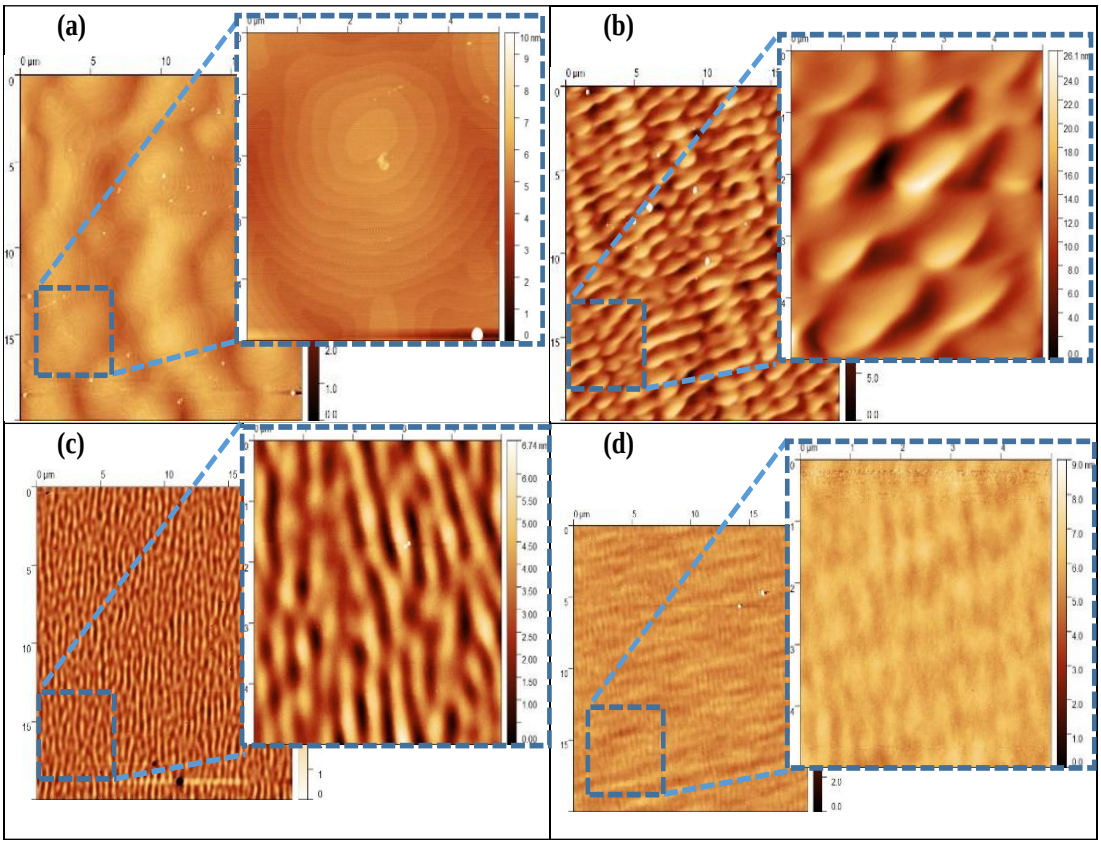


Figure 7.4: AFM images for all solar cell samples grown on different GaAs substrate orientations in a 20 × 20 and 5 × 5 μm^2 scan area with different misoriented substrates: (**a**) $\theta_s = 0°$, (**b**) $\theta_s = 2°$, (**c**) $\theta_s = 6°$, and (**d**) $\theta_s = 10°$.

7.3.3 CURRENT-VOLTAGE (I-V) MEASUREMENTS

The I-V measurements were performed at room temperature for all samples grown on GaAs substrates with different orientations as shown in Figure 7.5. It can be seen from the Figure that the reverse current of all samples are low over the range of reverse biases used up to – 4 V. However, sample grown with $\theta_s = 2°$ shows low leakage current as compared with others devices as shown in Figure 7.5(a). The leakage current of devices may be affected by various factors, including surface defects, crystal defects, deep level defects, interface states, and crystal quality, etc. [17]. In addition, from the linear I-V plot (Figure 7.5(b)) a turn-on voltage (V_{on}) of

1.3 V, 1.7 V, 2.2 V and 2 V were obtained for samples grown on-exact (001) GaAs, 2° off, 6° off and 10° off towards (111)A, respectively. The higher V_{on} of the device grown on 6° off indicates that the crystalline quality of the InGaP-based solar cell is slightly deteriorating [18].This behaviour could be attributed to the increase of the excess capacitance due to the interface states [19].

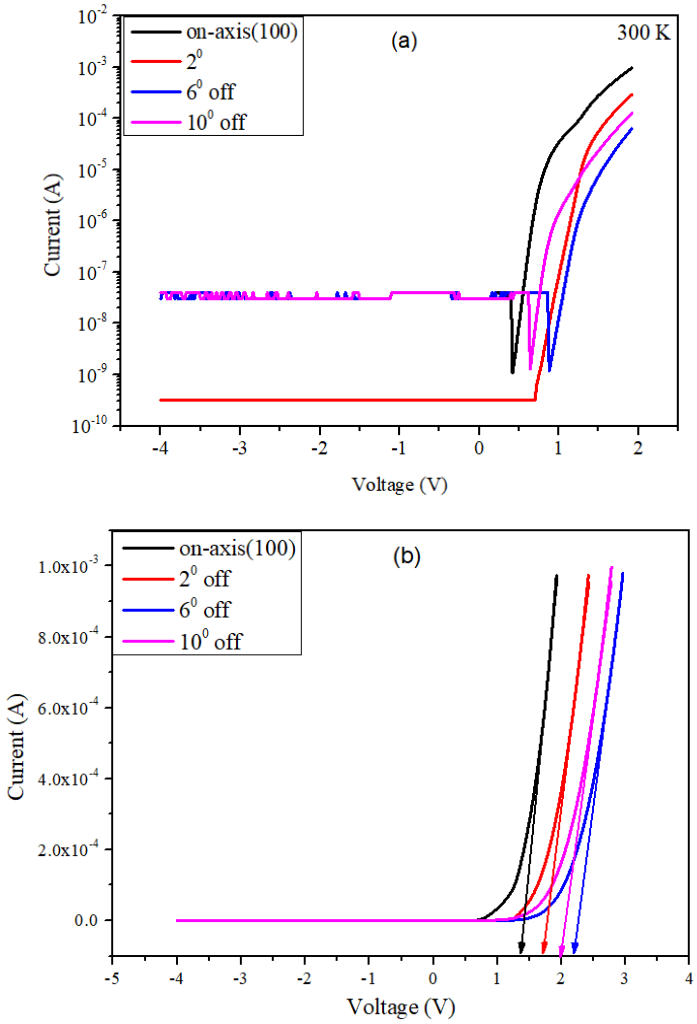


Figure 7.5: Room temperature I-V characteristics of all samples grown on GaAs substrates with different orientations: (a) Semi- logarithmic I-V plots; (b) linear I-V plots showing the turn-on voltage for each sample.

I-V measurements for all samples grown on different substrate orientations as function of temperature were carried out in the range of 20 - 300 K (with 20 K intervals) to extract the parameters of the solar cell devices and study their behaviour with temperature.

The I-V characteristics of an ideal diode [20] are described by the thermionic emission model given by equation 7.1:

$$I = I_s[exp\left(\frac{q(V-IRs)}{nKT}\right) - 1] \tag{7.1}$$

where q is the electronic charge, k is the Boltzmann constant, V is the forward applied bias, n is the ideality factor, I_s is the saturation current and T is the absolute temperature in Kelvin

where the saturation current I_s is given by:

$$I_s = AA^*T^2\, exp\left(\frac{-q\phi_b}{kT}\right) \tag{7.2}$$

where A is the area of the diode, A^* =14.1 $Acm^{-2}K^{-2}$ is the effective Richardson's constant for InGaP and ϕ_b is the built-in potential energy [21].

The ideality factor and built-in potential energy for all samples are extracted from the room temperature forward I-V characteristics as described in Chapter 4, Section 4.2. The values of n and ϕ_b summarized in Table 7.1 and Figure7.6 were obtained using the same procedure as in Chapter 5, Section 5.3.1. The ideality factors were found to be 1.29, 1.70, 2.02 and 1.24 for samples grown with $\theta_s = 0^0$, $\theta_s = 2^0$, $\theta_s = 6^0$ and $\theta_s = 10^0$, respectively.

Table 7.1: Room temperature experimental ideality factor (n) and built-in potential (ϕ_b) for samples grown on GaAs substrates with misorientation $\theta_s = 0^0$, $\theta_s = 2^0$, $\theta_s = 6^0$ and $\theta_s = 10^0$.

Samples	**Ideality factor (n)**	**built-in potential ϕ_b (eV)**
$\theta_s = 0^0$	1.290 ± 0.007	1.070 ± 0.006
$\theta_s = 2^0$	1.70 ± 0.06	1.100 ± 0.002
$\theta_s = 6^0$	2.02 ± 0.07	1.220 ± 0.003
$\theta_s = 10^0$	1.24 ± 0.01	1.240 ± 0.003

As can be seen from Figure 7.6(a), the built-in potential increases with increasing temperature. This temperature dependence of built-in potential is due to the effect of barrier inhomogeneities at the p-i-n interface [22] for all temperatures.

The ideality factor was greater than ~1.20 for all samples at all temperatures, indicating that the generation-recombination is the dominant current transport mechanism. The high ideality factor at low temperature can be attributed to the generation-recombination mechanism, interface states, the series resistance and barrier height inhomogeneities [23]

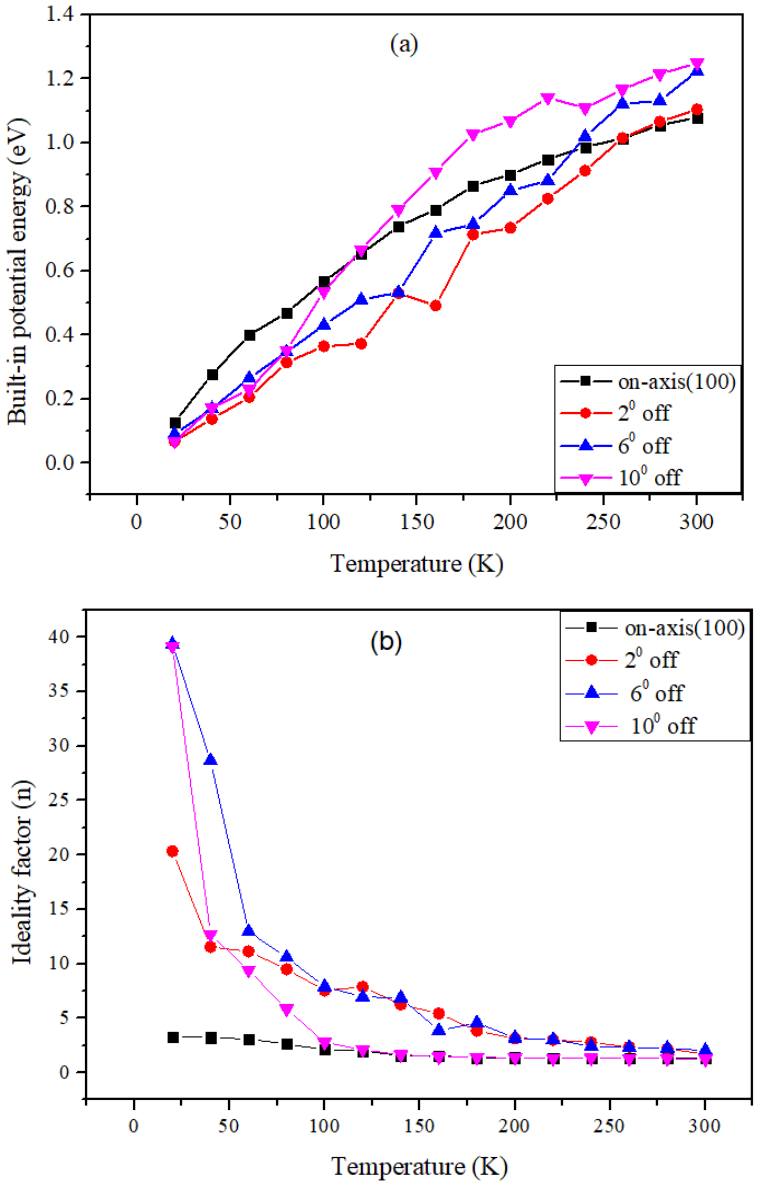


Figure 7.6: InGaP solar cell samples grown on different GaAs substrate orientations (a) built-in potential (ϕ_b) versus temperature; (b) ideality factor (n) versus temperature.

At cryogenic temperatures little thermal excitaton of the minority carriers occurs and most travel through traps within the depletion region [24]. Therefore, solar cells grown on GaAs substrates with θ_s = 6° and θs = 10° could have higher defect densities than samples grown with θ_s = 0° and 2^0 due to the fact that the ideality factors increase dramatically for temperatures below 50 K as clearly seen in Figure 7.6(b).

7.3.4 CAPACITANCE-VOLTAGE (C-V) MEASUREMENTS

The capacitance-voltage (C-V) measurements at room temperature have been carried out for all samples grown on different substrate orientations in order to determine the free carrier concentrations. As Figure 7.7 shows, sample grown with $\theta_s = 6^0$ has the highest free carrier concentration, while sample grown $\theta_s = 0^0$ has the lowest free carrier concentration. The free carrier concentrations, N_d, for all samples were calculated using the slope of the best fit of the plot $1/C^2$ versus reverse bias, as shown in Figure 7.7.

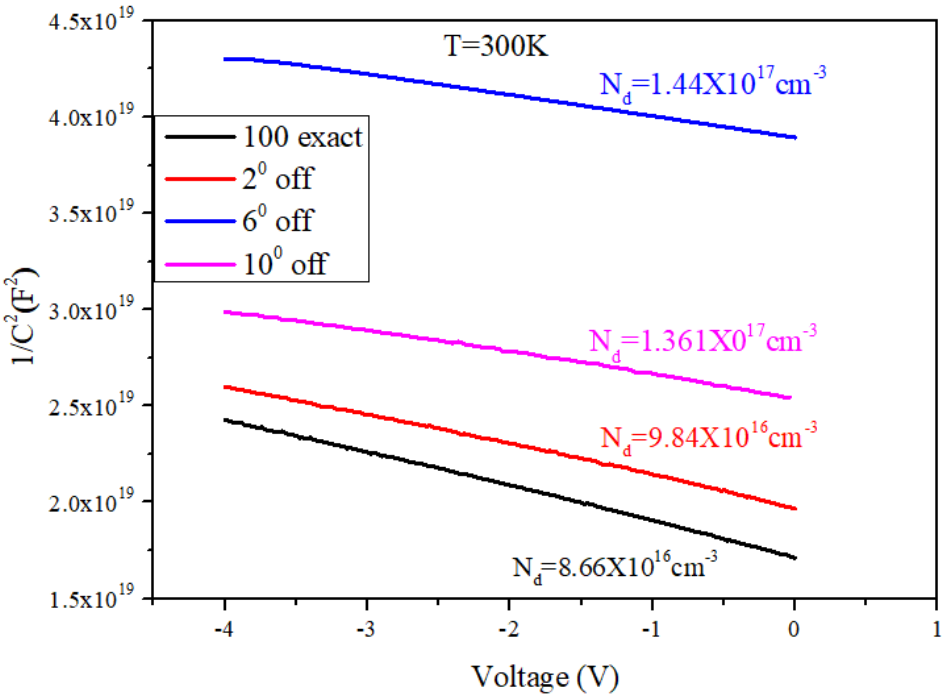


Figure 7.7: $1/C^2$ versus applied reverse bias plots at room temperature for all samples grown on different substrate orientations.

The free carrier concentration is found to be uniform for all InGaP-based solar cells samples as evidenced by the linear behaviour of the plot of $1/C^2$ versus applied bias over the reverse bias range of 0V to -4 V. The free carrier concentration is about

8.66×10^{16} cm^{-3} , 9.84×10^{16} cm^{-3}, 1.44×10^{17} cm^{-3} and 1.36×10^{17} cm^{-3} for samples grown on on-axis (100), 2^0 off , 6^0 off and 10^0 off, respectively.

7.3.5 DLTS AND LAPLACE DLTS MEASUREMENTS

The DLTS measurements [25] were carried out on p-i-n InGaP-based solar cells to to investigate the effect of the substrate orientation on the electrically active defects. In addition, Laplace DLTS (LDLTS) was used to separate the DLTS signals due to defects with closely spaced energy levels [26]. The following experimental DLTS parameters were used: reverse bias V_R = -4 V, a rate window of 200 Hz ,filling pulse characteristics Vp = 0 V and filling pulse duration t_p = *1 msec*. The samples were scanned from 10 K to 450 K.

Figure 7.8 presents the DLTS spectra for all solar cell samples which were fabricated on (100) exact, 2^o, 6^0 and 10^o off-oriented GaAs substrates. The electron and hole traps are labelled as E and H, and 1, 2, 3, and 4 refer to samples grown on GaAs substrates with $\theta_s = 0°$, $\theta_s = 2°$, $\theta_s = 6°$ and $\theta_s = 10°$, respectively. It can be seen from Figure 8.8 that all samples exhibit two electron and two hole traps, except the sample grown with $\theta_s = 2°$ which has only one electron trap. These are labeled as $E1_{(\theta s = 0°)}$ and $H1_{(\theta s = 0°)}$, $E2_{(\theta s = 2°)}$, $E3_{(\theta s = 6°)}$ and $H3_{(\theta s = 6°)}$, and $E4_{(\theta s = 10°)}$ and $H4_{(\theta s = 10°)}$ in samples grown with $\theta_s = 0°$, $\theta_s = 2°$, $\theta_s = 6°$ and $\theta_s = 10°$, respectively.

Figure 7.9 illustrates the Arrhenius plots for the traps in each sample which have been determined from Laplace DLTS measurements. The parameters of all traps in each sample are summarised in Table 7.2.

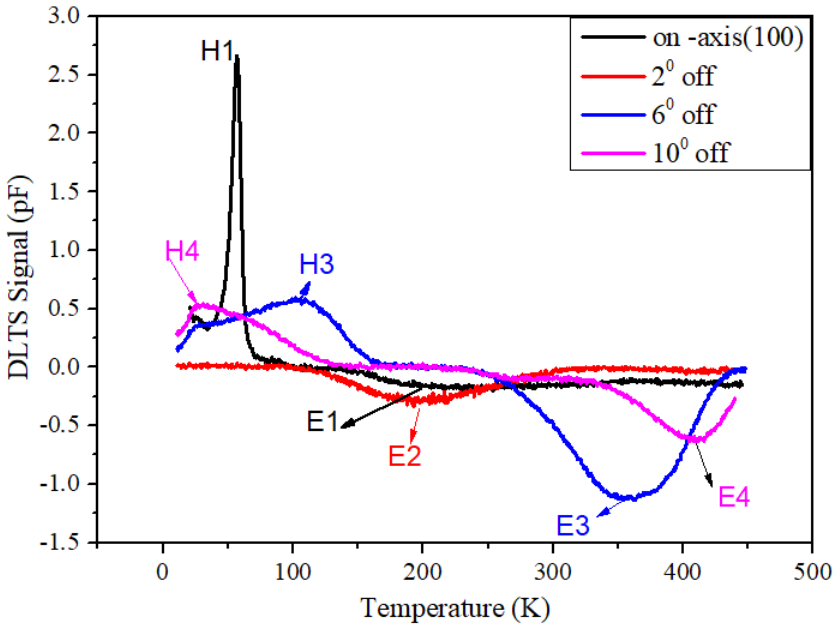


Figure 7.8: Typical DLTS spectra for all solar cell samples fabricated on different GaAs orientations. The electron and hole traps are labelled as E and H, and 1, 2, 3, and 4 refer to samples grown on GaAs substrates with $\theta_s = 0°$, $\theta_s = 2°$, $\theta_s = 6°$ and $\theta_s = 10°$, respectively.

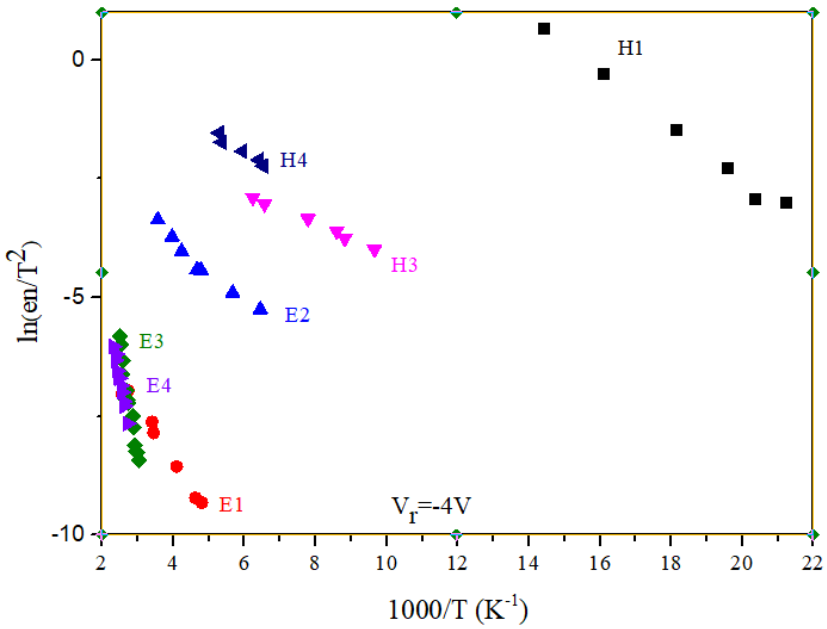


Figure 7.9: Arrhenius plots for the traps detected in each sample, which have been determined from Laplace DLTS measurements.

Table 7.2: Summary of traps activation energies, capture cross-sections (σ_n) and concentrations (N_t) for all InGaP-based solar cell samples grown on GaAs substrates with different orientations.

Samples	Activation Energy (eV)	trap concentration $N_t(cm^{-3})$	capture cross section $\sigma_n(cm^2)$
$\theta_s = 0^0$	H1 (0.049±0.002)	1.79×10^{14}	3.27×10^{-17}
	E1 (0.100±0.003)	2.48×10^{15}	1.19×10^{-22}
$\theta_s = 2^0$	E2 (0.050±0.004)	2.90×10^{14}	1.41×10^{-21}
$\theta_s = 6^0$	H3 (0.027±0.008)	1.07×10^{15}	1.91×10^{-21}
	E3 (0.39±0.02)	2.01×10^{15}	1.18×10^{-18}
$\theta_s = 10^0$	H4 (0.040±0.008)	9.11×10^{14}	1.18×10^{-20}
	E4 (0.34±0.01)	7.76×10^{14}	1.33×10^{-19}

Shallow and deep traps were observed in all samples except the sample grown on GaAs substrate with $\theta_s = 2^0$ which exhibit only one shallow electron trap in the temperature range 150 K – 250 K. As shown in Figure 7.8, a higher amplitude of the DLTS signal for trap E3 (sample with $\theta_s = 6°$) implies a higher trap concentration for E3 (2.01×10^{15} cm^{-3}) as compared to E4 (7.76×10^{14} cm^{-3}. The activation energies of E3 and E4 are 0.39eV and 0.34eV, respectively, and are very similar to the trap with activation energy of 0.40 eV found by Su et al. [27]. They suggested that the deep level in InGaP may be attributed to the excess interstitial atoms of P because by reducing the P vapour pressure to an optimum value, this deep level in the InGaP epilayer disappeared. Moreover, in another investigation Y.K et al. [28] observed a deep electron trap with activation energy of 0.39 eV and attributed it to the excess interstitial atoms of P in InGaP active region.

The electron trap of energy E1 ≈ 0.10 eV is likely to correspond to the same trap with energy of 0.17 eV reported by Chen et al. in InAlP grown by MOCVD

deposition technique [29]. They assigned this trap to oxygen impurity in the InAlP buffer layers. In addition, this electron trap was also reported by Brounkov et al. [30] in buffer layers with concentration of ~ 6.6 x 10^{15}cm^{-3} which is close to the concentration of E1 trap detected in this work.

Electron trap E2 with activation energy of 0.050 eV and concentration of ~2.90 x 10^{14} cm^{-3} observed in sample grown with $\theta_s = 2^0$ could be the same trap as the one observed by Feng et al [31] in InGaP grown by MOCVD with energy 0.070 eV. This was attributed to DX center which is associated with a donor impurity.

Trap H3 (0.027 eV) could be related to the trap called DX center with activation energy of about 0.020eV which was found at temperature around 130 K [32]. Shallow hole traps H1 (0.049 eV) and H4 (0.040 eV) detected in samples with $\theta_s = 0^0$ and $\theta_s = 10°$, respectively, could not be identified in this work, but these could be related to shallow impurities introduced either intentionally or unintentionally.

7.3.6: DISCUSSION OF THE ROLE OF THE DEFECTS ON THE PERFORMANCE OF SOLAR CELLS GROWN ON VARIOUS GaAs MISORIENTED SUBSTRATES

The photovoltaic measurements were performed at the Korea Research Institute Standards and Science (KRISS), Daejeon, Republic of Korea. The current density versus voltage (J-V) characteristics shown in Figure 7.10 were measured under standard test conditions (AM1.5G, 100 mW/cm^2 and 25°C) for GaInP-based solar cells grown on different GaAs substrate orientations. Figure 7.11 displays the open circuit voltage (V_{oc}) and short-circuit current (I_{sc}) of all samples as a function of substrate misorientation. *Voc* and *Isc* values are extracted from Figure 7.10. The performance parameters Fill Factor (FF) and efficiency (η) of all samples are

calculated from the obtained results shown in Figure 7.10. The procedure to extract these parameters is explained in Chapter 4, Section 4.10. The average photovoltaic parameters for InGaP solar cells grown on different substrate orientations (AM 1.5G, 100 mW/cm^2) are summarized in Table 7.3.

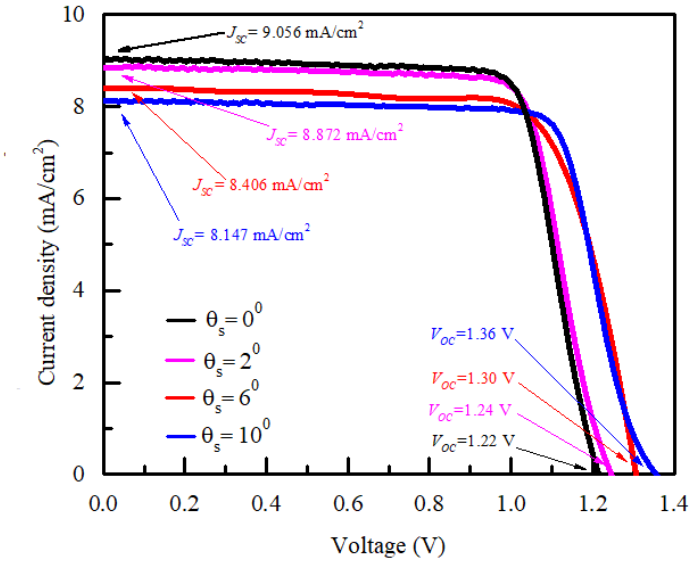


Figure 7.10: J-V characteristics of all solar cell samples under AM1.5G illumination.

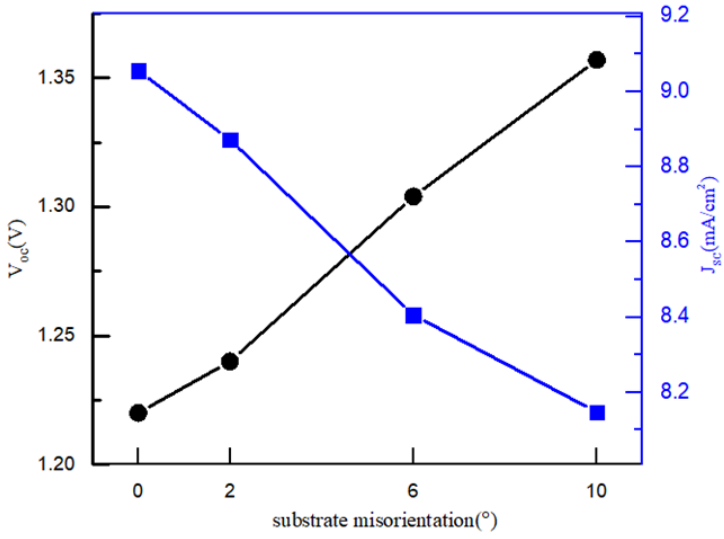


Figure 7.11: Open circuit voltage (V_{oc}) and short-circuit current density (J_{sc}) of all samples as a function of substrate misorientation.

Table 7.3: Performance parameters of samples calculated from measurements results shown Figure 7.10.

Substrate misorientation	V_{oc} (V)	J_{sc} (mA/cm^2)	Fill factor (%)	Efficiency (%)
(100) exact	1.22	9.056	77.3	8.49
θ_s = 2°	1.24	8.872	76.9	8.46
θ_s = 6°	1.30	8.406	75.3	8.26
θ_s = 10°	1.36	8.147	75.5	8.35

It can be clearly seen from Figuer 7.11 and Table 7.3 that the V_{oc} value increases with the increase of the substrate misorientation angle. In addition, by increasing the substrate misorientation angle J_{sc} value decreases. It is well-known that Jsc and Voc are directly and inversely proportional to the bandgap of semiconductor solar cell devices, respectively. J. Lee showed that the quality of InGaP epilayers enhances with the crystallographic orientation or off-axis angle due to a decrease of the strain [33]. Samples grown with $\theta_s = 0°$ and $\theta_s = 2°$ have closely similar efficiencies. However, sample grown with $\theta_s = 6°$ has the lowest values of efficiency (η =8.26) and fill factor (75.3). In addition, this sample has the highest ideality factor (n=2.2) as compared with the other samples. Previous studies reported that there are several factors that can significantly influence FF such as defects, series resistance, shunt resistance and higher ideality factor [34, 35]. Another investigation showed poor electrical quality of highly ordered GaInP solar cells which were grown on GaAs substrates misoriented 6° toward (111)B [36]. R. Oshima at al. [37] studied the effects of substrate miscut on the properties of lattice-matched $In_{0.52}Ga_{0.48}P$-based solar cells grown on (100) GaAs substrates by MBE with the aim to enhance their efficiency. In addition to exact (100) GaAs substrates, they used (100) GaAs substrates miscut 2^0 and 6° towards (111)B and 2^0 and 6° towards (111)A. It was found that the performance of the solar cells was affected

by atomic ordering. They observed that the B-type miscut induced single-variant atomic ordering, which was suppressed in the A-type miscut. Enhancements in V_{OC} were reported in solar cells grown on A-type miscut substrates, which was believed to be due to the reduced degree of atomic ordering. However, the use of B-type miscut substrates showed a large improvement in W_{OC} due to a reduction in the number of antiphase boundaries caused by single-variant ordering. W_{OC}, which is an empirical figure of merit, represents the difference between Eg/q and V_{OC} and helps in comparing the solar cell voltages. The highest (10.93%) and lowest (8.27%) efficiencies were obtained using InGaP solar cells grown on (100) GaAs miscut 2^0 towards (111)B and 6^0 towards (111)B, respectively. Similarly, as shown in Table 7.3, the sample with misorientation $\theta s = 6°$ is not ideal for the growth of InGaP-based solar on GaAs as it has the lowest efficiency. Garcia et al. [2] investigated the influence of GaInP ordering on the electrical quality and showed poor electrical properties of GaInP solar cells which were grown on GaAs substrates misoriented 6^0 toward (111)B. A strong correlation was observed between the increase in the activation energies and concentration of defects and the decrease of efficiency for samples grown on (100) exact ($\theta_s = 0°$), 6° and 10° misoriented GaAs substrates. Defects introduce energy levels in the bandgap, and act as recombination centres, which reduce the free carrier lifetime [38], and therefore degrade the efficiency of solar cells.

7.4: SUMMARY

The effects of the substrate misorientation on the surface morphology, optical, electrical and photovoltaic properties of p-doped $In_{0.48}Ga_{0.52}P$-based solar cells grown by MOCVD technique on (100) GaAs substrates misoriented by θ_S= 0° (exact), 2°, 6°, and 10° towards (111)A have been investigated using AFM, Raman, IV, CV, DLTS, Laplace DLTS and Solar Simulator. From Raman measurements, it was concluded that the disorder is quite irrelevant for samples grown on GaAs substrates with $\theta s = 0°$ and $\theta s = 2°$, however, it becomes relevant when the misorientation angle θ_s is greater than 2°. AFM studies showed surface morphology changes with substrate misorientation angles. Sample grown with $\theta_s = 0^0$ had the smoothest surface. I-V and DLTS measurments showed that sample grown with $\theta_s = 2°$ has a low leakage current as compared with others devices and exhibited only one electron trap. While the sample grown on $\theta_s = 6^0$ showed the highest trap actvation energies, concentrations and the lowest efficiency. These results represent a significant step towards the development of high efficiency multijunction solar cells grown by MOCVD.

REFERENCES

[1] G. Martín, C. Coll, L. López-Conesa, J. M. Rebled, E. Barrigón, I. García, I. Rey-Stolle, C. Algora, A. Cornet, and S. Estradé, "Understanding the Anisotropy in the Electrical Conductivity of CuPtB-type Ordered GaInP Thin Films by Combining In Situ TEM Biasing and First Principles Calculations," *ACS applied electronic materials,* vol. 4, no. 7, pp. 3478-3485, 2022.

[2] I. Garcia, I. Rey-Stolle, C. Algora, W. Stolz, and K. Volz, "Influence of GaInP ordering on the electronic quality of concentrator solar cells," *Journal of Crystal Growth,* vol. 310, no. 23, pp. 5209-5213, 2008.

[3] O. Martínez, V. Hortelano, V. Parra, J. Jimenez, T. Prutskij, and C. Pelosi, "InGaP Layers Grown on Different GaAs Surfaces for High Efficiency Solar Cells," *MRS Online Proceedings Library,* vol. 1167, no. 1, pp. 4-9, 2009.

[4] T. Suzuki, A. Gomyo, and S. Iijima, "Strong ordering in GaInP alloy semiconductors; Formation mechanism for the ordered phase," *Journal of Crystal Growth,* vol. 93, no. 1-4, pp. 396-405, 1988.

[5] S.-H. Wei and A. Zunger, "Fingerprints of CuPt ordering in III-V semiconductor alloys: Valence-band splittings, band-gap reduction, and x-ray structure factors," *Physical Review B,* vol. 57, no. 15, p. 8983, 1998.

[6] T. Lin, N. Lin, C. Xiong, L. Zhong, Q. Qi, Y. Zhao, C. Wang, E. Guo, S. Liu, and X. Ma, "Effects of the substrate misorientation on the structural and optoelectronic characteristics of tensile GaInP quantum well laser diode wafer," *Journal of Alloys and Compounds,* vol. 688, pp. 83-87, 2016.

[7] R. Loudon, "The Raman effect in crystals," *Advances in Physics,* vol. 13, no. 52, pp. 423-482, 1964.

[8] P. Wickboldt, E. Anastassakis, R. Sauer, and M. Cardona, "Raman phonon piezospectroscopy in GaAs: Infrared measurements," *Physical Review B,* vol. 35, no. 3, p. 1362, 1987.

[9] J. Groenen, G. Landa, R. Carles, P. Pizani, and M. Gendry, "Tensile and compressive strain relief in In x Ga 1− x As epilayers grown on InP probed by Raman scattering," *Journal of applied physics,* vol. 82, no. 2, pp. 803-809, 1997.

[10] E. Yaccuzzi, S. Di Napoli, E. J. Di Liscia, S. Suárez, M. Alurralde, A. Strittmatter, J. Pla, and P. Giudici, "Experimental re-evaluation of proton penetration ranges in GaAs and InGaP," *Journal of Physics D: Applied Physics,* vol. 54, no. 11, p. 115302, 2021.

[11] S. Zhu, W. Qiu, H. Wang, T. Lin, P. Chen, and X. Wang, "Raman spectroscopic determination of hole concentration in undoped GaAsBi," *Semiconductor Science and Technology,* vol. 34, no. 1, p. 015008, 2018.

[12] G. Moriarty, M. Kildemo, J. Beechinor, M. Murtagh, P. Kelly, G. Crean, and S. Bland, "Optical and structural properties of InGaP heterostructures," *Thin Solid Films,* vol. 364, no. 1-2, pp. 244-248, 2000.

[13] H. Dong, J. Sun, S. Ma, J. Liang, T. Lu, X. Liu, and B. Xu, "Influence of substrate misorientation on the photoluminescence and structural properties of InGaAs/GaAsP multiple quantum wells," *Nanoscale,* vol. 8, no. 11, pp. 6043-6056, 2016.

[14] S. Park, T. T. Nguyen, L. Q. Nguyen, Y. Kim, and S. J. Lee, "Material and device characterization of InGaP solar cells grown on GaAs misoriented

substrates by metal-organic chemical vapor deposition," *Solar Energy*, vol. 220, pp. 406-411, 2021.

[15] G. Landa, R. Carles, J. Renucci, C. Fontaine, E. Bedel, and A. Munoz-Yague, "Raman characterization of twinning in heteroepitaxial semiconductor layers: GaAs/(Ca, Sr) F2," *Journal of applied physics*, vol. 60, no. 3, pp. 1025-1031, 1986.

[16] P. Pizani, F. Lanciotti Jr, R. G. Jasinevicius, J. G. Duduch, and A. J. V. Porto, "Raman characterization of structural disorder and residual strains in micromachined GaAs," *Journal of Applied Physics*, vol. 87, no. 3, pp. 1280-1283, 2000.

[17] J. Li, C. Meng, L. Yu, Y. Li, F. Yan, P. Han, and X. Ji, "Effect of various defects on 4H-SiC Schottky diode performance and its relation to epitaxial growth conditions," *Micromachines*, vol. 11, no. 6, p. 609, 2020.

[18] L.-E. Cai, B.-P. Zhang, J.-Y. Zhang, C.-M. Wu, F. Jiang, X.-L. Hu, M. Chen, and Q.-M. Wang, "Improvement of efficiency droop of GaN-based light-emitting devices by a rear nitride reflector," *Physica E: Low-dimensional Systems and Nanostructures*, vol. 43, no. 1, pp. 289-292, 2010.

[19] M. Aziz, A. Mesli, J. Felix, D. Jameel, N. Al Saqri, D. Taylor, and M. Henini, "Effect of post-growth annealing treatment on interfacial misfit GaSb/GaAs heterostructures," *Journal of Crystal Growth*, vol. 424, pp. 5-10, 2015.

[20] S. Sze and M. Lee, "Semiconductor Devices. Physics and Technology, - John Wiley & Sons Singapore Pte. Ltd," 2013.

[21] D. Zhang, X. Wang, and S. Yoon, "Schottky contacts on wide bandgap InGaP grown with phosphorous cracker cells and their thermal reliability," *Materials Science and Engineering: B,* vol. 74, no. 1-3, pp. 143-146, 2000.

[22] A. Chitnis, A. Kumar, M. Shatalov, V. Adivarahan, A. Lunev, J. Yang, G. Simin, M. A. Khan, R. Gaska, and M. Shur, "High-quality p–n junctions with quaternary AlInGaN/InGaN quantum wells," *Applied Physics Letters,* vol. 77, no. 23, pp. 3800-3802, 2000.

[23] J. M. Shah, Y.-L. Li, T. Gessmann, and E. F. Schubert, "Experimental analysis and theoretical model for anomalously high ideality factors (n≫ 2.0) in AlGaN/GaN pn junction diodes," *Journal of applied physics,* vol. 94, no. 4, pp. 2627-2630, 2003.

[24] M. Aziz, J. F. Felix, N. Al Saqri, D. Jameel, F. S. Al Mashary, H. M. Albalawi, H. M. A. Alghamdi, D. Taylor, and M. Henini, "Electrical behavior of MBE grown interfacial misfit GaSb/GaAs heterostructures with and without te-doped interfaces," *IEEE Transactions on Electron Devices,* vol. 62, no. 12, pp. 3980-3986, 2015.

[25] D. Lang, "Deep-level transient spectroscopy: A new method to characterize traps in semiconductors," *Journal of applied physics,* vol. 45, no. 7, pp. 3023-3032, 1974.

[26] L. Dobaczewski, A. Peaker, and K. Bonde Nielsen, "Laplace-transform deep-level spectroscopy: The technique and its applications to the study of point defects in semiconductors," *Journal of applied physics,* vol. 96, no. 9, pp. 4689-4728, 2004.

[27] S. Lan, C. Q. Yang, D. L. Cui, W. J. Xu, and H. D. Liu, "Deep levels in undoped In0. 5Ga0. 5P and In0. 5Ga0. 5P0. 99As0. 01 grown on GaAs

(100) substrates," *Applied physics letters,* vol. 66, no. 7, pp. 872-874, 1995.

[28] Y. Su, M. Wu, C. Chang, and K. Cheng, "Electrical and optical properties of high purity In0. 5Ga0. 5P grown on GaAs by liquid phase epitaxy," *Journal of crystal growth,* vol. 76, no. 2, pp. 299-304, 1986.

[29] J. Chen, Z. Huang, K. Lee, and R. Kanjolia, "Effects of trimethylindium on the purity of In 0.5 Al 0.5 P and In 0.5 Al 0.5 as epilayers grown by metalorganic chemical vapor deposition," *Journal of electronic materials,* vol. 26, no. 4, pp. 361-365, 1997.

[30] P. Brounkov, T. Benyattou, G. Guillot, and S. Clark, "Admittance spectroscopy of InAlAs/InGaAs single-quantum-well structure with high concentration of electron traps in InAlAs layers," *Journal of applied physics,* vol. 77, no. 1, pp. 240-243, 1995.

[31] S. Feng, J. Bourgoin, F. Omnes, and M. Razeghi, "Defects in organometallic vapor-phase epitaxy-grown GaInP layers," *Applied physics letters,* vol. 59, no. 8, pp. 941-943, 1991.

[32] G. Sun, J. Bourgoin, N. De Angelis, M. Yamaguchi, A. Khan, T. Takamoto, and O. Gilard, "Metastability effects in InGaP solar cells," *Solar energy materials and solar cells,* vol. 75, no. 1-2, pp. 293-298, 2003.

[33] J. Lee, "Influences of crystallographic misorientation of GaAs substrateson misfit stresses and microhardness of InGaP epilayers," *Thin solid films,* vol. 320, no. 2, pp. 173-178, 1998.

[34] B. Qi and J. Wang, "Fill factor in organic solar cells," *Physical Chemistry Chemical Physics,* vol. 15, no. 23, pp. 8972-8982, 2013.

[35] T. P. Weiss, O. Ramírez, S. Paetel, W. Witte, J. Nishinaga, T. Feurer, and S. Siebentritt, "Metastable defects decrease the fill factor of solar cells," *arXiv preprint arXiv:2205.00826,* 2022.

[36] S. Yu, J. Dong, Y. Zhao, Y. Sun, K. Li, X. Zeng, and H. Yang, "Influence of GaInP ordering on the performance of GaInP solar cells," *Journal of Semiconductors*, vol. 37, no. 7, p. 073001, 2016.

[37] R. Oshima, Y. Nagato, Y. Okano, and T. Sugaya, "Effects of substrate miscut on the properties of InGaP solar cells grown on GaAs (001) by solid-source molecular beam epitaxy," *Japanese Journal of Applied Physics,* vol. 56, no. 8S2, p. 08MC08, 2017.

[38] N. Touafek and R. Mahamdi, "Excess defects at the CdS/CIGS interface solar cells," *Chalcogenide Letters,* vol. 11, no. 11, pp. 589-596, 2014.

CHAPTER 8: CONCLUSION AND FUTURE WORK

This chapter summarises the research work carried out on the structural, electrical and optical properties of dilute GaAsPN and GaInP based solar cell structures and devices. AFM, I-V, C-V, DLTS, Laplace DLTS, Raman and PL characterisation techniques were used to investigate these materials and heterostructures. In addition, suggestions of future work are presented in this chapter.

8.1 CONCLUSION

8.1.1 THE EFFECT OF V(P)/III(Ga) FLUX RATIO AND THERMAL ANNEALING ON THE ELECTRICAL PROPERTIES OF DILUTE NITRIDE GaAsPN

The effect of growth condition, namely V(P)/III(Ga) flux ratios on the electrical properties of dilute nitride $GaAs_{0.1}P_{0.89}N_{0.01}$ alloys grown by MBE have been investigated. From I-V measurements, the leakage current of the samples grown with low P/Ga flux ratio (5) is lower than the sample grown with high P/Ga flux ratio (21). For all samples, the values of the ideality factor are greater than unity, and these higher values can be attributed to the generation –recombination currents, interface states, and the series resistance effects. It was observed that the samples grown with higher flux ratio of 21 exhibited more defects as compared with samples grown on low flux ratio of 5. In addition, the influence of the thermal annealing treatment on the electrical properties of $GaAs_{0.1}P_{0.89}N_{0.01}$ alloys have been studied. After annealing both samples showed lower leakage currents and ideality factor values than the as-grown samples. Moreover, the sample grown with flux ratio of 5

showed two hole traps before and after annealing, however, their concentrations decreased after the thermal treatment with low concentrations. For sample grown with flux ratio 21 two new hole traps and one new electron trap appeared after annealing while the as-grown sample exhibited only three hole traps. All traps' concentrations decreased after thermal annealing. Considering the lower ideality factors and traps concentrations, it was concluded that the annealed devices are closer to the ideal solar cell diodes than the as-grown devices.

8.1.2 INVESTIGATION OF THE EFFECT OF GaAs SUBSTRATE ORIENTATIONS AND InGaP DOPING ON THE ELECTRICAL AND OPTICAL PROPERTIES OF InGaP-BASED SOLAR CELL STRUCTURES

The effects of GaAs substrate orientation and n-doping of InGaP in the i-region of the p-i-n structures on the electrical and optical properties of InGaP based solar cells grown by MOCVD technique were studied and analysed using J-V, C-V, DLTS, Laplace DLTS techniques, photoluminescence spectroscopy (PL) and SILVACO TCAD modelling.

From the J-V characteristics, the reverse current density and a turn-on voltage were higher for sample grown on (100) 2^0 off towards (111B) than those of samples grown on exact (100) GaAs substrates. In addition, the C-V measurements indicated that the free carrier concentration is non-uniform in the n-InGaP grown on exact (100). Furthermore, the DLTS technique has been used to investigate the electrically active defects in all samples. One trap has been detected in all samples grown on exact (100) GaAs substrates with activation energy ≈ 0.10 eV except for sample grown on (100) 2^0 off towards (111B) where two traps have been observed

with activation energies ranging from 0.10 eV to 0.26 eV. Silvaco TCAD was used for modelling the effect of GaAs substrate orientations and n-doping of InGaP in the i-region of the p-i-n structutes on the forward current characteristics. A good agreement between simulations and measurements was obtained for n-doped and undoped InGaP grown on exact (100) GaAs substrates by taking into account the properties of the traps detected in the samples by DLTS and the electron profiles determined using electrochemical capacitance-voltage measurements. For sample grown on (100) 2^0 off towards (111B), there was a disagreement between simulation and measurement, which might be attributed to the dominance of tunnelling via dislocation transport mechanism, however, a good agreement was obtained for a dislocation density of 1×10^3 cm^{-2}. PL spectra as function of temperature and laser power intensity showed different emission bands depending on the experimental conditions. At high temperatures and laser intensity, it was observed that the highest energy emission peak (A) dominates the PL spectrum. This band was associated with excitonic and free carrier's transitions in fully disordered InGaP. An additional low energy emission peak (B) was observed at lower temperatures which was attributed to spatially indirect transition in ordered domains, involving electrons at donors and photoexcited holes.

8.1.3 EFFECT OF GaAs SUBSTRATE ORIENTATION ON THE ELECTRICAL AND OPTICAL PROPERTIES OF InGaP SOLAR CELLS

Electrical and optical measurements were used to investigate the properties of p-type InGaP-based solar cells grown by MOCVD on (100) GaAs substrates misoriented by θ_S= 0° (exact), 2°, 6°, and 10° towards (111)A. From Raman

measurements, it was concluded that the disorder is quite irrelevant for samples grown on θs = 0° and θs = 2° GaAs substrates. However, it becomes relevant when the misorientation angle θs is greater than 2°. AFM measurements indicated that the surface morphology changes with substrate misorientation angles. Sample grown with θs = 0^0 showed the smoothest surface. The C-V measurements indicated that the free carrier concentration is uniform for all InGaP-based solar cells samples. I-V and DLTS measurements showed that the sample grown with θs = 2° has a low leakage current as compared with others devices. In addition to that , all samples exhibited two electron and two hole traps, except the sample grown with θs = 2° which has only one electron trap. The sample grown on θs= 6^0 showed the highest trap activation energies, concentrations and the lowest efficiency.

8.2 SUGGESTIONS FOR FUTURE WORK

Suggestions for further work based on the results obtained from this thesis are discussed in the following:

- GaAsPN has an important impact on developing GaP-based optoelectronics and multijunction solar cells, but the complex nature of the nitrogen incorporation into GaAsP is still not fully understood. The control and understanding of the incorporation of nitrogen during GaAsPN MBE growth continues to play an important role in GaP crystal growth. Therefore, a study of the effects of the growth temperature, V(P)/III(Ga) flux ratios and N contents on the electrical and optical properties of GaAsPN epilayers grown on GaP substrates by MBE is crucial in order to improve their properties for solar cell applications.

- It is well established that heat treatment procedures can eliminate defects and/or decrease substantially their concentrations. Using different thermal annealing conditions and techniques, such as furnace annealing and rapid thermal annealing techniques, will help determine the proper choice of annealing methods and parameters that could have a significant impact on both device performance and overall yield of GaAsPN-based solar cell devices.

- The high-speed crystal growth of III–V semiconductors by MOCVD is one of the most important technologies to decrease the cost-performance ratio of III–V semiconductor-based solar cells by increasing production throughput. Investigation of the influence of the growth rate and growth temperature on the quality of InGaP epilayers and the optimisation of the growth conditions are of paramount importance to achieve high efficiency solar cells.

- Due to radiation in space and the use of electronic, optoelectronic and photovoltaic devices in satellites, considerable amount of defects can be induced in semiconductors which, in turn, can cause degradation and decrease of the average lifetime of the devices. The effect of radiation treatment, for example in metal/semiconductor Schottky diodes using a variety of radiation sources such as electron, neutron and gamma radiation, has been studied previously. The influence of gamma irradiation on the structural, electrical and optical properties of InGaP epilayers can contribute to a better understanding of these materials for space applications.